Production of Functional Materials for Advanced Thermoelectric Applications

Dunlop, Tom O.

Swansea University
Prifysgol Abertawe

Production of Functional Materials for Advanced Thermoelectric Applications

Tom Oliver Dunlop

Thesis submitted to Swansea University in fulfilment of the requirements for the Degree of Engineering Doctorate

COATED/M2A/NRN

College of Engineering Materials Research Centre

2018

Abstract

With ever increasing energy costs, climate change and energy supply concerns there has been a drive towards sustainable and renewable energy sources. There are many industries which currently produce excess waste heat such as reactors, motorised transport, metal production, and gas turbines to name a few. These industries can reduce their carbon footprint with successful heat scavenging.

A much-overlooked technology is thermoelectric generators. These are solid-state devices which can convert heat directly into electricity using the Seebeck effect. There are number of advantages of thermoelectrics over conventional renewables including no moving parts, maintenance-free functionality in extreme environments, high-temperature resistance and long-life span. Thermoelectrics can function as both primary generators or as thermal scavengers, however they are not yet suitable for mass market applications.

This thesis will investigate the entire thermoelectric device and develop scalable alternatives to current technologies. In this the production of earth abundant thermoelectrics, focusing on transition metal silicides, was investigated using a novel pack cementation technique to produce high quality materials that are affordable and require only low-cost equipment to produce. This technique was shown to produce high purity materials; however, production rates were limited due to the diffusion rates.

The second part of this thesis investigated the soldered contacts for device construction; as current soldered contacts are subject to fatigue, can be costly and at times toxic. Molten liquid electrical contacts were developed and whilst promising are limited by their compatibility with current thermoelectric materials. The most successful work was that of printable, conductive polymers. These were developed to be stable at high temperatures, bind well with current thermoelectric materials and provide a new contact material allowing fully automated production.

To ascertain the viability of the developed conductive polymer contacts, further work was undertaken to prototype functional devices which led to promising results for future upscaling.

DECLARATION

This work has not previously been accepted in substance for any degree and is not being concurrently submitted in candidature for any degree.

Signed ..... (candidate)

Date .....

STATEMENT 1

This thesis is the result of my own investigations, except where otherwise stated. Where correction services have been used, the extent and nature of the correction is clearly marked in a footnote(s).

Other sources are acknowledged by footnotes giving explicit references. A bibliography is appended.

Signed ..... (candidate)

Date .....

STATEMENT 2

I hereby give consent for my thesis, if accepted, to be available for photocopying and for inter-library loans after expiry of a bar on access approved by the Swansea University.

Signed ..... (candidate)

Date .....

It is well known that a vital ingredient of success is not knowing that what you're attempting can't be done

Science is not about building a body of known “facts”. It is a method for asking awkward questions and subjecting them to a reality-check, thus avoiding the human tendency to believe whatever makes us feel good.

Think critically about what you are told. Do not accept the word of authority unthinkingly. Science is not a belief system: no belief system instructs you to question the system itself. Science does. (There are many scientists, however, who treat it as a belief system. Be wary of them.)

Terry Pratchett

Contents

Acknowledgements

I would firstly like to gratefully acknowledge the National Research Network in Advanced Engineering Materials (NRN072), EPSRC, European Social Fund, M2A and COATED for their continued funding and support throughout the course of this project. I would also like to acknowledge the Swansea University AIM facility (EP/M028267/1, ERDF 80708 and Ser Solar) for access to their fantastic SEM suites.

I would like to thank the European Space Agency, Gervaux and Scatec As for supporting me in this doctoral program, namely Prof. David Jarvis and Dr. Wayne Voice as my industrial supervisors. Their help has been greatly appreciated, and their advice, ideas and guidance allowed this project to maintain a continued progression without getting too bogged down.

A massive thank you to Prof. James Sullivan as my academic supervisor. My first port of call Prof. Sullivan constantly provided support, advice and suggestions helping me keep on track and not allowing me to get too demoralised when things did not work out as intended.

On a personal note I would like to give my thanks, with love, to my partner Sarah-Jane Potts, for without her constant support, advice, tidying up after me, and occasional prodding to write, this thesis would not have been written.

I would like to thank my fellow EngD students Becky Waldram, Phil Ansell, Henry Illsley and Ben Smith, who, at some point, over these last 5 years lived with me, putting up with my numerous hobbies and resultant bows, tools and other sporting paraphernalia littering the house. Particular thanks go to Becky and Phil who got me through some tough times with our lab-based chats and moans. Thanks also go to the King's School CCF (Grantham) and Swansea University Archery Club for allowing me to blow off steam by shooting stuff.

I would not be where I am today without my parents Sally and Peter, my little sister Megan and our loyal dog Ghillie. Without your love, support, encouragement and occasional nagging I would not have made it to university, let alone be completing this thesis. Thank you for supporting me in being myself and allowing me to follow my dreams, no matter how hard it got. I would like to dictate this thesis to my family. Without you none of this would be possible.

List of Figures

List of Abbreviations

The following table describes the various abbreviations and acronyms used throughout this thesis.

ABBREVIATION	EXPLANATION
5480PS	Product name for silver coated glass flakes sold by NSG
BS(D)	Back Scatter electron (Detector)
CB	Carbon Black
CNTS	Carbon Nanotubes
CSP	Concentrated Solar Power
CVD	Chemical Vapour Deposition
DSC	Differential-Scanning Calorimetry
EBSD	Electron Back Scatter Diffraction
EBSP	Electron Back Scatter Pattern (detector)
EDS	Electron Dispersive Spectroscopy
EHT	Electron High Tension (kV in an SEM)
EM	Electro-Magnetic (in terms of radiation)
GI-XRD	Grazing Incidence X-Ray Diffraction
HAPC	Halide Activated Pack Cementation
HMS	Higher Manganese Silicide
HTF	Heat Transfer Fluid
I PROBE	Probe Current within electron gun
ICPS	Intrinsically Conducting Polymers
IPC	Alternative term for standard HAPC
IPF	Inverse Pole Figure
KS6	A brand name of Carbon Black
MA	Mechanical Alloying
MWCNT	Multi-Walled Carbon Nanotube
NCL	Nowotny Chimney Ladder
N-TYPE	Semiconductor with electrons (negative) as charge carriers
OOPC	Variant of HAPC with substrate suspended above the pack
PAC	Poly(acetylene)s
PANI	Polyaniline
PCM	Phase Change Material
PEDOT	Poly(3,4-ethylenedioxythiophene)

PEGC	Phonon-Glass Electron-Crystal
PF	Pole Figure
PPS	Polyphenylene Sulphide
PPV	Poly(p-phenylene vinylene)
P-TYPE	Semiconductor with holes (positive) as charge carriers
RTEG	Radioisotope Thermoelectric Generator
SE	Secondary Electron
SEM	Scanning Electron Microscopy
SFG15	A form of synthetic graphite provided by IMERYS group, Standard Fuel Grade or Standard Flake Graphite
SPS	Spark Plasma Sintering
STA	Simultaneous Thermal Analysis
STEG	Solar Thermoelectric Generator
SVET	Scanning Vibrating Electrode Technique
SWCNT	Single-Walled Carbon Nanotube
TBTU	Trillion British Thermal Units
TEG	Thermoelectric Generator
TES	Thermal Energy Storage
TGA	Thermo-Gravimetric Analysis
THROWING POWER	The ability of a gaseous phase to travel from source to deposit onto a substrate
TMS	Transition Metal Silicide
US	Ultrasound
UV	Ultraviolet
VBG	Vertical Bridgman Growth
WD	Working Distance
XRD	X-Ray Diffraction
ZT	Dimensionless Figure of Merit, a measure of thermoelectric efficiency

Chapter 1 Introduction and Literature Review

1.1 Aims and objectives

The overall goal for this thesis is to investigate the entire thermoelectric device and develop scalable alternatives to current technologies. This thesis will focus on 3 key areas: materials, connectors and device design. These have been outlined in Figure 1.1. Chapter 1 will provide an introductory literature review to the current technologies and applications of thermoelectrics, along with more in-depth literature on the thermoelectric materials, molten salts and conductive polymer areas which will be relevant in later chapters. Chapter 2 will provide an overview of all the materials, methods and techniques used throughout this Thesis. Chapters 3 to 6 will investigate alternatives to current thermoelectric technologies and determine their viability for scale-up.

There are many materials available for thermoelectric elements, however many of these can be costly, scarce and rely on difficult to scale production methods. Bi_2Te_3 based materials are traditionally used in thermoelectric devices. These typically cost around $730/kg, whereas silicides offer a more economical option at $151/kg, however these have proven difficult to produce on a large scale. The materials making up the elements account for 50-80% of the Thermoelectric Generator (TEG) cost, leading to a drive to identify a more economical alternative[1]. Therefore, Chapter 3 of this thesis investigates the potential to produce thermoelectric devices with transitional metal silicides using a using a scalable pack cementation technique, which could significantly reduce the cost of the module parts.

Current Thermoelectric assembly procedures are very manual, consisting of hand soldering the module legs and manually mounting them to an insulating plate. Current devices range from 4.5 to 125$/W, whereas of 2014, 90% of thermoelectric modules were still assembled by hand, using pick and place technologies[2]. Therefore, the investigation of alternative designs and manufacturing methods could lead to economic improvements which would enable expansion away from the limited military and aerospace markets. Chapter 4 explores the viability of using conductive liquids as electrical contacts in the form of molten salts, as well as using the developments for thermal storage and transfer applications. In addition to this Chapter 5 investigates the usage of high temperature stability conductive polymers and developing a new alternative to allow sections of the thermoelectric device to be printed.

There is a large range of markets which could benefit from heat recovery devices. Current devices are capable of providing small scale applications for heat recovery and wireless power such as self-powered fans for wood burning stoves but are not economically viable for many larger applications. However, more suitable materials and manufacturing processes could enable these devices to be used in large scale applications such as providing heat conversion on internal combustion engines and steel plants. If the costs of thermoelectric devices can be dropped to more reasonable levels, their impact to industry could be massive. In 2010, the US iron and steel industry lost 334Tbtu in process heat. This could allow a thermoelectric potential recover of 489-1,223 GWh over the year. To allow the new materials and methods investigated in chapters 3-5 to be utilised in achieving this goal, Chapter 6 focuses on the development of new TEG designs and subsequent prototyping the most viable design.

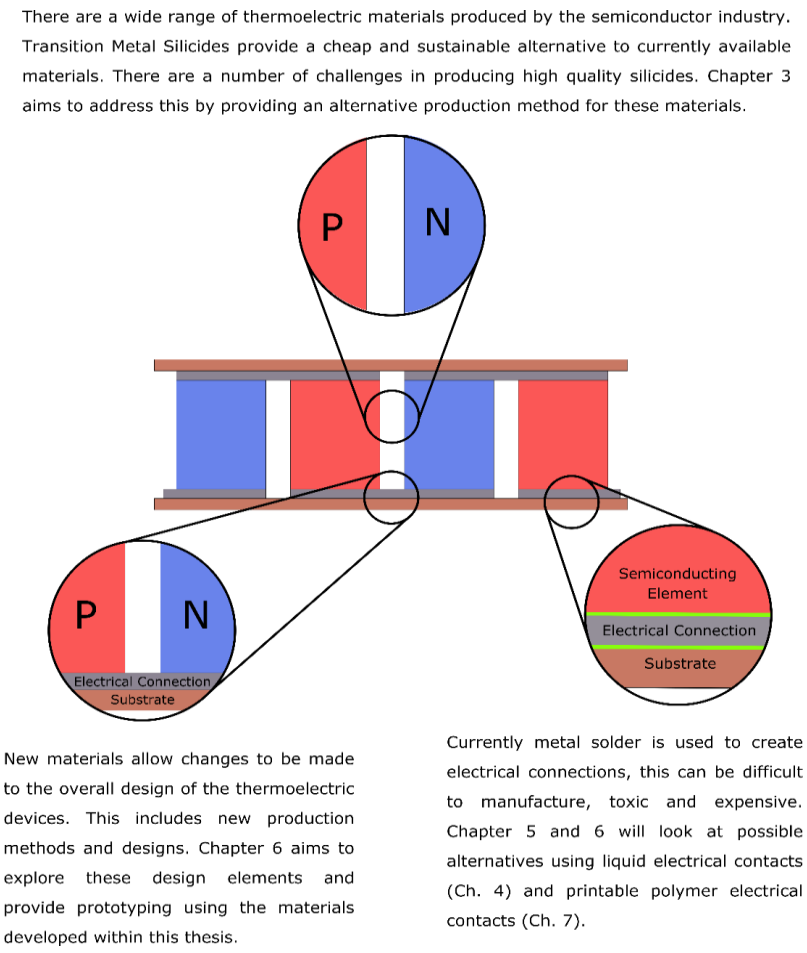

Figure 1.1: Schematic of a traditional thermoelectric device.

1.2 Applications for Thermoelectrics

Thermoelectric modules comprise of arrays of thermoelectric junctions (like that shown in Figure 1.2 and Figure 1.3), these are arranged electrically in series and thermally in parallel, as shown in Figure 1.2. Modules are solid state devices with no moving parts making them durable, reliable, and with an extremely long lifespan[3–6]. Figure 1.3 focuses upon a single couple, with movement of the electrons (circles marked with e-) and holes (circles marked with +) shown. The mechanisms will be explored in more detail later in this chapter. To summarise, the energy generation is due to the additional energy applied to the particles from the hot side. This causes a net movement of particles towards the cold side. Therefore, enabling a current to begin to flow due to the charge of the electrons and holes, in the n- and p-type semiconductors respectively.

Due to this, TEGs can be used in a wide range of fields including small body mounted power sources (such as thermal sensors), waste heat TEGs, solar TEGs and as Radioisotope TEGs for space applications[3,4,7–9].

Another market for these devices is waste heat recovery. Excess heat from the energy and transport sectors accounts for over half the energy generated. This is wasted as thermal loss within these applications, equating to 2.5 billion barrels of oil per year in the EU alone[9,10].

As previously mentioned there are two main fields, the space sector and the terrestrial green energy sector. Both of these applications have been well documented but prioritize different requirements. For space applications, the key quality factors are device reliability, efficiency and toughness. On the other hand, terrestrial applications focus on the applications cost, scalability and use of earth abundant materials[11–13].

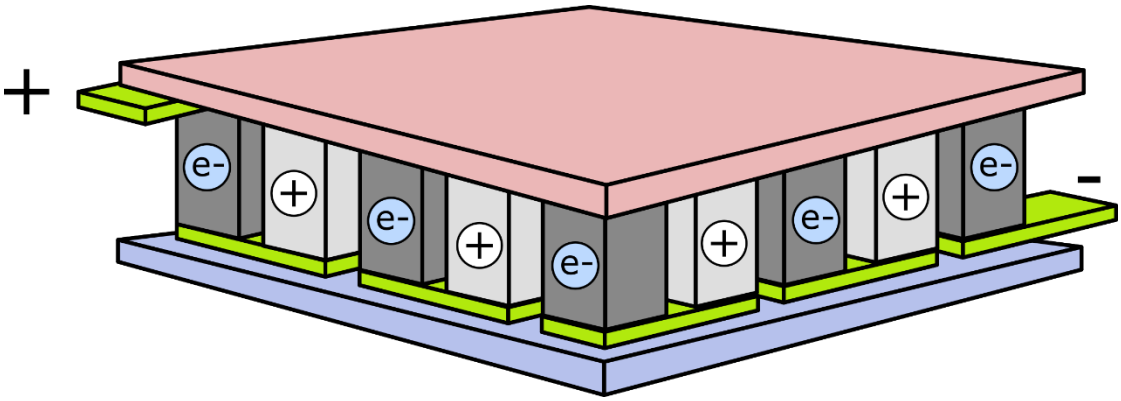

Figure 1.2 A thermoelectric model combining multiple pairs of N- and P-type semiconductors sandwiched between two substrates

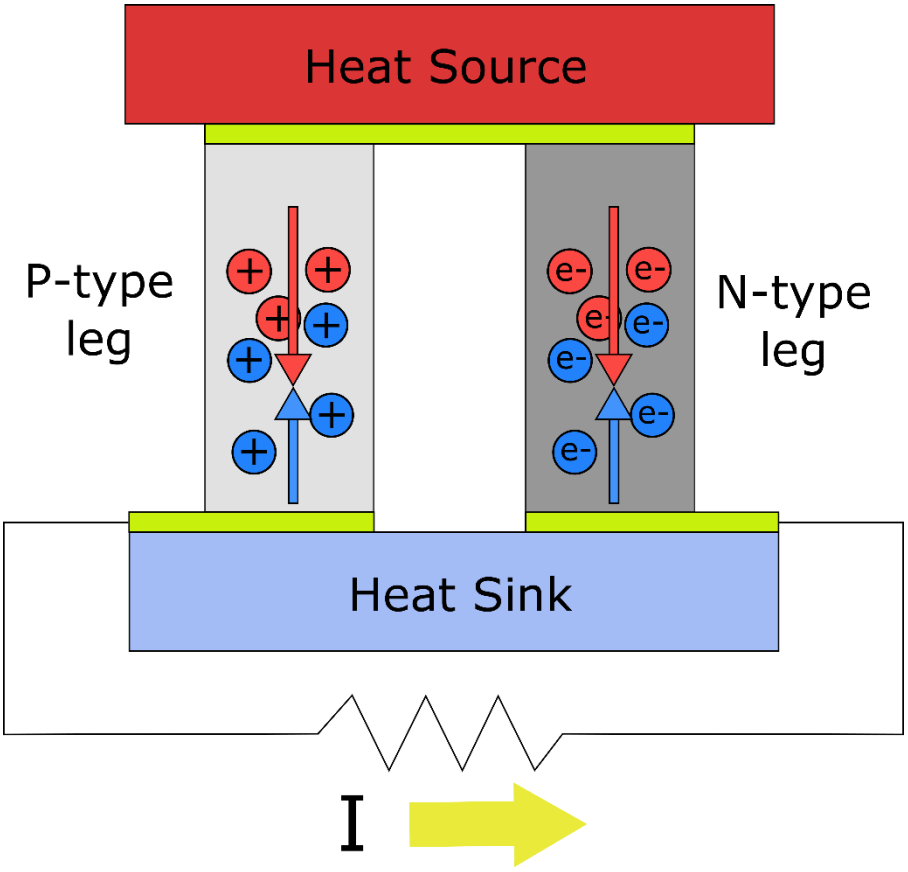

Figure 1.3 Thermoelectric junction consisting of an N and P-type semiconductor with an applied temperature gradient, a net downward flow of charged particles results in a current being generated

1.2.1 Space Applications

Some of the key benefits of Thermoelectric devices over more traditional power sources such as solar and fuel cell technologies is their superior life span and reliability[14]. Mission power sources, often termed a electrical or power 'buses', vary depending on the expected lifespan and the amount of power-drain from the equipment on board[15]. An example of these power buses is shown in Figure 1.4. Classically for missions below 1 week in duration batteries, fuel cells and chemical field turbines are used as power sources. However, for missions from 1 month onwards, Solar and Radioisotope TEG systems are the most practical. For devices above 100kW, these systems will struggle to provide the required power, therefore more complicated nuclear dynamic systems need to be developed, such as nuclear fusion drives[11].

The space environment is extremely harsh, leading to hardware maintenance tasks being unfeasible under such conditions. Therefore power buses must be able to withstand the stresses imposed by launch of the system from earth, the environmental degradation effects such as vacuum sublimation, EM radiation, thermal fatigue, meteoroid and corpuscular bombardment[16]. The two types of Thermoelectrics that may be used for space power are Solar Thermoelectric Generators (STEGs) and Radio-isotope Thermoelectric Generators (RTGs). RTGs are used for many missions operating far from the sun in dark environments[17], used on crafts such as the Mars Curiosity Rover and the Voyager. However, due to the nuclear component of these devices they are limited to these applications as they are not suitable for commercial use. On the other hand, STEGs are a direct competitor for solar cells within the space industry[11]. Photovoltaic (PV) have a limited range due to their inherent flaws meaning they could not operate too close to the sun, as efficiencies decrease with rising temperature[17,18]. As such, solar cells are only viable at a distance of 0.7 to 3.5AU from the sun. Partial shading will damage PV arrays and due to the array sizes the manoeuvrability of the spacecraft will be reduced[17]. These disadvantages allow the STEGs to compete with solar PV in the space environment.

RTGs are currently the most reliable power source available for spacecraft engaging in long lifetime missions (35 years in the case of the Pioneer spacecraft[19]). Earlier developments by NASA focused around the SNAP2 reactor consisting of a heat source, TE convertor and a heat transfer system. It was designed as a test piece which would have no moving parts, provide a continuous power supply for several years, as well as be able

to withstand the shock of a missile launch[20]. Additionally, RTG modules could be designed to withstand massive impacts, such as those which occur during uncontrolled entry to the lunar surface, where uncontrolled velocities of 10,000 ft/sec can be reached on impact in cases such as retrorocket failure[21].

RTGs have been used in spacecraft such as Pioneer, Voyager, New Horizons (Fig. 4), Ulysses and the Mars Curiosity Rover[22]. The Voyager 1 mission has been running since 1977, it is now located over $19x10^9$km from earth and is still functioning off of its RTGs[23]. The main downside of RTGs is the radioactive element which restricts their use to military or large space agency applications, meaning they could not be used for commercial missions[11]. This is the main reason solar PV is used for the near-earth orbit operations.

As mentioned earlier, STEGs are a direct competitor against solar PV for operation within the commercial space sector[18]. There is only a small amount of literature on these systems for space applications, revolving around flat-panel and concentrated STEGs[24]. Flat-panels function in a similar way to solar PV, although they will have cost and toughness advantages, like Solar PV, they do require large wings to be mounted onto. Concentrated STEGs have been studied less for space applications but have the potential to be lighter, more compact and more reliable than solar PV. These will be discussed in terms of their terrestrial applications later due to the wealth of literature on that application[18].

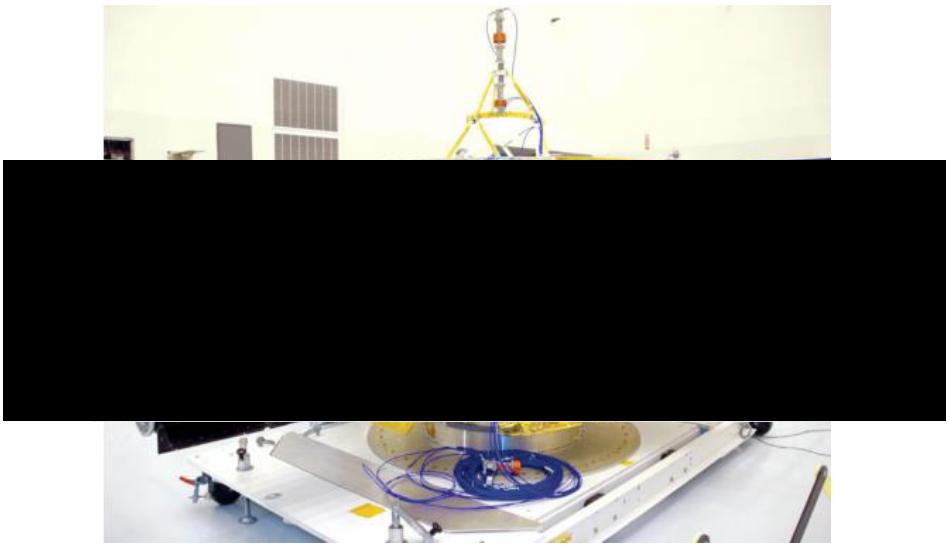

Figure 1.4 New Horizons spacecraft during construction with the RTG power bus shown in the left[13].

1.2.2 Terrestrial Applications

There are two primary uses for TEGs within the terrestrial market, these are STEGs and waste heat recovery. STEGs typically revolve around solar concentrators, a radiator for cooling and a small thermoelectric device at the focal point of the concentrator[25]. The concentrators are available in a number of forms such as simple Fresnel lens systems[26], central receiver systems using dish concentrators (Figure 1.5) or the larger more complex heliostat systems[25]. These concentrators are reaching concentration levels of up to 5,000 suns[25], allowing the high temperature Thermoelectric materials to be utilized for a solar application. Currently solar PV cost approximately $4 per watt-peak of power which concentrated STEGs would be able to realistically compete against[24].

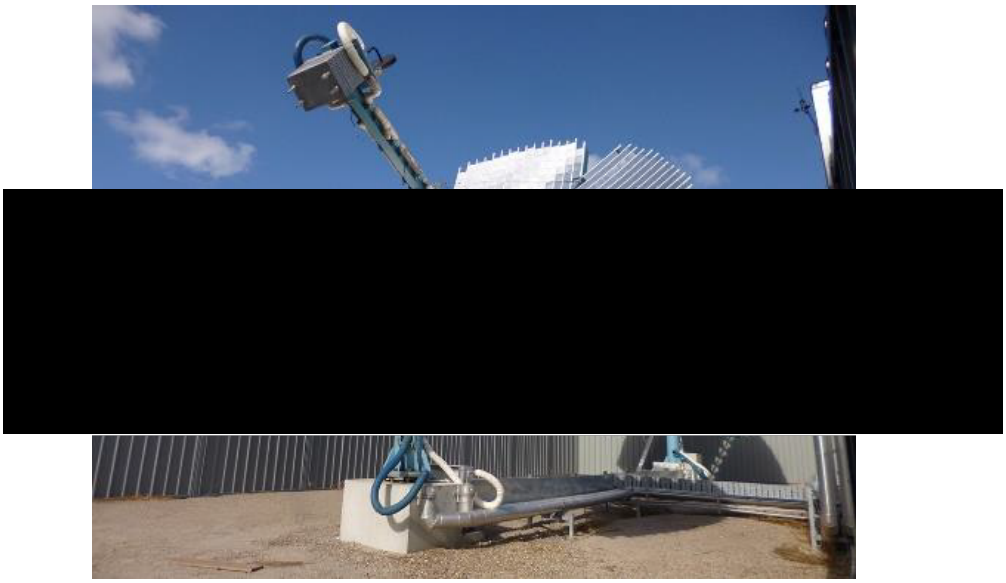

Figure 1.5 Parabolic Dish collectors in CSIRO's solar cooling research facility[147]

Linear Fresnel collectors utilise a series of flat mirrored surfaces in parallel lines which direct sunlight towards a single receiver, usually a tube of heat transfer fluid. Trough focusing systems, shown in Figure 1.6, employ a similar technique, but instead uses a single curved mirror to focus the light, this can dramatically increase the cost of the component compared to Fresnel lenses[4,25,26]. These systems are advantageous because they are simple to design, easy to maintain and could be scaled up easily by being used in arrays. However, they have a low concentration amount so are unlikely to reach 475^{o}C.

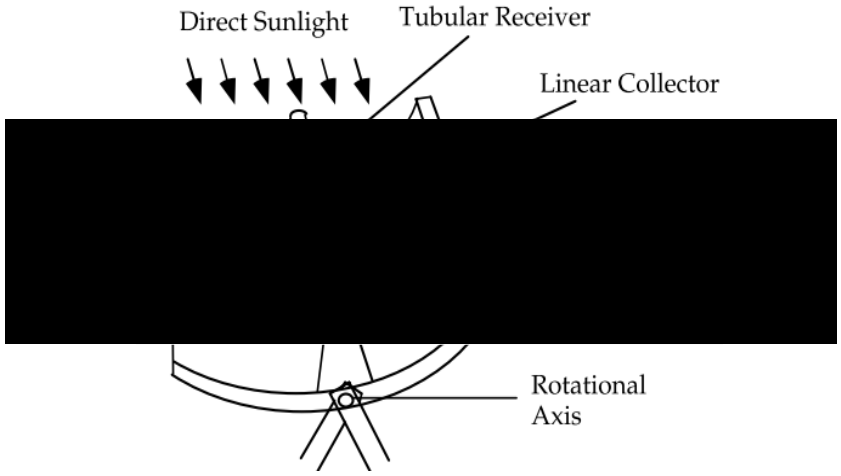

Figure 1.6 Schematic of a simple trough focusing system[25]

The tubular receiver in these systems typically consists of an evacuated tube, with a smaller cylinder of heat transfer fluid inside to allow cooling, also called a thermosyphon. Thermoelectric elements coated in a selective absorber then surround this inner tube.[4]

Larger more complex systems revolve around using a Fresnel array with two axes of rotation focusing about a single point, called Heliostats. This focal point could be a spot on a parabolic dish design which rotates with the sun, Figure 1.5, or on a stationary location atop a tower, Figure 1.7.

The two-axis tracking devices give higher temperatures and greater degrees of concentration allowing for much more efficient devices. However there is a limit to the individual device scale-up, because as size increases optical efficiency typically declines[25]. A balance must be struck between a higher temperature and lower optical efficiency. These devices primarily run with Rankine steam turbines by heating fluid or air which are used to generate steam[27]. Another possibility would be the use of compressed air at over 1,100K for a solar/fuel hybrid gas turbine.[25] Due to the current efficiency of solar concentrating devices, for instance the SunCatcher™ by Tessera Solar, these could easily be modified with thermoelectric devices to increase their efficiency and performance[28,29]. The SunCatcher™ device which utilises a hydrogen gas expansion engine and solar tracking is able to produce 25kW per catcher device, at approximately 630kWhr/m^2. Modulated designs are easy to implement at short notice reducing construction costs and allowing array sizes to be implemented depending on customer needs.

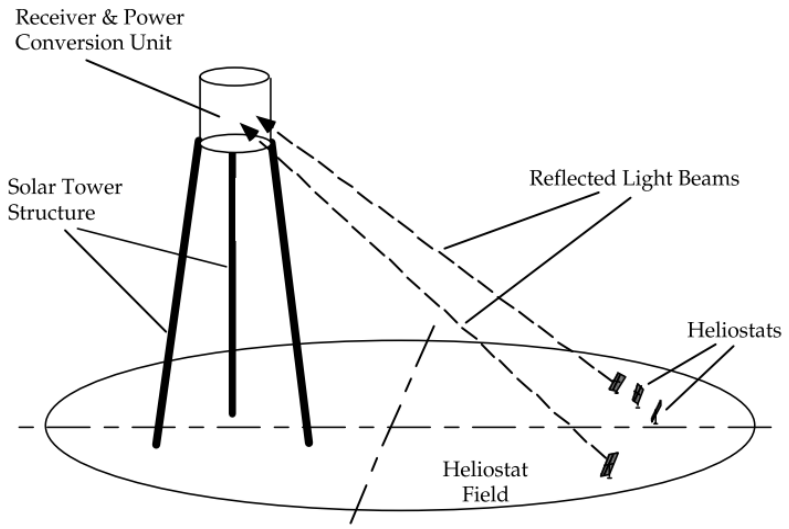

Figure 1.7 Schematic of a centralised tower receiver set-up, also known as a Heliostat

1.2.3 Device Designs

As stated previously each module consists of arrays of thermoelectric junctions, as shown in Figure 1.2, arranged electrically in series and thermally in parallel. Each of these junctions are comprised of an N-type and a P-type doped semiconductor. The effectiveness of the TEGs for space applications are best assessed as the power per unit weight, reliability, thermal cycling resistance and radiation resistance[19,30]. Solar TEGs for near earth space applications would classically be assembled with coatings onto the collector surface providing high absorption ratio, leading to increased efficiencies. The optimised leg dimensions are 0.1245cm^2 cross section by 0.25cm long, however this traditional structure may not be viable with TMS on sheet silicides. Once completely assembled the design can be tested and assessed in terms of power per unit area and power per unit cost as viable measures of effectiveness of terrestrial solar applications, however these are of minimal concern to space missions[18,30]. Some RTEG's have been shown to last over 35 years in the case of the Pioneer 11 power source, a Pb-Te based SNAP-19 RTG[19].

1.3 Thermoelectric Materials Background

1.3.1 Thermoelectric Properties

Thermoelectric devices function by converting a thermal energy gradient into electrical energy. This was discovered in 1821 and termed the Seebeck effect[31]. The

thermoelectric effect is a phenomena by which thermal energy is converted directly into electrical energy without moving parts or fluids[10].

The thermoelectric dimensionless figure of merit, ZT, was introduced as a measure of the thermoelectric efficiency. This is given in Equation 1.

$$ZT = \frac{S^2 \sigma T}{k}$$

Equation 1: Calculation of the dimensionless figure of merit, ZT

Where S is the Seebeck Coefficient, σ is the electrical conductivity, T is the absolute temperature and k is the thermal conductivity[4,5,32]. All three dependant parameters are a function of the band structure, carrier concentration and other factors. Ideal thermoelectric materials have a high Seebeck coefficient and electrical conductivity with low thermal conductivity[33]. This relationship is demonstrated in Figure 1.8.

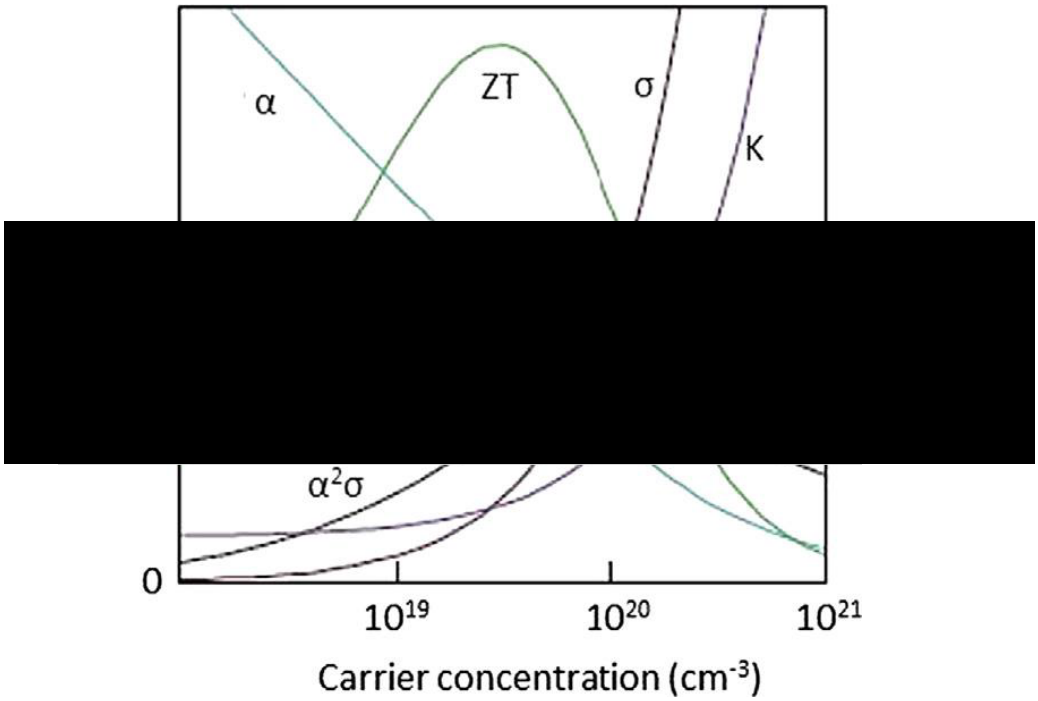

Figure 1.8 Chart showing the relationship between ZT, and its constituent variables with relation to carrier concentration[4,10]

1.3.2 Seebeck Coefficient

The Seebeck coefficient (S or α) indicates the magnitude of the Seebeck effect or thermo-power. It is expressed as V/K, or typically μV/K, and can only be measured by utilising a closed circuit of two different materials, a thermocouple that exhibits the

Seebeck effect[31]. Metals have low Seebeck coefficients, up to a maximum of 10μV/K, limiting their use. Semiconductors have considerably higher Seebeck coefficient, this is often in excess of 100μV/K.

The charge carriers come in two forms, electrons and holes. A material with an excess of holes is considered a P-type semiconductor while an excess of electrons is an N-type[34].

For a device to generate a thermoelectric effect it must have a thermocouple consisting of an N and a P-type material electrically connected at the ends, as shown in Figure 1.3[4–6,31,35,36]. The type of the material effects which direction the charge flows with regards to a temperature gradient. Charged particles are thermally excited on the hot side of the element, resulting in a net movement of particles towards the cold side. This results in the N-type materials becoming negatively charged on the cold side and the P-type materials becoming positively charged, setting up a current flow.

Seebeck coefficient is dependent on temperature which directly affects the carrier concentrations and mobilities. The temperature at which the Seebeck coefficient is measured must always be stated[4]. This is because the Seebeck coefficient is the change in electrochemical potential ($\delta_x\mu$) in x direction per unit charge 'e' per unit temperature (δT). This is described in Equation 2.

$$S = \frac{S_e n\mu_e + S_h p\mu_h}{n\mu_e + p\mu_h} = \frac{1}{e}\frac{\delta_x \mu}{\delta T}$$

Equation 2: Contributions of carrier concentration and mobility from N and P-type semiconductors to the Seebeck Coefficient

When S_e and S_h are electron and hole Seebeck contributions, μ_e and μ_h are electron and hole mobility, and p and n are hole and electron concentrations[4,5,34].

1.3.3 Electrical Conductivity

Electrical conductivity (σ), or electrical resistivity ($\rho=1/\sigma$) is a result of the carrier concentration and the mean free path of charge carriers. Electrical conductivity is measured in S/m and is extremely temperature dependant, semiconductors have low σ at low temperatures due to limited free electrons[5,34,37,38].

For ideal electrical conductivity the Fermi level is placed within the conduction band of the semiconductor, whereas the highest Seebeck coefficient occurs when the Fermi level is below the conduction band. As such these two are usually combined as a power factor ($S^2\sigma$) which gives the optimum value of both S and σ for maximum ZT value, typically when the Fermi level lies close to the conduction band[10].

Electrical conductivity of a highly doped semiconductor is given by $\sigma=en\mu$, where μ is electron mobility, n is the carrier concentration and e is electron charge[39]. Within thermoelectrics the optimum range of electrical resistivity is 10^{-3} to 10^{-2} Ωm [4].

1.3.4 Thermal Conductivity

As previously stated for high ZT values, low thermal conductivity is desired.[40] Thermal conductivity (κ) is the sum of lattice thermal conductivity (κ_L) and electrical thermal conductivity (κ_E), usually measured in W/mK. κ_E and κ_L represent the contributions of electron and hole transport by heat and phonon transport through the lattice respectively[4,40].

This is being represented in a number of ways, including:

$$k = dC_pD = k_L + k_E = k_L + L\sigma T = \Delta Q/T\Delta d$$

Equation 3: Contributing factors to a materials thermal conductivity

Where d is density, C_p is specific heat and D is thermal diffusivity. Wiedemann-Franz law ($\kappa_E=L\sigma T$) separates the two components, L being the Lorenz number[4,39].

This shows that an increase in σ will result in an increase in κ_E meaning this cannot be decreased without adversely affecting the power factor. As such the most effective way to reduce κ is by reducing κ_L. This can be done in a variety of ways, most effectively by doping and nano-structuring of the material. By disrupting the crystal lattice and introducing nano-grains that are smaller than the mean free path of the phonons. This will result in increased scattering thus reducing the κ_L value[35,37,41].

1.3.5 Improving ZT by structural modification

Three materials variables that make up the dimensionless figure of merit (Seebeck coefficient, electrical conductivity and thermal conductivity) can be optimised to produce the highest value possible. Ideal ZT values are difficult to maximise due to their need for high Seebeck coefficient and electrical conductivity, but with a need of low thermal conductivity. S and σ are determined only by the electronic properties so are termed as the power factor ($PF=S^2\sigma$) [4]. It is difficult to optimise the electrical conductivity and Seebeck coefficient to produce high ZT as they are inversely related[4,5]. High electrical conductivity is easier to achieve with metallic materials which have no band gap, semiconductors can be improved by reducing band gap which increases the carrier mobility or concentration. Seebeck coefficient on the other hand can be increased by electron scattering and energy filtering, decreasing the carrier mobility. Therefore conductivity cannot be increased without decreasing the Seebeck coefficient[42].

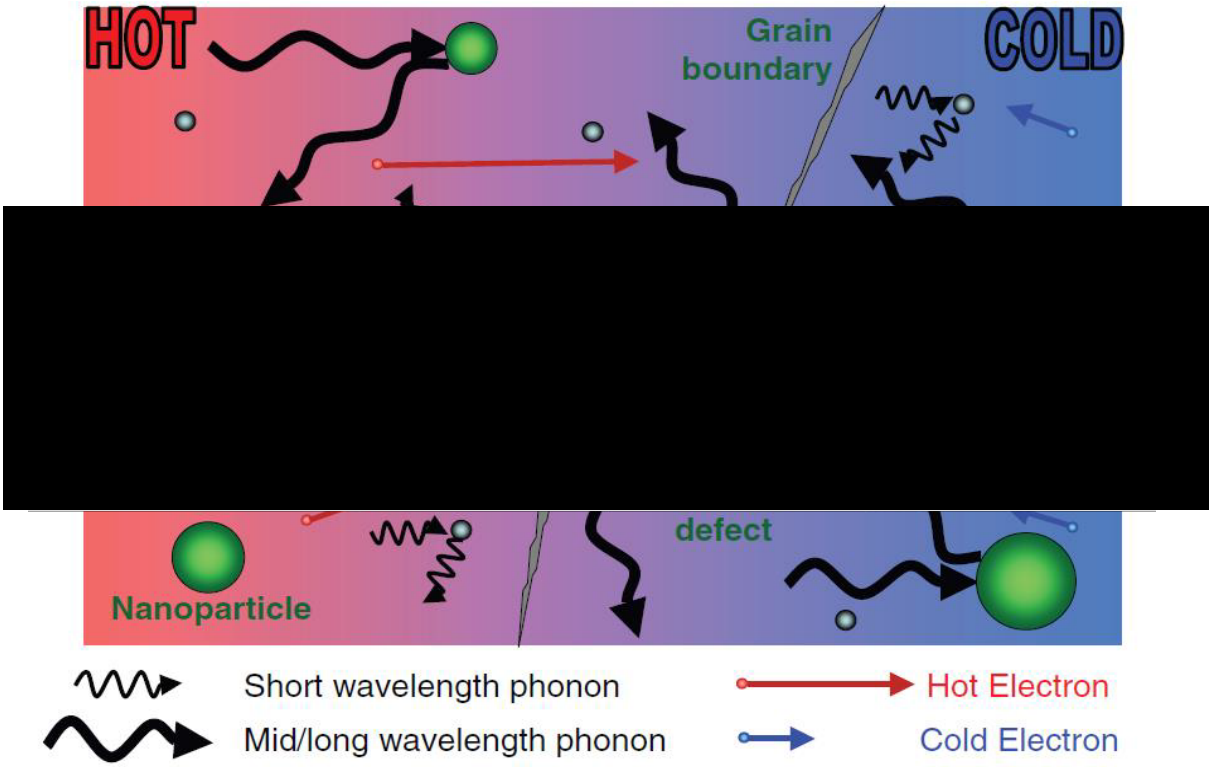

Figure 1.9 Illustration of the possible phonon scattering mechanisms within thermoelectric materials[148]

The thermal conductivity, κ, is a combination of $\kappa_e + \kappa_l$. An increase in electrical conductivity would increase the κ_e value resulting in little or no change of ZT value. However κ_l is effected by the rigidity, structure, atomic masses and other lattice

characteristics of the material[43]. It has been shown that introducing phonon scattering centres and grain boundaries increases κ_l with minimal effect on the electrical conductivity[42]. Phonon scattering occurs with small atomic defects scattering short wavelength, while larger particles and defects will only scatter the longer wavelength phonons, this is demonstrated in Figure 1.9. As a result, nanostructured materials promote phonon scattering and as such significantly reduce the thermal conductivity[42,43].

1.4 Current Thermoelectric Technologies

There are currently a wide range of materials used to make up thermoelectric devices, these are split into a number of categories: metals, ceramics, polymers and semiconductors.

Metals possess a very high electrical conductivity and thermal conductivity giving them ineffective thermoelectric properties. However, some heavy metals are contained in thermoelectric materials such as Bi, antimony, Pb and Te which are mostly toxic and unstable at high temperatures, alternatives such as metal oxides are much more stable at high temperatures and are also earth abundant. As such while these can be effective in the form of Bi_2Te_3 they are commonly used as dopants for other materials[4,5,44].

All thermoelectric materials, other than pure metals, are classed as semiconductors. Semiconductors are the most promising thermoelectric materials due to their band gap properties which results in Seebeck coefficient values of greater than 100μV/K and overall high ZT values[4,5,31]. Semiconductors are most notably based around silicon but a range of potential thermoelectric semiconductors are outlined below.

Ceramics are non-metallic materials comprising of inorganic compounds of metal, non-metal and metalloid atoms held in covalent and ionic bonds. Examples of ceramic oxide thermoelectrics are $BaPbO_3$ and $NaCo_2O_4$. These can be used as thermoelectrics with their enhanced stability making them better suited to higher temperature applications, however they are little used due to their difficulty in fabrication[4].

Polymers on the other hand are intrinsically thermal insulators but with low electrical conductivity, Seebeck coefficients and stability at temperature they are not useful as thermoelectric materials individually. When combined with other functional materials, such as SnTe and nanoparticles, they can provide a cheap printable thermoelectric material.

Phonon-Glass Electron-Crystal (PGEC) structures are particularly high performing thermoelectric materials, these include: Clathrates and skutterudites. Clathrates have tetrahedral co-ordinate atoms around a single metal atom for example Na_8Ge_{46}[4]. These have been shown to generate ZT<1. skutterudites are binary semiconducting compounds formed from transition metal (rhodium or iridium, M) and a pnictogen element (P, Arsenic or antimony, X) in the form of MX_3. Skutterudites have are high electron mobilities and high Seebeck coefficients but also large lattice thermal conductivities, reducing their effectiveness. A third additional element converts this to a PGEC, massively reducing the thermal conductivity and improving their performance.

A further example is that of Half-Heusler alloys have three component elements in a XYZ arrangement from different element groups. This gives a narrow band gap of the order of 0.1-0.2eV at the Fermi level. These alloys have large Seebeck values, mid-level electrical resistivity and high thermal conductivity, as such they are good for high-temperature thermoelectric power[4].

The environmental impact for the source metals must be considered when designing large scale thermoelectric materials. In this regard the materials must be affordable, earth abundant and accessible. Additionally, the ZT value should be as high as possible. Silicides best achieve this due to silicon being one of the most abundant elements in the earth's crust[4,6,10,32,38–40].

There are a wide variety of silicides usable for thermoelectrics. Examples of this include $CrSi_2$, $MnSi_{1.7}$, $FeSi_2$, Ru_2Si_3, $ReSi_{1.75}$, CoSi and $Mg_2(Si, Sn)$. These have proven ZT_{max} values of 0.25, 0.7, 0.2, 0.4, 0.7, 0.2 and 1.2 respectively. From these figures the best Silicides to use are $MnSi_{1.7}$, $ReSi_{1.75}$ and $Mg_2(Si, Sn)$. ruthenium is an extremely expensive element, so not worth developing, however manganese and magnesium are both earth abundant and therefore affordable[6,45–47].

As such there has been much focus on silicides, with the highest achieved ZT value coming from $Mg_2(Si, Sn, Ge)$ as an n-type and HMS (Mn_xSi) for p-type materials. Both of these meet the above criteria and doping further enhances their properties[48].

Higher Manganese Silicide (HMS) classically crystallise into a Nowotny Chimney Ladder (NCL) structure, as shown in Figure 1.10. HMS consists of several unique NCL

phases including: Mn_4Si_7, $Mn_{11}Si_{19}$, $Mn_{15}Si_{26}$ and $Mn_{27}Si_{47}$. All NCL phases have similar a lattice parameter and long c lattice parameters, with variations due to the complex structure[6,34,40,49]. Selective doping results in ZT values of 0.7 being achieved with HMS[34,47].

Mg_2X compounds have a narrow band gap (ΔE~0.3-0.6eV) and a high melting temperature (~1000^{o}C). These alloys have an anti-fluorite crystal structure with silicon in FCC sites and magnesium in tetrahedral positions[4,6,32,38,50]. Effective complex doping results in ZT values of up to 1.4 at 850K for $Mg_2Si_{0.53}Sn_{0.4}Ge_{0.05}Bi_{0.02}$ alloy[33,51].

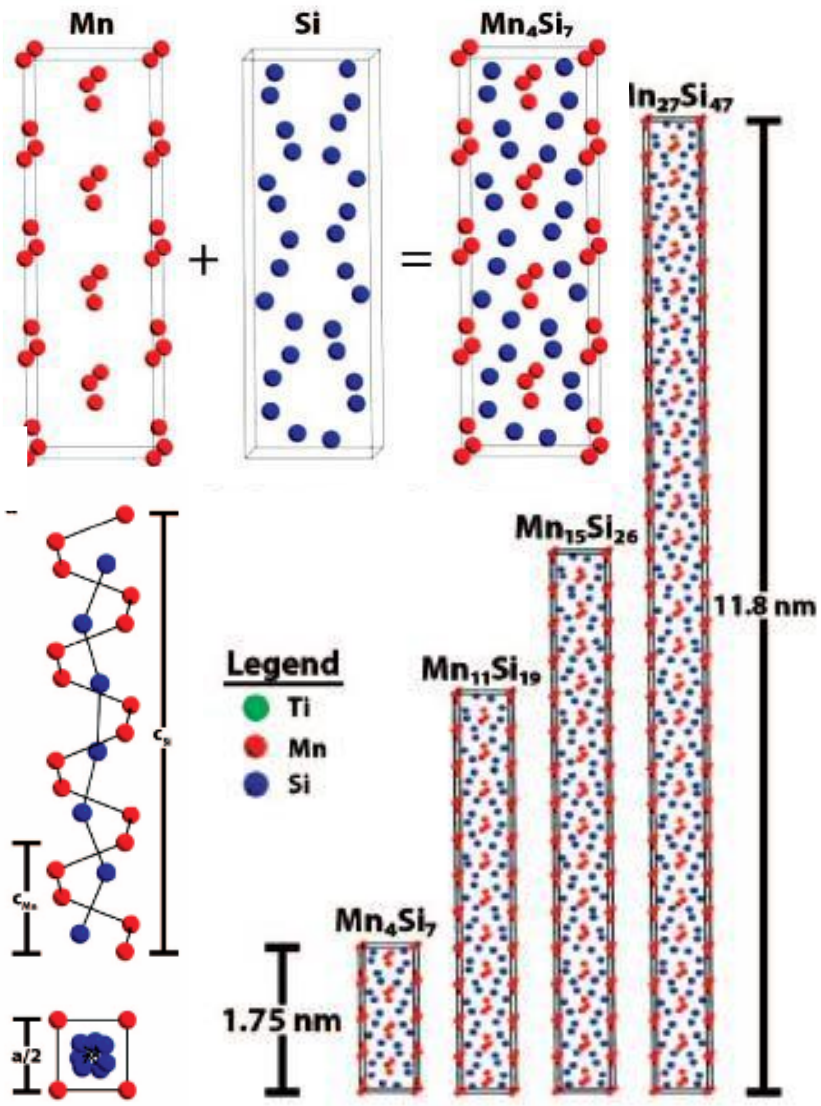

Figure 1.10 Nowtony Chimney Ladder Structures for Higher Manganese Silicide

1.4.1 Effective dopants of Mg_2Si

Doping of Mg_2Si is usually a complex process which utilises a number of elements depending on whether a p- or n-type semiconductor is required. For this project Mg_2Si is the n-type leg of the thermocouple with Higher Manganese Silicide (HMS) acting as the p-type.

Dopants previously used for Mg_2Si include aluminium, tin, germanium, bismuth, antimony, silver, yttrium and lanthanum[33,38]. The effectiveness of these dopants can be measured using the ZT value explained in section 1.3.1. aluminium -doped Mg_2Si has a maximum ZT value varying from 0.325 at 0.005at% aluminium, peaking at 0.5 at 875K at 0.01at% aluminium and dropping to 0.275 at 0.04at% aluminium [52]. Bi-doping of Mg_2Si peaks at a ZT of 0.74 at 840K for 2at% bismuth. This drops off to 0.45 at 1at% and 0.65 at 3at%[53]. Antimony-doping of Mg_2Si peaks at a ZT of 0.62 at 823K at 0.02at% antimony [54].

Best figures of merit can be obtained by combining a number of dopant materials including Ge and Sn directly replacing the Si. The highest recorded ZT values are 1.4 with $Mg_2Si_{0.53}Sn_{0.4}Ge_{0.05}Bi_{0.02}$[33,55], therefore $Mg_2(Si,Ge,Sn)$ have a huge potential for TE devices. The atomic miss-match of Si, Sn and Ge solid solutions provides atomic scattering and once doped allows a high thermoelectric figure of merit[56]. $Mg_2Si_{0.6}Sn_{0.4}$ also gives a ZT_{max} value of 1.1. This should be much easier to produce.

1.5 Thermoelectric Materials Production Methods

1.5.1 Traditional Methods

Magnesium Silicide and HMS are currently produced with two methods commercially: Vertical Bridgman Growth (VBG) and Mechanical Alloying (MA) with either Hot Pressing (HP) or Spark Plasma Sintering (SPS); and [39,57–60].

Mg_2Si is difficult to prepare by melting due to the low boiling temperature of magnesium (1106^{o}C) and the melting temperature of the resultant Mg_2Si (1084^{o}C). Lack of solubility and a large difference in the vapour pressures of magnesium and silicon present further issues with the production by melting[57,60]. In addition, magnesium's reactivity makes it nearly impossible to process at temperature in oxygen or nitrogen containing atmospheres without oxides forming.

1.5.1 Vertical Bridgman Growth

VBG is used to produce high quality single phase crystals from the molten phase. It requires a precision growth operation using a non-stick growth crucible, laid out as per Figure 1.11. This crucible is coated with a smooth BN-based anti-stick coating to prevent

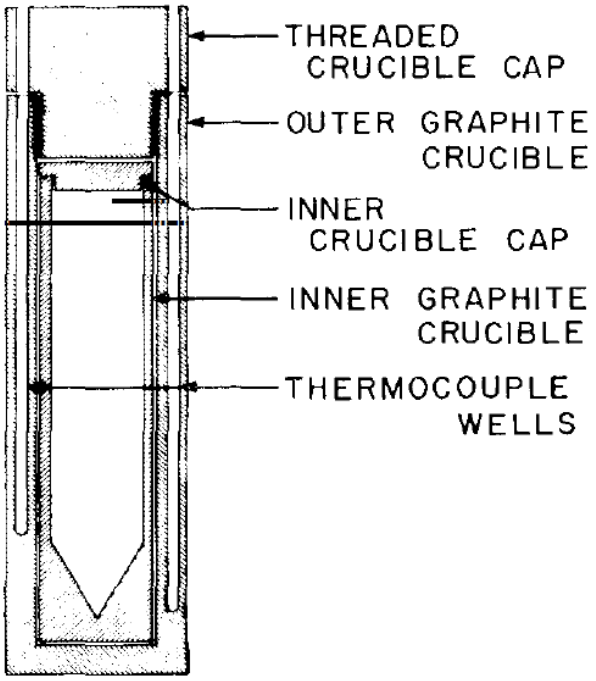

Figure 1.11 Double-walled crucible for Vertical Bridgman Growth

unwanted nucleation's, with any roughness negating this effect[61]. The crucible loaded with powder is placed in a quartz ampule and pressurized at 0.08MPa using a Ar-H_2 forming gas. The temperature was ramped at 50ºC/hr until the 1173ºC temperature was reached, then heated rapidly at 100K/hr until 1423ºC, and is then held for 2 hours[57,61]. Growth occurs at 3mm/h with a temperature gradient of 20ºC/cm up to 20ºC above the Mg_2Si melting point[57]. This normally gives single crystals orientated along crucible axis in the [100] direction[61].

1.5.2 Mechanical Alloying

The MA process relies on repeated mechanical impact during high-energy ball milling to produce a solid phase transition. To produce this mechanical work high purity powders of magnesium and silicon and hardened steel balls are loaded into a steel vial and sealed inside an argon glove box with O-rings[58]. This milling is limited at regular intervals to prevent heating. MA is used as industrial scale applications but is not entirely effective due to agglomeration during the milling process[58].

1.5.2.1 Hot Pressing

Milled powder is then consolidated by HP to produce a polycrystalline pellet of the Mg_2Si. A cylindrical tungsten-carbide die is used to hot press the powders at up to 800^oC under a pressure of 70MPa for up to two hours, a slow heating rate was used. This must all be done under an inert atmosphere, however oxides are still formed which is undesirable, typically due to impurities and atmospheric leakage[39]. Densities were gained at 1.97g/cm^3, which is ~99% of theoretical value[58].

1.5.2.2 Spark Plasma Sintering

The SPS process starts like MA with high energy ball milling in an inert atmosphere. The sintering process is carried out under a vacuum and powders are filled into a graphite die, using the Spark Plasma Sintering apparatus. Temperature and pressure are raised simultaneously to around 775^oC and a maximum 50MPa respectively. It is essential to have a temperature plateau at 450^oC to prevent magnesium evaporation[35,62]. SPS is typically much quicker than hot pressing, however if larger grains are needed a further heating stage can be applied. SPS results in a cylindrical solid. There are similar problems to HP with oxidation sometimes occurring, especially with an Mg_2Si nano-powder. However, SPS preserves a much finer grain structure and gives compaction density of 97%.

1.5.3 Halide Activated Pack Cementation

All the methods outlined in section 1.5.1 involve costly equipment, with powder methods result in a lower density and some oxidation. As a result, a 4th method has been developed focusing around the Halide Activated Pack Cementation (HAPC) process. HAPC is an in-situ chemical vapour deposition process and has been used commercially to apply coatings for corrosion and wear resistance[63]. The production of silicides by HAPC has been shown by Stathokostopoulos et al[64–66] to great effect.

HAPC involves three main components: the substrate, powder and alumina crucible. The substrates are placed within a sealed crucible filled with a powder. This powder consists of a master material (in this case magnesium or manganese, however this can be a combination of metal and dopant), a Halide Activator (in this case using ammonium chloride, NH_4Cl) and an inert filler powder (Al_2O_3)[63–65]. The crucibles are placed in a tubular argon-purged furnace and heated for up to 72 hours at up to 650^oC for

magnesium deposition, as shown in Figure 1.12. In commercial processes for other materials these temperatures can be over 1000ºC[63,67]. Samples are kept in a desiccator in order to minimise the oxidation of magnesium. This results in a pure Mg_2Si sample produced using a simple, economic method with no high cost equipment needed[64,65]. This technology is currently used to deposit oxide protection coatings on alloys so is readily available for large scale production[63,68].

HAPC process relies on two processes to produce the desired material. First the gaseous diffusion formed by magnesium chloride onto the substrate[63,67,69]. The second stage is the solid-state diffusion step of magnesium through the silicon and Mg_2Si. This solid-state diffusion is the rate limiting step, resulting in a parabolic curve where the growth amounts slow with time. An example of this can be seen in the Chapter 3. Developing the HAPC process for Thermoelectrics allows the production of efficient, economic, reliable and environmentally friendly TEGs.

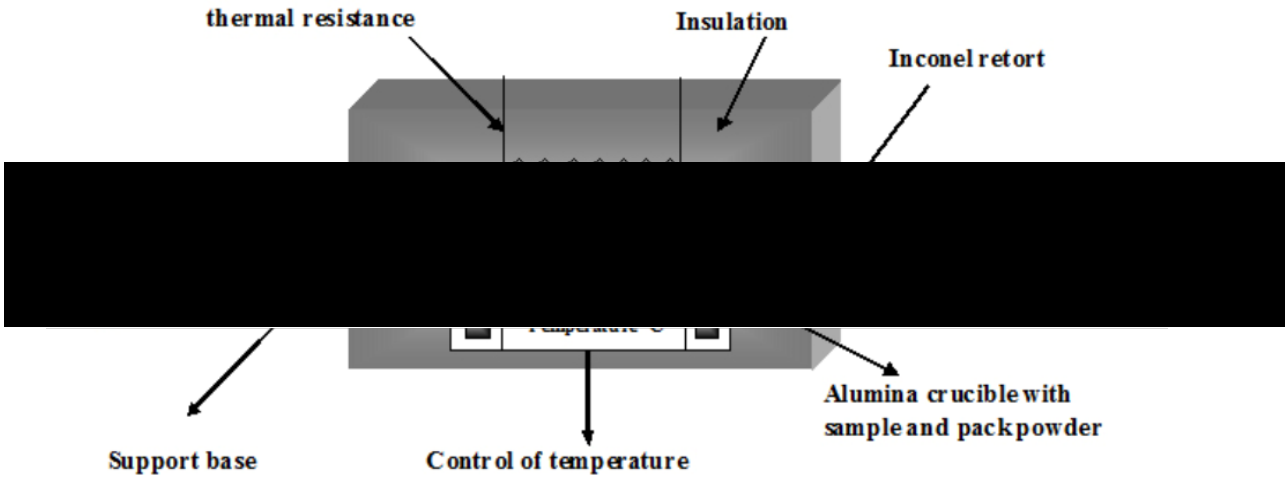

Figure 1.12 Schematic diagram of the pack cementation process[64]

1.6 Phase Change Materials for Electrical Contacts and Energy Storage

Phase-Change Materials (PCMs) are substances with high latent heat of fusion. This allows the storage, transfer and release of high amounts of energy. These materials are broadly split into 4 categories: organic, inorganic, eutectic and hygroscopic materials.

Phase change materials, with additions, may serve as a conductive liquid contact. Their thermal behaviour, including melting and stability, is customisable to suit a variety of device operating temperatures. Developments in thermal behaviours are also applicable to the heat transfer and storage applications.

1.6.1 Organic Phase Change Materials

Examples of organic PCMs include Paraffin (C_nH_{2n+2}) and Lipid derived Diamides. Lipid Diamides have a key advantage over Paraffin and other alternatives due to their renewable nature as they are produced from fatty acids. These Diamides have been shown to melt at around 150^{o}C. Degradation begins at around 350^{o}C, with complete degradation at around 412^{o}C. Diamides are capable of latent heats of 190-210J/Kg, however long-term behaviours have not been widely studied. The advantages of organic PCMs are that they typically self-nucleate and freeze with little undercooling. Organic PCMs do not segregate and they are typically chemically stable. However, they have relatively low thermal conductivity, can be highly flammable, and typically exhibit a low thermal storage to volume ratio, reducing energy storage powers.

1.6.2 Inorganic Phase Change Materials

Inorganic PCMs typically consist of salt hydrates, these have a high thermal storage to volume ratio. This results in an increased energy absorption. Typically, inorganic PCMs have high heats of fusion and are not flammable. However high super cooling is needed to encourage solidification and they have high degrees of thermal expansion. These hydrates also suffer from degradation during thermal cycling.

1.6.3 Other Phase Change Materials

These are typically inorganic compounds and are a more recent development, consisting of phase change salts[70–72]. Typically, these materials have a sharp melting point, high energy storage density and good latent heat values. Due to their compound nature they are readily customised to suit the application.

Hygroscopic materials operate on the absorption and evaporation of moisture from the environment. The process of condensation gives off heat and whilst vaporization absorbs heat, allowing cooling of the environment. These provide a limited power transfer but can be useful in the built environment.

Solid-solid phase transitions rely on crystalline structure changes to absorb and emit substantial amounts of heat. It is claimed these can have similar Latent Heat capacities to solid-liquid transitions and are useful for fixed energy storage. However, due to their solid nature they cannot provide any heat transfer, so for the purposes of this research are not considered. Microencapsulated PCMs fulfil a similar function to the solid-state PCMs as there is little danger of liquid material escaping. These can be used in paint and mixed with a wide variety of construction products such as foams and plasterboards.

1.6.4 Applications and uses of Phase Change Salts

Phase change salts are used in a wide variety of applications including as Heat Transfer Fluids (HTF) and for Thermal Energy Storage (TES). These technologies are used in Concentrated Solar Power (CSP) or solar thermal plants where they absorb the heat from concentrated solar energy and convert it into electricity using water steam generators. The utilization of relatively inexpensive molten salts also allows a period of heat storage, enabling the release of energy overnight. The most prevalent CSP technology is that of the central tower design spoken about in section 1.2.1, these are also referred to as heliostats.

TES is essential to the efficiencies of solar thermal plants, which due to their high energy absorption allows electricity to be generated when there is no sunlight present. Molten salts can be used to improve plant efficiency and reduce cost by allowing more efficient device operation. For maximum efficiency, it is desired that the salts should have a low melting point and high temperature stability. By making the working range wider the salt can absorb and transfer more energy. The working range is the operating temperature between the melting point and high temperature decomposition of the material.

Two traditionally popular salt mixtures have been Solar Salt (a binary mixture of sodium nitrate ($NaNO_3$) and potassium nitrate (KNO_3)) and HITEC® Solar Salt (53wt% KNO_3 – 40wt% Sodium Nitrite ($NaNO_2$) – 7wt% $NaNO_3$)[71,73]. The addition of sodium nitrite to the traditional Solar Salt mixture has reduced the melting temperature from 220^{o}C to 142^{o}C. HITECs upper operating temperatures have been reduced from the Solar Salts 600^{o}C to 454^{o}C for long term (and 538^{o}C for short term behaviour), giving a long

term working range of 312°C. Additions to this ternary mixture have been used to improve the stability somewhat, but little stability above 500°C has been observed.

Low melting temperature eutectic materials are ideal for heliostat applications[74]. Materials such as Lithium Nitrate ($LiNO_3$), $NaNO_3$ and KNO_3 have eutectic temperature of 120°C and below[70]. These eutectics and the result of other works[75] show that the melting temperatures of quaternary salts with cations of Ca, K, Li and Na may be reduced to below 100°C. In particular nitrate anions can result in melting points of less than 80°C, providing large amounts of improvement if the upper decomposition temperatures can remain stable[75].

Metal chloride salts have been introduced as a viable alternative for higher temperature applications. Chlorides have the advantages of high latent heat and high operating temperatures (424-700°C). Metal chlorides do however have disadvantages including being corrosive and melting at higher temperatures. This results in a reduction in overall usefulness to the concentrated solar power industry. For CSP applications an ideal salt would have a melting point lower than 142°C and long-term stability closer to that of the metal chloride mixtures. The advantages of Li additions have been seen to give lower melting temperatures for ternary mixtures providing potential cost savings when utilised as a transfer fluid[74,76].

Initial work into undisclosed chloride additions was undertaken by Peng et al[73]. However, whilst this work showed an improvement in salt operating temperatures it failed to state which additions were tested[72,73]. A wide variety of metal chlorides were tested within this study, with their melting points initially compared to a standard HITEC salt to ensure no increases in melting behaviour occur with salt additions.

1.7 Conductive Polymers

Polymers consist of numerous smaller repeating units (monomers) arranged in large chain-like molecules. Traditionally polymers were considered insulators, however they are being made to conduct either by their intrinsic structure or by metallic additions, allowing conductive pathways to be formed. Since the 1970's there has been a great rise in the number of conductive polymers available. These are typically tailored to serve as substitutes for metallic conductors and semi-conductors for a wide variety of applications. Since their discovery a wide range of intrinsically conductive polymers have been

developed, which can be divided into a number of groups depending on what the main polymer chain contains. The most utilised of these groups are those which contain aromatic cycles such as Polyphenylenes, Polyanilines[77] (PANI), Polyphenylene Sulphide (PPS) and Poly(3,4-ethylenedioxythiophene) (PEDOT). This group can be further split depending on the heteroatoms present (none, nitrogen or sulphur). The other groups include those with double bonds, Poly(acetylene)s (PAC), and combined aromatic cycles and double bonds, Poly(p-phenylene vinylene) (PPV). Examples of these structures are shown in Figure 1.13 below.

PANI is one of the oldest known conducting polymers with good stability within oxygen and moisture rich environments. It was discovered in its polymer form as "aniline black" as early as the 1830's[78,79]. PEDOT is used extensively within the research community for developing solar cells and other printable electronics[80]. Whilst these materials have good conductivity (PANI = 200s/cm), they tend to be costly and have a low thermal stability making them undesirable for thermoelectric devices.

Conducting polymers have the advantage over metallics and semiconductors as they are more easily processed through spin coating, flexography, screen printing or slot-die coating. Polymers are typically dispersed in a solvent, then after evaporation a layer of polymer chains is left. Further curing can then be used to produce crosslinking, creating a stable and often flexible conductor.

Due to their thermal stability alternative printable polymers were considered. To achieve this, insulating polymers with conductive fillers were investigated to produce a thermally stable, printable, conductor.

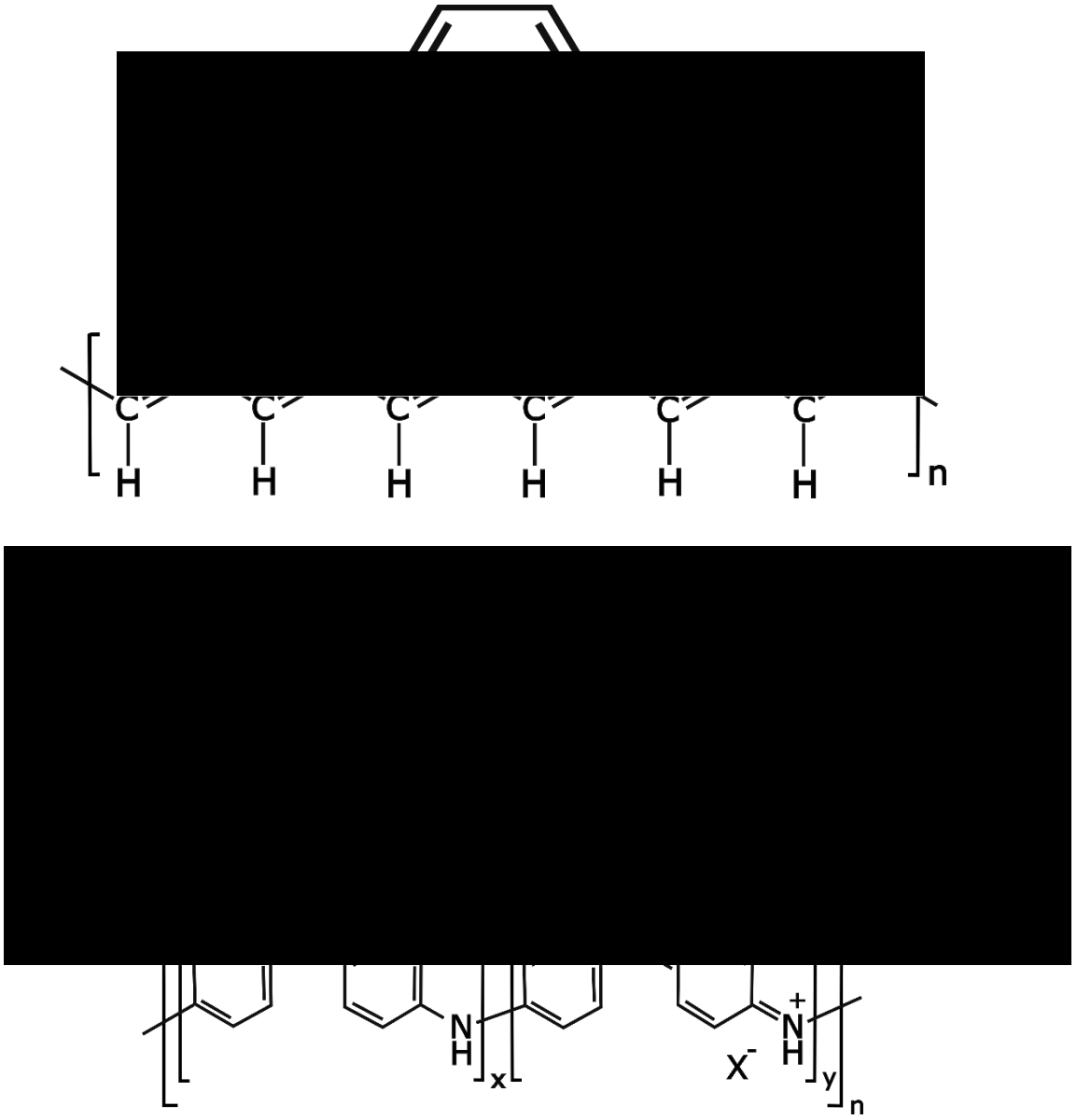

PANi

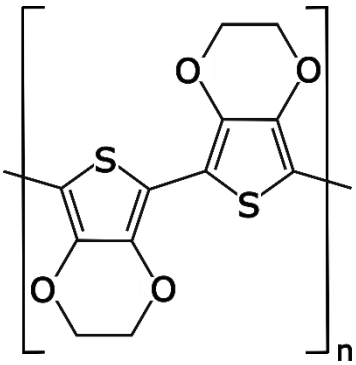

PEDOT

Figure 1.13 Structures of a range of conductive polymers[81]

1.7.1 Conductive Mechanism for Intrinsically Conductive Polymers

Intrinsically Conducting Polymers (ICPs) can be split into three categories:

- Electron-conducting
- Ion-conducting
- Proton-conducting

The most common type of polymeric conduction will be discussed here. Traditional inorganic semiconductors contain 3D covalent bonds with low level atomic substitution, this provides doping without major distortion of the lattice. Polymers on the other hand typically contain only 1D covalent bonds (along the backbone) with weaker bonds between the chains (Van der Waals). Doping is then achieved using redox chemistry, this extrinsic dopant is then used to transfer the charge, resulting in deformation of the chains as the charge transfers.

A useful example is Polyacetylene (PAc) which were doped to high conductivity levels. This polymer consists of two alternating structures with the same energy allowing the support of a defect in the form of a free radical or neutral soliton[82]. This is a 1-D domain wall separating the two ground state structures, also termed a "kink" in the chain. This "kink" will propagate down the polymer links[83], allowing the appearance of a localized electronic state at the mid-gap.

A spin of ½ is observed on this soliton defect due to an unpaired electron, this is then either removed (by oxidation) or an additional electron is being added (by reduction), ionising the polymer chain. This soliton may then migrate along the chain by a bi-polaron hopping mechanism, limiting the charge transfer rate[84]

Polyaniline (PANi) is an example of a polymer which does not follow this transfer mechanism, its structure is shown in Figure 1.13. The ground state energy of these polymers are substantially higher than that of the aromatic benzenoid structure, giving different charge defects[85]. PANi's quinoid structure requires oxidation for its formation. Further conductivity improvements have been made by doping the polymer chains.

1.7.2 Usage of Non-Conducting Polymers as Conductors

Whilst intrinsically conducting polymers have their advantages, they have limited uses for thermoelectric applications due to their thermal stability and cost. For example, a

dispersion of PEDOT commonly used within the PV industry costs around £2670/kg, which is not viable for the targeted large-scale applications. As such a conductive filler added to a traditionally non-conducting polymer is the ideal solution. A wide range of conductive additions are available including allotropes of carbon, nano-particles, rods and wires of a wide variety of metals. Once an additive is dispersed into the polymer above its percolation threshold it allows the bulk polymer to be an effective conductor. The desired conductivity depends on the application, typically semiconductors have conductivities up to 10^6S.cm^{-1} , however conductivities can be as low as 10^1S.cm^{-1} for some semi-conducting applications[86,87]. For a polymer to be an effective conductor conductivity of greater than 1S.cm^{-1} is needed[87,88]. Carbon based, or low uses of precious metals were determined to be the primary affordable options available for conductive additions.

The most important consideration for conductive fillers is the percolation threshold, this is the point where the filler concentration allows the electrical conductivity to increase sharply[89,90]. This sharp increase of a few orders of magnitude is due to a complete conductive pathway being provided by the filler material. When below this percolation threshold the electrons must travel through large amounts of the insulating polymer, this increases the resistivity greatly. When the threshold is reached, conduction is primarily along the conductive fillers from one particle to the next. Above this threshold the conductivity variations are minimal with increasing filler amounts. This, for nanotubes can be defined by Equation 4 below:

$$\sigma \propto (m - m_c)^{\beta m}$$

Equation 4: Relationship between the conductivity and filler amounts

Where σ is electrical conductivity, m is the nanotube mass fraction, βm is critical exponent and m_c is concentration threshold.

The percolation threshold is controlled by the polymer and filler interactions, if the filler to filler interactions are stronger than the polymer-filler bonds then agglomeration will occur. If the filler to filler bond is weaker than the polymer-filler bonds then the particles will become well dispersed[86,91]. The percolation threshold typically increases with the surface tension of the polymer[86,92], causing filler percentages to rise from 2wt% in Polypropylene to 25wt% in Nylon-6.

The polymer crystallinity can also affect the dispersion and percolation of fillers. Crystallising sections of polymers will eject fillers into the amorphous area, resulting in further agglomeration of the particles.[86]

1.7.3 Conductive Additives for Polymers

1.7.3.1 Carbon Nano-Tubes

A much-publicised functional filler material for polymers is CNTs in both single-walled (SWCNTs) and multi-walled (MWCNTs) forms. Nano-tubes vary in characteristics from batch to batch and significantly depending on the suppliers, so reliable sources of CNTs are vital. In the case of SWCNTs often percolation thresholds are below 1wt%, primarily due to the extreme aspect ratio of the SWCNTs. A key limiting factor with SWCNTs is the distribution of the materials. Due to the strong interactions with the high C-C bond strength in comparison to that of the polymer-C bonds, the resultant Van Der Waals interactions result in agglomeration and aggregation of the CNTs. This has the effect of reducing their aspect ratio, which increases the percolation threshold. The higher aspect ratio fibres typically need less filling; however, they agglomerate much more easily. To correct this additional surface treatments are needed to reduce the Van der Vaal's bonds, allowing the nanotubes to disperse.

The main limiting factors for CNTs are toxicity and cost. Due to the needle like nature of the CNTs, particularly those with larger aspect ratios, can cause inflammation and disease within living tissue due to the mammal immune systems being unable to deal with them[93]. This is similar to asbestos which could possibly result in cancers such as mesothelioma[94]. They are particularly dangerous when dry as they can be easily inhaled. In addition to their danger, they happen to have a high cost of over £3000/kg, which leads to them being far too expensive even with their low fill factors.

1.7.3.2 Carbon Black

Conductive Carbon Black (CB), is an amorphous carbon with a wide variety of uses within polymers. Some applications include: UV stabilisation, as a pigment, a dimensional stabiliser and as a conductive filler[86]. With carbon black the particle size, structure and surface chemistry are vital. There are several reported structural behaviours associated with CB including turbo-static stacking orders as identified by. identified by

X. Bourrat[91]. This leads to a wide behaviours and properties. The ideal CBs for conductive polymers have high porosity and surface area.

Carbon black readily agglomerates within polymers, which can be reduced by applying large amounts of shear to the polymer-CB mixture[95]. Large amounts of shear in the early stages of mixing (from batch mixers, triple-roll mills and shear mixers for example) break the CB up, this allows the polymer to move between the particles. This produces a superior dispersion and a lower percolation threshold[96]. Ideal dispersion of CB is achieved when each particle is entirely covered in resin, however too much coverage can increase the resistivity of the polymer by removing conductive pathways, therefore longer mixing steps may be detrimental[86].

High quality CB is an extremely useful filler and typically works best when combined with another conductive filler such as graphite to increase conductivity and fill density. It is however still expensive and presents a number of risks due to its nano-particulate nature. The traditional layered structure of graphite is shown in Figure 1.13.

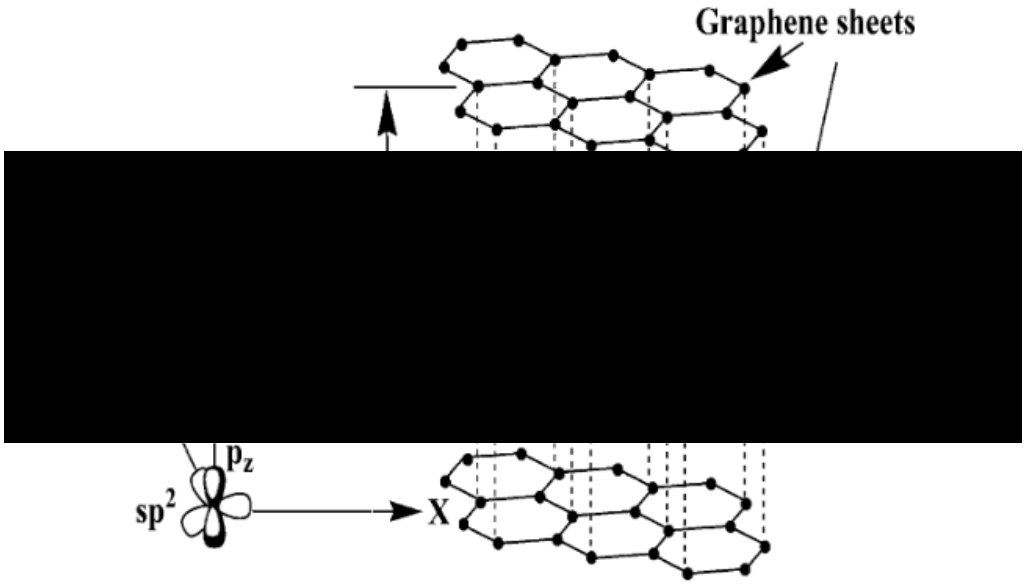

Figure 1.14 Layered structure for graphite, with the sp^2 hybridized carbon atoms bonded in hexagonal rings[97]

1.7.3.3 Graphene

Graphene is the most recently discovered allotrope of carbon, typically consisting of a single layers of carbon atoms along the hexagonal lattice. This structure provides high conductivity and strong mechanical properties, making it an extremely favourable

conductive filler material. It is however difficult to manufacture, typically coming in the form of graphene nanoplatelets. Due to the high cost of these fillers this was determined to be unsuitable for the desired applications.

1.7.3.4 Graphite

Graphite is the most affordable form of carbon and is available for costs of below £10/kg. Graphite consist of multiple hexagonal layers linked weakly together allowing the layers to slide or cleave readily. This reduces their conductivity and mechanical properties but allows them to be used as lubricants. Graphite can come in natural and synthetic forms as it is found naturally occurring within the earth's crust. Synthetic graphite is produced by heating high-carbon materials up to 3000^{o}C, driving off the volatile materials and leaving 99% carbon. This material is readily available from companies such as Imerys and has a reliable high quality supply chain.

1.7.3.5 Metallic Additions

In addition to carbon inclusions, metals are also used to increase the conductivity of polymers. For polymers to gain metallic conductivity, particles must be in contact to form a conductive pathway. There are two conduction mechanisms within the polymer, if there is contact between particles the standard metallic conduction mechanisms apply (i.e. band type conduction). However, if the polymer fully surrounds the particles, effectively isolating them, the conductive properties change significantly. If the particles are in close proximity (<10nm), electrons pass between particles via tunnelling. Metals are typically used in powder, nano-wire or flake format[89,98,99]. For materials with anisotropic electrical conductivities, powders are ideal, however these need extremely high fill factors (50+%). By using metallic flakes higher conductivities can be achieved at a much lower fill factor, this however leads to significant isotropic behaviour. Conductive metallic additions used typically include silver, copper, nickel, gold, and palladium[100,101]. The limiting factor with metallic additions is their cost. Precious metals such as silver flake cost an upwards of £400 for 100g, which for many conducting polymers is uneconomical. Alternatives have been considered with coated glass products presenting themselves as a possible candidate. Several suppliers produce these products for applications such as the cosmetics industry, leading to them being significantly cheaper due to the competitive nature of the sector. SG35F30 is a silver coated glass flake product from the PQ Corporation[102], with the same fill factor as standard silver flakes whilst being

10% of the cost. Alternatives are available from NSG Pilkington, in the form of Metashine[103] and Glass Flake Limited, in the form of ECR glassflake[104] and AgFlake[105].

These coated materials are available in number of arrangements, the most basic and viable, product is the flake form shown in Figure 1.15. In flake form the silver coating varies between a few nm to 10 microns[103]. Other alternatives include silver coated copper flakes which are significantly better conductors but suffer from diffusion in higher temperatures (>100^{o}C). Glass fibres are also coated in a similar fashion.

Figure 1.15 Example of the reflective properties of the Metashine Glassflake product[103]

1.7.3.6 Silver Nanowires

Silver nano-wires and to a lesser extent copper, are becoming an increasingly popular addition to conductive polymers, particularly when transparency is required.

Silver nano-wires are produced by a number of different methods. These include: Reduction of $AgNO_3$, microwave-assisted synthesis, hydrothermal synthesis using glucose as a reducing agent, electrodeposition, and aqueous solution synthesis. The percolation threshold has been shown to be 2wt% for shorter nanowires. Nanowires with 25nm diameter and 200-400 aspect ratios percolate at 0.5-0.75wt%, allowing them to be used as an effective filler in a wide range of environments[89]. As with other nano-particulates are extremely costly and have a number of health hazards as stated in Section 1.7.3.1.

1.8 Thermal Decomposition of Polymers

At high temperatures long chain polymer molecules begin to break down and can significantly change properties before completely disintegrating. Polymers can degrade in several ways including: thermal degradation, oxidation, photo degradation and general

weathering. Degradation can typically result in a change in molecular weight. This can also result in the polymer chains becoming embrittled or softened, caused by chain hardening and chain scission respectively. Optical and conductive properties also change, with the most extreme degradation causing charring and cracking of the polymer with corresponding weight loss.

In the scope of this project the primary decomposition mechanism of concern is thermal-oxidative degradation. This can be split into 3 segments: initiation, propagation and termination[106]. Light or heat are typical causes of initiation. During this hydrogen abstraction or scission of C-C bonds allows a radical to form. A free radical in this case is a molecule that has an unpaired valence electron, allowing it to react with the surrounding atmosphere (R-H -> R· + H·).

Once the radical has been exposed the degradation propagates via a series of reactions. The free radical can firstly react with atmospheric oxygen to form a peroxy radical (ROO·*), which then reacts with a hydrogen from the polymer lattice. This will form a hydroperoxide (ROOH), which further splits into two new free radicals (RO·) + (·OH). These may then continue to react with exposed hydrogens on other chains. Each initialised reaction can then form two new radicals, allowing decomposition to rapidly propagate.

It is possible for this reaction to cease locally due to termination. This can be achieved by the recombination of two radicals, or by hydrogen abstraction. This recombination results in two chains combining, increasing the molecular weight and crosslink density, causing embrittlement. The second termination mechanism is chain scission, which decreases the molecular weight, softening the polymer. The termination types depend on the polymer and conditions available, therefore controlling this degradation is vitally important.

1.8.1 Stabilisation of Polymers Against Thermal Degradation

Due to the degradation mechanisms seen in Section 1.8 and the desired high temperature applications, it was determined that stabilisation was needed for any polymer binder used for thermoelectric application. As this is primarily focused upon the silicon-oxide polymer provided by industrial partners, SILRES 604, this was the resin chosen for modification.

According to the information provided by Wacker, SILRES 604 is capable of long term stability up to 250ºC and short-term stability up to around 300ºC. There is a predicted yellowing at around 270ºC. The gloss loss of a coating, a loss of aesthetic gloss finish, while not a factor for this application, indicates potential decomposition of the polymer. Pure coatings are seen to lose gloss from 230ºC, at which point there is an 85% gloss retention down to 65% at 300ºC.

The chosen product was the 604 grade SILRES powder coat. 604 grade is a Polysiloxane containing 4.5-6% functional groups, with the resin structure is shown in Figure 1.16. The MSDS shows the production of small amounts of formaldehyde at 150ºC through oxidation and Benzene at above 180ºC. These should not cause a problem however it is worth noting in the case of weight loss during testing[107].

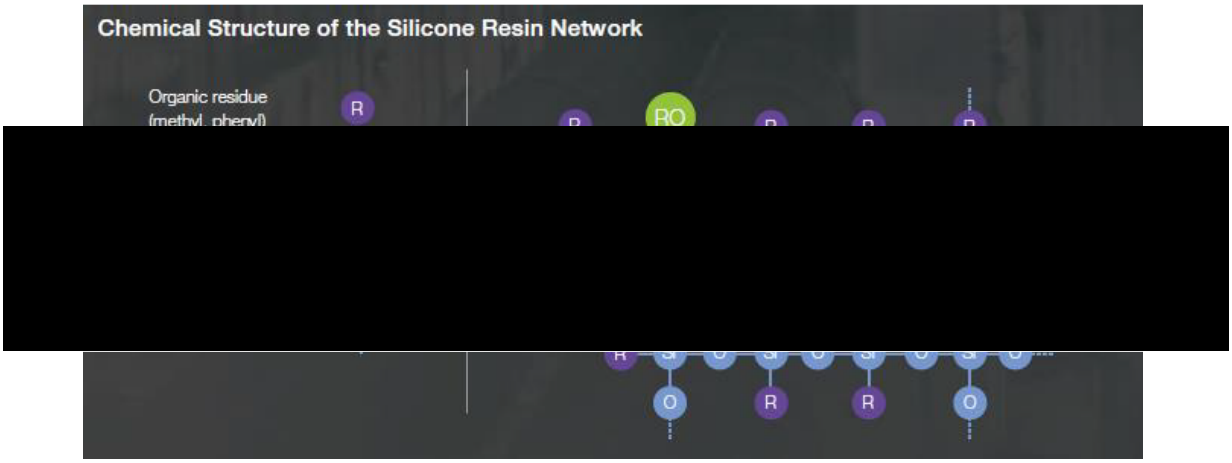

Figure 1.16 Theoretical structure of the polysiloxane polymer with functional groups of hydroxyl and remaining organic residue shown[108]

Literature indicates that high pigment loading leads to improvements of the stability of the silicone. Wacker's own guide indicates that low pigment content gives thermal stability up to 200ºC. The addition of metal pigments, such as aluminium or zinc, allows the methyl groups to react forming coatings with thermal stability up to 650ºC. Figure 1.17 displays a range of fillers and their effect on the stability for a generic Silicone resin. This is further shown in Figure 1.18 from Dow Corning wherein they give similar information.

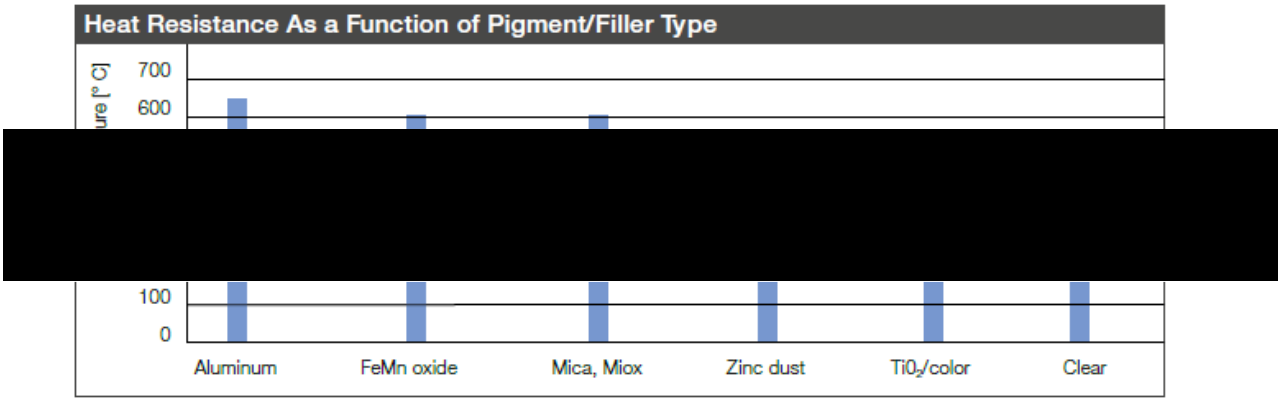

Figure 1.17 Effect of fillers on the heat resistance of polymer coatings[108]

Performance Temperature Range[1]	Resin Type	% Silicone	Pigment
121-204°C (250-400°F)	Silicone-modified organic	15-50	All pigments
538-760°C (1,000-1,400°F)	Silicone	100	Ceramic

[1]1,000 hours minimum

Figure 1.18 Dow Corning effect of additions on silicone polymers[109]

There is no information on the addition of carbon and its effect on these thermal properties for this particular polymer. The hydroxyl reactivity of leafing aluminium pastes, zinc, iron oxide and titanium oxide allow the formation of a more stable metal-silicone composite than plain SILRES 604, as indicated in Figure 1.17 and Figure 1.18.

Chapter 2 Materials and Methods

2.1 Materials

This chapter outlines the general materials and methods used throughout the 3 primary development areas. These are thermoelectric materials, polymer electronics and phase change materials. The thermoelectrics primarily focused around Transition Metal Silicides (TMS). Polymers produced contained three basic components: binder (SILRES 604), conductive filler (for instance carbon, metal powders, etc.) and an ionizing solvent (IPA, acetone, etc.). Finally, the phase change materials contained a variety of salts. A full list of materials is included at the end of this chapter.

2.2 Transition Metal Silicide Materials

Silicon substrates of 200-800 microns thickness were used as the base for these experiments. These thick substrates allow for easy cutting and growth rate determination within the research. The substrates used in this experiment are outlined below:

- Polycrystalline silicon. 200 microns in thickness, 99.9% purity obtained from the European Space Agency
- Pyramid textured silicon. 800 microns in thickness, 99.9% purity obtained from the centre for Nanohealth, Swansea University. This is shown in Figure 2.1.

For deposition onto these substrates three readily available transition metals were used:

- Magnesium powder. technical grade, 96% purity obtained from Fisher Scientific (CAS - 7439-95-4).
- Manganese powder. ~40 mesh, 99+% purity obtained from Arcos Organics (CAS - 7439-96-5).
- Iron puriss powder. 99.5+% purity from Sigma-Aldrich Co LLC (CAS – 7439-89-6)

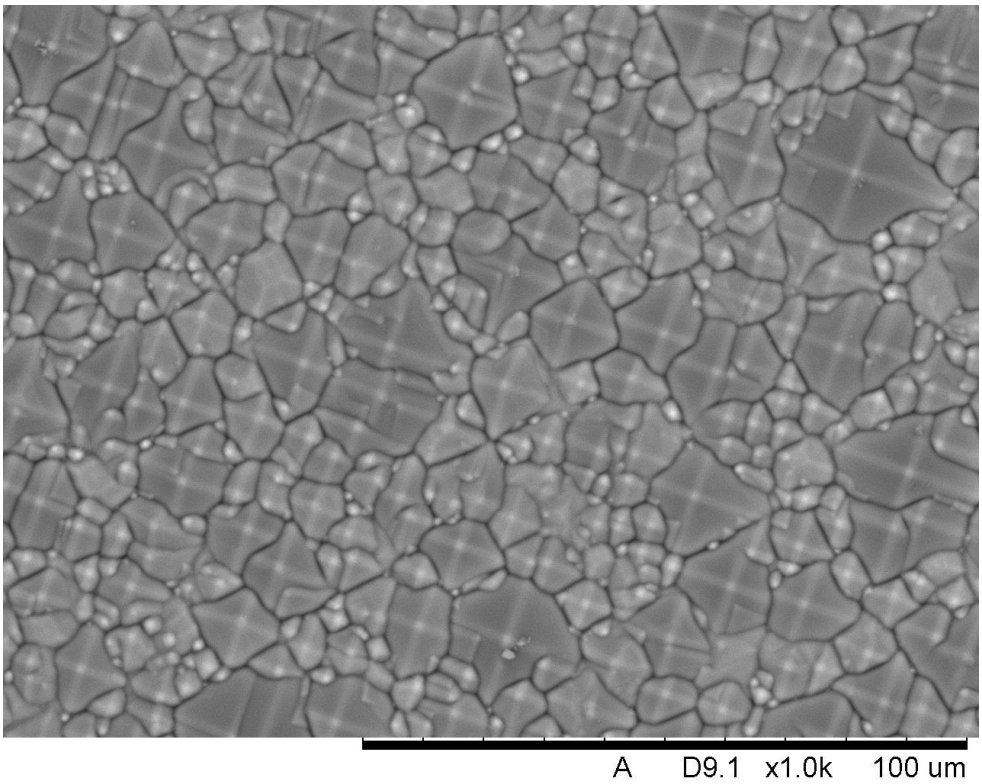

Figure 2.1 Pyramid textured silicon substrates taken using SEM.

2.3 Pack Cementation

The pack cementation process is generally similar regardless of metal deposited, with changes in pack composition depending on the atomic ratios desired within the material.

Silicon substrates were cut to size to ensure they fitted within each crucible, cleaned using a light solvent spray and dried. Each substrate was weighed to calculate the amount of active ingredients needed per g of silicon. Magnesium packs had 1.73g magnesium, 0.21g NH4Cl, manganese packs contained 0.7g manganese and 0.14g NH4Cl while iron packs had 2g iron and 0.15g NH4Cl to create the correct atomic ratio of the final product. Once the powders had been weighed out to the correct ratio, they were mixed with alumina powder to ensure the pack was full. Shake mixing was undertaken for a period of 5 minutes by shaking the powders to ensure a relatively even dispersion of active ingredients prior to preparing the pack. All powders were stored in a desiccator with care taken to avoid excess moisture. However older Mg powder was seen to be less effective, indicating some oxidation had taken place. This process is shown in Figure 2.3.

Sealed crucibles were then placed inside a controlled atmosphere tube furnace (Lenton Horizontal split tube furnace, CSC 12/90/300H), with a quartz or IAP work tube, this set-

up can be seen in Figure 2.4. The furnace was sealed and purged with either argon or nitrogen gas at an initial rate of 2 l/min, before dropping down to 1 l/min to maintain atmosphere. All pack mixtures can be heated in argon however magnesium cannot be undertaken in a nitrogen atmosphere, due to the formation of magnesium nitride (Mg_3N_2). Slow heating and cooling rates of 3.5°C/min were utilised to prevent any uneven heating of the furnace. Samples were held at a variety of temperatures and times, outlined in the relevant chapter. Temperature programs were set using a standard 8 segment PID controller. Temperature ranges were 400-650°C for magnesium, 650-1000°C for manganese and 400-900°C for iron respectively. This can be seen in Figure 2.2.

Upon cooling, crucibles were opened while the powder and substrates were removed. Substrates were cleaned with a solvent spray and compressed air to remove all remaining powder. These samples were then tested as described later in this chapter.

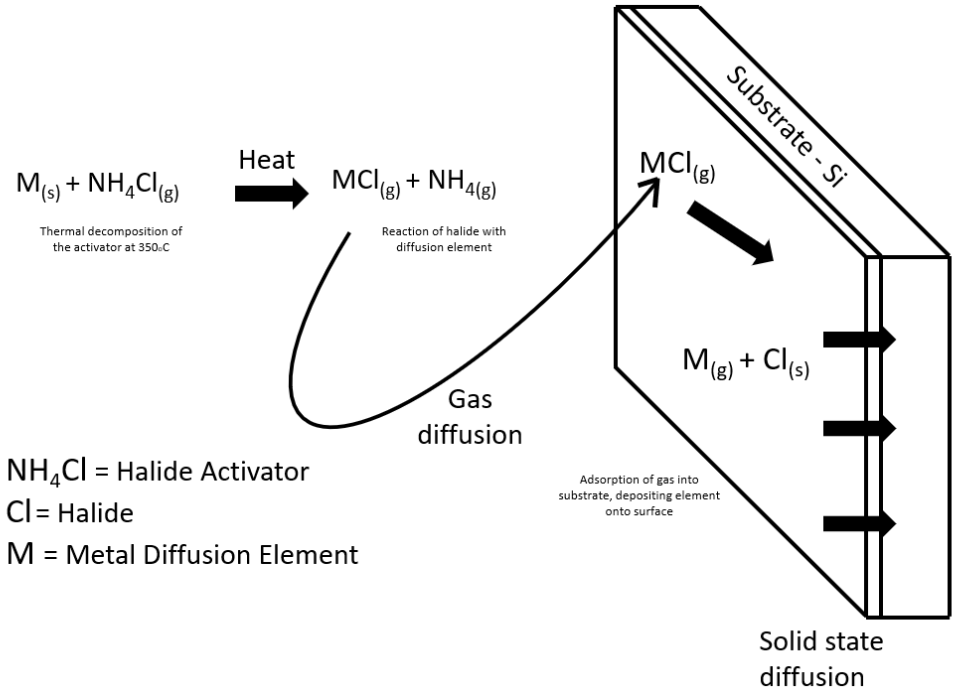

Figure 2.2 Metal deposition process within the pack crucible

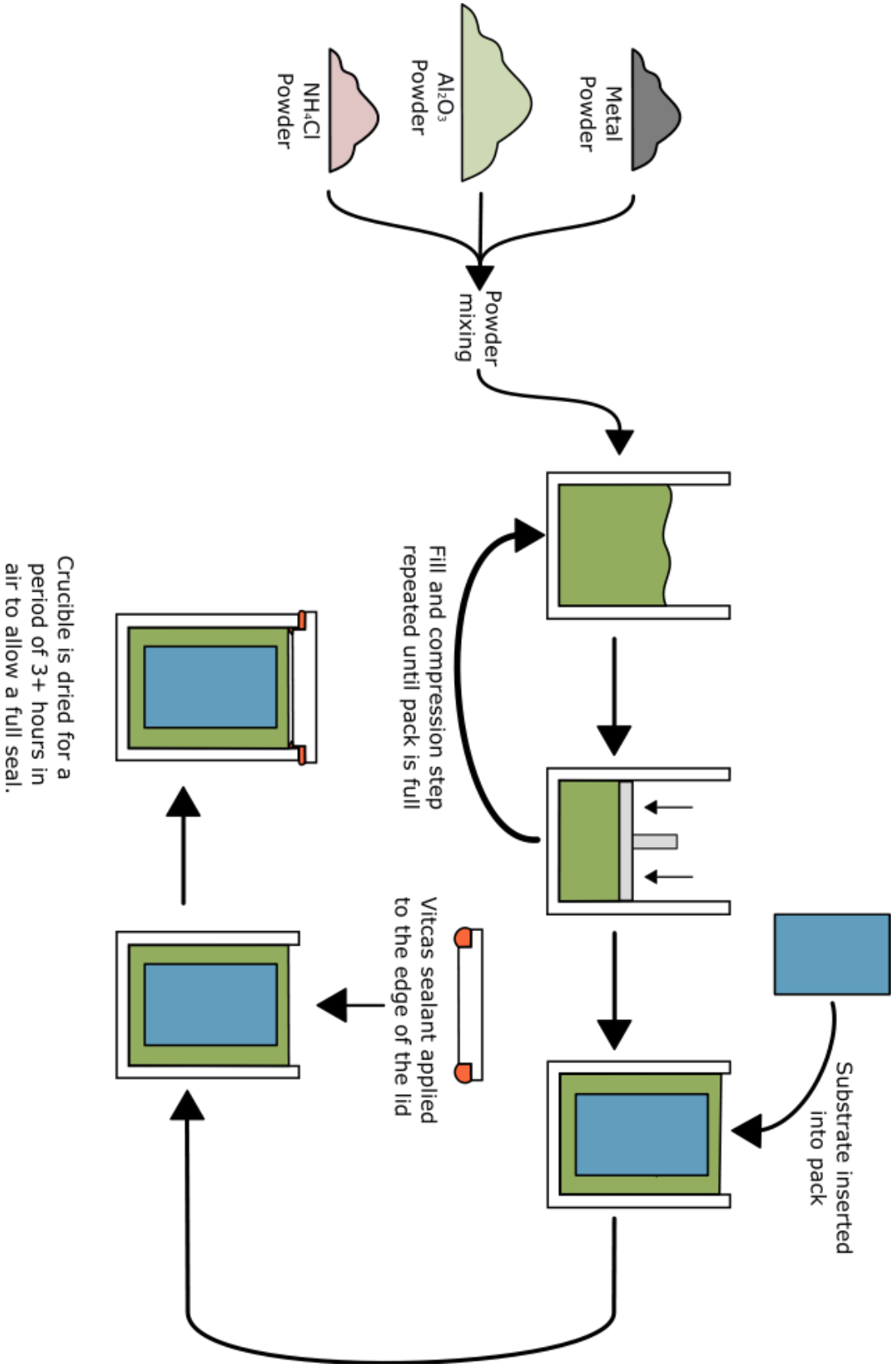

Figure 2.3 Schematic of the crucible preparation for the pack cementation process

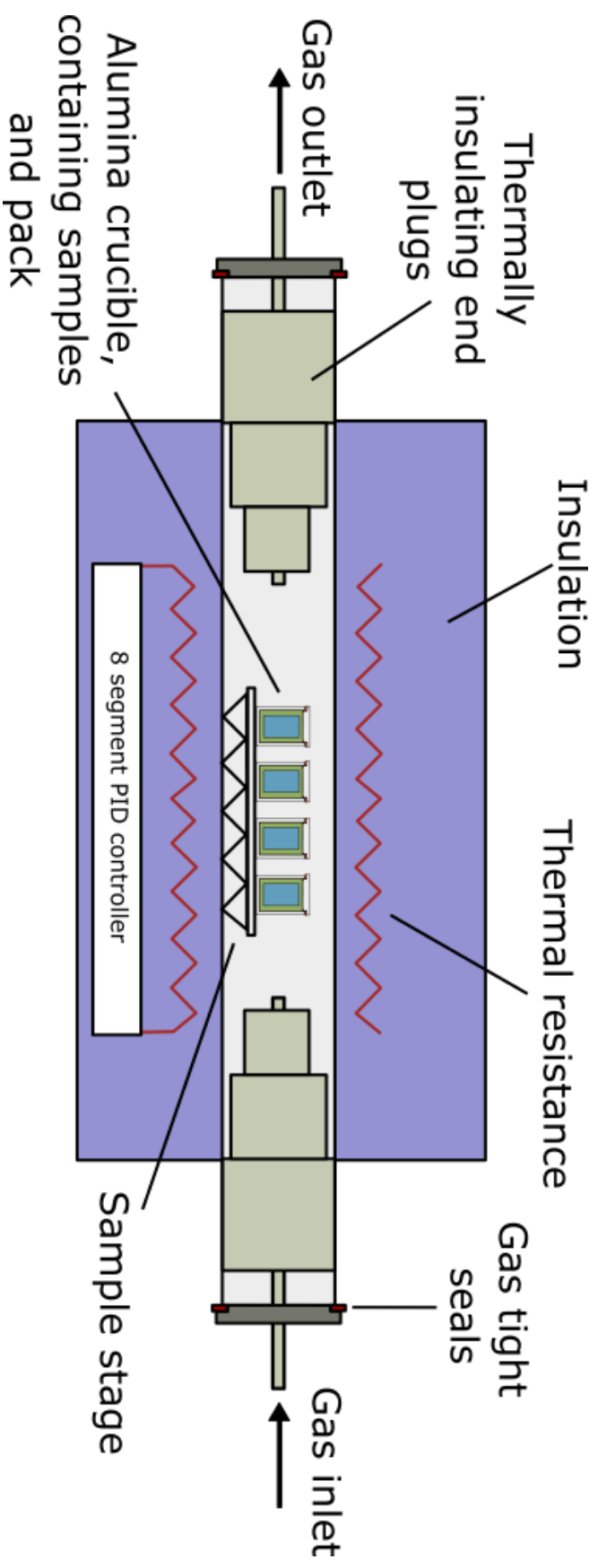

Figure 2.4 Schematic of tube furnace layout for the pack cementation Process

2.3.1 Out of Pack Cementation

This variation of standard pack cementation was developed to produce high purity Higher Manganese Silicide. The production of the pack is outlined in the schematic in Figure 2.5. For this technique a lower amount of alumina was used (around 0.5g) in order to remove any contact effects. The heating process was the same as standard pack cementation.

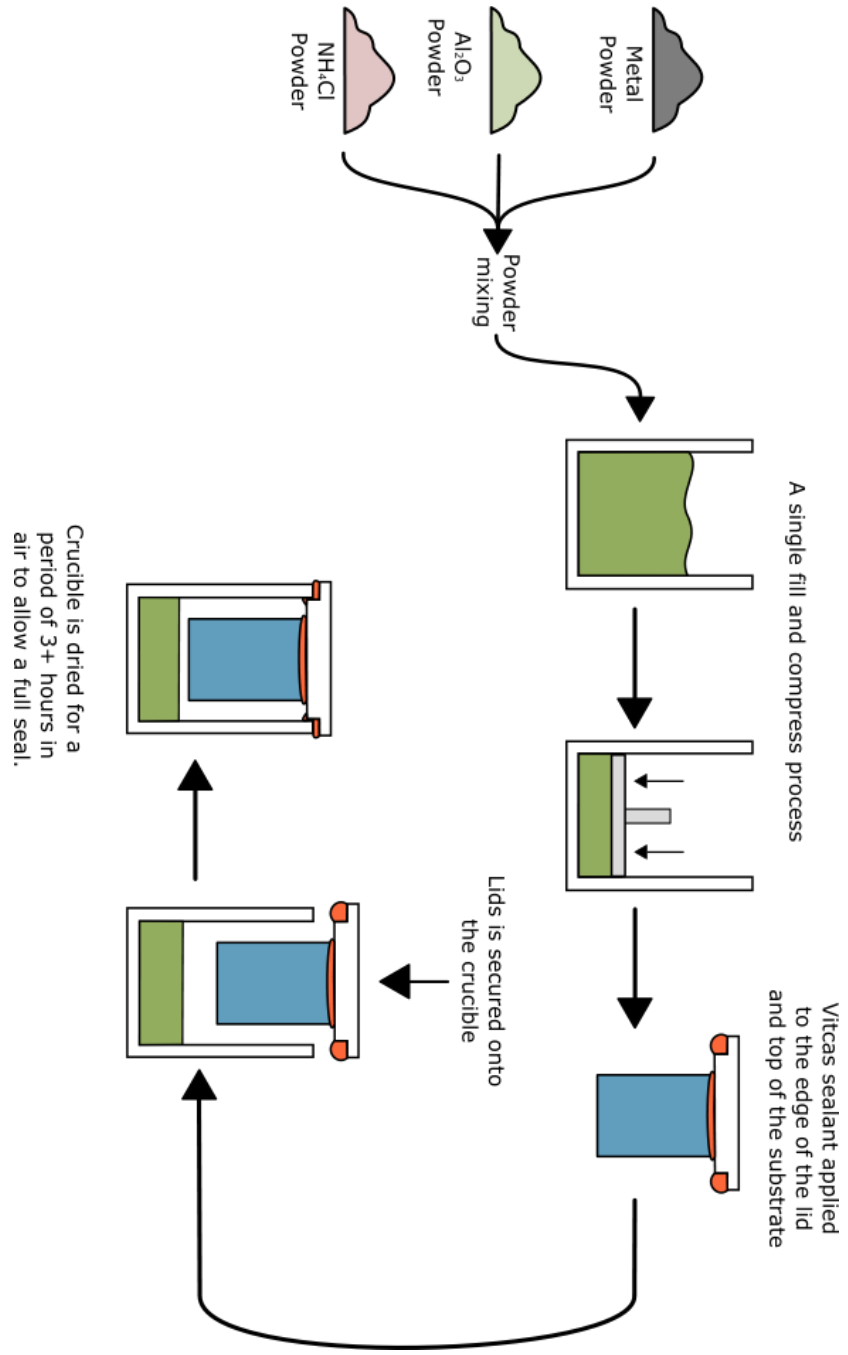

Figure 2.5 Schematic of the crucible preparation for the out of pack cementation

2.4 Polymer Electronics

The SILRES 604 resin, a high temperature powder coating product, was specified by the sponsoring company. SILRES 604 is a hydroxy-functional phenyl-methyl polysiloxane resin. This is best shown in Figure 1.16, where these hydroxy and phenyl-methyl groups reside on an inorganic, Si-O backbone. SILRES can be stabilised up 650ºC using a variety of additions and is low cost, non-toxic with good organic compatibility. SILRES is soluble in non-toxic solvents such as Isopropanol alcohol (IPA) and can therefore be made into a liquid of known viscosity, at a cost of around £10/kg. This material is specified as follows:

- SILRES 604. Polysiloxane with functional groups, in flake form. From Wacker Chemie AG.

Several conductive and stabilising additions were trialled for this research, these will be listed at the end of this section. The final product was composed of a mixture of synthetic graphite, cosmetic grade silver coated glass flakes and zinc powder for stabilisation as outlined in the following:

- TIMREX SFG15. Synthetic graphite, 99.5+% purity from Imerys graphite and carbon, with an average of 17.9μm particle size (CAS - 7782-42-5)
- Metashine 5480PS. silver coated glass flakes. Composition of these flakes equates to 85-90% glass (CAS - 65997-17-3), 10-15% silver (CAS - 7440-22-4) and <0.1% tin dioxide (CAS - 18282-10-5) from Nippon sheet glass co. LTD.
- Zinc powder. 1-5μm 99% purity from Goodfellow metals.

2.5 Phase Change Salts

In order to create a basic salt structure, a standard commercially available ternary salt was selected (HITEC) and made from its constituent components to allow for additions to be added later. HITEC has surpassed the traditional binary sodium nitrate and potassium nitrate salt in recent years by dropping the melting point from 221ºC to 142ºC. The HITEC salt was chosen as it has the highest current long term operating range (142-454ºC) for a ternary salt. It can also be used for short term stability up to 538ºC. This base salt is already in heavy industrial use and is readily available to industry as a bulk, affordable product. Its three primary constituents are KNO_3 (53wt%), $NaNO_2$ (40wt%) and $NaNO_3$ (7wt%):

- Potassium Nitrate, KNO_3. reagentPlus, 99+% purity from Sigma-Aldrich (CAS – 7757-79-1)
- Sodium Nitrite, $NaNO_2$. reagentPlus, 99+% purity from Sigma-Aldrich (CAS - 7632-00-0)
- Sodium Nitrate, $NaNO_3$. reagentPlus, 99+% purity from Sigma-Aldrich (CAS – 7631-99-7)

Following on from work done for alternative applications Li containing salts and metal chlorides where tested. All initially trialled additions to this salt are listed at the end of the chapter. Two primary additions within this research were LiCl and KCl due to their effect on the materials stability. Metal chlorides have been shown to improve high temperature stability, whilst salts containing Li have been shown to have a lower melting temperature:

- Potassium Chloride, KCl ACS reagent (CAS -7447-40-7)
- Lithium Chloride, LiCl ACS reagent, 99% purity (CAS -7447-41-8)

2.6 Conductive Polymers

The production of the final iteration of conductive polymers is straight forward. Several production methods were trialled, and their effects will be reported on in the relevant chapters. SILRES 604 was initially ground with a pestle and mortar to speed up any reactions with the solvents. Once ground the SILRES was weighed, along with SFG15 graphite, zinc powder and 5480PS flake. The final mixture for low cost, high temperature stability and maximum efficiency is 1g graphite, 0.05g zinc powder and 0.7g 5480PS for every gram of SILRES. These powders were lightly mixed through shaking prior to the addition of solvent. IPA was used as the base solvent, with around 2g added for every gram of SILRES. This is enough to dissolve the SILRES. An additional 2g of terpineol was added to ensure the polymer mix remained liquid whilst in operation, this has the added advantage of increasing the drying time and prevents drying in of any screens used in the process.

Upon addition of the solvents, pots were sealed and placed on a rotation mixer, which allowed a gentle, non-destructive mixing of the polymer. After 180 minutes the polymer was fully dispersed and could reach its optimum properties and could then be cast onto the desired substrates.

2.7 Bar Cast onto Glass

Glass substrates (C. G. Toft LTD) were cut to 50 mm^2, cleaned with soapy water and acetone, then air dried. Once the substrate was dried it was secured onto a cutting mat using electrical tape to prevent shifting of the substrate. The tape also provided two level surfaces for the bar to slide along, allowing a controlled deposition level. It was ensured that the tape had no folds or air bubbles as these would affect the quality of the cast. A small amount of polymer was placed at the top of the substrate, where the glass bar was drawn down at a steady and uniform rate by hand. This resulted in the polymer being forced between the glass substrate and the bar, channelled by the electrical tape. After the cast, the sample was left to allow some solvent evaporation before the tape was removed. All samples were cured at 200^oC for a period of up to 1 hour to fully evaporate any solvent and ensure full curing of the polymer. Prior to testing, all samples were lightly brushed with a cloth to remove any loose carbon from the surface.

2.8 Rheological Testing

Viscosity behaviour of the conductive polymer mixtures were tested using a rheometer (Gemini Bohlin Nano, from Malvern Instruments), with a cone and plate set-up. For this test a 4^o 40mm stainless steel cone was used to improve accuracy. A large gap of 1500 microns was used due to the large particulate size. Samples were placed on a plate held at 25^oC whilst the shear rate was increased from 1 to 200s^{-1}. This testing regime is regularly used within the printing industry and allows analysis of the shear thinning behaviour of the inks for screen printing and other techniques[95,110,111].

2.9 Production of Molten Salts

Quaternary eutectic salts were prepared by mixing individual component salts, with analytical reagent grade materials sourced from Sigma-Aldrich. All salts were dried in an oven at 110^oC and kept in a vacuum prior to weighing and mixing. The HITEC mixture (53wt% KNO_3 – 40wt% $NaNO_2$ – 7wt% $NaNO_3$) was prepared initially, with additions of chlorides added later (KCl, LiCl, CaCl, ZnCl, NaCl and MgCl). For conductive additions a number of forms of carbon were added to the salts at this stage. Carbon forms included CNTs, CB, SFG15 and 20μm flake graphite. After mixing salts were heated to

200ºC for 2 hours, allowing melting and homogeneity to be reached ready for testing. Once ground down these have a fine grainy appearance seen within Figure 2.6.

Figure 2.6 Salt solutions with 1wt% Carbon Black and Graphite respectively prior to heat treatment

2.1 Scanning Electron Microscopy (SEM)

2.1.1 Sample Preparation

Cut edge analysis was undertaken on pack cementation samples to determine conversion percentages. For examination under Scanning Electron Microscopy (SEM), the samples were held in a plastic coil and set in Behuler two-part cold mount resin with 100wt% addition of Nickel based conductive filler. After these solidified samples were ground with a range of papers down to 2500 grit, before polishing to a 1µm metallographic finish.

2.1.2 SEM and Electron Dispersive Spectroscopy (EDS)

SEM analysis was undertaken on a variety of machines throughout this research including a Hitachi TM 3000 and Zeiss EVO. Surface and structural analysis was undertaken using the Secondary Electron (SE) detectors, which due to their lower interaction volume allowed a much better view of surface topography. For cut edge and phase analysis, Back-Scatter (BS) detectors were used to give a clear distinction between each phase, allowing accurate measurements of material conversion. Energy Dispersive Spectroscopy (EDS) was also utilised to gain a measure of the elements present within the materials. EDS functions by simultaneously recording X-rays of all energies, results in a curve for intensity (x) vs X-ray photon energy (y).

This technique has several limitations due to interaction volume and machine set-up. First is interaction depth, wherein SE represents the initial few nm of the material, however BS electrons can penetrate as much as a micron into the surface. This is acceptable for the feature size being analysed however EDS can gain signals from around

3µm deep, potentially resulting in elemental readings from lower features. This was accounted for with a higher degree of experimental error during analysis.

Secondly, a beryllium (Be) window shields the EDS detector which absorbs lower energy X-rays, including the characteristic X-rays of lithium. This makes it impossible to undertake true analysis of the lithium containing salts using this technique. Compounding this, the broad peaks of the EDS spectra reduce its effectiveness where neighbouring elements in the periodic table have closely located peaks, making distinguishing closely located elements difficult. The interaction effects are shown in Figure 2.7.

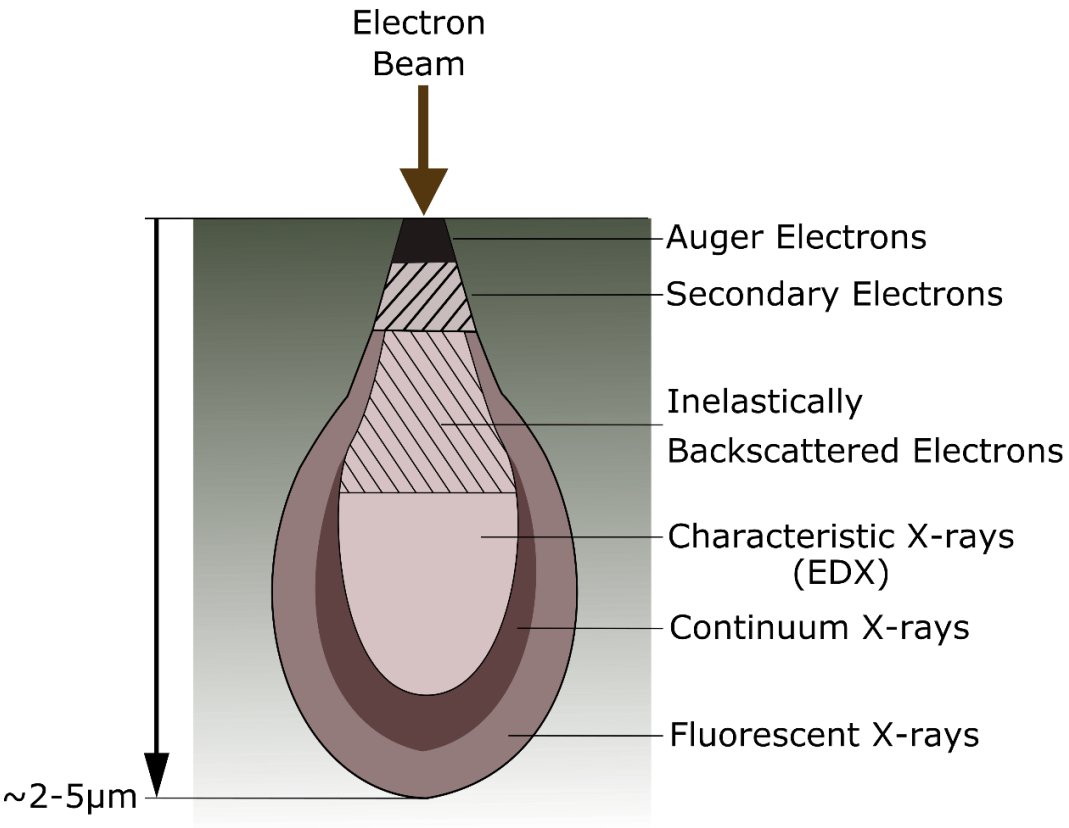

Figure 2.7 Interaction effects of electrons with a conductive material

2.1.1 Electron Back Scatter Diffraction

Electron Back Scatter Diffraction (EBSD) is a crystallographic technique which allows the interpretation of structure, crystal orientation and phase analysis of materials within an electron microscope. This technique is conducted by tilting the sample to 70°. This can be seen in Figure 2.8. The high angle allows the diffracted electrons to form a pattern on a phosphorus screen. This pattern is characteristic of the crystal structure and is termed a Kikuchi pattern. The use of the mapping function in the SEM allows the generation of

orientation maps of samples, enabling individual crystals to be identified. This work focused on the analysis of cut edge samples, polished to a mirror sheen. Each layer was identified by crystallographic phases and then orientation with respects to the Inverse Pole Figures. On average the EBSD maps required up to 12 hours machine time at 20kV with 5nA probe current.

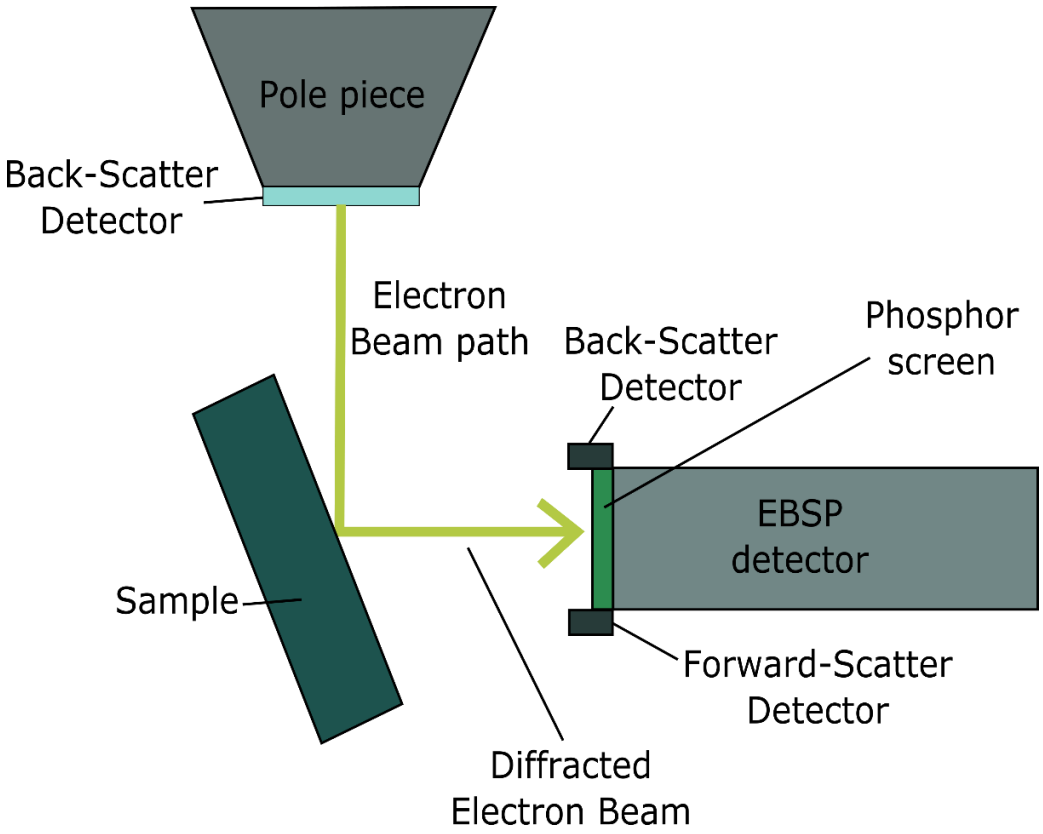

Figure 2.8 Schematic diagram of the SEM chamber in EBSD set-up

2.2 X-Ray Diffraction

X-ray powder diffraction (XRD) was undertaken using a Bruker D8 Discover, with Da Vinci monitoring software, and copper Kα radiation with a λ of 1.5418 Å. For all scans an applied voltage of 40kV and a current of 40mA was used. The scanning range varied between 5 and 70^{o} depending on the desired area. A wide variety of parameters were used depending on resolution or signal needed. Step sizes varying from 0.015 to 0.5^{o} were used to provide the correct peak resolution. Time per step varied from 0.5 seconds for standard scans up to 20 seconds for Grazing-Incidence (GI) scans.

Three setups were used on the machine. For rapid analysis of rougher samples a Göbel Mirror[112], or parallel beam, setup was used. For finer peak analysis divergent slit settings were chosen and for grazing incidence a true parallel beam setup was used.

The Göbel Mirror basic setup can be seen in Figure 2.9. The incident arm consisted of the copper source, a Göbel Mirror, a 0.6mm fixed slit, an axial soller of 2.5° and a rotary absorber, set to automatic. The detector arm consisted of an adjustable slit, another axial soller of 2.5° and the 192-channel Lynxeye 1D detector. This setup allows high signal for rougher samples. The Göbel Mirror, as shown in Figure 2.10, provides parallel beams reducing the effect of surface roughness on the results, it also has the advantage of removing the unwanted Kβ radiation.

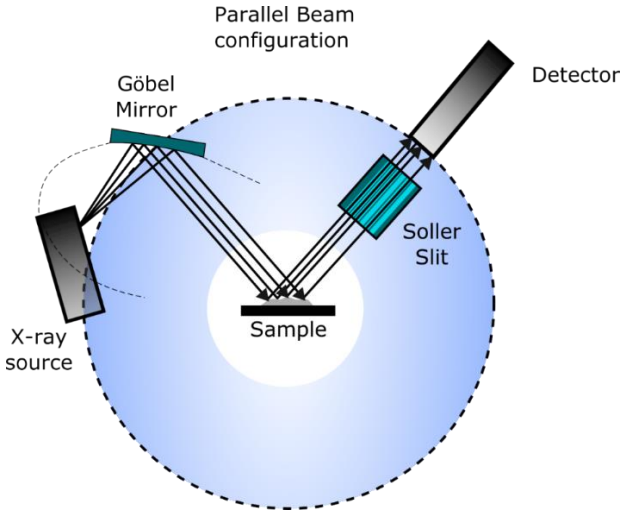

Figure 2.9 Schematic of the Göbel Mirror set-up for XRD

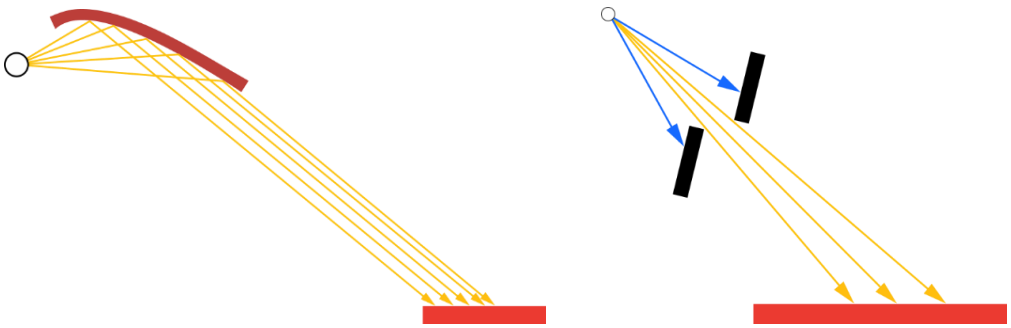

Figure 2.10 Effect of Gobel Mirror (left) and Divergent Silt (right) components of the XRD on X-rays

The divergent beam set-up represents the classical Bragg-Brentano geometry for XRD. In this set-up the Göbel Mirror is swapped out for an adjustable slit and a nickel filter inserted into the secondary arm. Without a Göbel Mirror there is no removal of the Kβ radiation, resulting in a nickel filter becoming necessary. Advantages of this set-up is a higher peak resolution allowing closely formed peaks to be easily resolved. However due to the divergent nature of the beams there is a greater effect from rough samples, as such only optically flat samples were tested using this technique.

For thin films and corrosion products the GI XRD technique was used. This uses a true parallel beam experiment, utilising the Göbel Mirror and swapping out the secondary motorised slit for an equatorial soller. The incident arm is kept fixed between 1-3^{o} to reduce the penetration depth, allowing thin films of <1μm to be effectively analysed. This test used a z-scan and rocking scan to determine the height and tilt of the sample ensuring accurate measurements of corrosion products. Due to the low angle, these GI-XRD tests took up to 6.5 hours to get a clear, high-resolution signal.

2.3 Thermal Analysis

Thermal analysis is essential for the understanding of melting and long-term stability for usage of materials in high temperature environments. There were two primary techniques used in this research, Differential-Scanning Calorimetry (DSC) and Thermo-Gravimetric Analysis (TGA). These can be combined using a Simultaneous Thermal Analysis (STA) technique. Heating control and data collection was undertaken using the Pyris software from Perkin Elmer for all techniques.

2.3.1 Differential Scanning Caliometry

The Perkin Elmer DSC 4000 was used to determine melting points of salts and curing steps within a polymer[113,114]. The DSC functions by measuring the difference in heat input to raise the temperature of a sample in comparison to a reference sample. Samples of 10-20 mg, were put into an aluminium pan, alongside a matching reference pan. Samples were then heated at a standard rate of 20^{o}C/min, to 300^{o}C, in a nitrogen atmosphere with a 20 ml/min flow rate. This cycle was completed twice to ensure any moisture absorbed was burnt off in the first run.

2.3.2 Thermo-Gravimetric and Simultaneous Thermal Analysis

Both of these techniques were used to determine the upper decomposition temperature of samples[115]. Temperature routines were the same for both techniques, where 1-20 mg samples were placed into an Alumina crucible and heated at a slower rate of 10^{o}C/minute in air to 700^{o}C. The set-ups on both machines were different. TGA (Perkin Elmer Pyris 1 TGA) utilises a hanging balance set-up seen in Figure 2.11(a) whilst Simultaneous Thermal Analysis (Perkin Elmer STA 6000) uses a bottom balance setup, seen in Figure 2.11(b). Weight loss due to decomposition was monitored and plotted to show this behaviour.

2.3.3 Long Term Decomposition Testing

For long-term decomposition, a muffle furnace (from Lenton furnaces) was used. 10g of the salt mixtures were placed in porcelain crucibles for periods of up to 30 hours and held at temperatures of 550^{o}C, 600^{o}C and 650^{o}C. Ramp rates of 3.5^{o}C/min were used to ensure the crucibles did not fracture and weight measurements were taken every 5 hours.

2.1 Corrosion Testing of Molten Salts

Due to the high operating temperature of these devices it was not possible to perform standard Scanning Vibrating Electrode Technique or potentio-dynamic polarisation at our facility[116]. As such long time high temperature corrosion immersion tests were undertaken in an argon atmosphere. Specimens of skutterudites were immersed in the molten salt solution at 400^{o}C for 144 hours in atmosphere. This is around the maximum consistent operating temperature of a thermoelectric device using skutterudites. Samples were placed in the furnace whilst immersed in salt solutions, this can be seen in Figure 2.12. A Lenton LTF 12/100/940 tube furnace with a 100 mm diameter quartz tube was used in these experiments, which allowed viewing of the molten salts, see Figure 2.12. The samples were removed from the furnace at intervals of 24, 48, 96 and 144 hours.

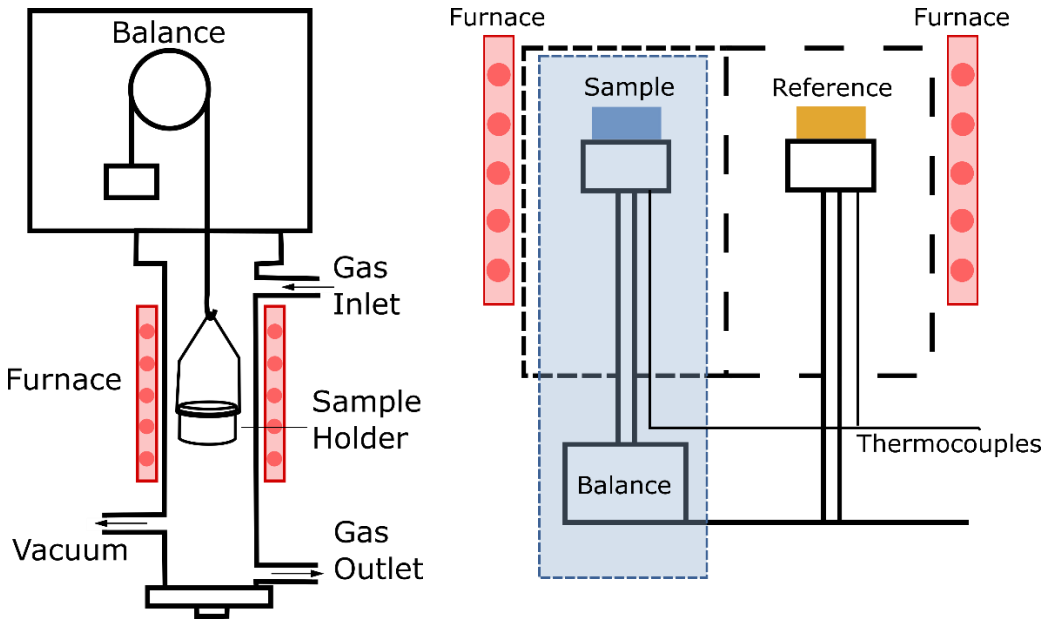

Figure 2.11 Schematic diagrams of the (a) TGA and (b) STA test set-ups

The samples were removed from the molten salts before solidification occurred, followed by a rinse with water and acetone once cool to remove remaining salt. These samples were then investigated under the SEM to see if there were any corrosion products or wear on the samples caused by the salts. In addition to basic SEM analysis a multi-point GI-XRD was performed to examine any corrosion products formed over the testing period of a week.

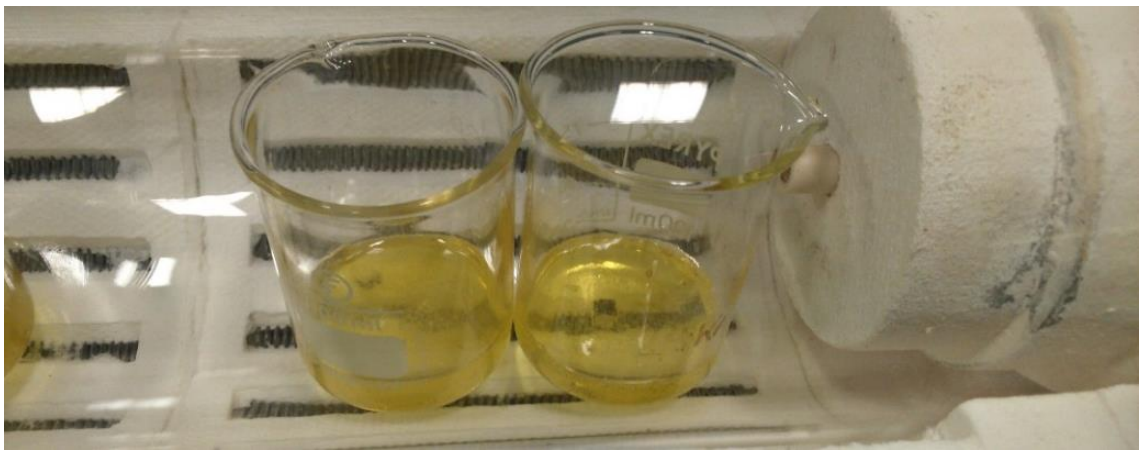

Figure 2.12 The setup within the tube furnace for testing of thermoelectric elements within molten salt at high temperature

2.2 Conductivity Testing

There were 3 methods used for conductivity testing depending on the materials situation. Room temperature conductivity measurements were undertaken on bar cast specimens, these have a length of 50 mm, a width of 40 mm and a thickness of around 0.1-0.2 mm. Sheet electrical resistance was measured using a 4-point probe device with cylindrical head from Jandel Engineering Ltd[78]. This measured resistance over a recorded distance, samples were normalised against their thickness to give a more representative resistivity value. For this experiment the 4 in-line probes used had electrode needles made from tungsten carbide of 0.4mm diameter. The nominal radius of the probe tip was 100μm with a spacing of 1mm. A downward probe force of 60g was applied.

A constant current was passed through the specimen by the two outer probes with a DC power source. A basic sheet resistance equation was used, and film thickness was measured using a Vernier calliper, allowing a conversion of a Ω-Square reading to a resistance value in Ωm. This can be seen in Equation 5:

$$R = \frac{\rho}{t}\frac{L}{W} = R_S\frac{L}{W}$$

Equation 5: Relationship between Resistance and Sheet Resistance

Given that we measure resistance, R, in Ω. L, W and t are length, width and thickness respectively, with all measured in m. Sheet resistance (R_s) also equates to Ω while resistivity, ρ, is given as Ω.m[117].

Finally, for high temperature liquid conductivity a hand-made 4 probe capillary setup was used. This was modified from the works by Monaghan et al.[117] with suitable equipment. In this experiment 4 platinum wires were placed inside capillary tubes with two wires carried the voltage while the other two were used to measure the current. A potential of 1V was passed through the sample at a variety of temperatures from 400 to 250^{o}C. The resultant current was then measured and converted into resistance using the standard $V=IR$ equation. In this V is voltage, in volts and I is current in amps. This figure could then be converted into resistivity by the use of Equation 6.

$$\rho = RAl$$

Equation 6: Resistivity to resistance relationship

In this equation ρ is resistivity (Ω.m), A is cross-sectional area of the sample (m^2), and l is the distance between the potential measuring electrodes (m). A BST brand DC power supply was used and the current was measured with a meterman 37XR multimeter. Because of the DC measurements electrolysis occurred producing some decomposition of the salts tested, due to high resistances it became difficult to measure at low voltages. This resulted in long term testing being impossible, meaning there were several issues with any results gained. To confirm a conductivity variation, a basic battery and light bulb test with the salt integrated as part of the circuit was used, as seen in Figure 2.13. In this a current of 4V was passed through the circuit with a blue LED bulb attached. Images were then taken, levelled with ImageJ (an image manipulation program) and light intensity compared.

2.3 Prototype Thermoelectric Testing Rig

After prototype devices were constructed it was essential to test and compare their performances. For this a custom rig was constructed to provide a measure of loaded performance with the equipment available in the lab. As such a rudimentary setup is useful for comparative studies but lacks the accuracy of other more advanced techniques. A standard laboratory hot plate was used to heat the lower part of the device. Aluminium spacers allowed type K thermocouples to be inserted above and below the thermoelectric device, these allow effective heat transfer over the setup. The heat sink consisted of an aluminium container filled with iced water maintaining a steady 0°C cold side. This can be seen in Figure 2.14.

Electronic measurements were taken of the current in series and the voltage in parallel, whilst a load of 1kΩ was applied using a resistor to obtain true loaded power outputs. Simultaneous readings of current, voltage, along with hot and cold side temperatures were made to allow accurate determination of a devices performance.

Voltage and current were measured using a multimeter whilst the thermocouples were used in conjunction with a digital thermometer to provide the temperature readings.

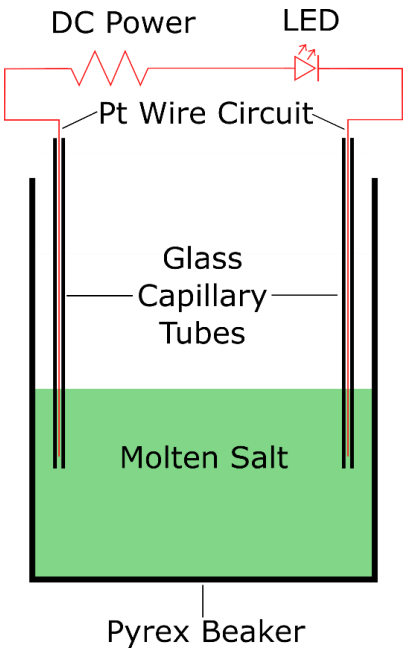

Figure 2.13 Schematic diagram of the light bulb test undertaken to provide qualitative data on the conductivites of molten salts at temperature

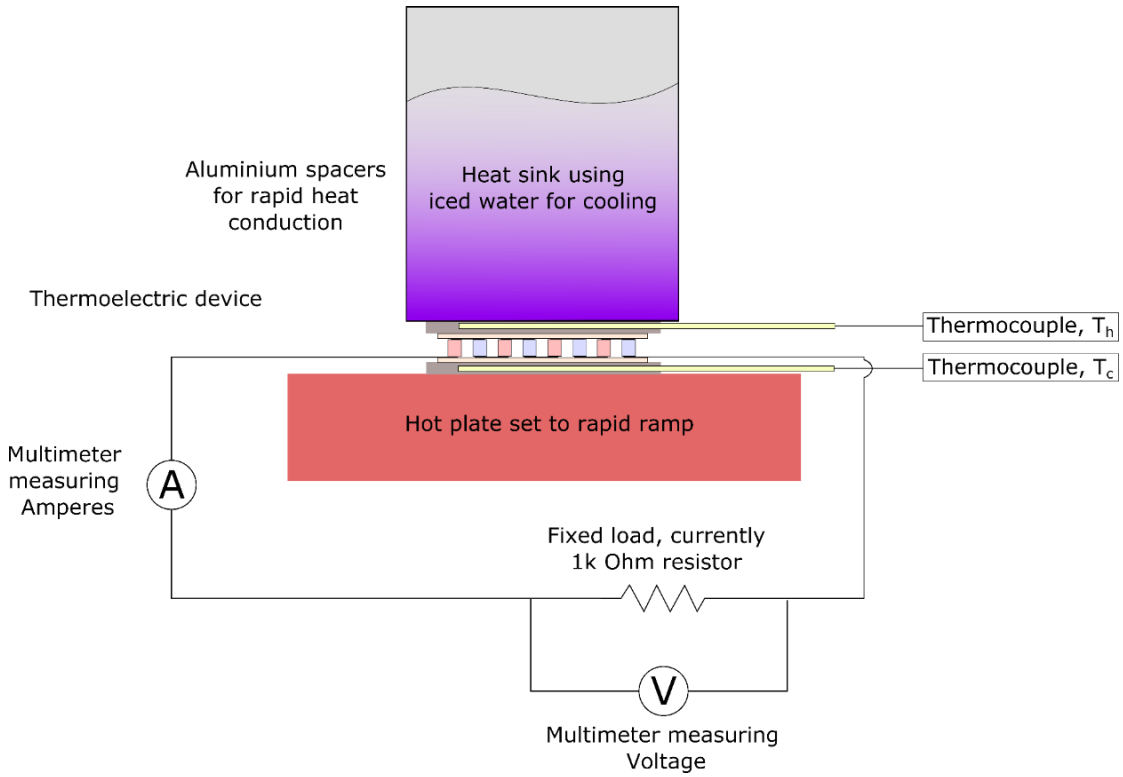

Figure 2.14 Schematic diagram of the thermoelectric testing rig including electrical circuit

2.4 Additional Materials List

Material	*Purity*	*Supplier*	*CAS number*
Alumina	GP	Fisher Scientific	
Ammonium Chloride (NH_4Cl)	99.6%	Arcos Organics	12125-02-9
Vitcas sealant	N/A	Vitcas	N/A
Tellurium (Te)	99.8%	Sigma Aldrich	13494-80-9
Bismuth (Bi)	99%	Sigma Aldrich	7440-89-9
Silver Flake (Ag) TS 2222	N/A	Johnson Matthey	7440-22-4
Silver Powder (Ag) EG 1887	N/A	Johnson Matthey	7440-22-4
Silver Powder (Ag) CAP 9	N/A	Johnson Matthey	7440-22-4
Copper (Cu)	99%	Sigma Aldrich	7631-00-0
20µm graphite	N/A	Sigma Aldrich	7782-42-5
Carbon Black	Super P	Imerys G&C	N/A
KS6	N/A	Imerys G&C	N/A
2-propanol (IPA)	98%	Fisher Scientific	67-63-0
Terpineol	anhydrous	Sigma Aldrich	8000-41-7
Ag-Glass flake MC2080PS	20-30% Ag	Metashine	Glass 65997-17-3
Ag-Glass flake MT1030PS	20-30% Ag	Metashine	Silver 7440-22-4
Ag-Glass flake MC5480PS	10-15% Ag	Metashine	SnO_2 18282-10-5
LiNO3	99%	Sigma Aldrich	7631-99-4
CaCl	93%	Sigma Aldrich	10043-52-4
ZnCl	98%	Sigma Aldrich	7646-85-7
Nitrogen	99.9%	BOC gases	
Argon	99.9%	BOC gases	
Primary Synthetic Graphite (SFG15)	N/A	Imergys Carbon	7782-42-5
Skutterudites mixed	N/A	Scatech	

Chapter 3 Production of Transition Metal Silicides using Pack Cementation

3.1 Introduction

This chapter focuses upon the production of thermoelectric materials, represented by the area highlighted in Figure 3.1. The bulk of current thermoelectric materials fall into two broad categories, large-scale materials with toxicity issues and low volume, highly efficient and expensive materials. For example, the most popular thermoelectric materials are bismuth telluride variants. Whilst these are mass producible bismuth telluride is classified as harmful according to EU directives, with specific inhalation toxicity, and a workplace exposure limit of $10mg.m^{-3}$ [118]. Its raw materials can be considered even more dangerous. On a small scale this is less of a concern, but this leads to limited mass marketability and scale up potential. Many new thermoelectric materials fall into the second category. Materials like quantum-dots and those with complex nano-structures are extremely efficient but are currently small scale and limited in their production capacity due to cost. As such TMSs were chosen to be investigated within this chapter. They have the potential to be affordable, efficient, non-toxic and producible on a large scale, making them a desirable material for renewable generation materials[46,48].

As discussed within the literature review TMS are a viable thermoelectric material operating within the 25-500ºC range. The major downside is their production cost which currently uses expensive techniques such as SPS and VBG. A new alterative was presented by Stathokostopoulos et al.[64–66,119,120] in the form of in-situ CVD in the form of HAPC. This technique was used to produce thin films of Mg_2Si but has not progressed further. The following chapter outlines work undertaken, at the beginning of this doctorate, to expand this process to longer times for the original Mg_2Si and other viable TMS materials.

Of the possible options for thermoelectric TMS two have been selected for further study. Mn-Si alloys form unique NCL structures which have self-doping P-type properties, whilst β-$FeSi_2$ is a proven affordable thermoelectric, with alternative applications for hydrogen generation. Research has been undertaken by Stathokostopoulos et al.[64,65,119,120] into the production of $CrSi_2$. Ru_2Si_3, $ReSi_{1.75}$ and CoSi were deemed too costly and rare for mass scale up. $MnSi_{1.7}$ and Mg_2Si are the most promising contenders for performance with $(ZT)_{max}$ values of 0.7 and 1.2 achieved in other studies. $FeSi_2$ has a much lower

$(ZT)_{max}$ of 0.2, but its alternative properties and low cost make it worth consideration for development.

This chapter will outline the production and analysis of these three materials including SEM, EDS, EBSD and XRD characterisation where relevant. More attention has been given to the Mn-Si production as this proved to be the most promising material.

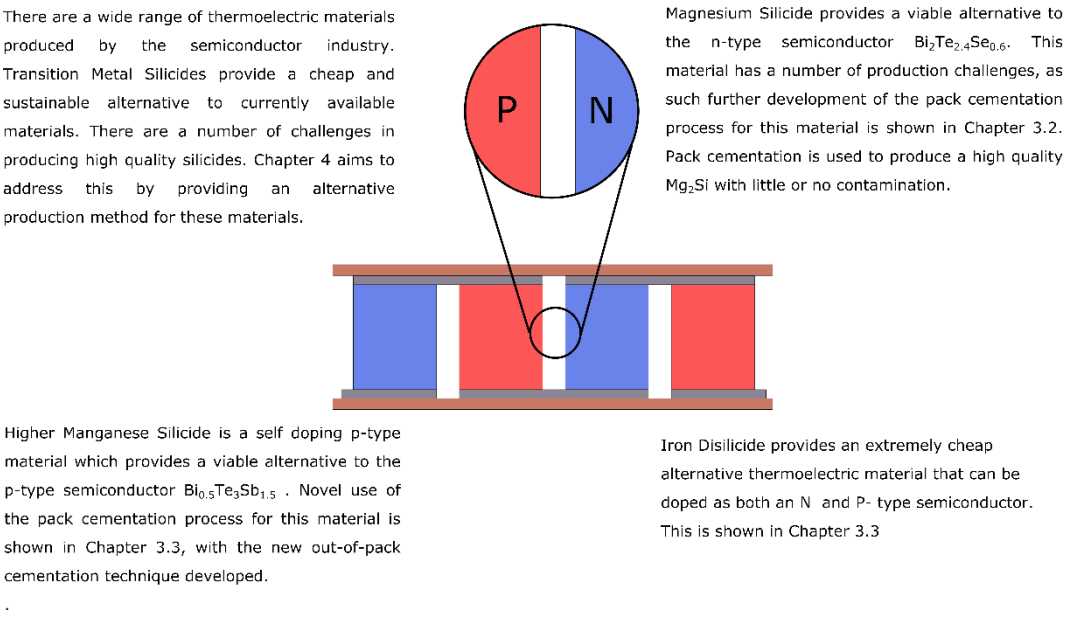

Figure 3.1 Infographic image of a traditional thermoelectric device, with focus upon the thermoelectric elements

3.2Magnesium Silicide

Magnesium Silicide (Mg_2Si) as described in the previous chapters, is a high ZT N-type semiconductor. It is relatively difficult to produce on a large scale with current methods due to the low boiling point of magnesium (1100^{o}C) and the melting temperature of Mg_2Si (1085^{o}C)[35]. Due to this Mg_2Si production requires a high degree of temperature control and current techniques usually require expensive specialised equipment. This section will cover the use of the HAPC process to produce these materials. HAPC is considered a viable alternative as it allows direct gas to solid transformations removing the issues faced by other production methods.

3.2.1 Pack Cementation Process

Works by Stathokostopoulos et al.[64,119] proved it was possible to produce Mg_2Si by HAPC onto high quality single crystal Si. In this work they investigated the growth at 500°C and 650°C for up to 3 hours. The HAPC process is described in section 2.3 and consists of a sealed crucible containing the pack materials within a controlled argon atmosphere tube furnace. Furnaces are ramped up initially at a rate of 5°C/min, with 3 maximum temperature ranges tested: 650°C, 750°C and 850°C. These higher temperatures were tested to determine the behaviour of the HAPC process close to the constituent materials melting points. Resultant structures can be seen in Figure 3.2 (a-d). These initial tests were carried out with 200μm polycrystalline Si, with grains of approximately 1cm in diameter.

Of the three temperatures tested the treatment at 650°C resulted in a single consistent layer of Mg_2Si, this is shown in Figure 3.3. Treatment at 750°C also resulted in a single layer, and displayed increased growth for the same time, as seen in Figure 3.3 (b) and (d). Lower temperatures allow for a slower, more consistent growth. At 750°C it is believed some magnesium particles melted resulting in initial inconsistent growth. In addition, the thicker films show clear evidence of cracking along grain boundaries. The increased temperature of treatment likely results in increased thermal cracking, owing to increased thermal stresses applied by the cooling. Alternatively, these cracks could be due to the harsh mechanical stresses applied on the samples when mounting and polishing. Cold mount resin was used to minimalize the contraction around the substrate, however there are still some stresses applied. It can be seen in Figure 3.3 (e) and (f) that after a short time the conversion rate does not vary noticeably. This is most likely due to the diffusion restricting growth effects. Allowing the samples to slowly cool down within the furnaces allows further grow to occur. This is shown in Figure 3.4.

From these micrographs, growth amounts could be determined and compared against current literature. This is shown in Figure 3.5 The amounts vary to that previously published in works by Stathokoupolus et al.[64,119] This is most likely due to the furnace cooling effect, in that slower furnace cooling can result in significantly higher growth amounts for the same time at temperature. The total width of the sample is also recorded in Figure 3.5. This shows that there is a significant expansion in conversion from silicon to Mg_2Si, which is to be expected. The unit cell volume of silicon is 160$Å^3$ whilst that of

Mg_2Si is 261Å^3 [121,122] . Standard deviation has been calculated for the growth amounts, and error bars in Figure 3.5 show ±1 standard deviation

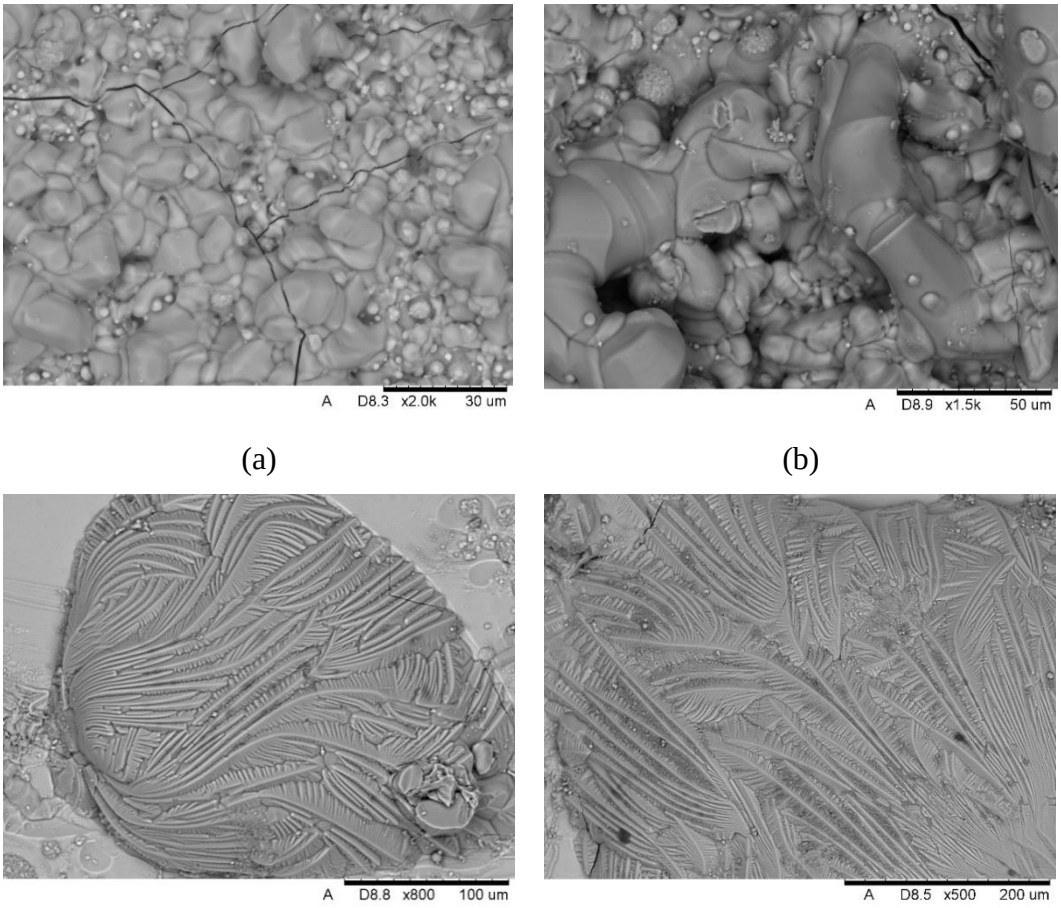

Figure 3.2 SEM images of the surface structures for Mg_2Si produced via pack cementation for (a) 3 hours at 650^{o}C, (b) 3 hours at 750^{o}C, (c) 3 hours at 850^{o}C and (d) 3 hours at 850^{o}C

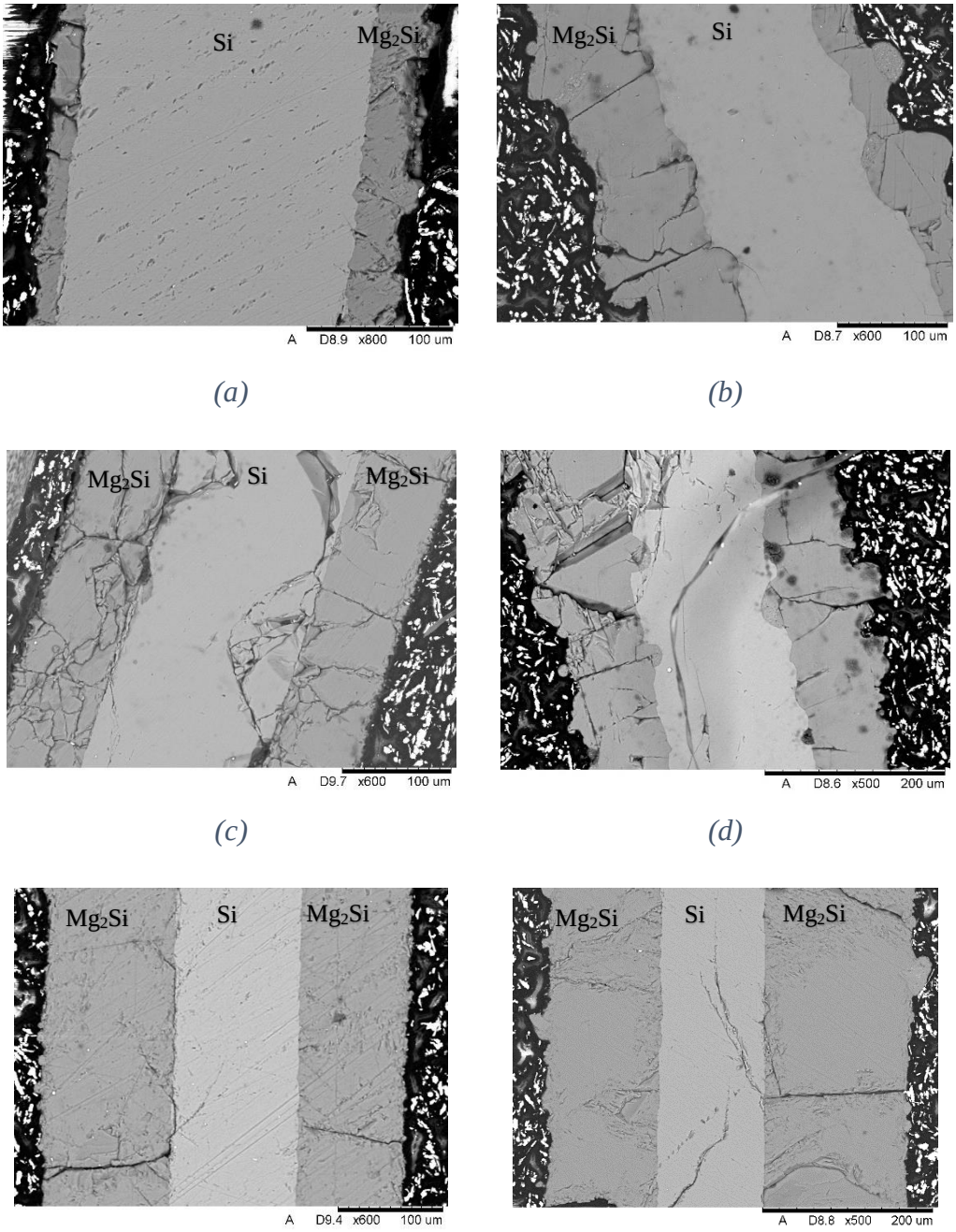

Figure 3.3 SEM micrographs of Mg_2Si cut edge samples, without furnace cooling. These samples are mounted in conductive resin with Silicon in the middle. (a) 3 hours at 650°C, (b) 3 hours at 750°C, (c) 6 hours at 650°C, (d) 6 hours at 750°C, (e) 24 hours at 650°C and (f) 72 hours at 650°C

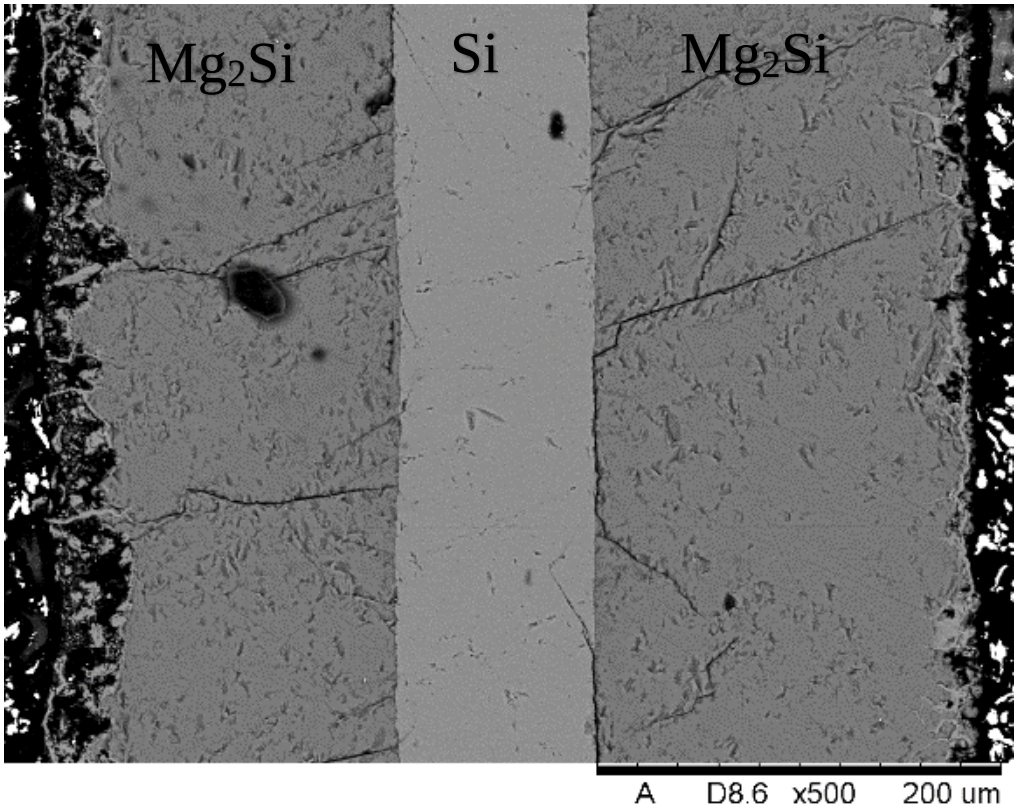

Figure 3.4 Cut-edge SEM image of furnace cooled sample at 24 hours at 650°C

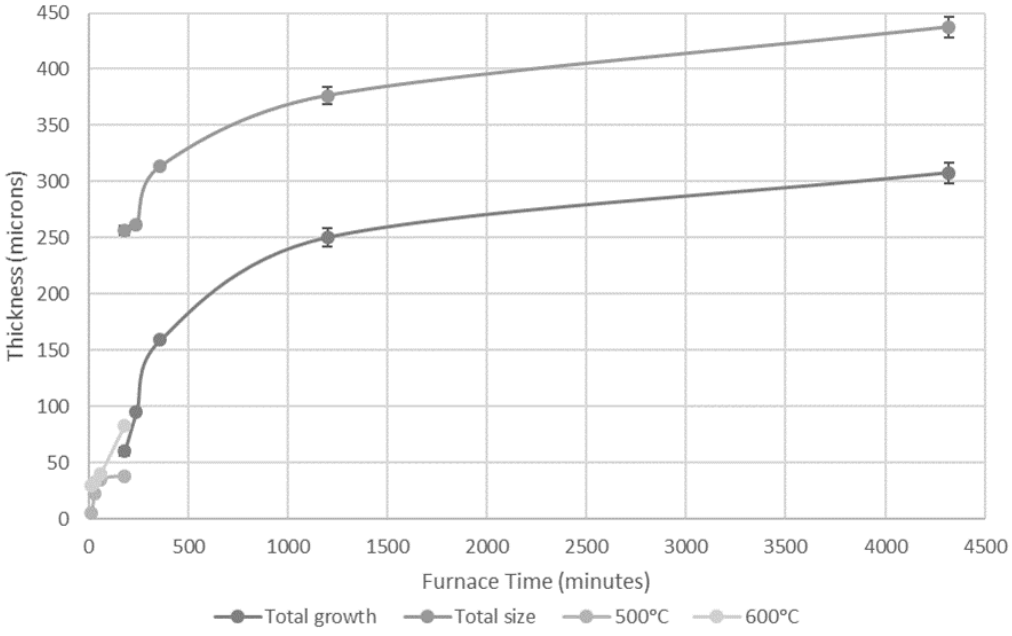

Figure 3.5 Growth amounts of Mg_2Si growth of polycrystalline silicon at 650°C

Growth amounts follow a clear power law logarithmic growth curve. The growth can be readily described by Equation 7.

$$d = (kt)^{\frac{1}{n}}.$$

Equation 7: Power law growth

In this d is the layer thickness, k is the growth rate and t is the growth time, with n = 2 if parabolic[64,65]. With this equation the diffusion coefficient of magnesium in Mg_2Si was shown to be $1x10^{-8}m^2s^{-1}$. This is most likely as the magnesium has a greater distance to ingress through the already formed Mg_2Si before reaching untransformed Si. This indicates that this is a diffusion-controlled process, thus limiting the total conversion amounts achievable. This can be advantageous for devices which require thin films on one or both sides of the silicon substrate. However, it limits the total conversion amount achievable for traditional devices.

3.2.2 Thin Film Quality

Both SEM: EDS and XRD were used to confirm the elemental composition of these layers. EDS was used for imaging and quantitative elemental analysis. Readings were repeatedly taken along the film and consistently showed a composition of 66% magnesium and 33% silicon was gained from the EDS analysis of the transformed sections, with less than ±2% error. An example EDS map of Mg_2Si growth can be seen in Figure 3.6, indicating that the material present is indeed Mg_2Si. This was to be expected as the Si-Mg phase diagram, shown in Figure 3.7, has only one phase present. Which means any combination of both silicon and magnesium will produce Mg_2Si, silicon or magnesium and these are all clearly definable from the image analysis.

The effect of temperature is particularly noticeable with the cut edge EDS images, as seen in Figure 3.8, for the 750^{o}C heat treatment. It can be seen there are large amounts of aluminium and oxygen entrapped within the Mg_2Si samples. Indicating that the rapid growth and slight melting has caused the alumina filler to become entrapped within the silicide. The growth inconsistency is also particularly pronounced in this image, as seen by the large nodules and heavy cracking.

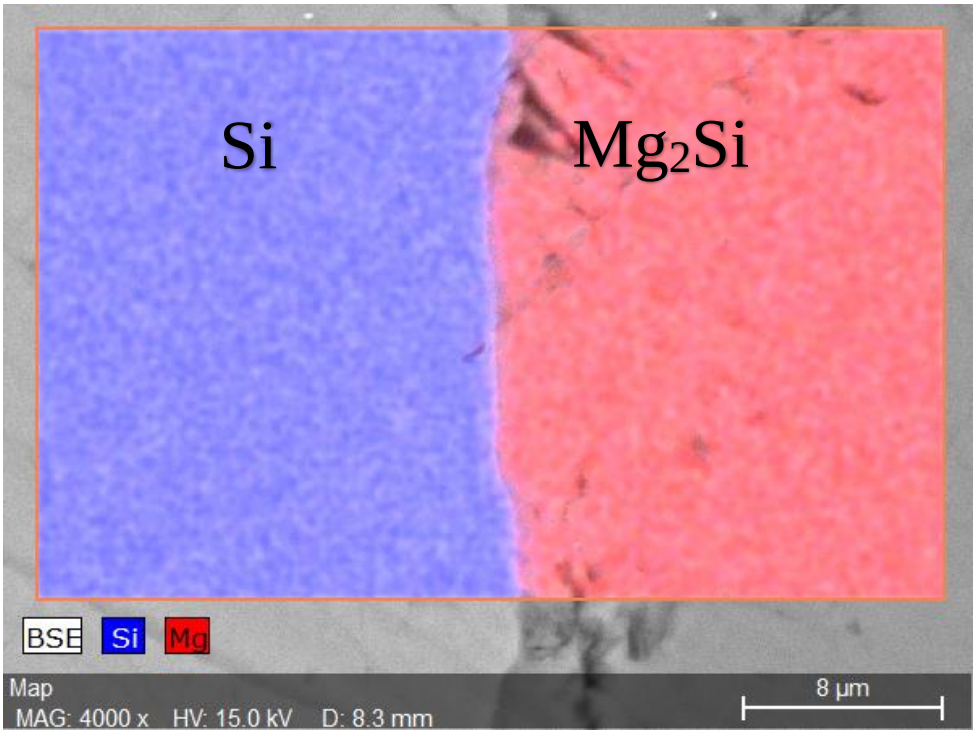

Figure 3.6 SEM-EDS image of cut edge from a 650°C pack cementation process, blue indicates silicon and red indicates magnesium

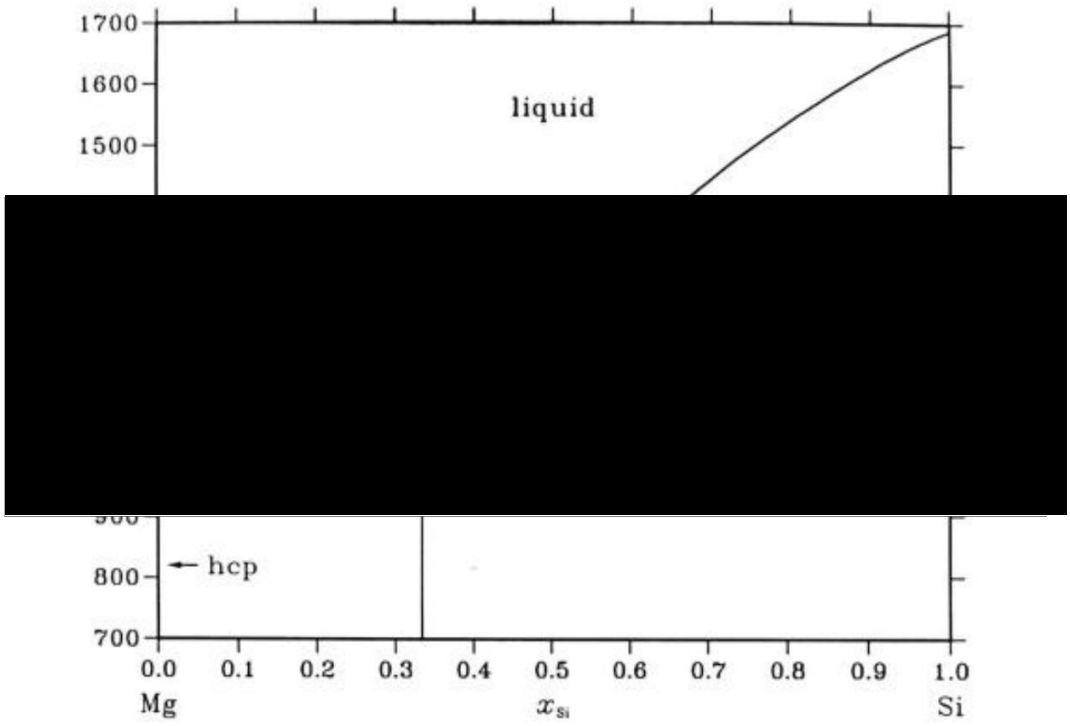

Figure 3.7 Mg_2Si phase diagram[123]

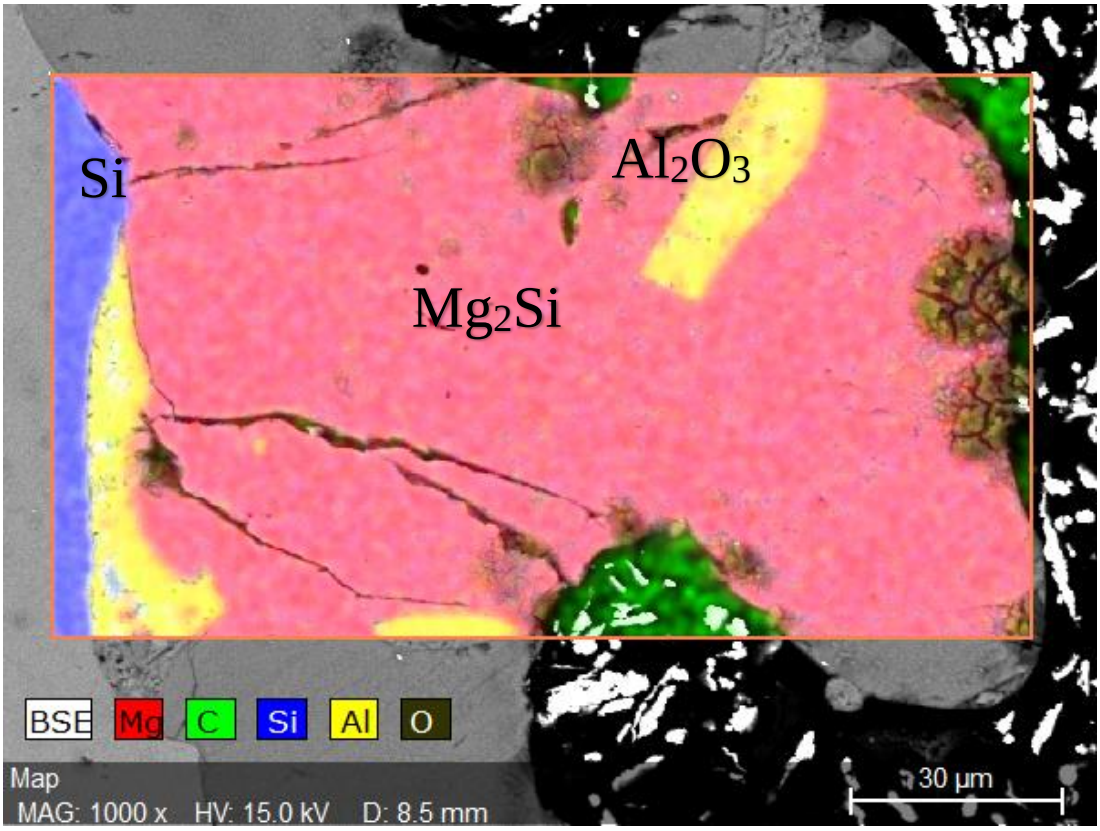

Figure 3.8 SEM-EDS image of cut edge from a 750°C pack cementation process, blue indicates silicon, yellow indicates aluminium and red indicates magnesium

3.2.3 X-Ray Diffraction

XRD was used to confirm the purity of the deposited Mg_2Si. Figure 3.9 shows that the surface layers are almost entirely Mg_2Si, with a Cubic structure (Space group Fm-3m), and a lattice parameter of 6.35Å. Peaks were identified at 24.26, 28.08, 40.10, 47.43, 49.71, 58.06, 63.84 and 65.72°, which correspond to the (1 1 1), (2 0 0), (2 2 0), (3 1 1), (2 2 2), (4 0 0), (3 3 1) and (4 2 0) planes respectively. The relative intensities match the known data for Mg_2Si[124]. There are trace amounts of aluminium and magnesium, which are left over from the process, with silicon being detected through the Mg_2Si layers. The full range of peaks matching standard calculated patterns of peaks indicates there is little or no preferred orientation for the Mg_2Si crystals.

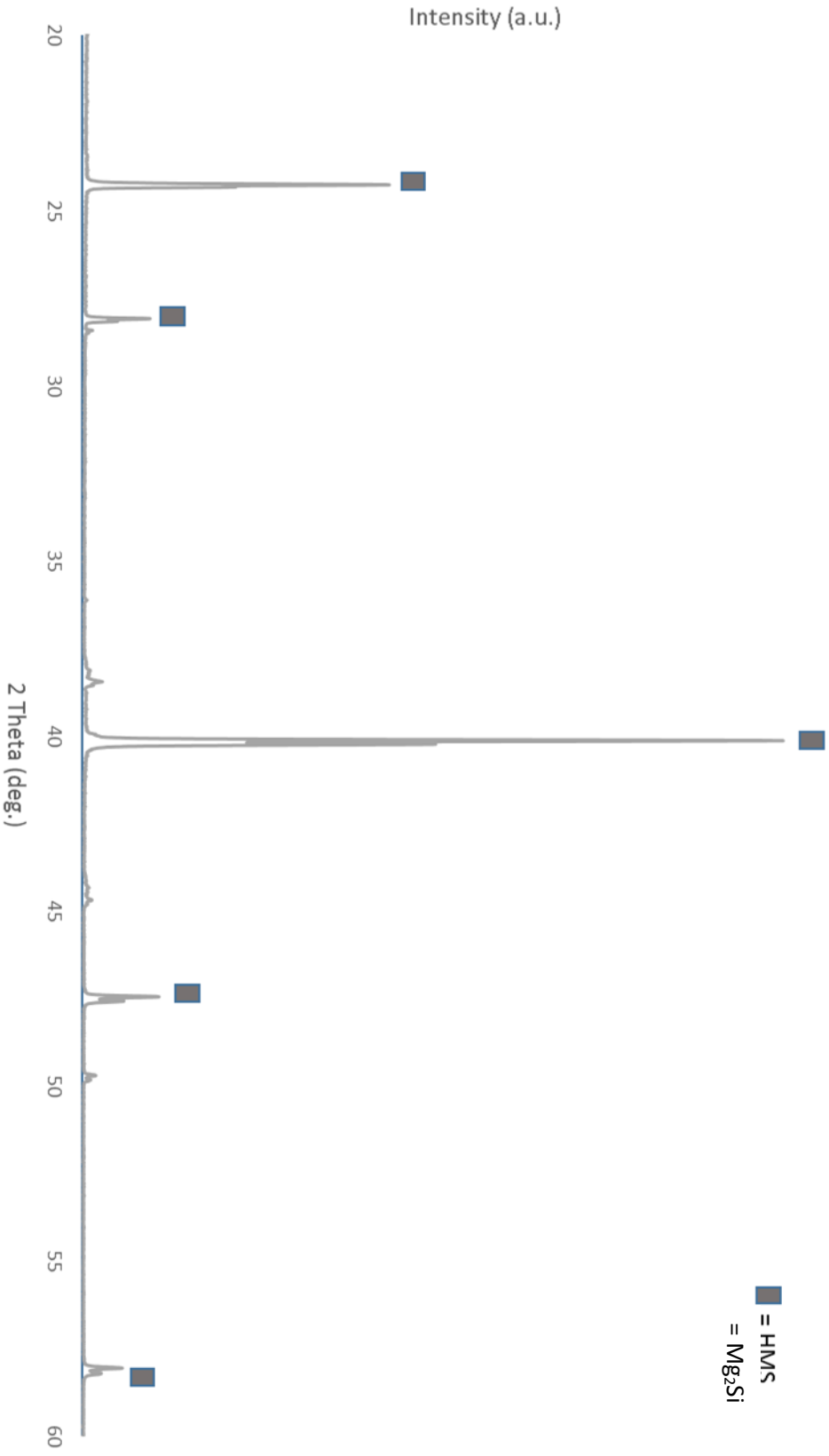

Figure 3.9 XRD spectra of Mg_2Si produced by pack cementation, showing its high purity

3.2.4 Grain Orientation and Texture Analysis

For texture analysis it is typical to look at three planes to get an overall orientation picture. For Mg_2Si these were the (1 1 1), (2 0 0) and (2 2 0) planes respectively. Figure 3.10 shows the crystal structure of Mg_2Si, whilst Figure 3.11 (a-c) shows the planes diffracted at each orientation. This model was generated using a cubic Fm-3m (225) unit cell, with magnesium atoms located at the 8c (-43m) sites and silicon atoms located at the 4a (m3m) sites.

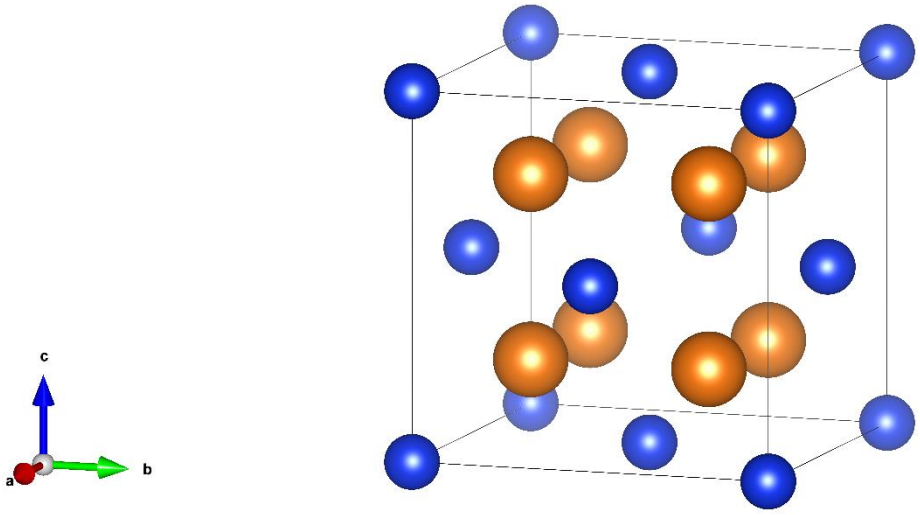

Figure 3.10 Unit cell representation of the Mg_2Si crystal structure, silicon is represented by blue spheres and magnesium is represented by orange spheres

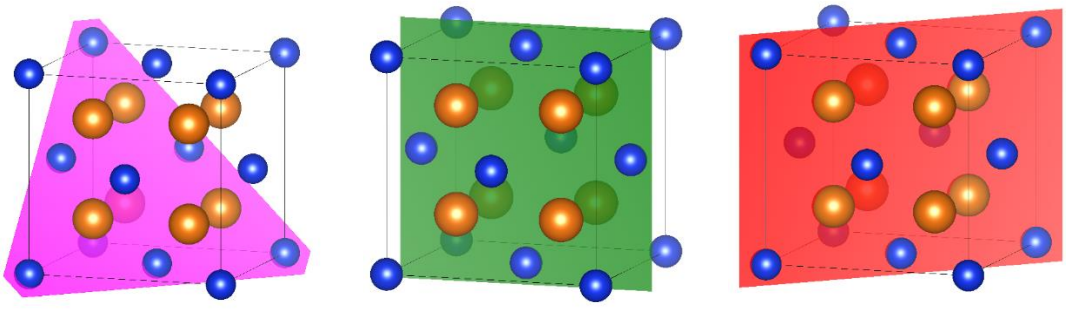

(a) (b) (c)

Figure 3.11 Planes within the Mg_2Si crystal for the 3 primary orientations. (a) is (111), (b) is (200) and (c) is (220)

Analysis of the surface structure indicates growth consistent with a eutectic transformation. Whilst grain size is difficult to determine with SE and BS imaging on the SEM, due to the surface structures, in certain locations surface damage has revealed a more refined grain structure. This is shown clearly in Figure 3.12. Here a wide range of grain sizes can be seen, typically within the range of 5–15 microns. Etching of the surface was not possible with this material without the use of strong acetic and picric acid etchants[125]. Two non-chemical methods can be used to provide grain size and orientation analysis, the first uses a XRD peak analysis, however due to the lack of preferred orientation and fine peak size within that of the instrument width this is not a viable technique in this case. Initial analysis of the curve shown in Figure 3.9 shows extremely sharp peaks, indicating high amounts of crystallinity without straying into the nano-crystalline region. In order to check the crystallographic growth and orientation of the Mg_2Si EBSD was used to generate maps of the cut edge sample.

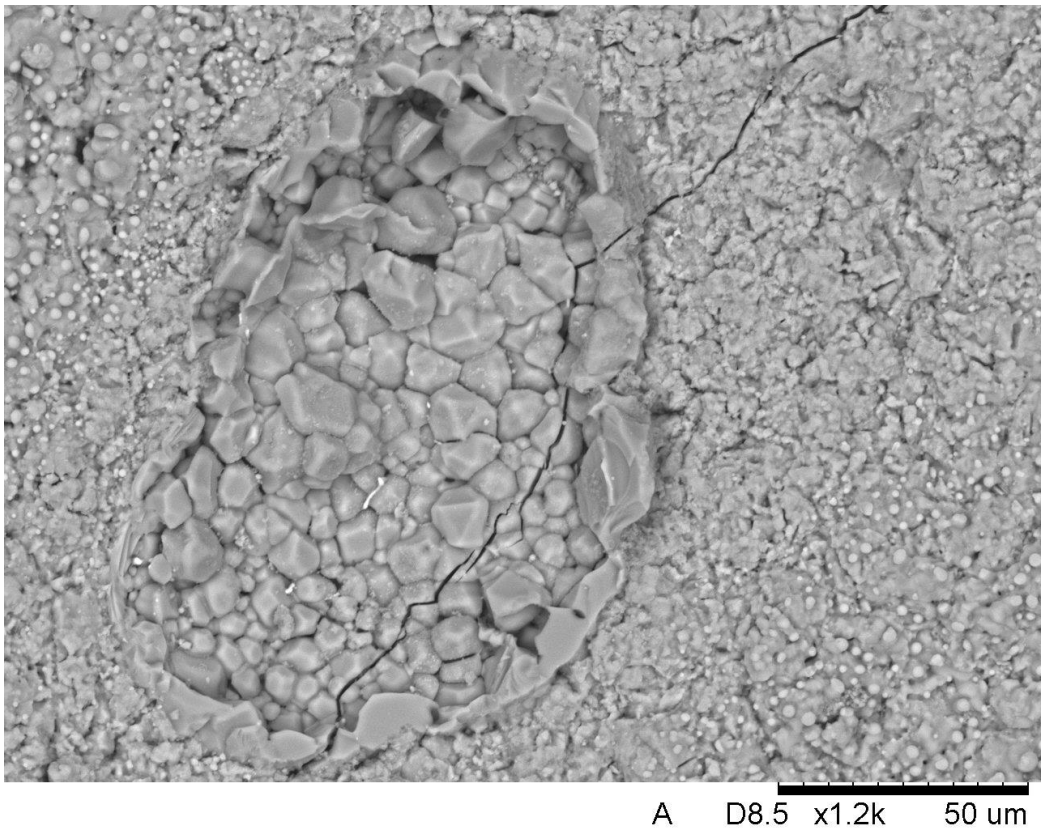

Figure 3.12 Surface damage of Mg_2Si thin films during the pack cementation process

Figure 3.13 shows the band contrast image generated on this cut edge. This shows the large columnar grains growing from the nucleation point of the single crystal silicon substrate. These columnar grains cover the entire thickness of the Mg_2Si and have a ratio of around 3:1 length to diameter. Diameters of these larger grains vary from 15 microns at their widest point down to the 5 microns as seen in Figure 3.13Figure 3.13 Band contrast image from the EBSD analysis technique showing both sides of the silicon substrate. This orientation of growth is advantageous in thermoelectrics as the grain boundaries can provide additional scattering of longer wavelength photons, thus reducing thermal conductivity. In addition, smaller features deflect shorter wavelength phonons, so atomic sized defects are effective at deflecting these shorter, higher energy wavelengths. This will decrease the lattice thermal conductivity as mentioned previously[37,43]

Figure 3.14 shows the orientation within the grains through their inverse pole figure. They display a reasonably random orientation with few trends being visible. With grains being seen orientated in the (1 1 1), (1 0 1) and (0 0 1) directions within every scan.

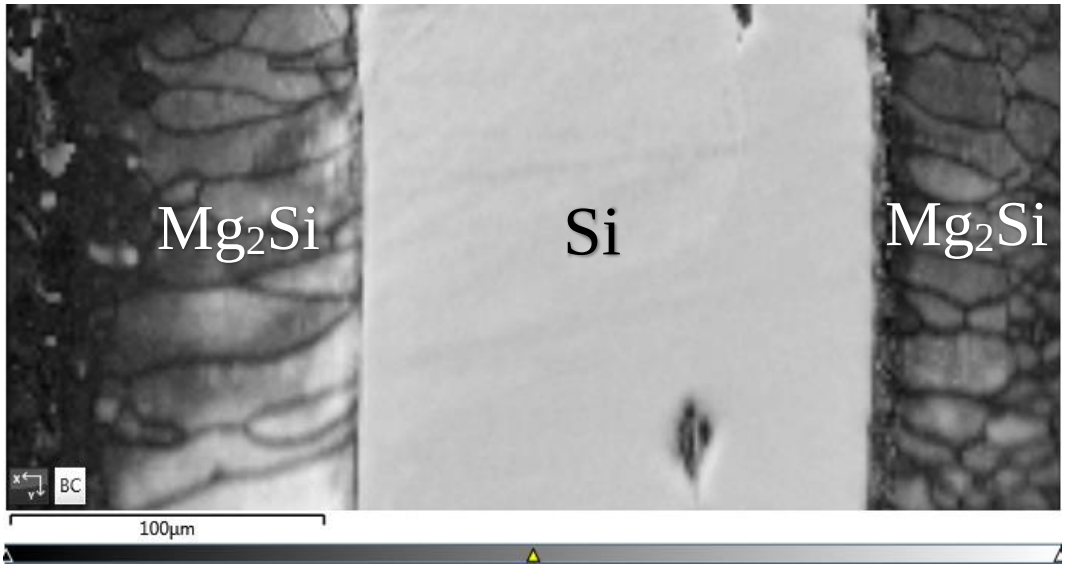

Figure 3.13 Band contrast image from the EBSD analysis technique showing both sides of the silicon substrate

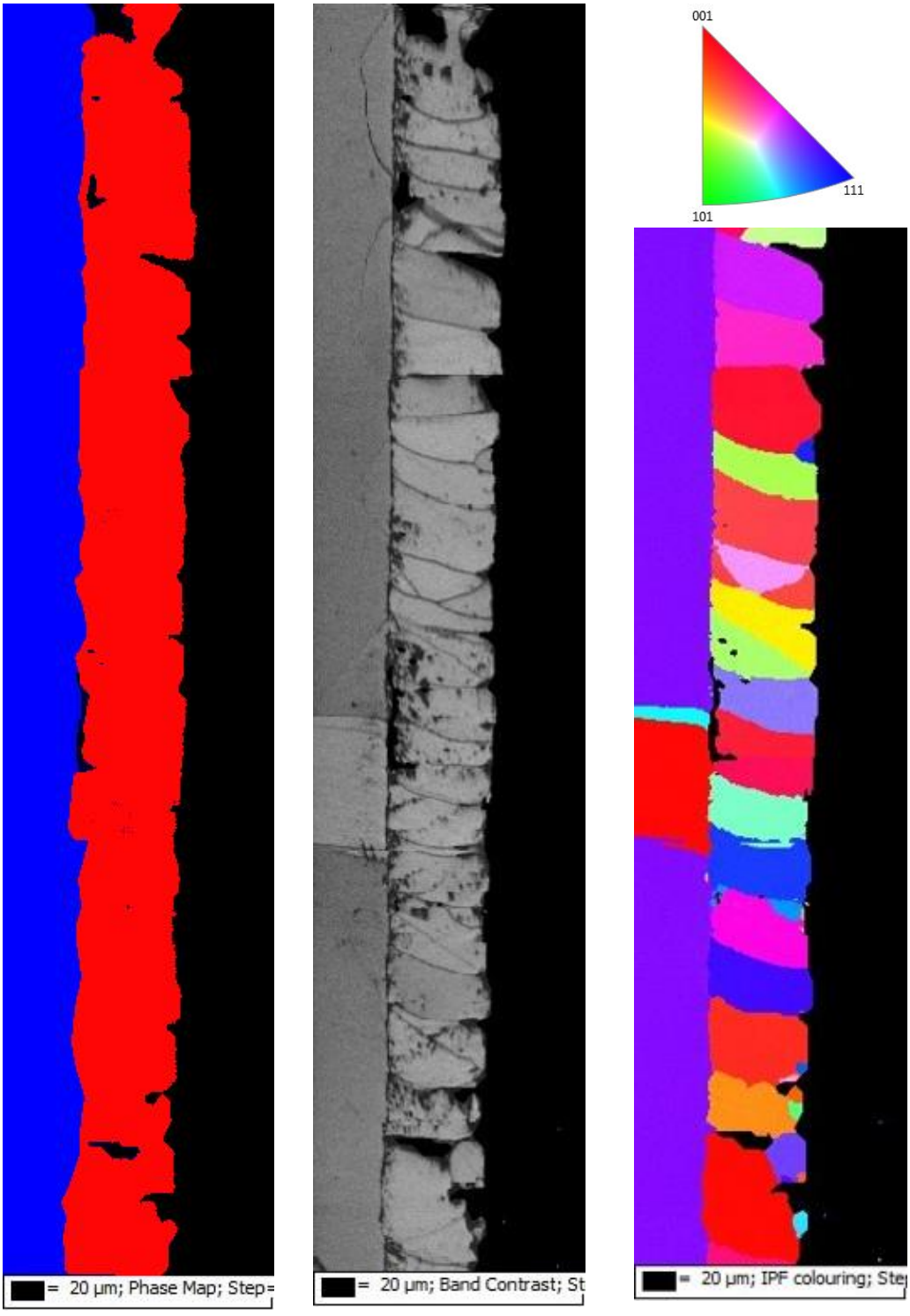

(a) *(b)* *(c)*

Figure 3.14 SEM-EBSD plot of the (a) phases present in the sample (blue = silicon and red = Mg_2Si), (b) the band contrast showing grain locations and (c) showing the IPF colouration map for grain orientation of Mg_2Si thin films

3.2.5 Magnesium Silicide Production Summary

In summary HAPC can be used to produce high purity Mg_2Si on silicon substrates, with this research expanding on previous studies. It is a promising process with a strong probability that the silicide material can be simultaneously doped to produce a high quality and high ZT material. The HAPC technique is limited by the diffusion of the magnesium through the Mg_2Si material already transformed, limiting its growth rate and applications to thin film production only. To make this a viable production technique a powder process has been theorised. By exchanging the silicon substrate for powder full transformation of the material can be achieved and sintering can be used to produce elements in the desired shape. However, there are potential challenges with the high reactivity of Mg_2Si powders with water due to the higher surface area increasing the reactivity in comparison to the bulk material.

3.3 Higher Manganese Silicide

Higher Manganese Silicide (HMS) is an extremely promising thermoelectric material with a self-doping effect. The Mn-Si phase diagram provides a large number possible room temperature phases, with HMS being the highest Si-rich phase possible. These have a wide range of uses due to their low resistivity, large Seebeck coefficient, low cost and low toxicity. Their crystallography varies greatly due to the slight structural differences between the complex crystals. The HMS phases have a Nowotny Chimney Ladder (NCL) structure, which consists of several unique. NCL phases including: Mn_4Si_7, $Mn_{11}Si_{19}$, $Mn_{15}Si_{26}$ and $Mn_{27}Si_{47}$. Each phase has a similar a lattice parameter and long c lattice parameters[6,34,40,49]. These phases are derived from the $TiSi_2$ parent structure with a chimney of Silicon and a ladder of Manganese. With doping ZT values of 0.7 can be achieved with HMS[34]. There are two primary pack types within this section, the original In Pack Cementation (IPC) and the modified Out of Pack Cementation (OOPC), these will both be covered in turn. The differences in experimental set-up between these two techniques can be seen in the materials and methods section.

3.3.1 Standard in Pack Cementation

3.3.1.1 Temperature Effects

The production process for HMS used the same equipment as that for Mg_2Si, however it has a lesser requirement for shielding gas, allowing both argon and nitrogen to be used. At low temperatures there was no noticeable deposition, with temperatures over 800^{o}C being required for deposition. As can be seen in Figure 3.15(a) there are clear areas of exposed and untransformed silicon, indicating higher temperatures were required. Upon raising the temperature to 900^{o}C a complete coverage was achieved, as shown in Figure 3.15(b). Samples began to exhibit contamination at the higher 1000^{o}C temperatures, seen in Figure 3.15(c) as darker patches. Whilst not visible in the figure the samples largely disintegrate at this higher temperature, with the converted Mn-Si shearing away from the silicon substrate reducing their usage. As such 900^{o}C was chosen to be pursued.

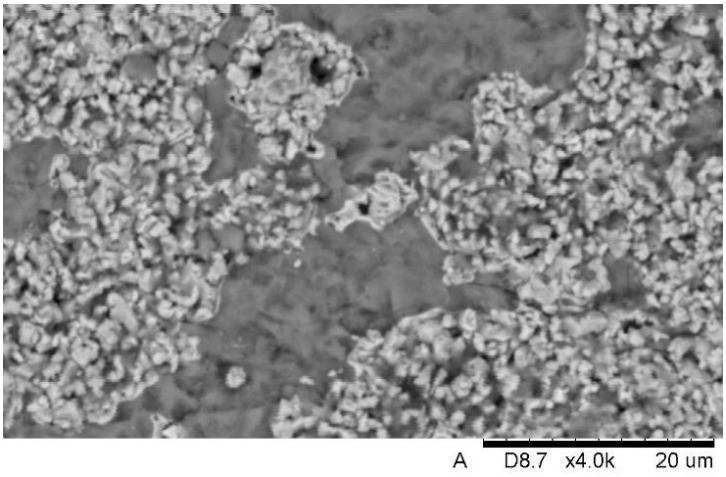

(a)

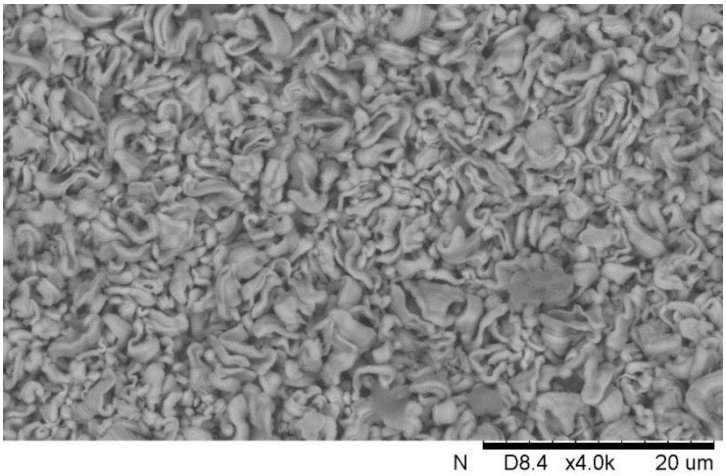

(b)

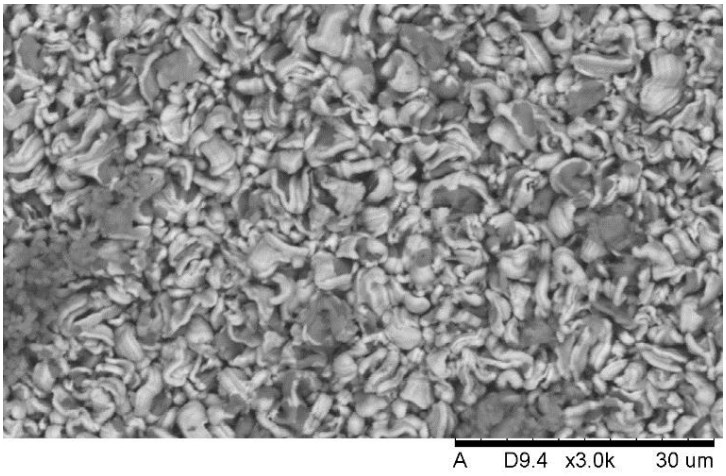

(c)

Figure 3.15 Surface of Mn-Si thin films grown using IPC at (a) 800°C, (b) 900°C and (c) 1000°C

3.3.1.2 Time Effects

A range of treatment times were tested at the 900°C operating temperature, with resultant cut edge analysis performed. Micrographs were taken between 3 and 48 hours, these have been shown in Figure 3.16. Here it can be seen that the growth follows a largely similar pattern to Mg_2Si. With around 35µm growth after 5 hours in the furnace, as seen in Figure 3.17(a), which increases to around 65µm after 25 hours, as seen in Figure 3.17(d). These growth amounts are more inconsistent than that of Mg_2Si, which can be seen by the larger error bars, this is likely due to the multiple layers present. Within Figure 3.17(a-c) two distinctive layers can be seen growing outside the silicon, this increases to 3 visible in some cases, as shown in Figure 3.17(d). Growth amounts can be modelled using the power law logarithmic growth curve as discussed in the previous chapter. Indicating that the growth is diffusion controlled. This has been shown previously in Equation 7. Due to the multiple layers having an impact on the growth rate any calculated diffusion coefficient would be highly inaccurate.

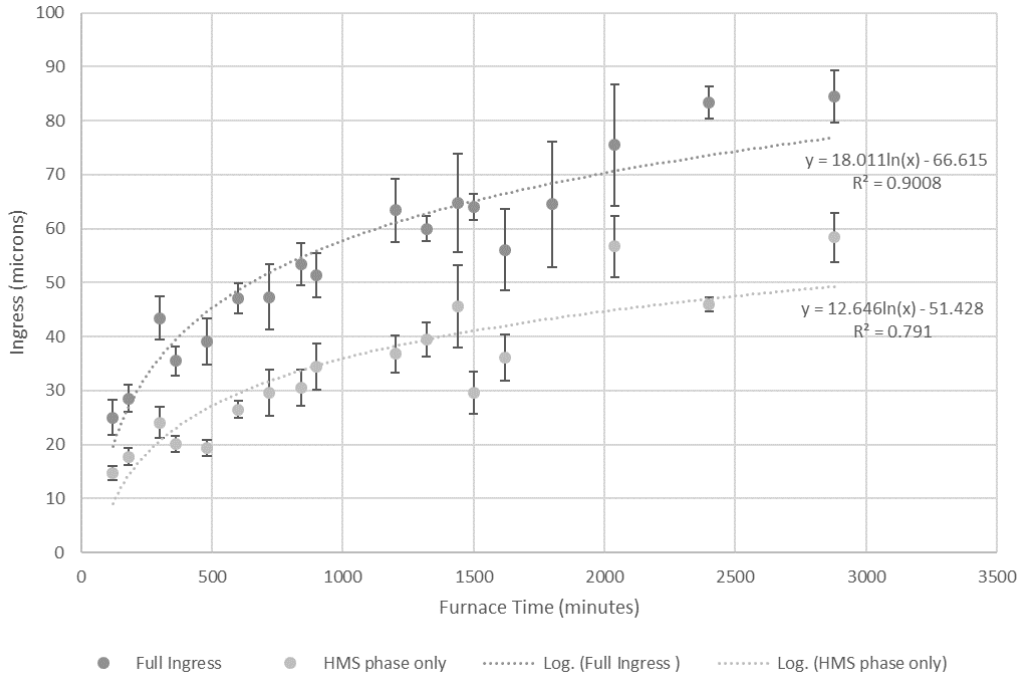

Figure 3.16 Growth amounts of Mn-Si growth of polycrystalline silicon at 900°C

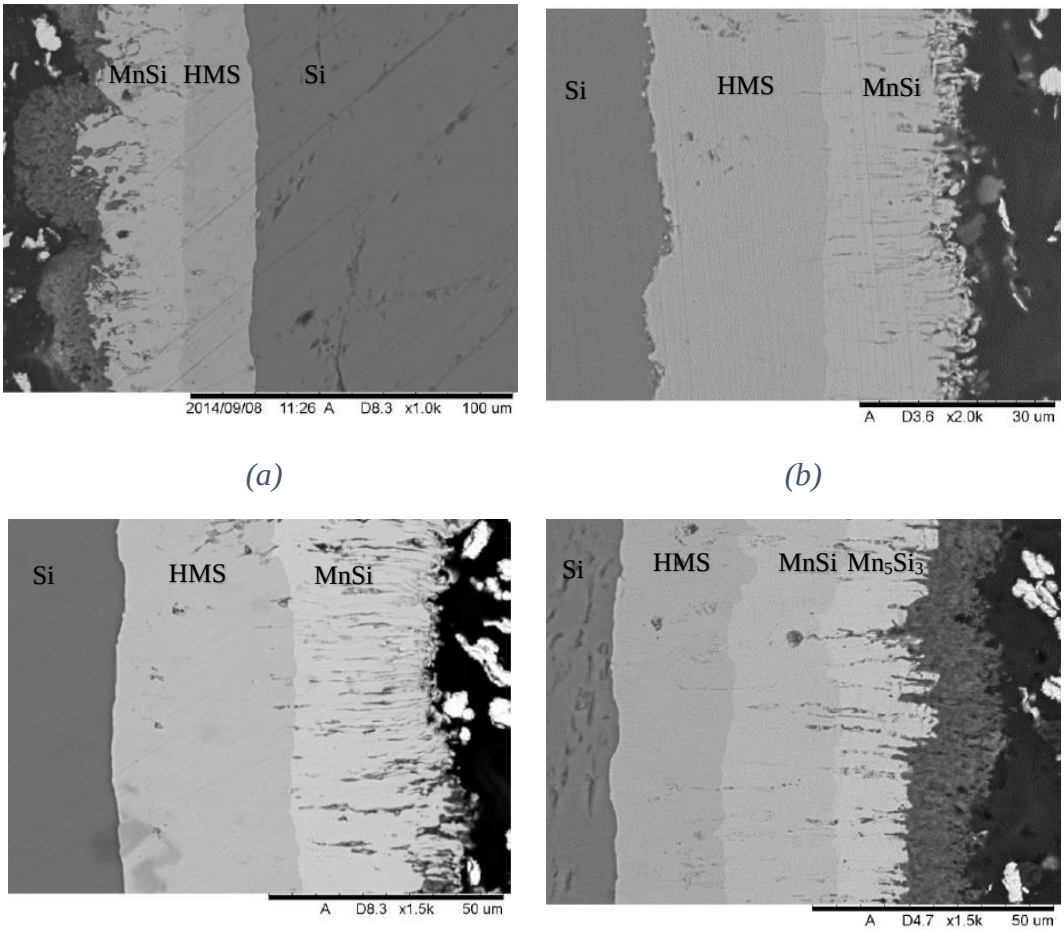

Figure 3.17 SEM micrographs of Mn-Si cut edge samples created at 900°C. These samples are mounted in conductive resin with silicon in the middle. Sample treatment time was varied such that (a) is 5 hours, (b) 10 hours, (c) 15 hours and (d) 25 hours.

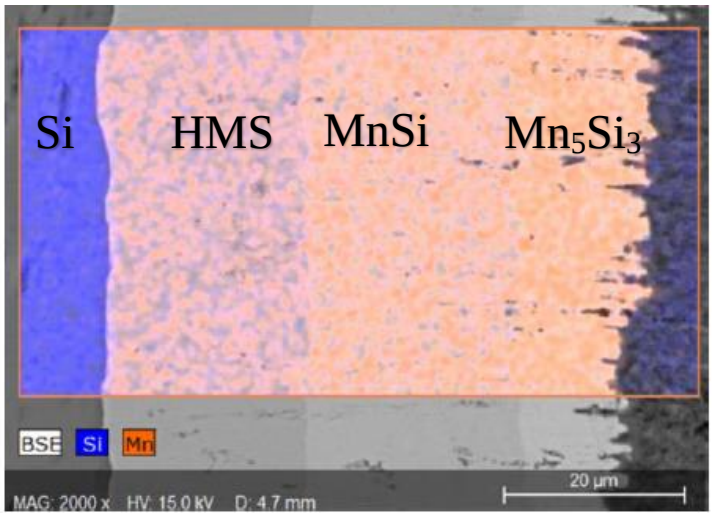

Figure 3.18 SEM-EDS map of Mn-Si IPC at 900°C for 25 hours

3.3.1.3 Thin Film Quality

Unlike the Mg_2Si film, significant porosity is observed within the outer layers, this implies a loosely bonded layer that may be possible to remove.

In order to determine the purity and phases of each layer, EDS was carried out along with the micrographs. Elemental contrast can be seen with Figure 3.18. This image shows the phase closest to the substrate is clearly the most silicon rich, with silicon intensity decreasing as the phases move away from the substrate. The EDS readings are shown with ±1 standard deviation. The outer phase was extremely thin and consisted of 60.99±1.68 at% manganese and 39.01±1.68 at% Si. This relates to a Mn_5Si_3 phase, however this was only seen in a few cases and often not appearing at all. The middle phase was 47.65±2.66 at% manganese and 52.34±2.66 at% Si. This relates to approximately 50-50 manganese and Si, matching closely to the MnSi phase. The innermost Mn-Si containing phase is composed of 35.14±1.54 at% manganese and 64.86±1.54 at% Si. This corresponds to the desired HMS phases i.e. Mn_4Si_7 to $Mn_{27}Si_{47}$. Only the inner HMS is wanted whilst the porous outer phases must be removed.

3.3.1.4 X-Ray Diffraction

EDS analysis only provides the atomic percentages, and it is possible that the phases are not in fact present and just have the correct atomic ratios in solid solution or localised multiphase combinations. As such XRD analysis was undertaken to determine the phases. The XRD trace for these curves can be seen in Figure 3.19, with the peaks at 32.4º, 39.5º, 41.6º, 46.4º, 47.08º, 47.988º and 53.673º corresponding to (1 1 3), (2 1 2), (1 0 5), (2 2 0), (2 2 1), (2 1 4) and (2 1 5) orientations of $Mn_{27}Si_{47}$ (HMS) respectively. Additional peaks of 38º, 40.4º, 42.6º, 44.3º, 46.7º, 47.6º and 52.5º were also identified. 44.3º and 46.7º correspond to the MnSi phase, at (1 1 0) and (2 1 0) orientations respectively. The peaks at 40.4, 44.3 and 52.5º correspond to the Mn_5Si_3 phase previously identified by the EDS analysis, at (-1 0 -2), (-3 1 -1) and (-4 2 0) orientations respectively. There is some overlap in these phases at 44.3º which makes it difficult to determine which is present, however there is a distinct orientation of growth in the (2 1 0)/(-3 1 -1) directions, depending on the phase present, indicates a potential preferred growth direction.

The remaining 36.9º, 38º, 42.6º, and 47.6º peaks correspond to the Mn_5Si_3 phase identified in other works[126,127]. These relate to the (-1 -3 -1), (-1 -1 -3), (-4 0 -2) and (0 0

-4) orientations. From this it can be seen IPC results in an impure sample that is unlikely to function well as a thermoelectric unless these additional phases were removed.

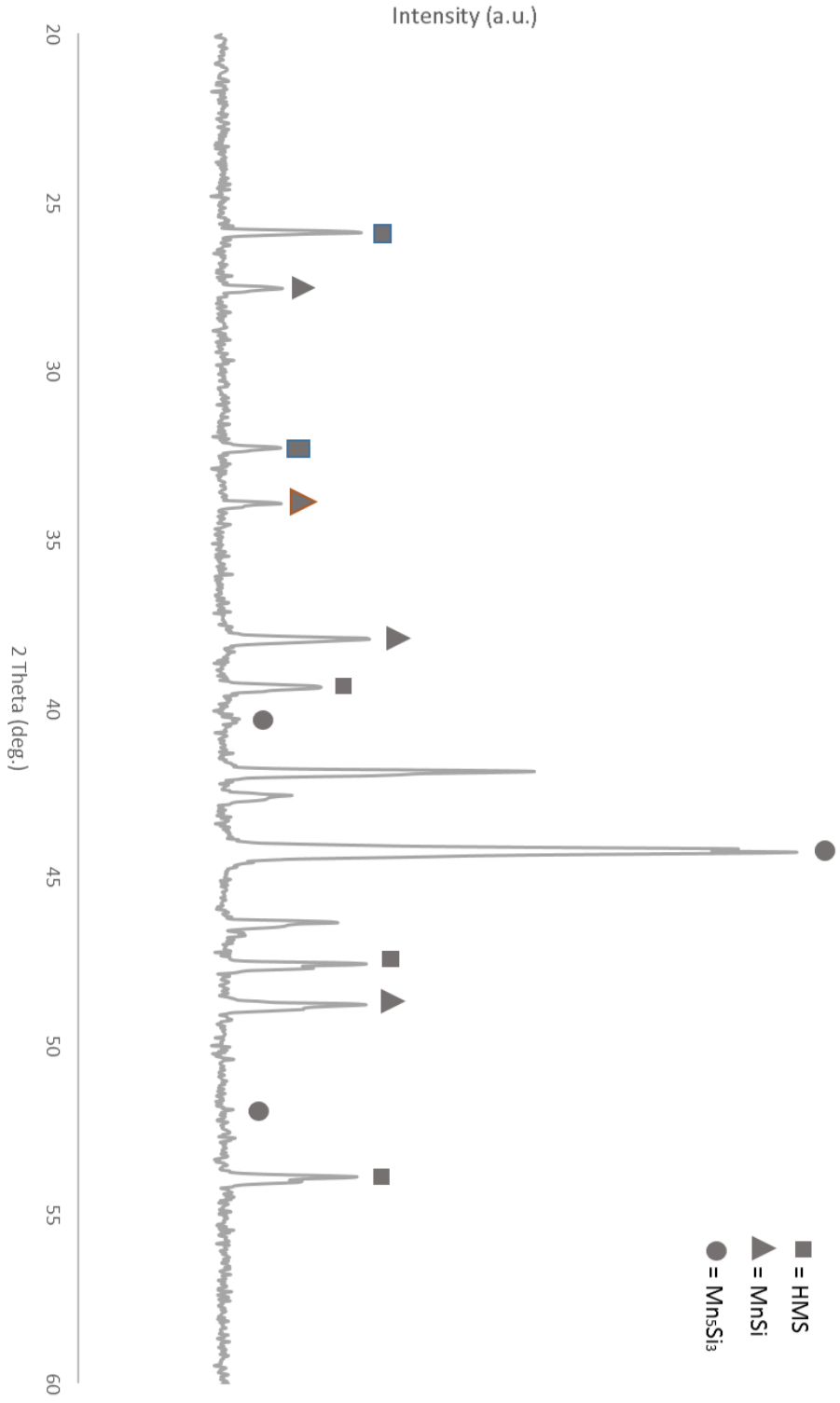

Figure 3.19 XRD scan of Mn-Si produced by pack cementation, showing its multiple phases

3.3.1.5 Texture and Grain Alignment

In addition to the standard SEM imaging and EDS techniques EBSD analysis was undertaken on the HMS films. For this conductive hot mount resin was required to avoid charging over time. This applied large amounts of pressure on the sample causing excessive cracking. However, with adequate polishing reasonable Kikuchi patterns could be generated. Figure 3.20(a) shows the resultant phase analysis from the EBSD scans. This provides further evidence to the XRD and EDS data that the layers consist of silicon, a form of HMS (identified here as $Mn_{11}Si_{19}$), and MnSi. Figure 3.20(b) shows the band contrast image from the EBSD data allowing the grains can clearly be identified. The growth shows a larger number of nucleation points for $Mn_{11}Si_{19}$ on the pyramid textured Si. These grains which grow reasonably equiaxed, before allowing longer columnar grains to nucleate outwards away from the surface. These terminate with many equiaxed MnSi grains that make up the rest of the growth. Due to the orientation of the crystals within the $Mn_{11}Si_{19}$ layer there will be increased barriers to thermal phonon transportation in the vertical axis, which is advantageous to thermoelectrics. Utilising the generated grain data from the EBSD map it can be seen that around 73% of the MnSi grains have an aspect ratio of 2 or below, indicating they are reasonably equiaxed. These grains can be divided into 4 categories, with 78% of grains being between 2.5 and 10µm in area, 24% being between 10 and 20µm, 13% between 20 and 40µm, with the remainder being below 85µm. This shows there are many small equiaxed grains within this porous outer layer.

Within the HMS phases two distinct growth patterns were identified, around 680 of the grains were below 20 µm in area with an aspect ratio of below 3:1, this relates to the larger number of smaller equiaxed grains seen in Figure 3.20(b), between the initially nucleated grains and the larger columnar grains. Those with aspect ratios of higher than 3:1 can comfortably be considered columnar grains, these linked closely with the HMS.

Figure 3.21(a) displays the complete inverse pole figure colouration for the grown layers, with Figure 3.21(b and c) showing the individual layers respectively. Figure 3.22 shows the corresponding pole figures (including theoretical patterns). The pattern from the silicon clearly shows a single crystal orientation, which is to be expected. Those of the MnSi and HMS show little or no orientation.

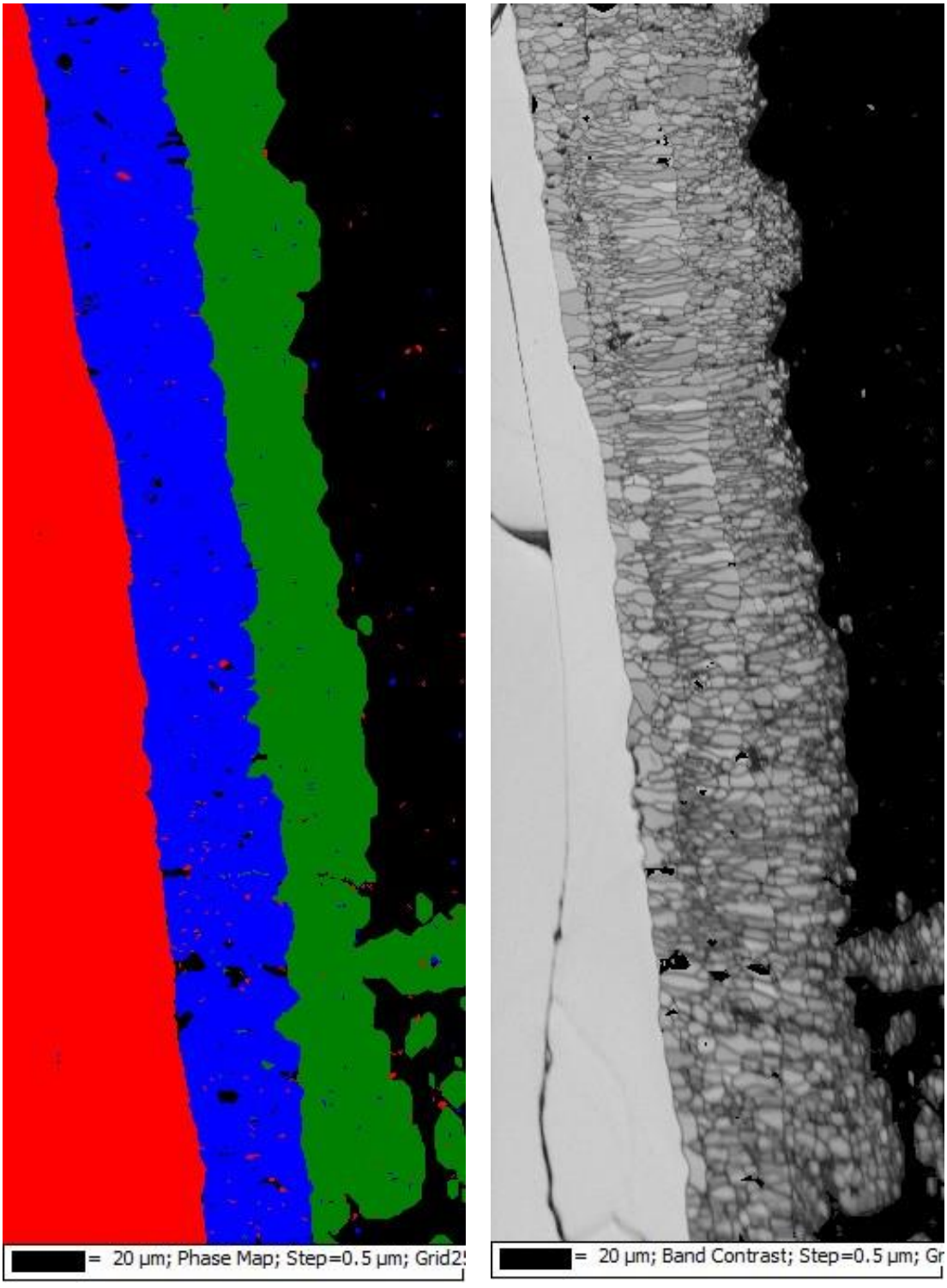

(a) *(b)*

Figure 3.20 SEM-EBSD plot of the (a) phases present in the sample (red = silicon, blue = $Mn_{11}Si_{19}$, green = MnSi) and (b) the band contrast showing grain locations

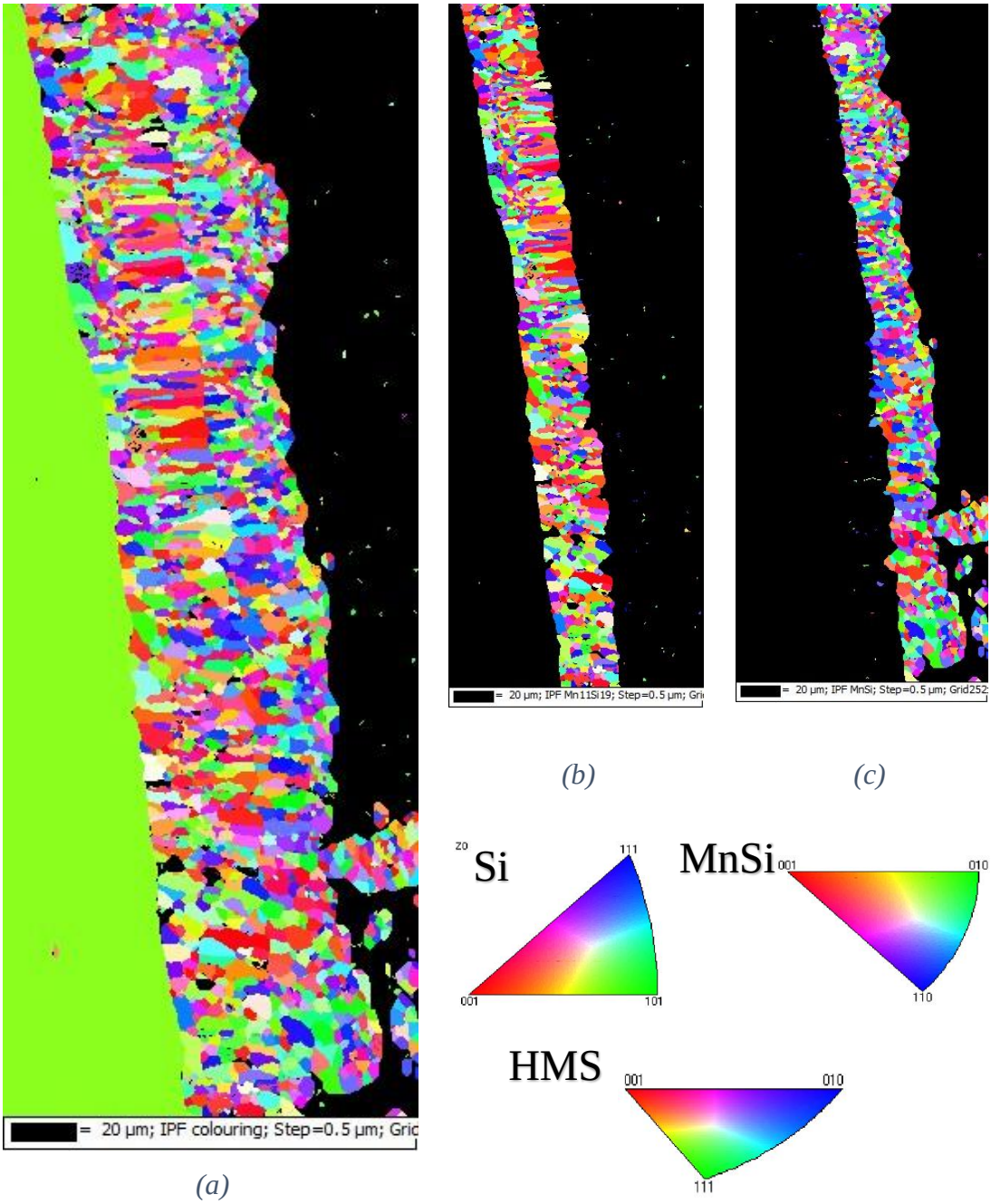

(a) *(b)* *(c)*

Figure 3.21 SEM-EBSD map of the (a) inverse pole figure colouration for grain orientation (b) IPF of $Mn_{11}Si_{19}$ layer (c) IPF of MnSi layer, colours represent grains orientation.

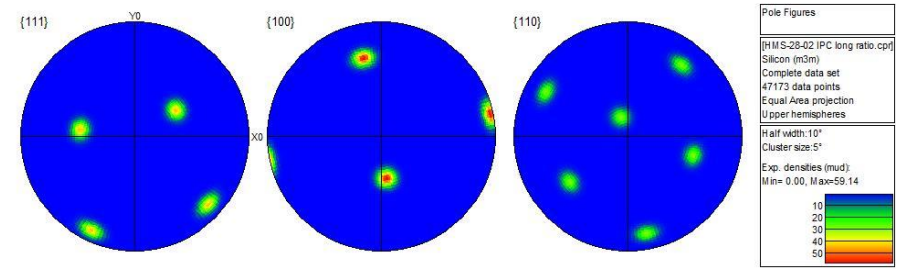

(a)

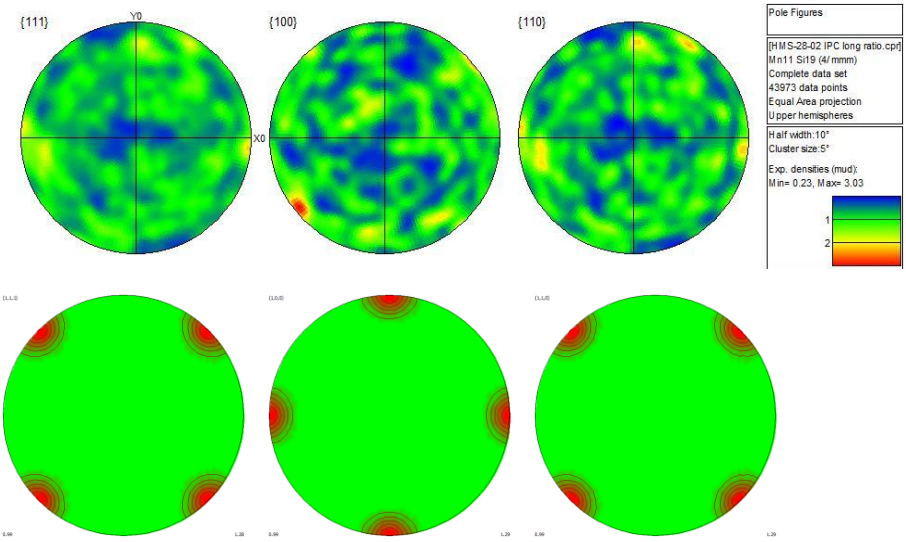

(b)

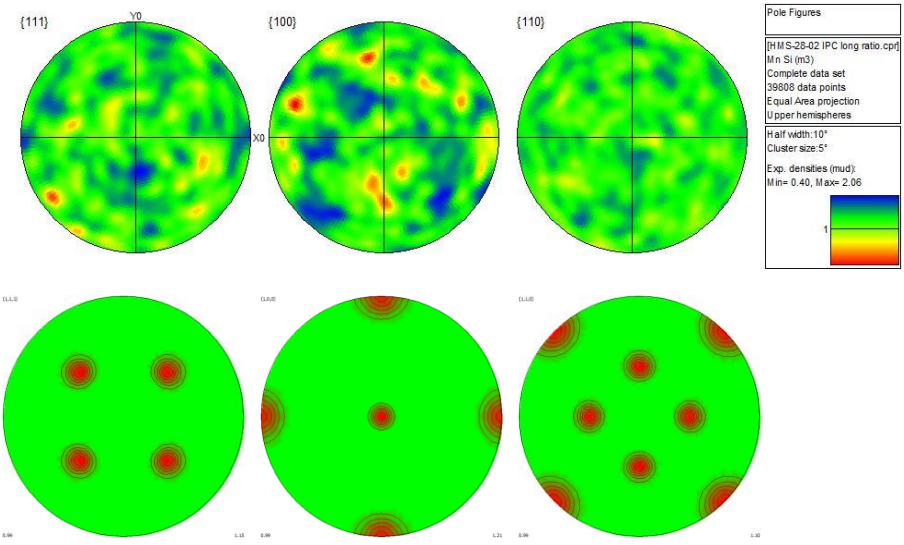

(c)

Figure 3.22 Pole figures generated by SEM-EBSD of the Mn-Si phases formed, (a) shows the silicon single crystal, (b) shows $Mn_{11}Si_{19}$ and (c) the MnSi phase, theoretical pole figures are shown below (b) and (c)

3.3.2 Out of Pack Cementation

The Out of Pack Cementation (OOPC) technique varies from the standard HAPC in that it ensures there is no direct contact between the substrates and the pack. Instead relying entirely on the throwing power of the metal halide to deposit manganese onto the substrate. This is shown schematically in section 2.3.1.

3.3.2.1 Time Effects

Given the optimum temperature was already determined with the IPC technique 900^{o}C was used for all IPC experiments. Cut-edge micrographs are shown in Figure 3.23(a-d). There was around 18 µm growth after 5 hours in the furnace, as seen in Figure 3.23(a), which increases to around 40 µm after 25 hours, as shown in Figure 3.23(d).

This growth was noticeably different to that of the IPC technique, with only a single Mn-Si layer being visible. Growth amounts can be modelled using the logarithmic growth curve as discussed in the previous sections. This would again indicate that the growth is diffusion controlled. The growth amounts are clearly visible in Figure 3.24. Ingress can be seen to reach around 50 µm after 40 hours, which was comparatively slow in comparison to the overall IPC growth shown in Figure 3.16. However, the actual content of the HMS layers was largely similar, indicating growth was not actually affected by the change in crucible set-up.

3.3.2.2 Wire Foam

Instead of growing in a coherent layer the additional MnSi layers appear to form a foam-like structure consisting of wires 200-300nm in diameter with lengths in the order of hundreds of microns, this is shown in Figure 3.25.

It has been shown in previous works[128] that the CVD technique can be used to produce MnSi nanowires for nano-electronic applications. By utilising an inert atmosphere flow within a tube furnace nano-wires can be grown on a silicon substrate with the use of $MnCl_2$. This is good for scientific purposes however manganese powder and ammonium chloride are only 10% the cost of $MnCl_2$ for a similar purity powder (Sigma-Aldrich).

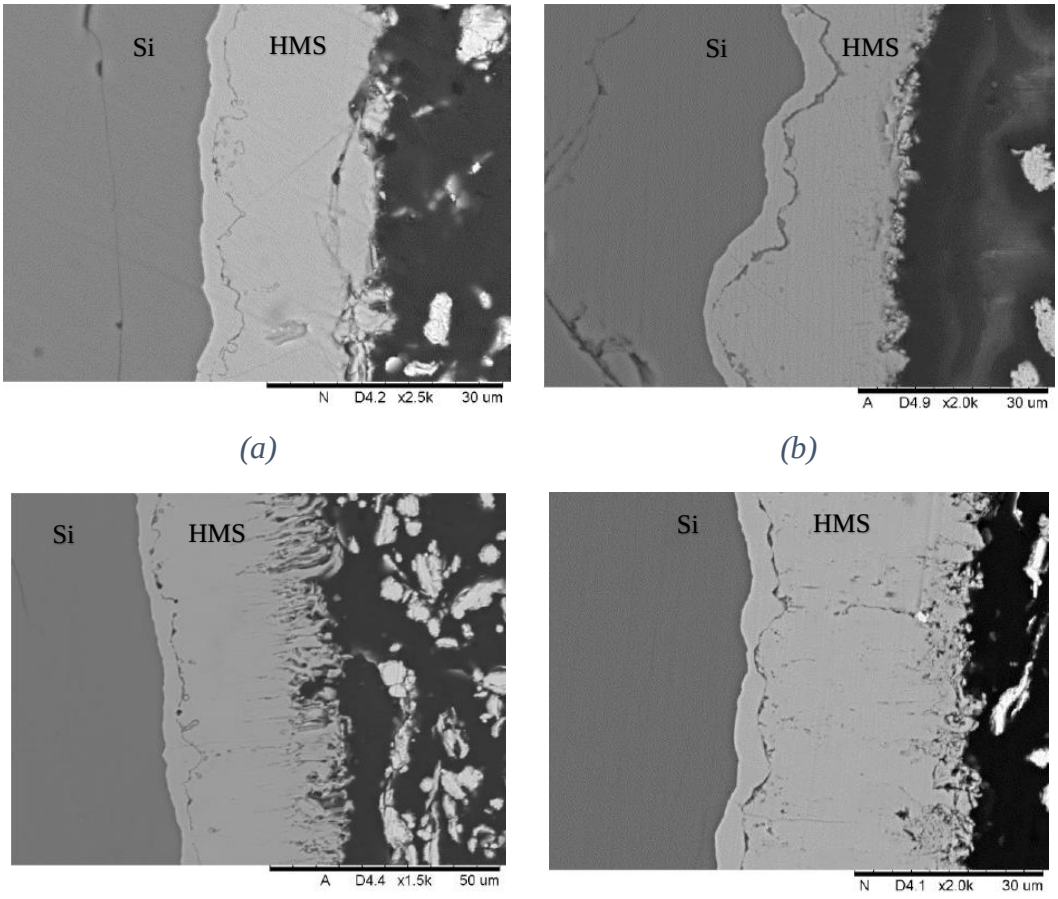

Figure 3.23 17 SEM micrographs of Mn-Si cut edge samples created at 900°C using the OOPC technique. Sample treatment time was varied showing that (a) is 5 hours, (b) 10 hours, (c) 15 hours and (d) 25 hours.

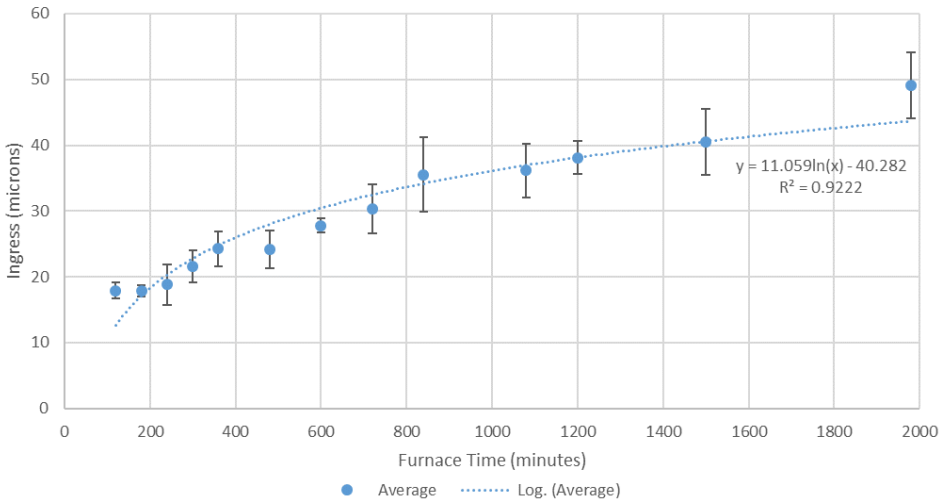

Figure 3.24 Growth amounts of Mn-Si growth of polycrystalline silicon at 900°C using the OOPC technique

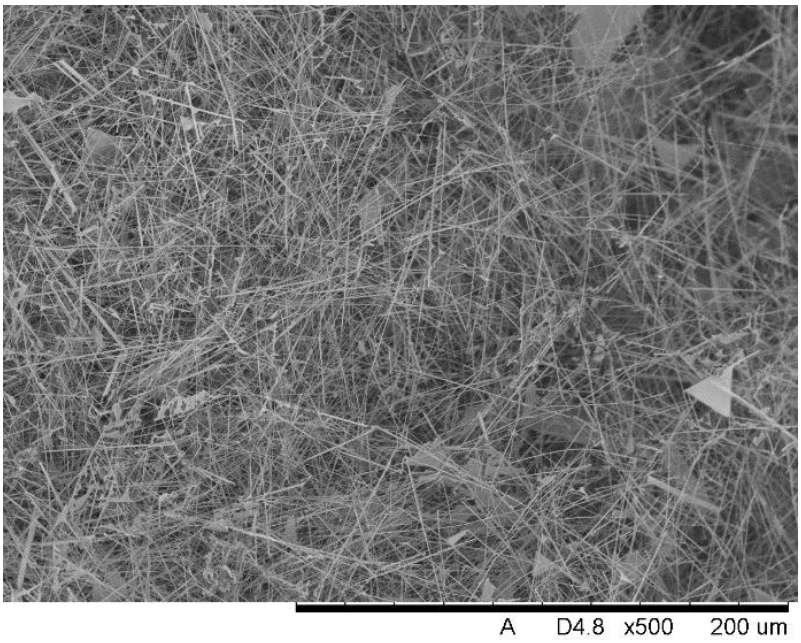

(a)

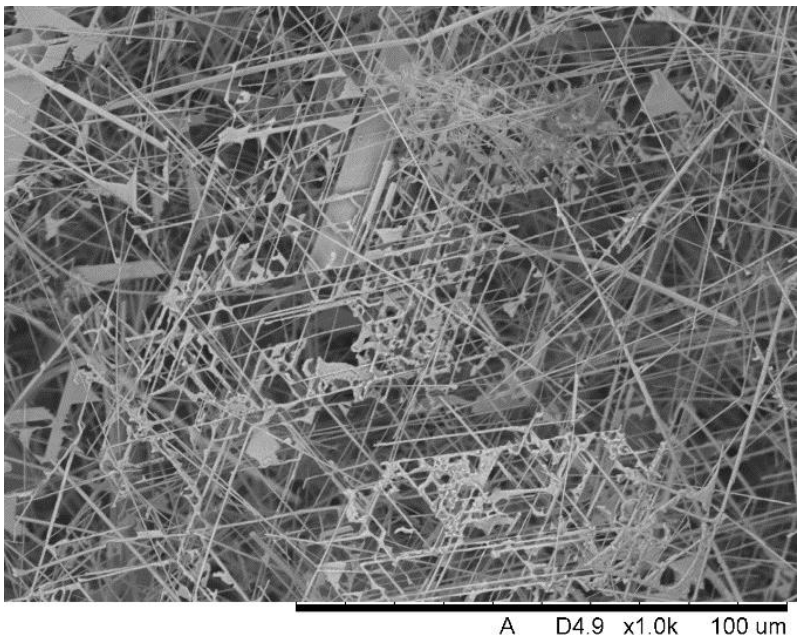

(b)

Figure 3.25 SEM micrographs of the wire-foam identified during the OOPC process at (a) 500x and (b) 1000x zoom

3.3.2.3 Film Quality

In order to determine the film quality EDS and XRD analysis was undertaken. Figure 3.26 shows an EDS map of the resultant growth for OOPC. In comparison to the IPC technique there is little or no variation in elemental composition throughout the Mn-Si layer. The elemental analysis determined this layer to be approximately of 34.4±1.09 at% manganese and 65.6±1.09 at% Si. This corresponds to the desired HMS phases. There is a slight increase in manganese towards the edge, possibly indicating a secondary phase, but using this technique it is difficult to determine exact compositions.

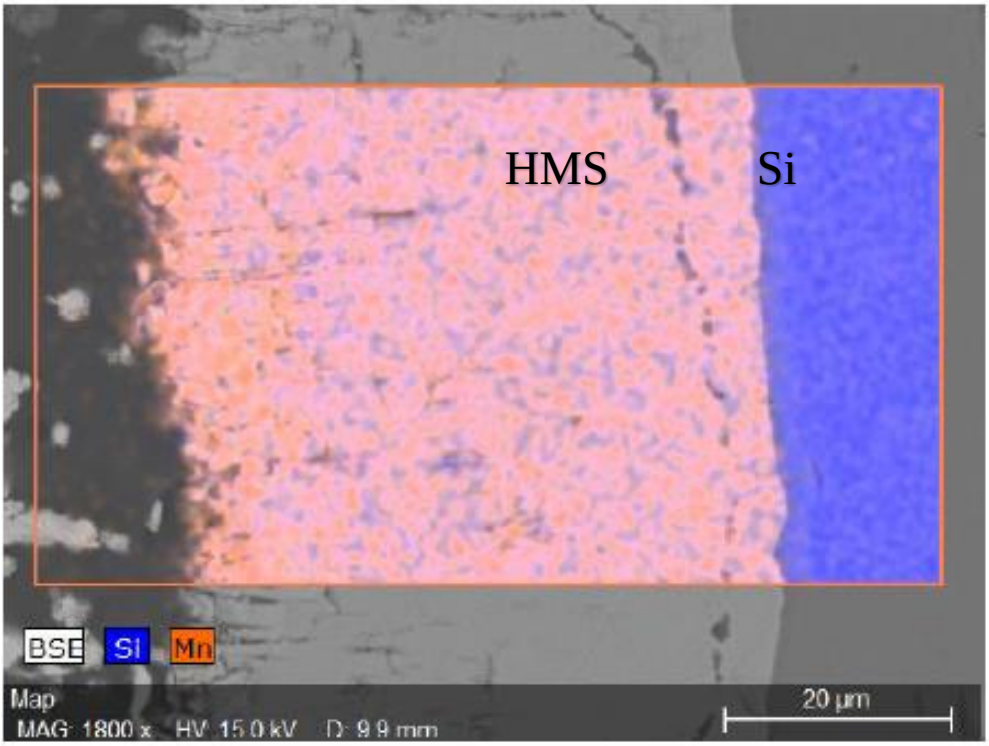

Figure 3.26 SEM-EDS map of Mn-Si OOPC at 900°C for 25 hours

3.3.2.4 X-Ray Diffraction

Figure 3.27 shows the XRD trace for the OOPC 20-hour sample. It can be seen that the HMS layer is very clear, with a trace amount of MnSi detectable. Observations of the OOPC samples show 9 primary peaks. Those of 26°, 32.4°, 39.5°, 41.9°, 46.3°, 47.5°, 53.9° correspond to HMS phase, $Mn_{11}Si_{19}$. There is considerably less MnSi detected in the structure of the OOPC samples.

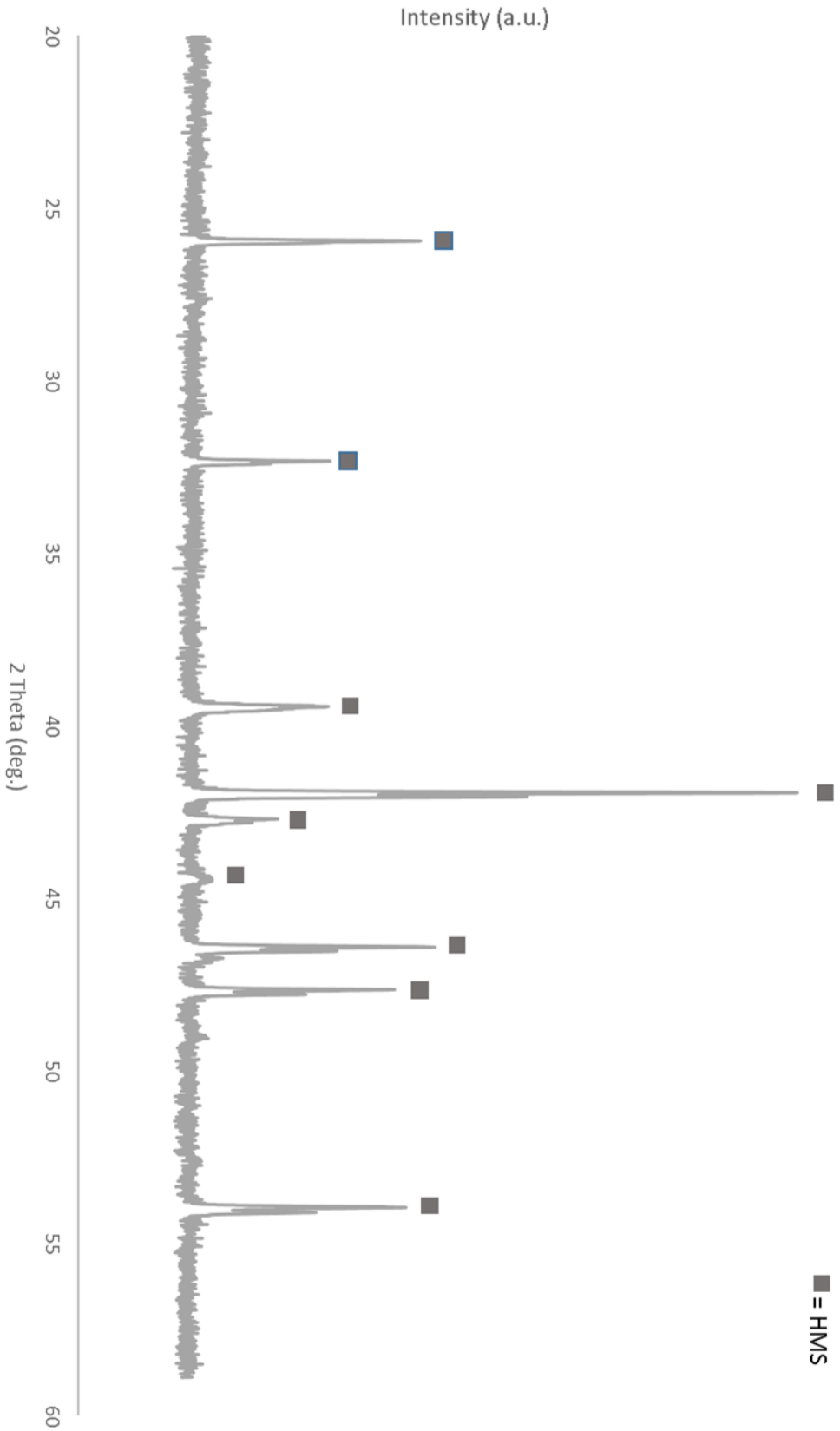

Figure 3.27 XRD scan of Mn-Si produced by OOPC, showing its high purity HMS phase.

3.3.2.5 Texture and Grain Alignment

In order to fully quantify the variation between IPC and OOPC, EBSD was again undertaken. Figure 3.28 shows the phase analysis (a) and band contrast (b) images for the OOPC sample. It is shown when comparing Figure 3.19 and Figure 3.27 that there are significant differences, with considerably lower amounts of MnSi present. The small surface layer of MnSi is loosely bound and can be easily removed. This layer acts as the nucleation point for the wires seen in Figure 3.25(b). There are several similarities to that of the IPC technique (Figure 3.20) in that there are equiaxed grains seen at the Si-HMS boundary, which give way to larger columnar grains. These grains terminate with a boundary layer of MnSi grains on the surface.

84% of the grains within outer MnSi are below the aspect ratio of 2:1, implying they are reasonable equiaxed, like those of the IPC. With the grains divided into the 3 categories used previously, 34% are below 10µm, 42% are between 10 and 20µm, and the remainder being below 40µm. These grains are slightly larger than those produced in the IPC technique.

Within the $Mn_{11}Si_{19}$ phase two distinct growth patterns were identified, these can be clearly seen in the EBSD maps. These are very similar to the IPC, indicating the initial nucleation and growth mechanism is not affected by contact effects. There are significantly fewer grains present than that of IPC. These 329 $Mn_{11}Si_{19}$ grains can again be split into two categories. 232 are below 20µm, these relate closely to the 237 equiaxed grains with an aspect ratio of 3:1 or below. The smaller grains are identified as the nucleation grains against the substrate. The grains which make up the bulk material are significantly larger, with more than 60 grains being over 50µm. These relate to the high aspect ratio of the columnar grains. They are visibly larger than those of IPC, indicating that the columnar growth is significantly restricted with direct contact of the pack onto the substrate.

Figure 3.29 shows the inverse pole figures with Figure 3.30 showing the pole figures. As with the IPC technique there is little orientation visible. There is a slight increase in orientation with the {100} direction, however this is not high enough to be considered highly textured. As such the columnar growth gives no preferential growth orientation to be observed.

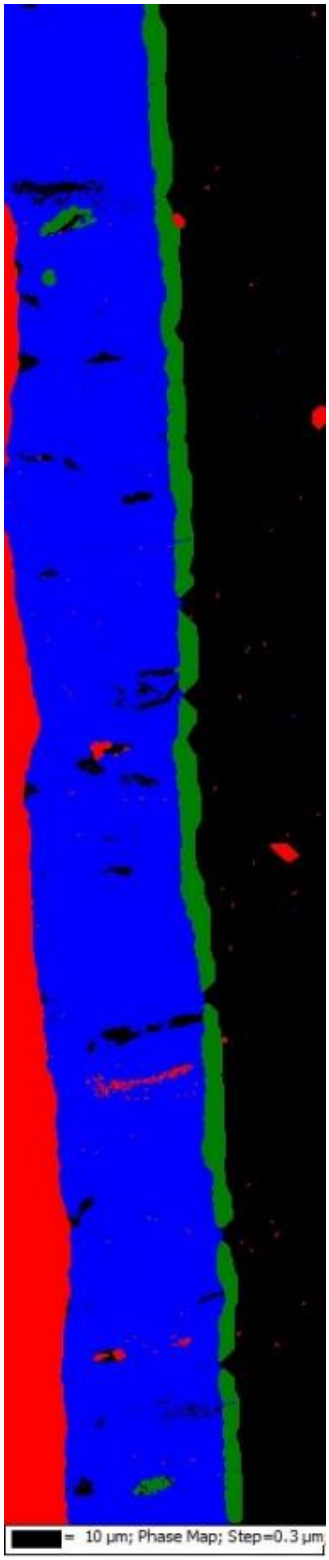

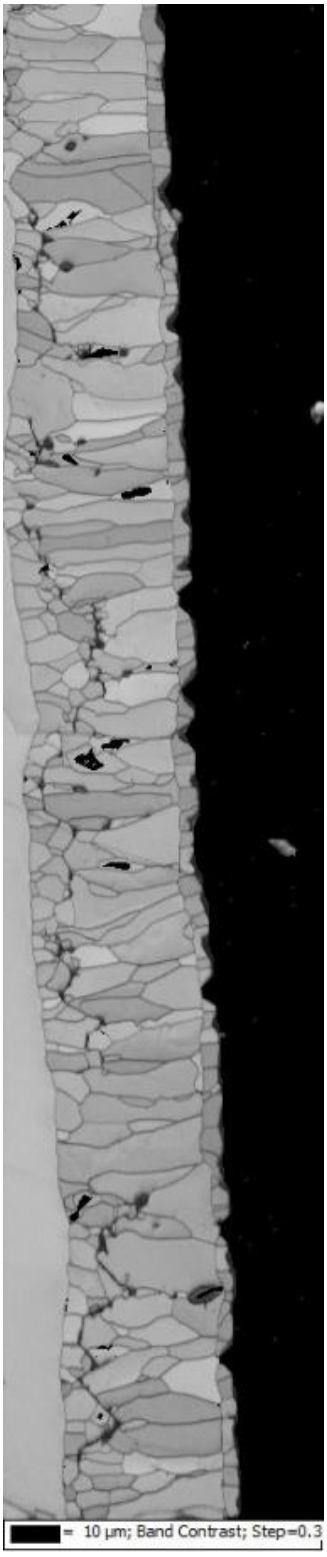

(a) *(b)*

Figure 3.28 SEM-EBSD plot of the (a) phases present in the sample (red = silicon, blue = $Mn_{11}Si_{19}$, green = MnSi) and (b) the band contrast showing grain locations, from the OOPC process

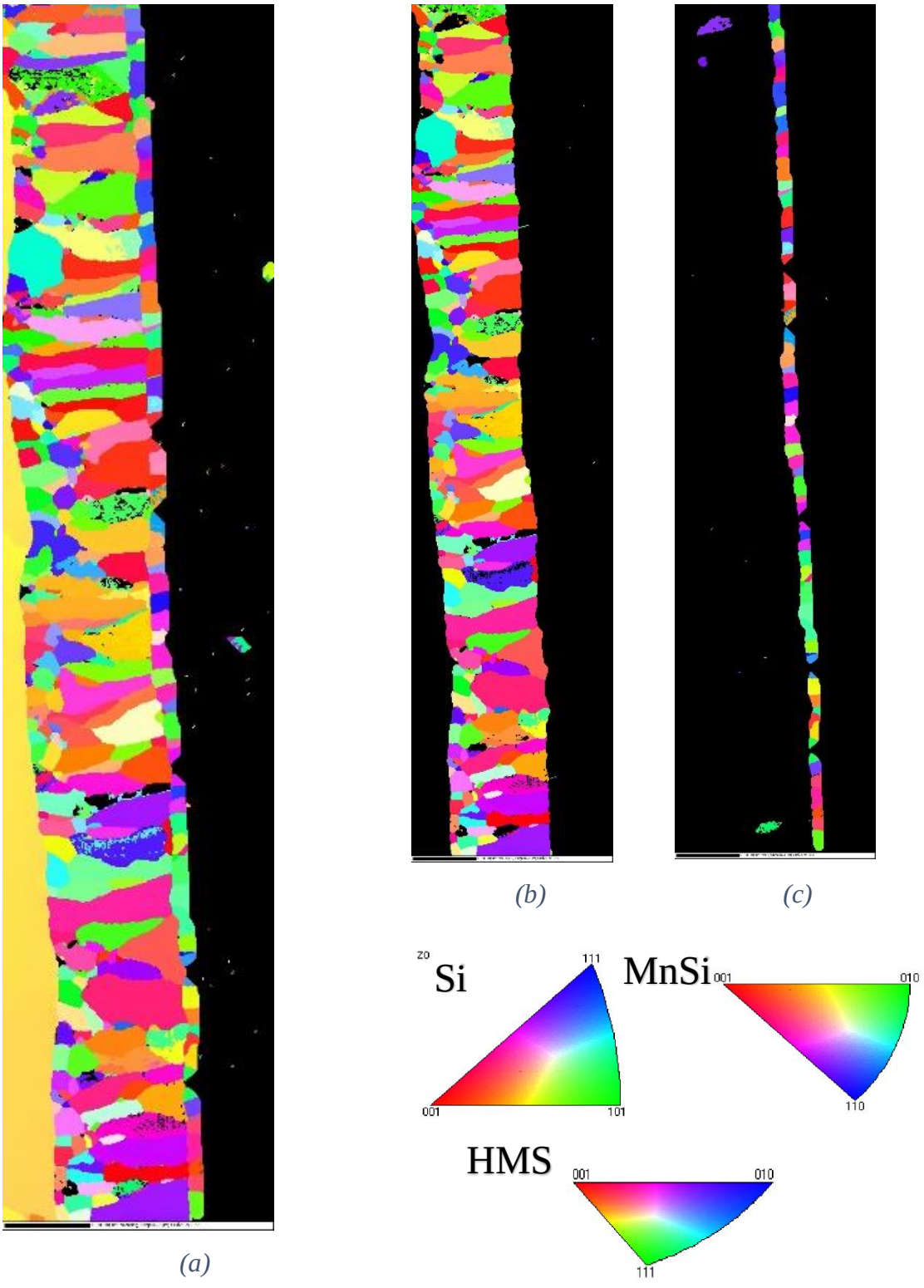

Figure 3.29 SEM-EBSD map of the (a) Inverse pole figure colouration for grain orientation (b) IPF of $Mn_{11}Si_{19}$ layer (c) IPF of MnSi layer, colours represent grains orientation produce by OOPC

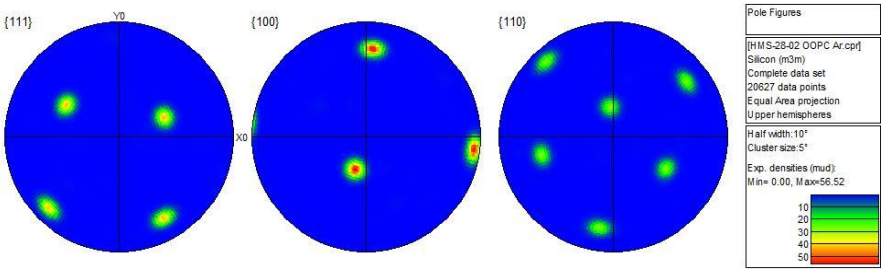

(a)

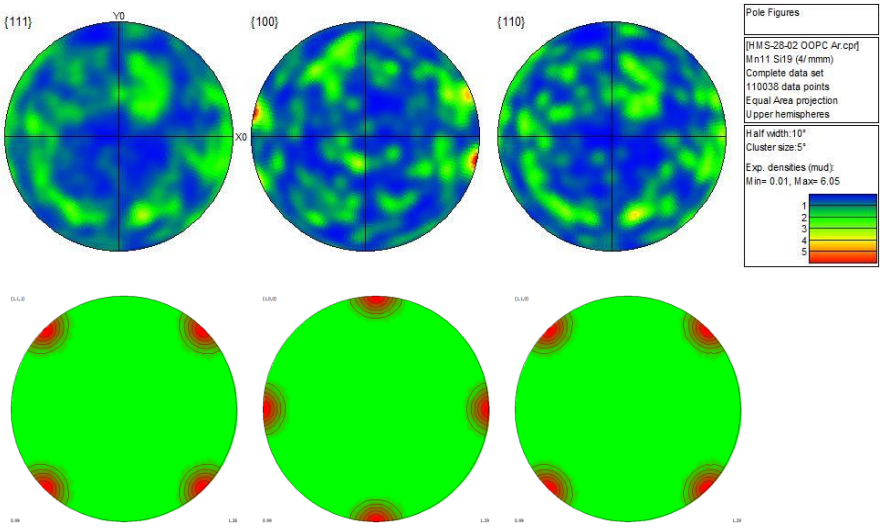

(b)

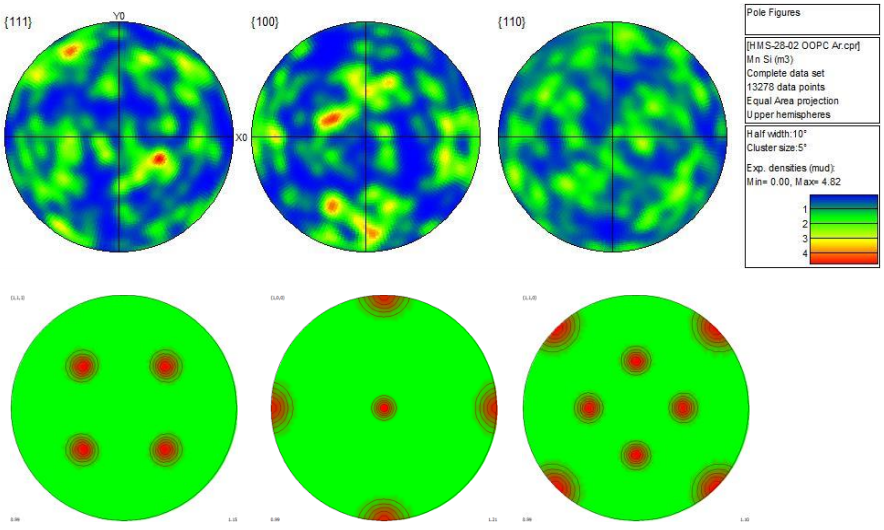

(c)

Figure 3.30 Pole figures generated by SEM-EBSD of the Mn-Si phases formed from OOPC, (a) shows the silicon single crystal, (b) shows $Mn_{11}Si_{19}$ and (c) the MnSi phase, theoretical pole figures are shown below (b) and (c)

3.3.3 HMS Production Summary

In summary HMS can be produced in high purity using the OOPC variation in comparison to the standard HAPC process, despite the significantly more complex phase diagram in comparison to Mg_2Si, this is shown in Figure 3.31. The growth behaviour was less consistent than the Mg_2Si production but was reasonably predictable. The key issue will be implementing this on a larger scale, as it is difficult to replicate an OOPC process with powders. Due to this a current scale-up approach would be to use thinner substrates, which can then can then be layered to create a block with directional grains. There was also an interesting effect in visible surface colouration with argon used as a shielding gas rather than nitrogen. Argon results in a much shinier looking final product, this indicates there is a small amount of nitrogen doping in the process currently. Investigating the effect of this nitriding was not within current the scope of this work however should be investigated in the future.

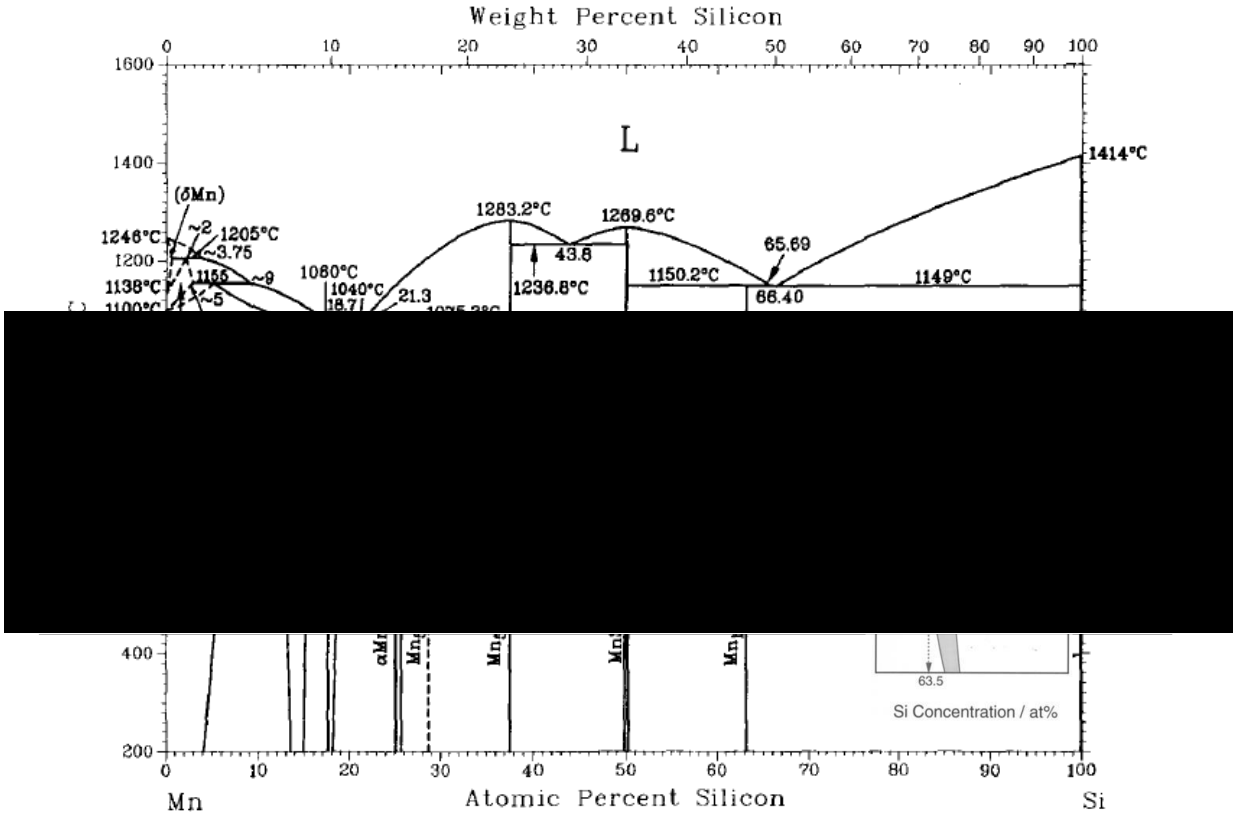

Figure 3.31 Silicon-manganese phase diagram, inset of HMS region[129]

3.4 Beta Iron Disilicide

Beta iron Disilicide (β-$FeSi_2$) is an extremely low cost thermoelectric semiconductor that can be doped to perform as an N and P-type semiconductor. Whilst its performance is low with a ZT of around 0.2, its low cost and sheer earth abundancy make it a viable material. The Fe-Si phase diagram, see Figure 3.32, shows only 2 combination phases stable at room temperature, of these $FeSi_2$ is a prime semiconducting material.

$FeSi_2$ exhibits a noticeable phase change at around 955°C. The α-$FeSi_2$, a relatively simple metallic tetragonal unit cell, experiences lattice distortion resulting in an energy level shift and a distortion of the structure. The resulting β-$FeSi_2$ octahedral "Cmce" structure (64) exhibits very low symmetry and many iron atom vacancies. This results in a unit cell that only repeats every 48 atoms, this goes some way to enhance its semiconducting properties. Both unit cells are shown in Figure 3.33.

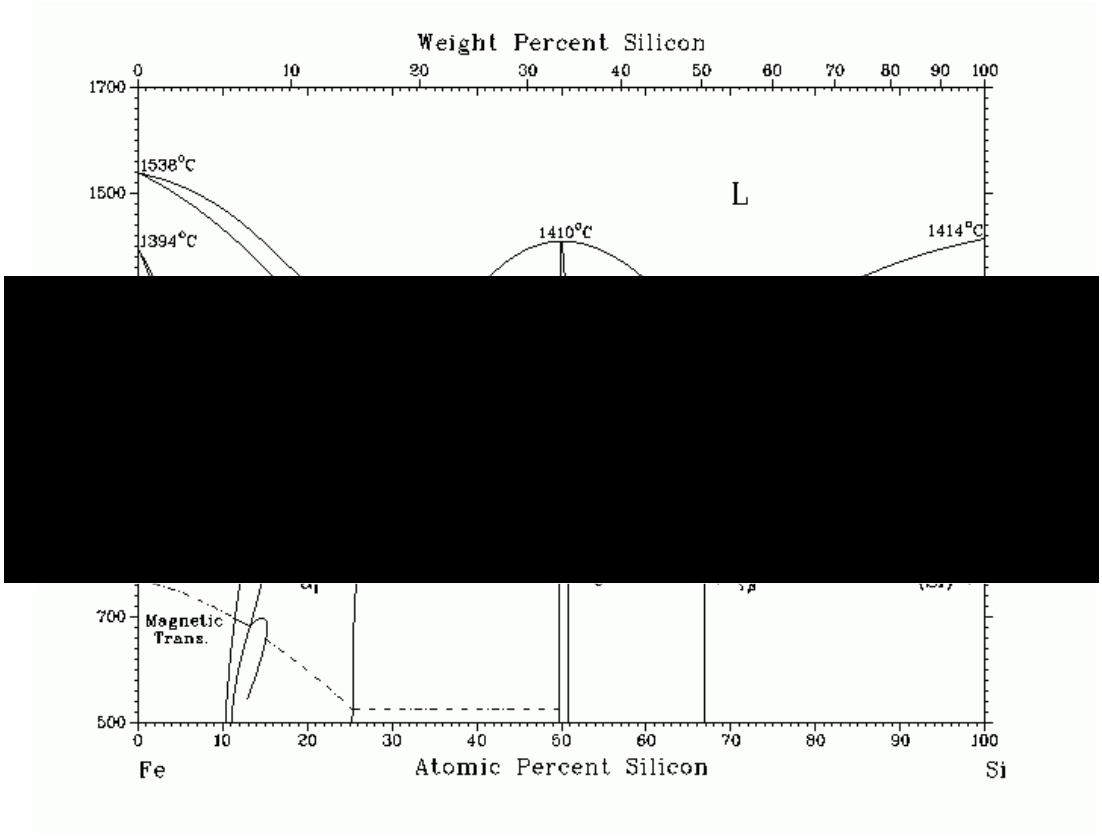

Figure 3.32 Fe-Si phase diagram[130]

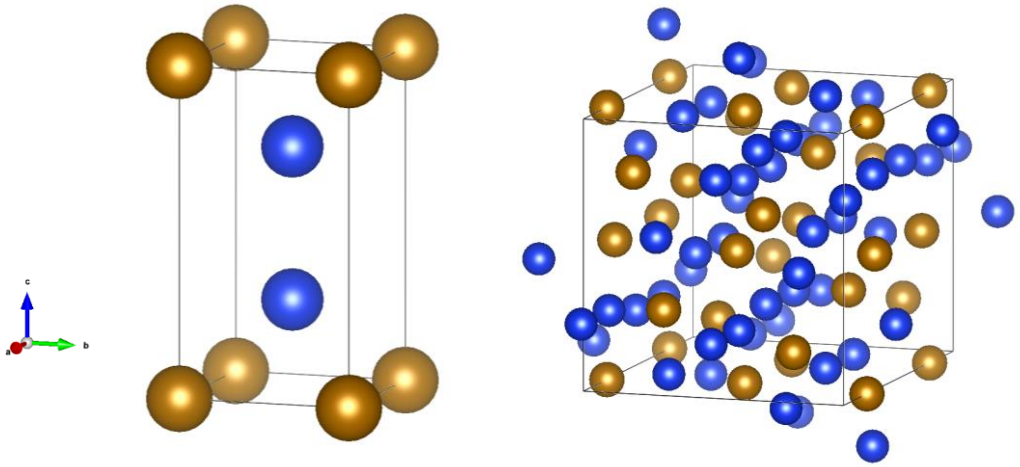

(a) (b)

Figure 3.33 Crystal structures for α and β-$FeSi_2$ phases

3.4.1 Pack Cementation Process

Using the HAPC technique with iron as the active metal allowed the rapid deposition of iron onto a silicon substrate. HAPC can be undertaken at any temperature above 650ºC, however it appears to be an entirely uncontrolled reaction.

Figure 3.34 shows the layered structure like that observed in the vast majority of samples. Due to the size increase caused by the phase change the converted material expands greatly resulting in separation between the substrate and the $FeSi_2$ layers. Figure 3.34(a) gives a view of the many layers present in the skin of the separated areas.

Due to the varied growth and surface roughness within this material it is not viable to scan using EBSD, Figure 3.36 shows the cut edge of one of these voids mounted and polished. This micrograph was generated using Backscatter electrons, indicating the sample is primarily a close composition of phases. Further EDS analysis shows that there is a slight composition variation raising towards higher iron amounts around edges. The inner edges result in a 2-3:1 ratio of Fe:Si, whilst the outer areas are close to 4:1 Fe:Si ratio. This implies these phases are more of a solution of silicon in iron as opposed to the desired FeSi phases.

It is believed that the structures seen in Figure 3.37 are due to the confinement of preferential growth much like the MnSi wire phase seen previously. The curved shapes exhibited are a result of the Fe-Si growing around the alumina filler. If samples are not

cleaned thoroughly, entrapped alumina is regularly observed. These grow on the main coherent layer. This layer appears to be split into an outer solid section and a more porous inner layer. This inner layer displays large crystallites growing from it. Given the pulling away of this layer, the crystals can grow uninterrupted into a void allowing these unusual crystal shapes seen in Figure 3.34 to be observed.

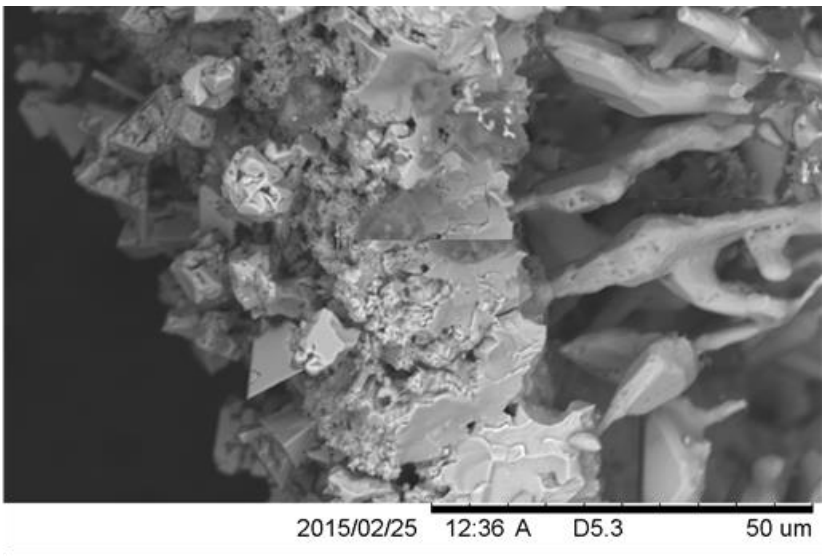

(a)

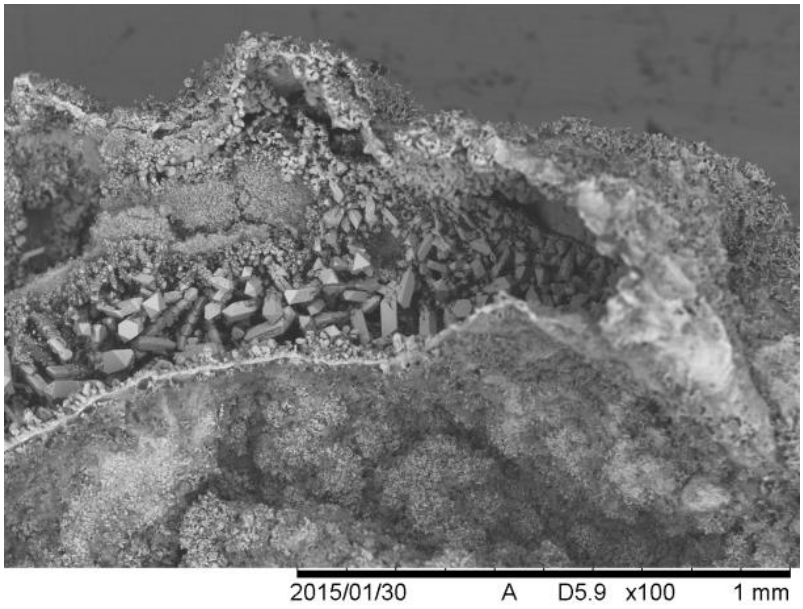

(b)

Figure 3.34 Micrographs showing the broken bubbled structure of Fe-Si, with (a) showing the many layers present and (b) showing the entire structure

The tube seen in Figure 3.37(a) is likely formed via solid metal particle catalysed CVD (vapour-solid) with the particle having broken off later. The crystallites shown in Figure 3.37(b) and (c) almost appear to be hopper crystals at times and are clearly showing the preferred growth directions of the FeSi structure. The nanowires are seen often, examples are shown in Figure 3.37(d) and the fibre shape is like that of Solid-Vapour phase growth which would imply amorphous properties when below the Tg of the material.

Nanowires that were identified growing in the samples and are most probably FeSi. These measure in the order of 200nm in diameter, up to 30 microns long. These may be worth further study in the future.

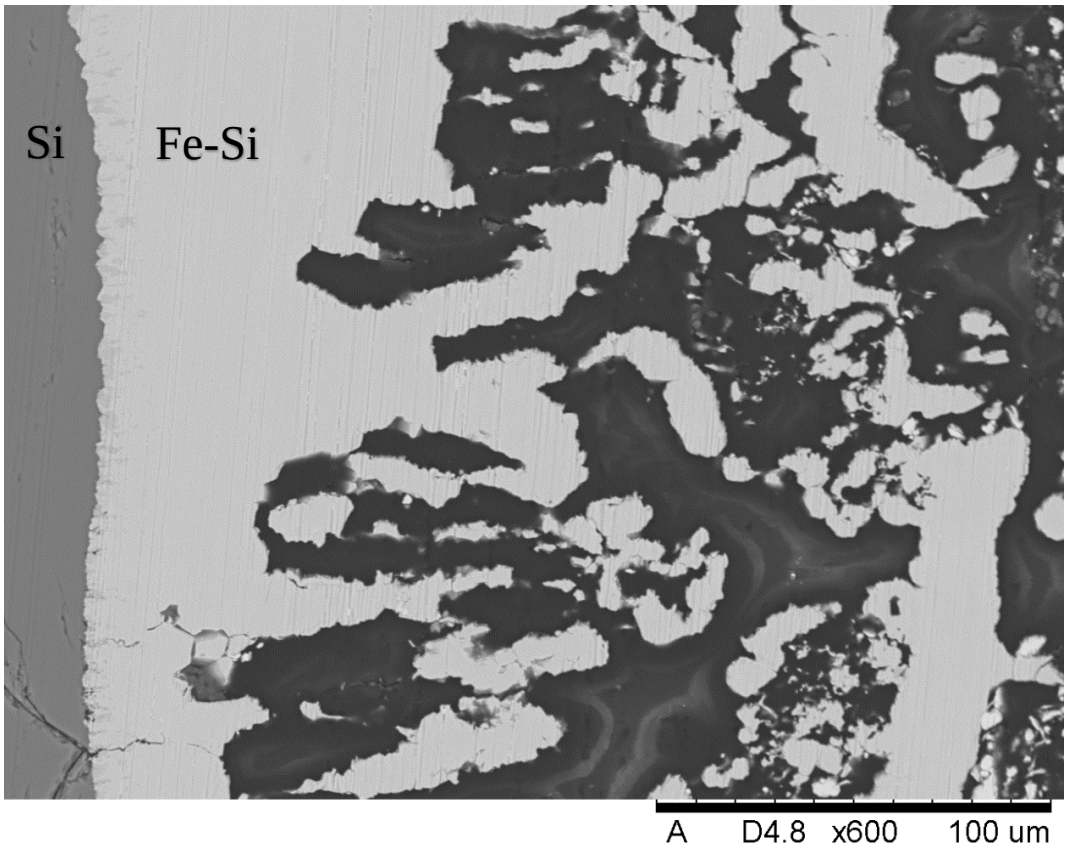

Figure 3.35 SEM micrographs of Fe-Si cut edge samples created at 650°C. These samples are mounted in conductive resin with silicon seen to the left

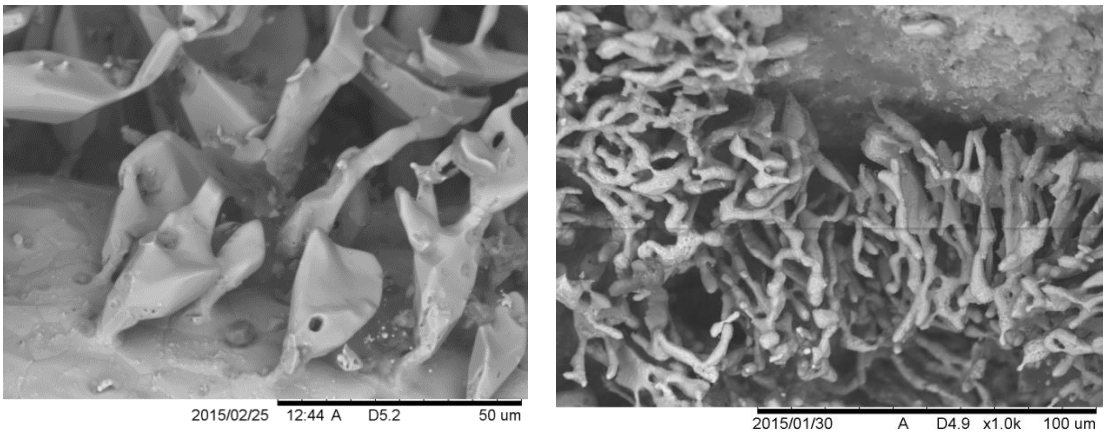

(a) *(b)*

Figure 3.36 SEM micrographs of the outer surface from pack cementation at (a) x3000 and (b) 1000x zoom

(a)

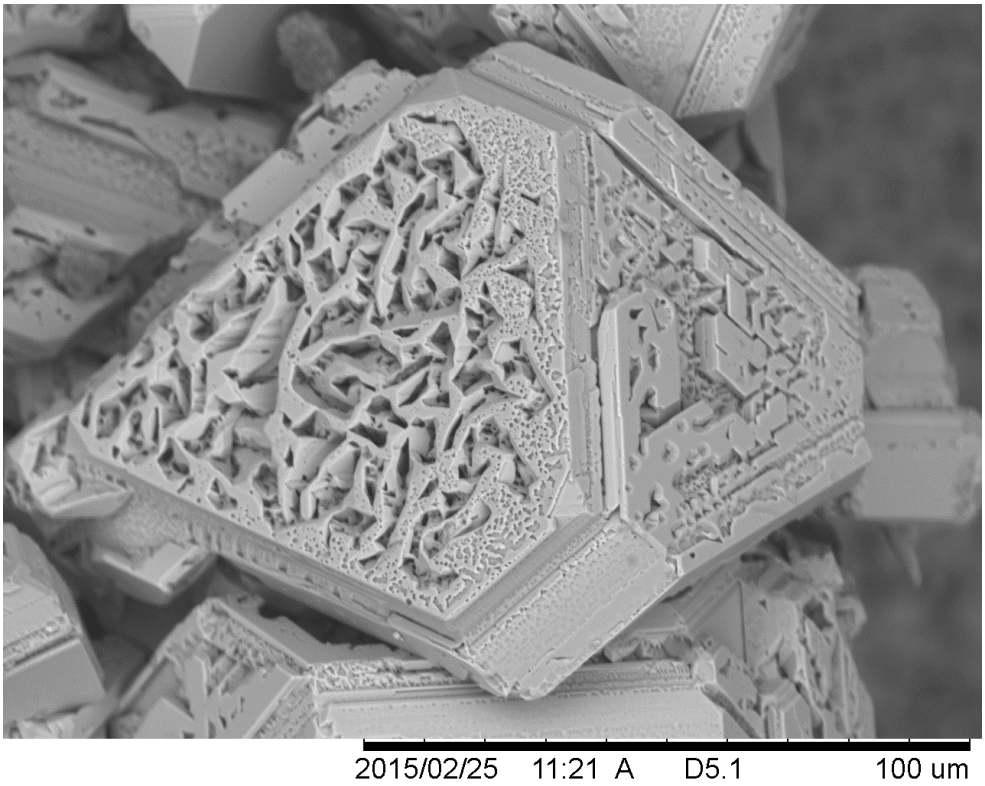

(b)

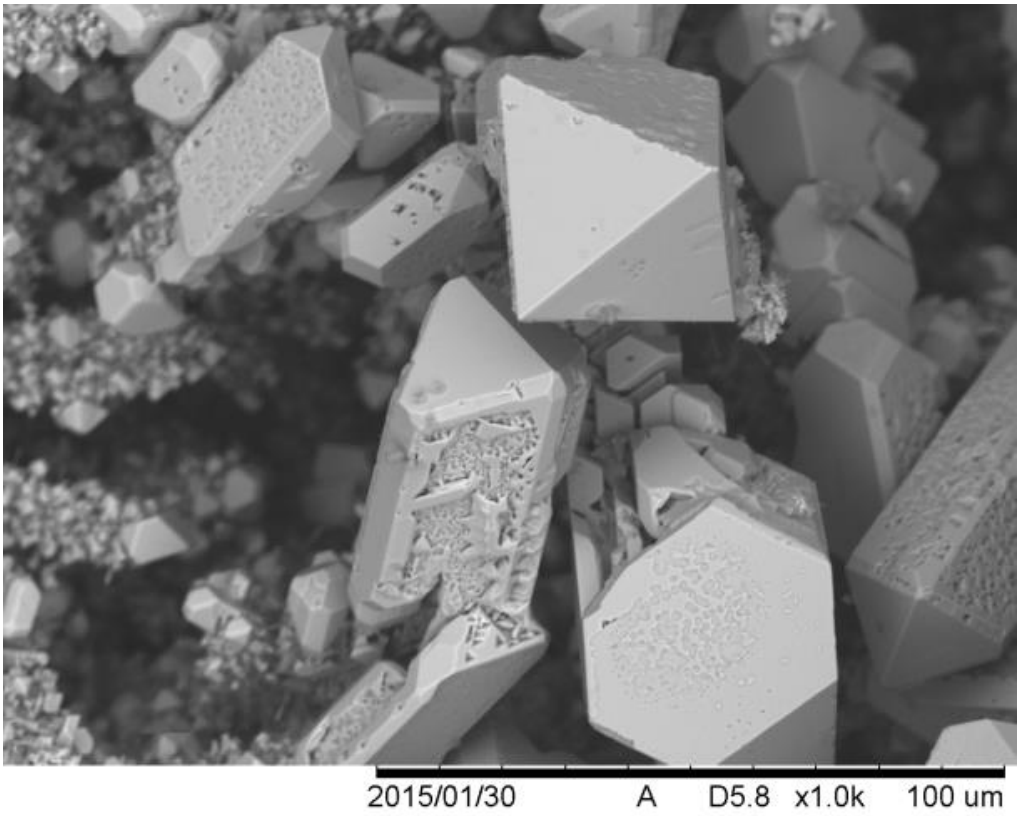

(c)

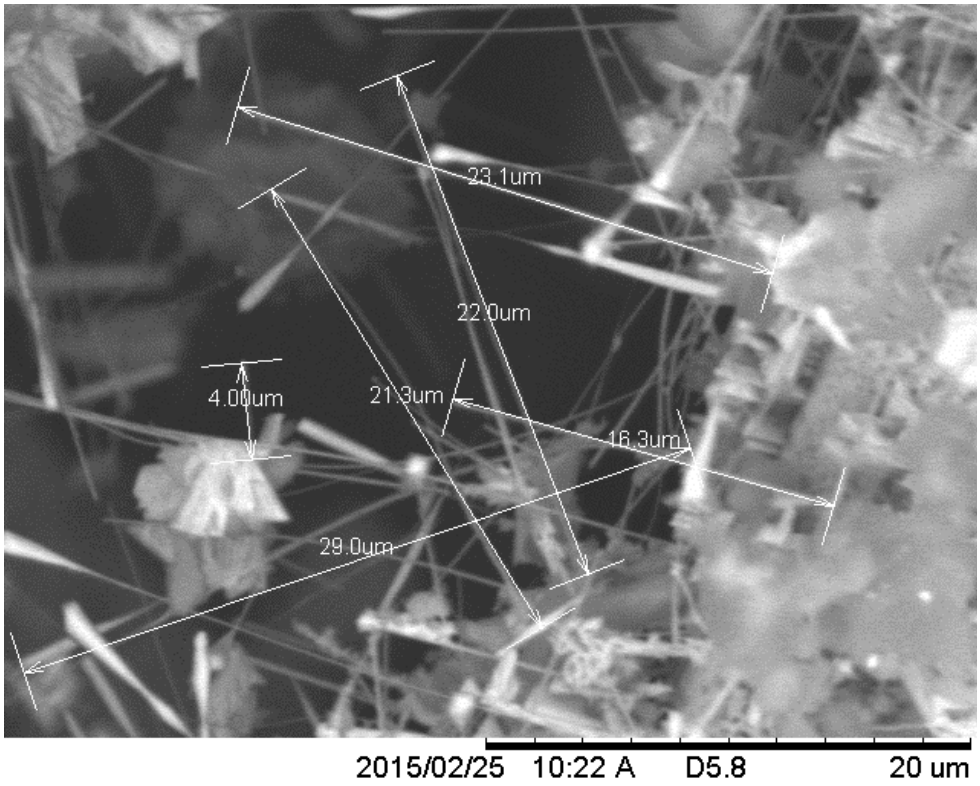

(d)

Figure 3.37 SEM micrographs of structures formed within the bubble voids showing (a) the elongated tube structures, (b) and (c) the large crystallites formed whilst (d) the finest nanowires observed

3.4.2 Fe-Si Production Summary

This technique produces a wide range of phases and if it can be better understood it has a great potential for high surface area applications. Future developments into this material can further control the phases produced and determine the overall surface areas of the materials generated. It opens the possibility for using this technique to generate catalyst materials or nanowires for applications such as catalytic convertors and the production of hydrogen. This would require further research considering the control of this process, and the potential applications.

3.5 Transition Metal Silicide Production Conclusion

This chapter has covered the use of the HAPC process to produce 3 materials within the TMS group. Fe-Si materials produced using this method are currently not useable for thermoelectric applications due to their currently uncontrollable growth characteristics. They do however provide an interesting option for a high surface area reactive material. This also shows that the HAPC technique could be effectively used to produce a variety of material structures depending on the constituent components. This opens up HAPC for a number of applications including high service area TMS for catalytic[46,131] and magnetic[132] applications this wild growth could prove useful. Work on Mg_2Si shows it is a reliable but slow production method, which when combined with new generator designs might present a viable production technique. Finally, the HMS production is shown to be a reliable technique with both high quality HMS and high aspect ratio MnSi nano-wires being produced. Both products could have uses, with the OOPC technique revealing that surface interactions play a key part in the HMS production process.

This chapter has shown that the HAPC technique can be used to produce alternatives to the more commonly used thermoelectric materials within current devices. The production process is relatively low waste and uses readily available technologies, making it a possibility for future production.

Chapter 4 Development of Molten Salts as Liquid Electrical Contacts

4.1 Introduction

This chapter focuses upon the development of an alternative to solid electrical contacts, represented by the area highlighted in Figure 4.1. A current issue that affects the lifetime of thermoelectric devices is the thermal fatigue upon the electrical connections. To address this, the idea of encapsulated conducting salts was proposed to provide a contact. This could then be melted and solidified in such a way that cracking would not occur and fail under cycling.

This chapter will look into the production of a number of salt mixtures along with a look at their thermal and electrical properties. The initial salt starting point will be based on thermal storage salt laid out by Peng et al[133]. This salt has been developed for two applications, firstly as a molten electrical contact, and then as a thermal storage salt and heat transfer solution for heliostats. The paper shown in Appendix 2.

This chapter will develop on previous works with reference to the thermal properties for both electrical and heat transfer. Further analysis will look at the electrical and then corrosion properties of the salt. Varying carbon additions were added to increase its conductivity. This allowed the viability of the salts as a contact material to be determined and any possible issues that may arise with the use of these materials. The general production of these salts has been outlined in section 2.5 Phase Change Salts.

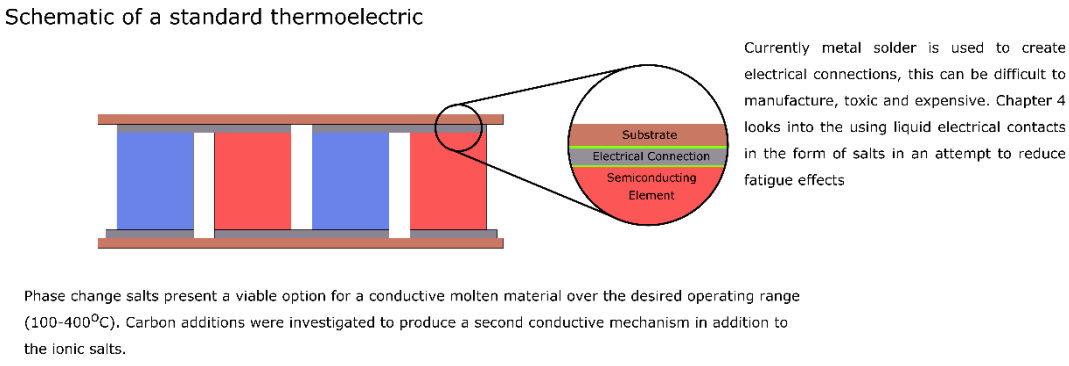

Figure 4.1 Infographic image of a traditional thermoelectric device, with focus on the electrical contacts

4.2 Thermal Behaviour

4.2.1 Melting Behaviour Modification

Melting behaviour was the first property to be tested. For a viable device using Skutterudite thermoelectric elements, a melting temperature of below 100°C was desired to allow the salt to be molten during operation. The current best performing commercial product is a ternary salt of 53wt% KNO_3, 40wt% $NaNO_2$ and 7wt% $NaNO_3$, which was tested using the DSC to serve as a control, this can be seen in Figure 4.3. This control showed a melting point of 146.7°C, matching well with other literature[133]. Following this a selection of salt additions of 5wt% were prepared and tested using DSC. Literature indicated that $LiNO_3$ and a range of metal chlorides were possible viable additions to modify the melting and stability behaviour of these materials[74,113,134]. Initial testing revolved around $LiNO_3$ and KCl additions. This showed that whilst KCl had no noticeable positive or negative effects on the melting point, $LiNO_3$ additions vastly decreased the melting point to below 100°C. This however came with a reduction in the decomposition temperature.

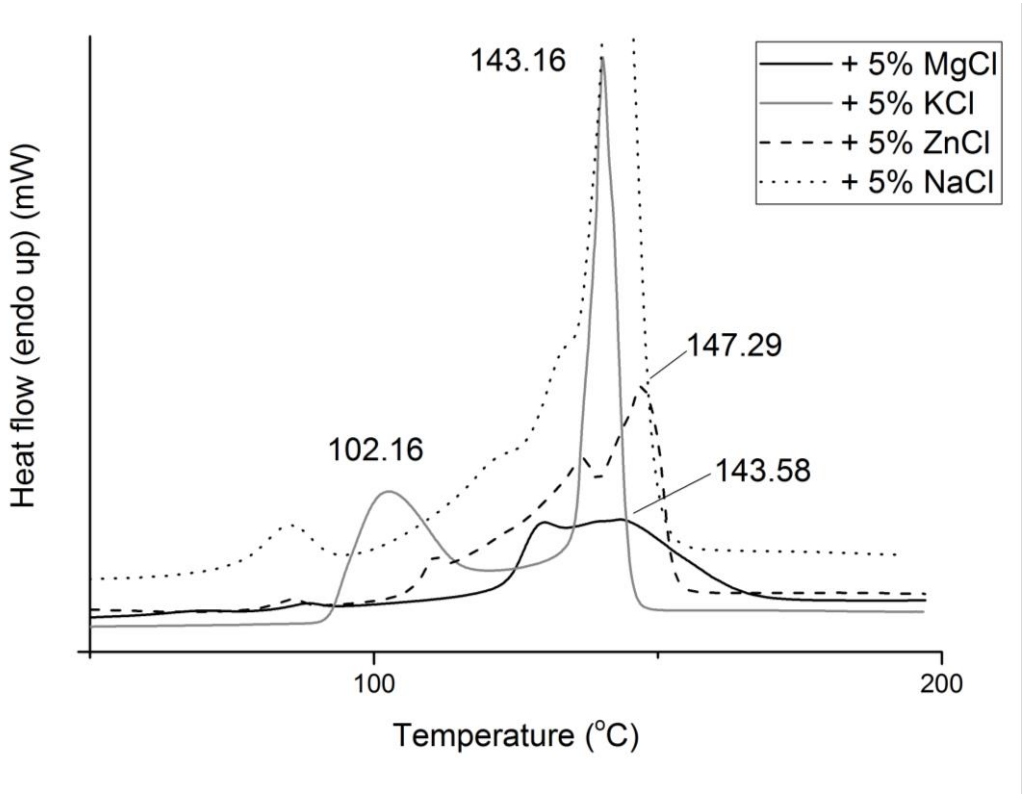

Figure 4.2 DSC traces showing the effect of 5wt% addition of various metal chlorides on the ternary salt

In addition to KCl a wide range of chlorides were tested. Figure 4.2 shows the onset of melting for each mixture. It was seen that additions of MgCl significantly reduced the latent heat of transformation and raised the melting point to 148^{o}C. Similarly, the addition of ZnCl significantly reduced the heat flow, this is indicated by the lower peak intensity. Both these chlorides have partial melting, or phase transitions, at lower temperatures, however the lower latent heat and lack of complete melting is undesirable for the application. NaCl and KCl additions do not adjust the melting point considerably in comparison to the standard ternary salt, allowing these additions to be taken through for further study. LiCl was the most promising addition as the endotherm peak is significantly shifted down to 80^{o}C, as shown in Figure 4.3. Figure 4.3 strongly indicates that this was a direct result of the Li metal, as $LiNO_3$ also has a similar drop, whilst most chlorides fail to lower the melting point. The melting point of pure LiCl is over 600^{o}C whilst $LiNO_3$ is over 250^{o}C, so it can be assumed a new phase is being formed with the current eutectic.

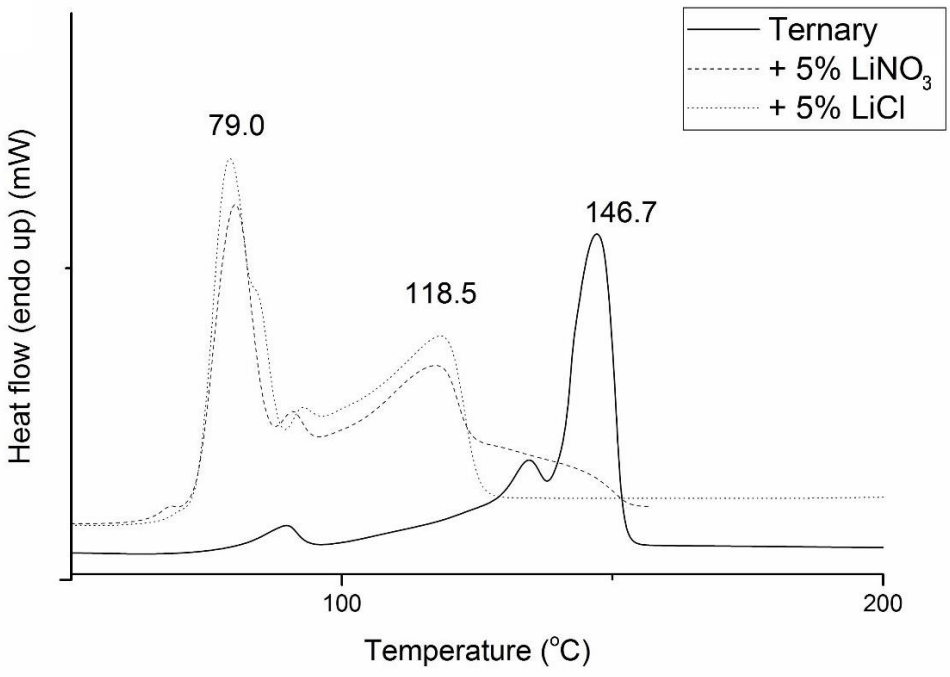

Figure 4.3 DSC traces showing the effect of 5wt% addition of $LiNO_3$, and LiCl on the ternary salt

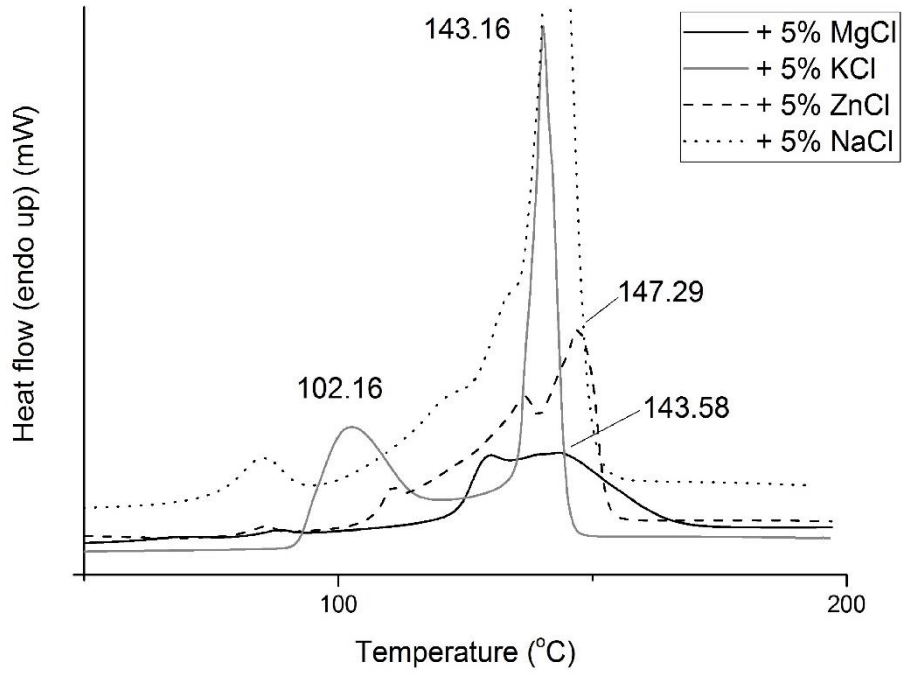

Figure 4.4 DSC traces showing the effect of $LiNO_3$ on the ternary salt

4.2.2 Short Term Thermal Decomposition

The chosen salts were tested for their short-term decomposition behaviour using the TGA technique in a nitrogen atmosphere. $LiNO_3$ was seen to have negative effects on the thermal stability of the salts, as such was not pursued any further on its own. The effects of these additions can be seen in Figure 4.5. It was theorised that given the increased stability of Cl phases that Cl acted as a temperature stabilising agent. Initial investigations showed metal-chloride additions resulted in a stabilisation effect, as indicated by Peng et al[73,133]. Two values were chosen for comparing decomposition temperatures, these have been used previously in literature, with 1% weight loss set as the initial decomposition and 7% weight loss chosen as where rapid decomposition is undergone. Rapid decomposition was seen in the ternary salt at 610°C as shown in Figure 4.5. Additions of 5wt% KCl resulted in a stability increase of 38°C to 648°C. This was further increased to a maximum of 741°C with the addition of 10wt% KCl. The large stabilisation effect from KCl allowed the operation at higher temperatures for periods of less than 30 minutes.

LiCl additions behave differently, with a more noticeable oxidation stage. This is shown in Figure 4.3 as an increase in weight. There is an initial stabilisation effect caused

by the LiCl, allowing the sample to reach 685°C before weight loss occurs. It was seen that additions of LiCl above 5wt% result in a reduction in stability, as shown by the lower temperature of decomposition seen in Figure 4.6. Given $LiNO_3$ shows a reduced decomposition temperature compared to many other nitrates[75], it is believed that the Cl within the melt aids in stabilisation. However, the Li additions can cause some short-term instability decreases, meaning a balance between the Cl stabilisation and the Li destabilisation must be achieved. Overall KCl and LiCl were chosen for long term testing due to their improved upper temperature stability behaviour.

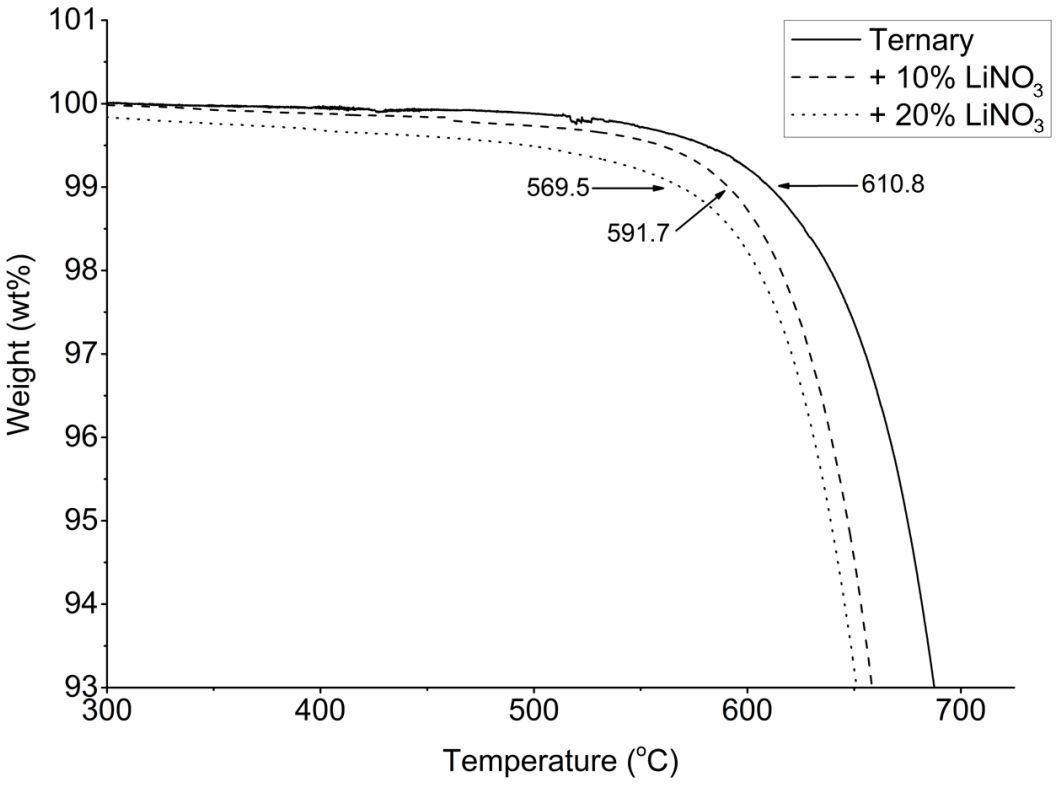

Figure 4.5 TGA trace showing the effect of additional $LiNO_3$ upon the thermal decomposition temperature of the HITEC salt

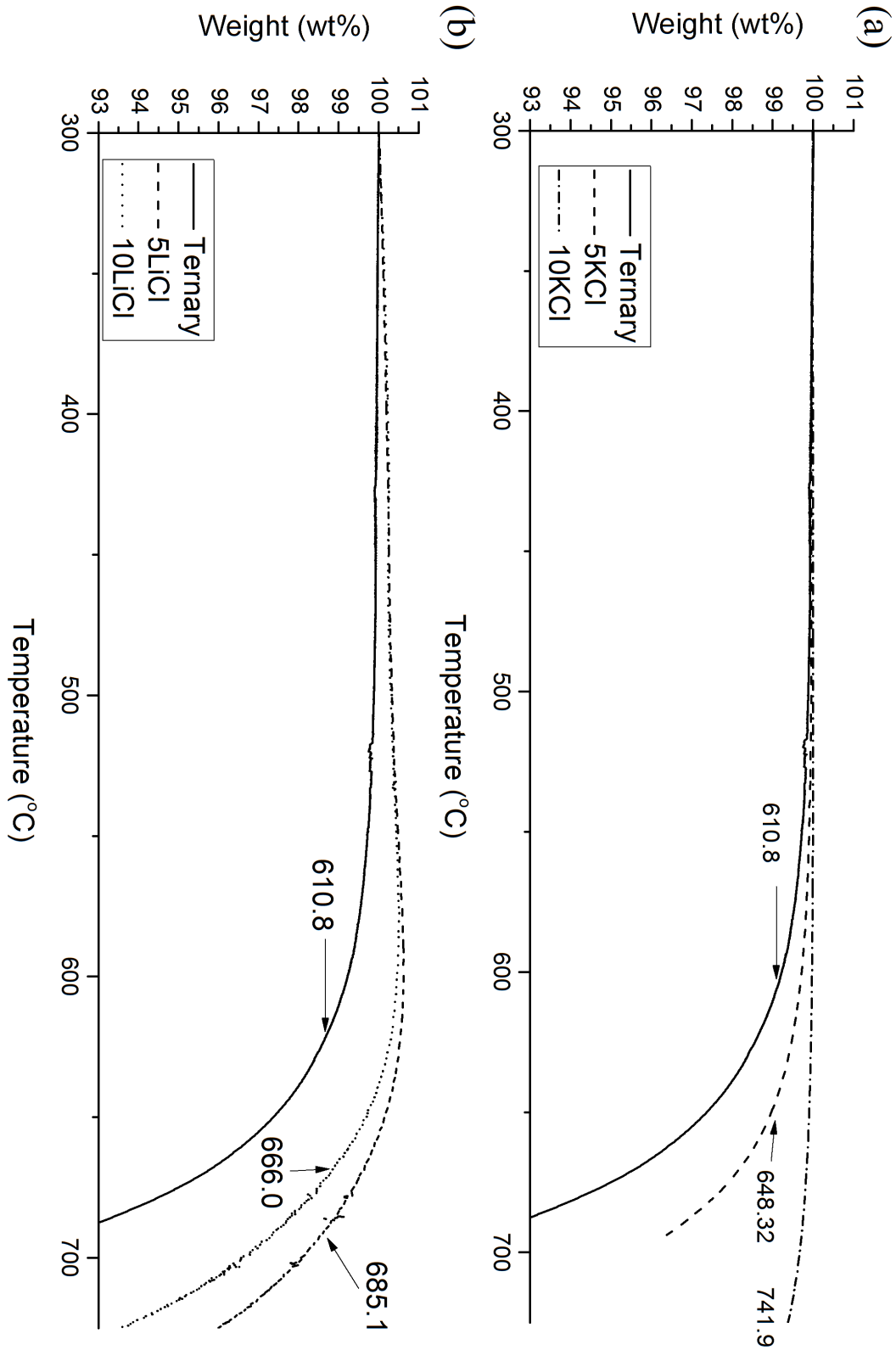

Figure 4.6 TGA traces showing the effect of additional (a) KCl and (b) LiCl on the ternary HITEC salt

4.2.3 Long Term Thermal Stability

Long term thermal stabilities were tested using standard muffle furnaces over a 30-hour time span. Long term tests showed a noticeable variation in stability with additions of both KCl and LiCl. Any weight gains shown in Figure 4.7(a) and (b) can be attributed to oxidation of the salts. It can be seen in Figure 4.7(b) that 5wt% KCl does provide some high temperature stability improvements. Whilst Figure 4.7(d) allows the comparison of varying chloride additions after 30 hours at 650^{o}C. The weight loss was 60.1wt% for the ternary salt, whilst a 5wt% addition of KCl reduces this weight loss by 7.7wt% to 52.4wt%. Weight loss of the all salts was lower than anticipated at 550 and 600^{o}C, this was determined to be due to cooling effects within the furnace. Small weight gains are seen in the ternary salt at all temperatures, most probably due to the conversion between NO_2 to NO_3, which will negatively affect the melting behaviours. The weight gain is seen in KCl containing salts, but at a much lower rate.

The most noticeable improvement to the traditional ternary salt is with the addition of LiCl, where a 5wt% addition results in a weight loss of only 24.84wt% after 30 hours. Figure 4.7(d) also shows that there is little or no improvement with additions higher than 5wt%. This ties up with the data from the short-term experimentation.

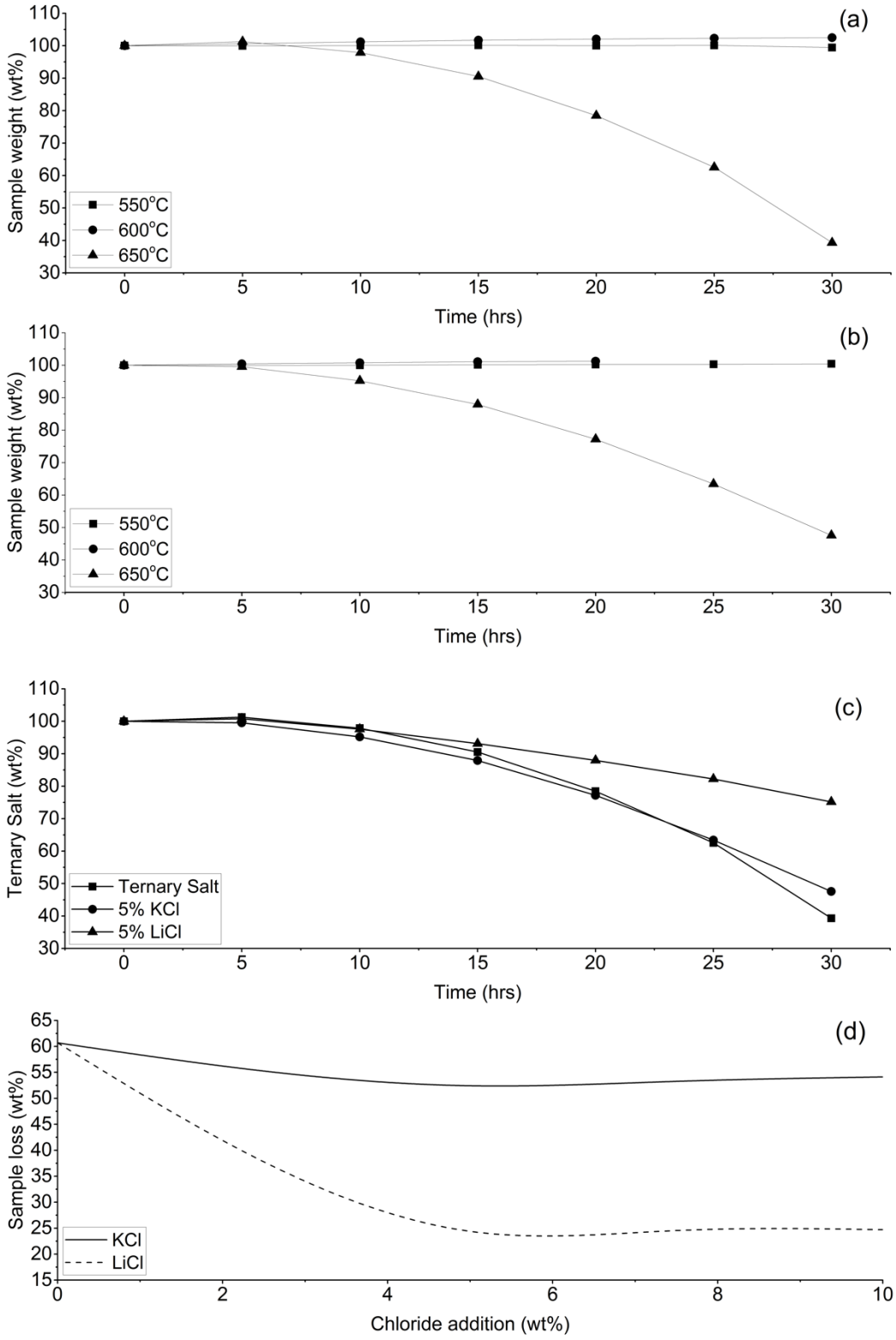

Figure 4.7 Long term decomposition of (a) ternary and (b) 5wt%KCl addition salts. (c) decomposition behaviour at 650°C and (d) salt weight loss after 30 hours at 650°C.

4.3 Phase Analysis

4.3.1 X-Ray Diffraction

In order to gain a better understanding of the phases formed by the additions of LiCl and KCl to the ternary salts, mixtures were scanned at room temperature using XRD. This allowed the identification of phases present, which were compared with standards from an open database[135]. Figure 4.8(a) and (b) shows the effect of the LiCl additions on the solid crystal structure of the ternary salts. There are 6 noticeable increases in peaks and two significantly reduced peaks with the addition of LiCl. These have been marked by x and n respectively in Figure 4.8. These peak increases are seen in both the decomposed ternary and LiCl containing samples (As shown in Figure 4.8(b) and (c)). It is likely the LiCl allows for a room temperature transformation to produce a phase that shares a similar crystal structure to that of the decomposed ternary phase. The most likely decomposition phase, sodium oxide (Na_2O), would increase the melting point. This is seen to form in the LiCl samples, however it does not raise the melting point of the eutectic, so it may be a yet unidentified phase. Given the change in melting point it can be assumed that the peaks, marked x in Figure 4.8, (27.72^o, 29.7^o, 46.6^o, 58.2^o, 60.9^o and 61.7^o) correspond to a beneficial phase that enables the more rapid melting.

Following the resultant decomposition of the ternary phase, there is a reduction in the primary KNO_2 peak and an increase in the peak relating to KNO_3. This is indicative of an oxidation reaction occurring. There is a noticeable increase in the Na_2O peaks, whilst a few peaks relating to KNO_2 and K_2O decrease, indicating that these are the primary phases decomposing. A similar peak (at 27.72^o) can be seen in the XRD trace obtained from HITEC with LiCl additions, this closely resembles that seen in the case of the decomposition phase. An increase in the peaks relating to the Na_2O phase are also present in both curves. Na_2O is a high temperature phase that should remain solid until 1132^{o}C, however no signs of any solid are present at elevated temperatures, indicating that it is dissolving into the melt.

Resultant decomposition phases for ternary and LiCl containing phases are remarkably close to each other, indicating that the same bulk decomposition is occurring through the

same process. There is less weight loss with the LiCl stabilising addition, possibly due to a binding of Na and O_2 preventing further oxidation and decomposition.

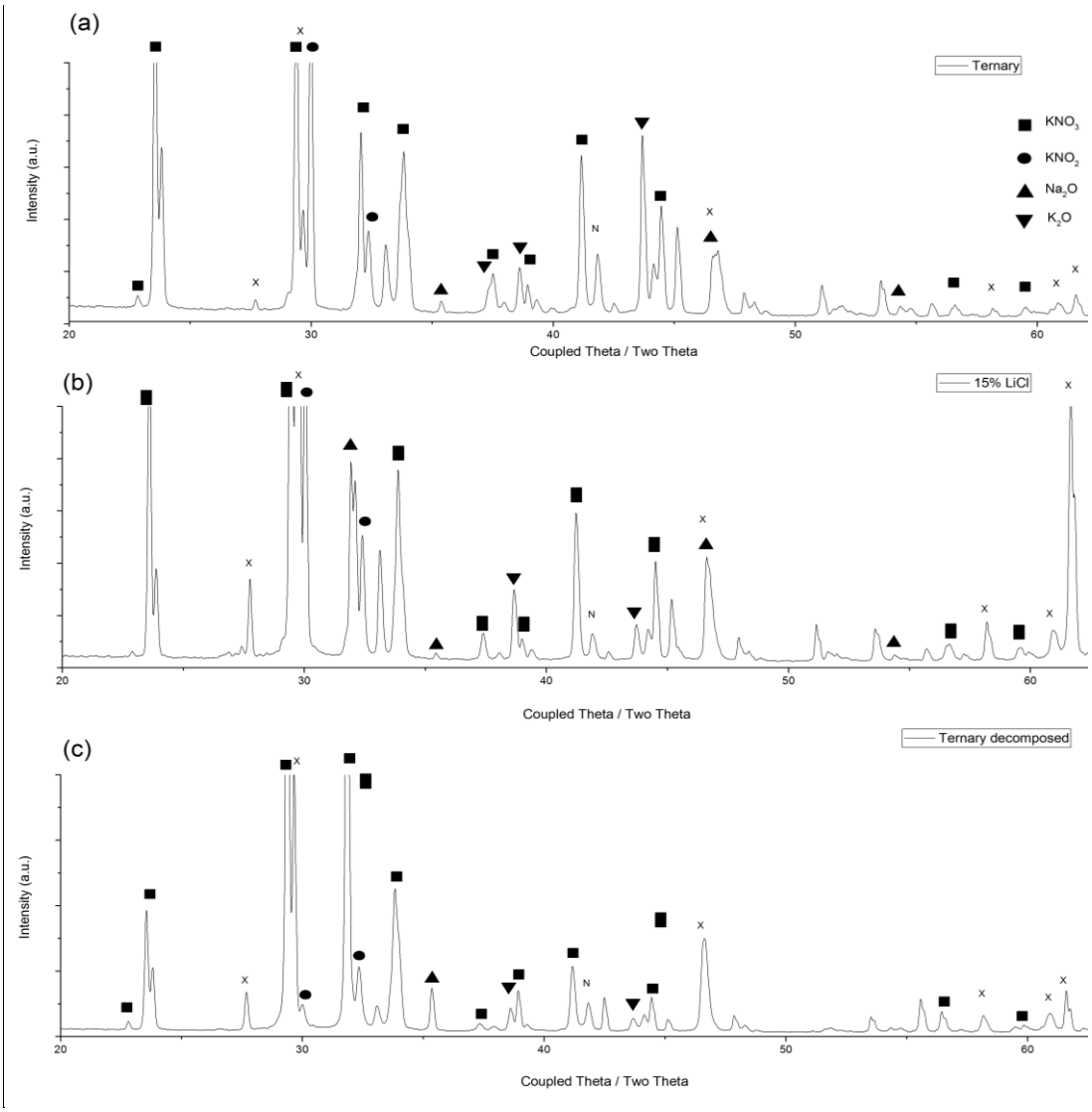

Figure 4.8 XRD trace of (a) ternary salt; (b) 15wt% LiCl addition; and (c) ternary salt after 30 hours at 650^{o}C

4.3.1 Imaging of Crystal Structures

In addition to attempting to the determine phases with XRD, SEM imaging allowed the viewing of the solidified structure of the material. A standard ternary salt has a fine structure with 3 separate phases possible to identify using BSE detectors, this can be clearly seen in Figure 4.9. Figure 4.10 (a), (c) and (e) show the effect of KCl additions to the microstructure. There is a slight increase in one phase, most likely a high potassium

phase like K_2O. This changes the morphology of the salts makeup giving a larger dendritic type structures. However due to the penetration depth of the electrons when using EDS analysis, it is difficult to scan phases without viewing deeper into the sample which may result in a mixed reading.

Lithium additions (Figure 4.10(b), (d) and (f)) are seen to have a much greater effect on the solid structure of the salts. Although due to the limitations of the EDS it is impossible to detect Li within a phase, the structural changes are noticeable, with considerable increases in the darkest matrix phase. This can be related to the increase in Li present, matching the generation of additional phases detected on the XRD. There are slight concentration variations within the darker matrix, seen in Figure 4.10(f) as shade variations. These are difficult to identify in the EDS software, as Li, which is a likely constitute of these phases, cannot be detected.

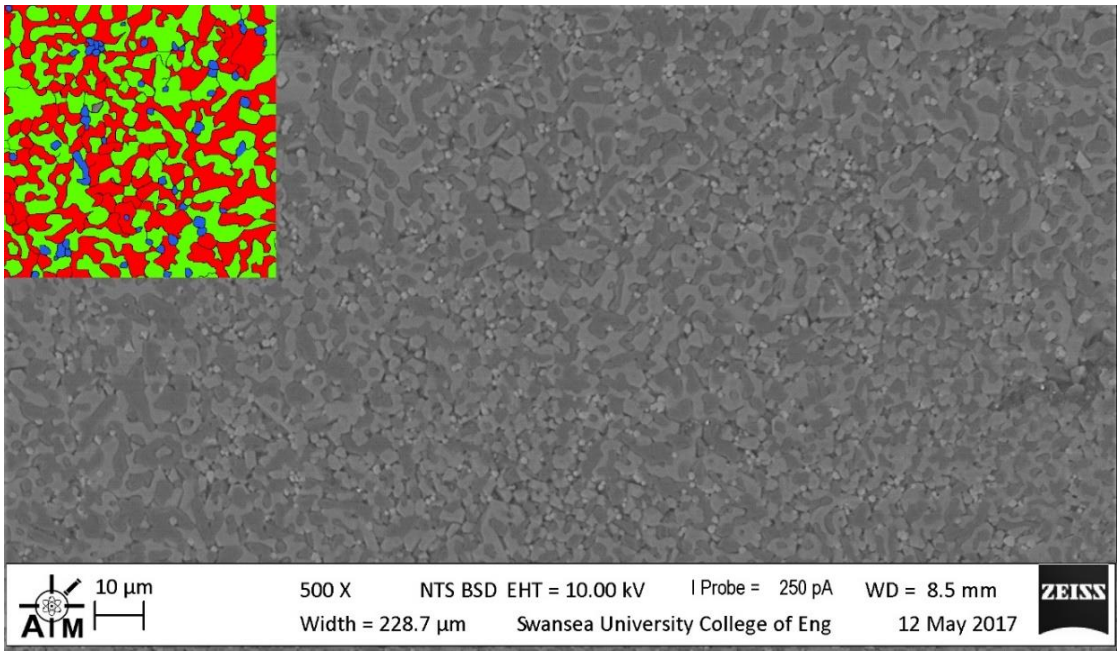

Figure 4.9 SEM micrograph using back scatter imaging showing the original ternary salt

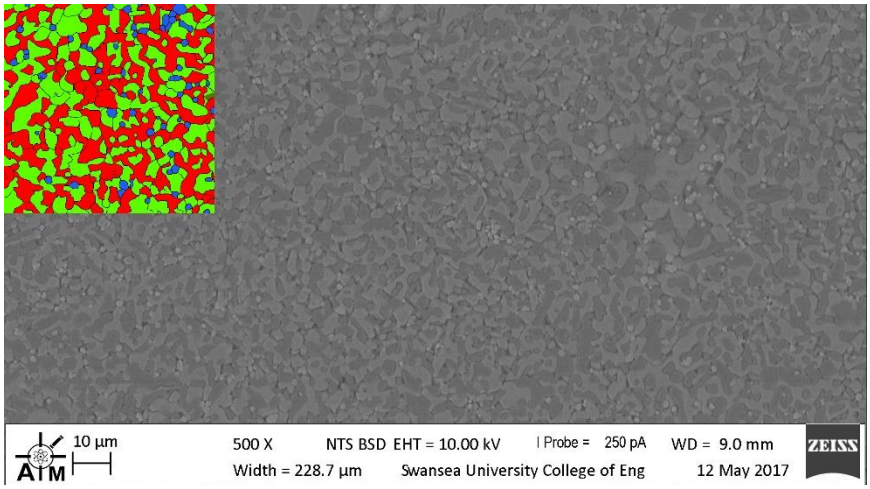
10 µm
500 X NTS BSD EHT = 10.00 kV I Probe = 250 pA WD = 9.0 mm
Width = 228.7 µm Swansea University College of Eng 12 May 2017
ZEISS

(a)

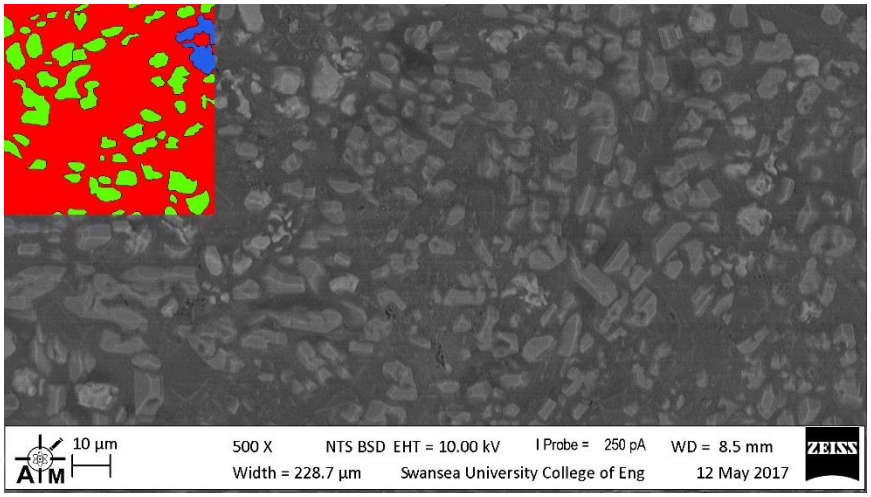
10 µm
500 X NTS BSD EHT = 10.00 kV I Probe = 250 pA WD = 8.5 mm
Width = 228.7 µm Swansea University College of Eng 12 May 2017
ZEISS

(b)

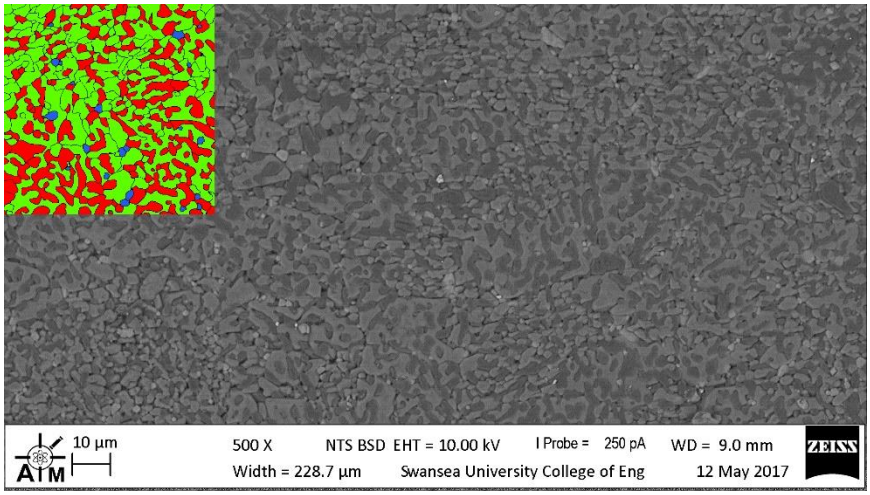
10 µm
500 X NTS BSD EHT = 10.00 kV I Probe = 250 pA WD = 9.0 mm
Width = 228.7 µm Swansea University College of Eng 12 May 2017
ZEISS

(c)

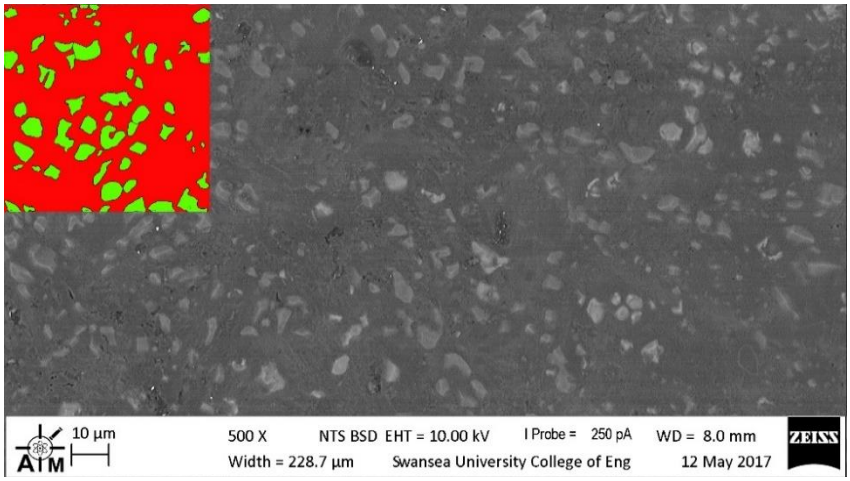

(d)

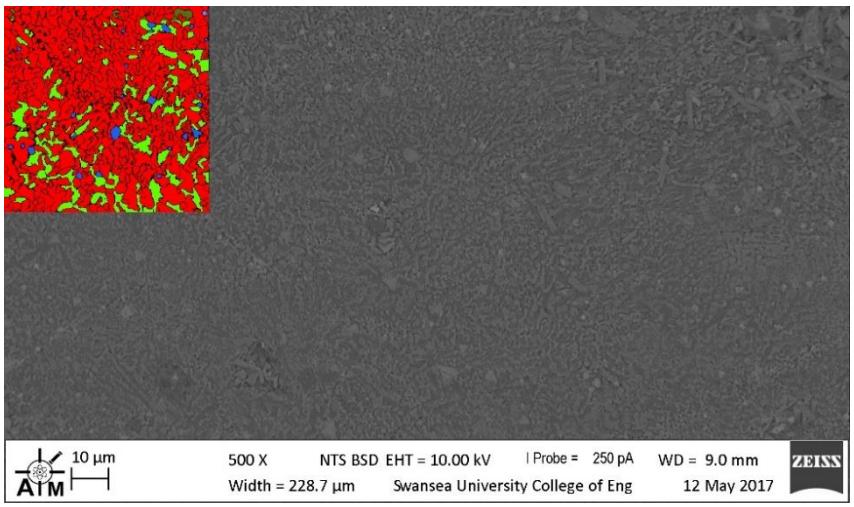

(e)

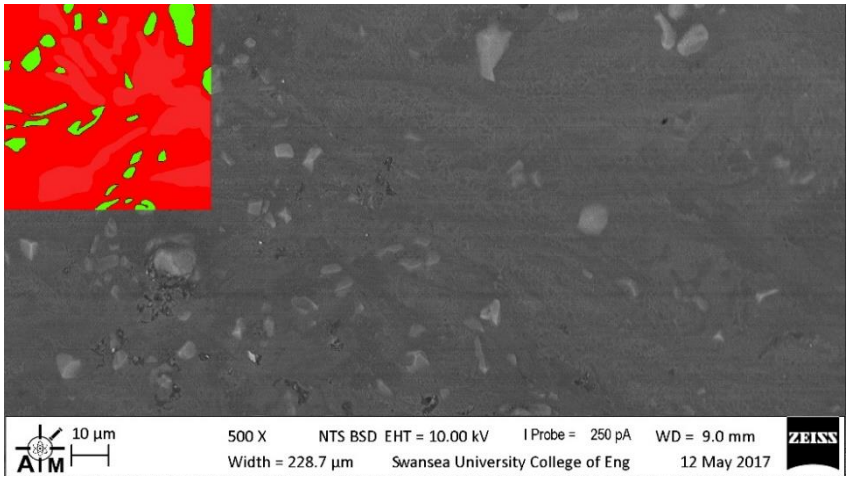

(f)

Figure 4.10 SEM micrograph using BS imaging showing the changes in a ternary salt with (a) 5% KCl (b) 5% LiCl , (c) 10% KCl, (d) 10% LiCl, (e) 20% KCl and (f) 20% LiCl

4.4 Usage of Molten Salts as Conductors

4.4.1 Effect of Conductive Additions

Whilst the electrical conductivity of these solutions is the most important property, it has been difficult to get any reliable readings of conductivity using DC or direct resistance measurements, this is primarily due to the corrosive environment of the salts damaging the multimeter contacts. There is a clear increase in the conductivity of the upper layer when switching from the pure salt to CNT or graphite additions of 1% or more, when separation had occurred. Proportionally this accounts for a factor of 10 increase in conductivity. The tests showed conductivity of between 0.2 and 20S/m for 5wt% KCl salt. The CNT and graphite additions showed conductivity of 58 to 470S/m and 350 to 600S/m respectively rising from 200^{o}C to 350^{o}C in a linear fashion. Testing was done over 200^{o}C due to the high viscosity of the salt with high carbon loadings at lower temperatures, which prevented accurate readings of conductivity.

The light bulb test, outlined in section 2.2, confirmed that there was conductivity within all molten samples, the conductivity through the salt is ionic, whilst the carbon additions provide a more typical electronic conductive pathway. The standards for this are shown in Figure 4.11, with (a) indicating no current flowing and (b) showing the maximum current or voltage effect. The additions can be seen in Figure 4.13 with graphite appearing to be the brightest and most conductive addition. Little or no conduction was seen at

(a) *(b)*

Figure 4.11 Optical images showing a blue LED bulb wired through a basic circuit, (a) has no current passing though whilst (b) has a 4V potential difference.

temperatures where the pure salt would be solid, typically below 150°C. However, large amounts of conductivity were seen within the carbon containing samples at similar temperatures. All carbon containing samples remained conductive at room temperature, these images showed that graphite was the most conducting addition. This agrees with the electrical conductivity readings above that graphite is the most efficient addition, this has been displayed in graphical format in Figure 4.12. As can be seen these conductivities are very low, which is not desirable when acting as electrical contacts, likely due to the salt preventing an effective conductive pathway being formed.

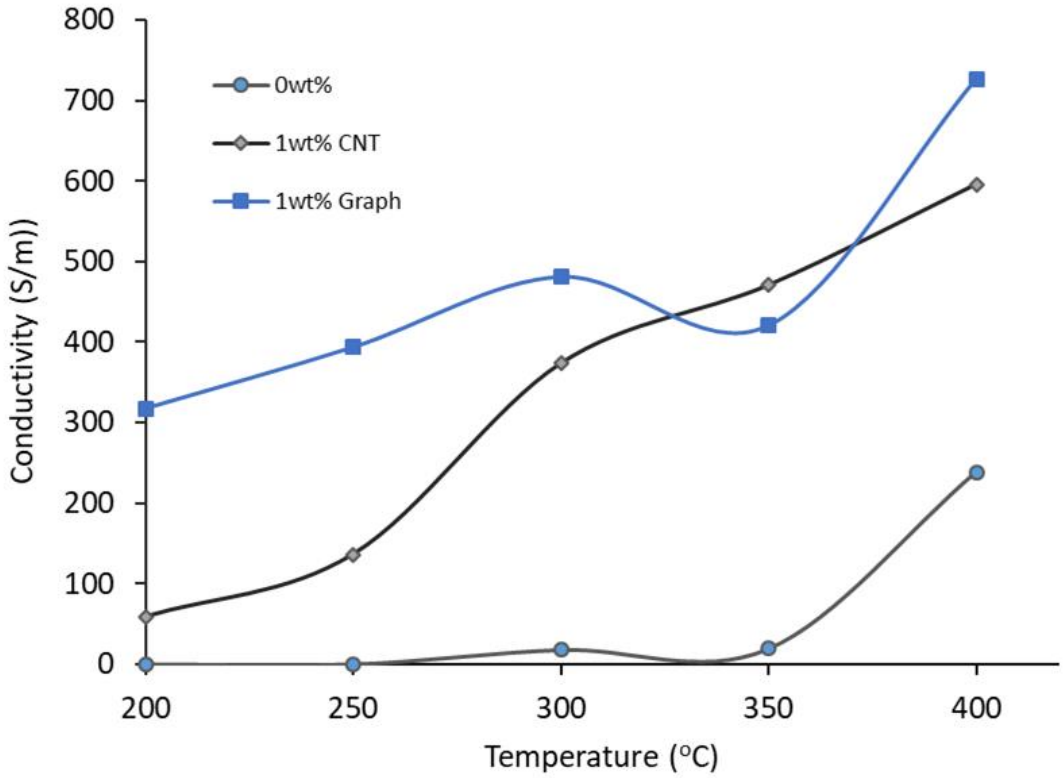

Figure 4.12 Conductivity measurements with varying carbon additions, when heated up from 200°C to 400°C

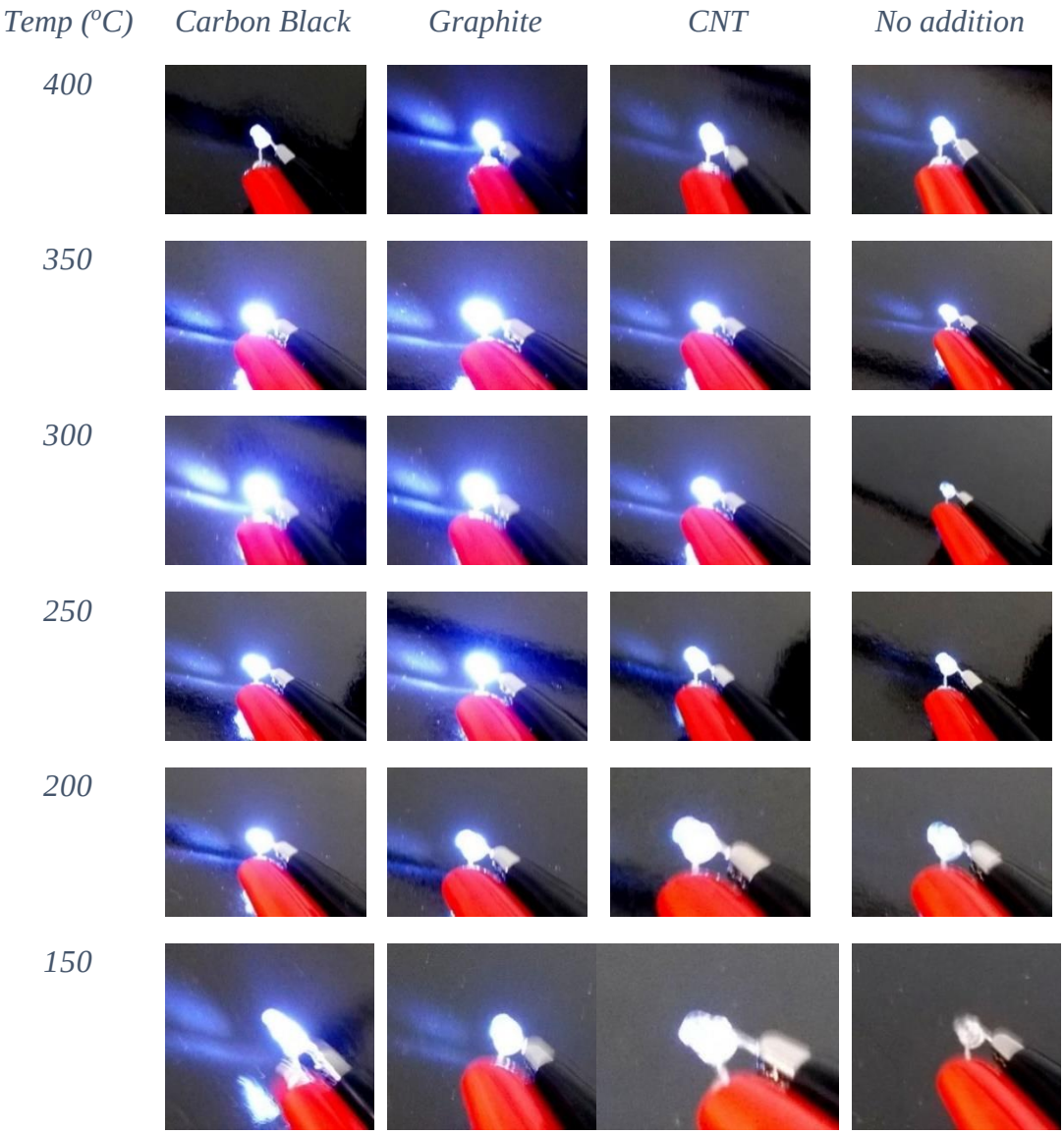

Figure 4.13 Optical images showing a blue LED bulb wired through a basic circuit, utilising the molten salt, with additions, as part of the conductive pathway

4.4.2 Effect of Graphite Additions

At elevated temperatures the carbon rose to the top of the liquid over time. This can be seen in Figure 4.14. Within this figure the lower green tinged segment is the liquid salt and the upper black layer is a mix of carbon and salt. This is the same with all types of carbon trialed.

To minimise separation effects, a critical loading factor was determined by allowing the molten salt to separate with varying fill levels of carbon. A selection of these test samples, once cooled, can be seen in Figure 4.15, with their conversion amounts shown graphically in Figure 4.16. With complete filling there was no white salt visible. This occurs at graphite levels at above 18.5wt%, levels above this would result in no separation during molten phase.

Figure 4.14 0.5 and 1wt% CNT additions to molten salts during heat treatment stage

2wt% *5wt%* *10wt%* *15wt%* *18wt%*

Figure 4.15 Solidified salt with varying amounts of carbon, grey areas contain the carbon, white is the solidified salt

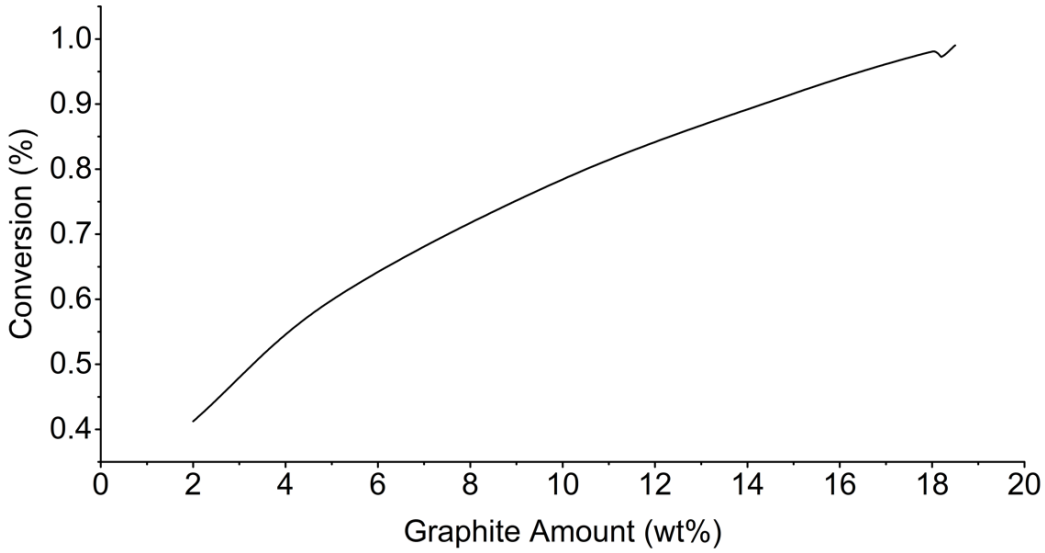

Figure 4.16 Conversion of graphite to salt filling with respect to wt% graphite

4.5 Degradation Effect of Salt Usage

4.5.1 Corrosion of Skutterudites in Salt

If molten salts are to be used in a thermoelectric device, the salt would contact the TEG material, e.g. skutterudites. Therefore, the degradation of such materials in salt solutions were assessed. XRD analysis was undertaken using the GI-XRD variant to determine the change in surface structures of skutterudites after the periods of time within the salt solution at 400^{o}C, in an argon atmosphere. Samples were removed at the periods of 24, 48, 96 and 144 hours, which were then analysed together with two scans on each sample at 3 hours each. The comparison between the 5 samples is shown in Figure 4.17.

This GI-XRD scan can be seen in Figure 4.17 with peaks for $CoSb_3$ and $CoSb_2$ shown. Skutterudites start as entirely $CoSb_3$. Unidentified phases are most likely to be more complex corrosion products. Further study could better match products to these peaks, most notably those at 16 and 27 theta. It can clearly be seen that there is a progressive surface decomposition with the removal of antimony from the skutterudite compound. However, it can still be seen that there is an increase in the amount of the $CoSb_2$ and pure antimony phases present, leaving a mirror-like sheen on the material. The overriding phase is of course the $CoSb_3$ structure of the bulk skutterudite.

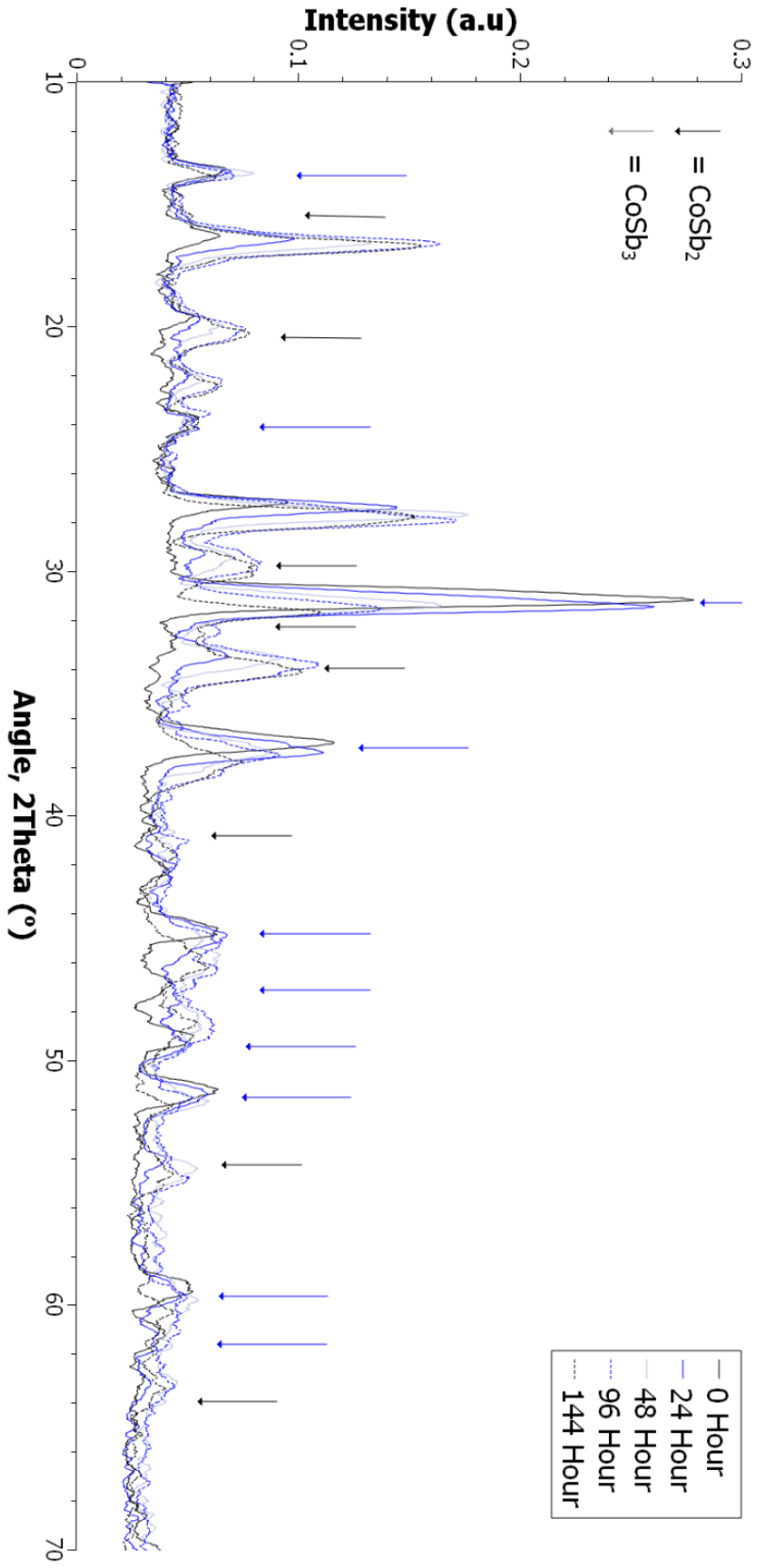

Figure 4.17 GI-XRD trace of the skutterudite material when subjected to molten salts for between 0 and 144 hours

Further surface analysis was undertaken using the SEM combined with EDS to see how the surface had changed over the corrosion times. Examples of this can be seen in Figure 4.18 and Figure 4.19. Interestingly a large number of parallels are seen to that of works on general high temperature corrosion of skutterudites. These were seen within these lower temperature environments implying the same process is occurring with the salts reducing the temperature of the reaction[136].

The two most notable parallels with standard corrosion are the surface depletion of antimony inside the $CoSb_3$ and the deposition of antimony onto the pyrex beakers. While large pores did not seem massively common, EDS analysis revealed a systematic decrease in antimony on the surface. Antimony levels dropped to 60% of the original amount after 144 hours, appearing to be in a parabolic fashion. This increased down to 73% after 24 hours of treatment, after 96 hours this reduced to 61% and reached 60% at 144hrs, implying the surface materials removal was slowing at this time. This loss of antimony would account for the transformation of $CoSb_3$ to $CoSb_2$ as seen clearly in the GI-XRD scans.

The antimony leached from the surface did not visibly deposit onto the side of the container as seen in previous papers[136]. Instead it was deposited onto the surface of the skutterudites as a bright reflective layer. This is seen clearly in Figure 4.18 and Figure 4.19, with SEM and EDS micrographs of these deposits shown on both the 24 and 96 hour samples. It is possible that these would deposit onto the sides of any container used in close proximity to the skutterudites at working temperature and provide both thermally and electrically conductive paths. Whilst these deposited layers are considerable in the 24 and 96-hour specimens, they are seen in smaller amounts on the 48 and 144-hour samples. It is likely the any missing antimony has been deposited on other surfaces during the process including onto the sides of the beaker.

These results show that the molten salts appear to significantly reduce the temperature at which the corrosion reactions happen in comparison to those within argon or inert atmospheres, as studied by Leszczynski et al[136]. The pores created by the removal of antimony, along with the evidence of deposition of antimony were seen at 700^{o}C, while the decomposition of $CoSb_3$ was seen to occur at 575^{o}C[136]. This could be because the

salts, as well as providing an aggressive environment, may act as impurities like iron additions which lower the starting temperature of oxidation.

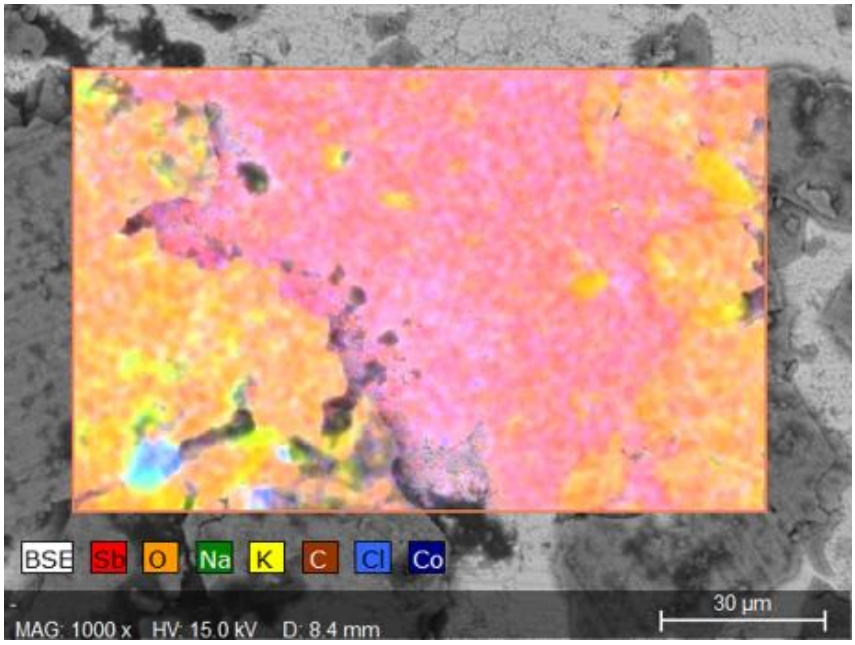

Figure 4.18 SEM-EDS map of the corroded skutterudite surface showing the removal of Sb from the surface

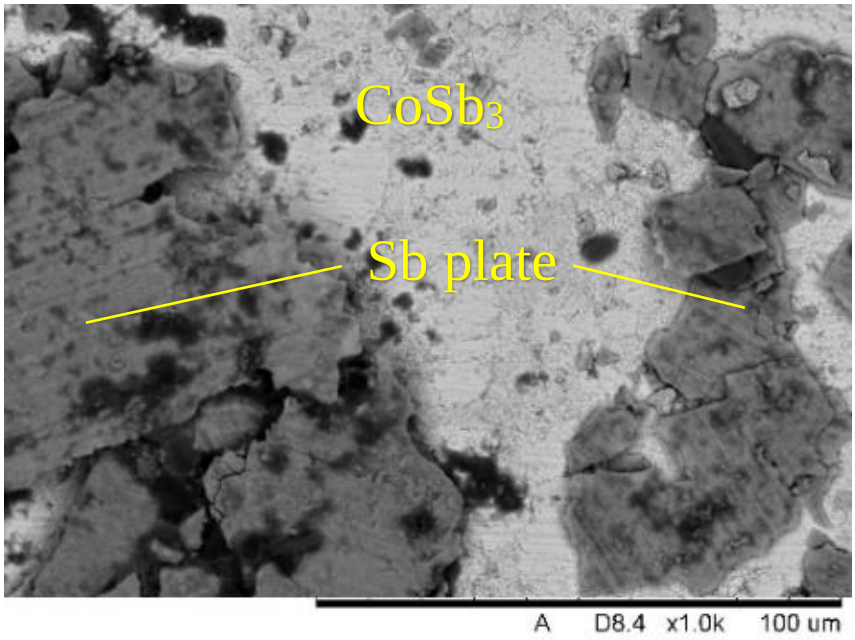

Figure 4.19 SEM micrograph showing the replating of Sb on the skutterudite surface

4.5.2 Fatigue of Silver Contacts

The cycling of the molten salts with skutterudites was tested during this work. Skutterudites were immersed in salt with thermal cycling up to 400°C and down to 50°C, resulting in a large amount of expansion and contraction of the salts. During this testing while liquid, papers show that the density of the base ternary salt increases from 1986.558 to 2166.758 kg/m^3, with a drop-in temperature from 400°C to 150°C. It is safe to presume that the density change will, in a similar fashion, results in a large contraction effect[73]. This contraction can cause cracking of the Pyrex beakers used in production and will apply similar forces to any material it is in contact with. Slow cooling can reduce the damage to equipment, which may not be possible within device usage. The elements provided for these experiments contained silver contacts for soldering, whilst these are not needed for this set-up they provide a useful example of the fatigue effects generated when materials are immersed within the molten salts.

Skutterudites were heated within the salts between 50 and 400°C for a total of 8 heating and cooling cycles. After the 4th cycle fatigue resulted in a 0.2%wt loss over the 24-hour immersion period, however the most notable damage was on the silver contacts. This was further increased with another 4 cycles resulting in a 0.94%wt loss, most likely due to the silver contacts being degraded further. As seen in Figure 4.20, there is some removal of the silver layer as well as considerable cracking. This causes issues within devices due to flakes of silver, leading to potential conduction issues or short circuiting. This also indicates that the salts put large amounts of pressure on the elements which will cause more fatigue damage than having metal to metal contacts. However, this may not be a serious factor if the materials are kept at temperature for long periods of time without

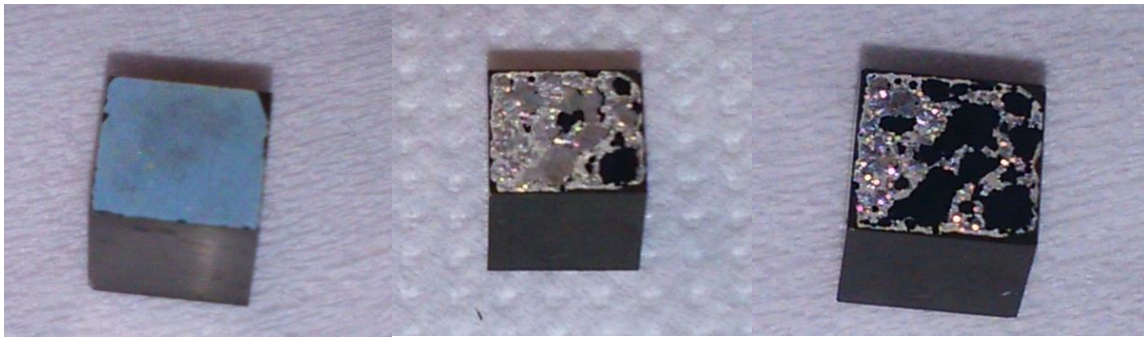

(a) *(b)* *(c)*

Figure 4.20 Images showing the state of the silver contacts degraded from the Skutterudites (a) before cycling, (b) after 4 cycles and (c) after 8 cycles

cycling to solid regularly or at speed. Constant high temperatures would not be viable for thermoelectrics currently suffering from fatigue. Whilst silver contacts would not be necessarily needed for molten salt devices they act as an effective demonstration of the forces applied onto the materials when thermal cycling is undertaken.

4.6 Conclusion

In comparison to the standard ternary HITEC salts, the additions of metal chlorides showed an overall improvement in their long-term stability behaviour. Additions of KCl and LiCl are shown to not raise the eutectic melting point of the salts, ensuring no detrimental effects on the overall performance. Further to this the addition of 5wt% LiCl allowed partial melting prior to the 140^{o}C eutectic point, increasing the operating range of the material. This salt modification makes it ideal as a next generation material for solar-thermal generation and thermal storage applications.

Analysis indicates that a new phase was formed with the addition of LiCl, which at room temperature allows more rapid melting. Small additions of LiCl reduce the weight loss over long time periods from 61% to 25% in comparison to standard ternary salts. Given $LiNO_3$ additions did not result in the stability increase seen with LiCl, it can be deduced that additional nitrates do not improve stability. Further to this it has been shown that Cl is the initial stabilising agent, whilst Li allowed a phase with a lower melting temperature to be formed. Overall, small LiCl additions can potentially allow the standard HITEC salt to be molten from 100^{o}C, then reach over 630^{o}C in the short term. Small LiCl additions can also allow longer term operating temperatures above 550^{o}C, with no signs of oxidation. A potential issue with increasing additions of chlorides over 5wt%, is that they allow other instability effects to occur. This provides a potential working range improvement of over 100^{o}C in comparison to the standard HITEC salt.

With regards to materials conductivity, salts with 5wt%KCl additions conduct electricity as desired. The addition of KCl causes higher temperature stability compared to other options, with carbon additions. The molten salt environment at 400^{o}C is shown to cause corrosion of the $CoSb_3$ samples. This happens primarily by the leaching of antimony from the structure, causing the transformation of $CoSb_3$ to $CoSb_2$. The removed antimony has been shown to deposit onto the surface again as a layer coating on the

skutterudite or onto the surrounding area, which is less than desirable. This corrosion is also shown to occur at lower temperatures than in an inert atmosphere. These corrosion products reduce the efficiency of the thermoelectric material and may cause electrical and thermal conduction around the elements of a functioning device. The addition of carbon to the system may cause this corrosion rate to increase from the introduction of a galvanic couple, which is a corrosion cell formed when two different conductive materials (in this case the element and the carbon) are connected with an electrolyte (the salt) resulting in corrosion of the active metal (the element). The physical properties of the salt also result in large thermal expansion and contraction putting strain on the silver contacts and skutterudites, possibly causing cracking of the contacts.

Whilst molten, all combinations tested conducted electricity to varying degrees. There was a notable increase in conductivity with the addition of any form of carbon to the material. Interestingly from the tests undertaken it appears that a 1wt% graphite addition, performs better than a 1wt% CNT addition. This is most desirable and could be put down to structural transformation in the carbon during the heat treatment step resulting in exfoliation of the graphite sheets, and agglomeration of the CNTs. Pure salt is seen to decompose with a direct current passing through it, however this is less noticeable in the carbon rich layer.

Overall, from this current work, the best proposed salt composition for the conductive applications has been found to be the standard salt with 5wt% KCl and a 18wt% Graphite addition. This has several advantages over the usage of CNTs in the production and deconstruction phases as CNTs present a high health risk. Corrosion and fatigue have both been shown to affect the skutterudites while immersed in the salts reducing their use as a conductive contact. The salts of the above composition have the potential to be effective self-healing contacts for thermoelectric devices if the issues of separation, convection and corrosion can be minimized.

Chapter 5 Development of Conductive Polymer Electrical Contacts

5.1 Introduction

This chapter focuses on the development of conductive polymers in order to directly replace the soldered contacts of traditional thermoelectric devices, represented by the area highlighted in Figure 5.1. By maintaining the traditional design a suitably conductive and stable polymer can serve as the electrical contacts, reducing some of the material cost and allowing fully automated production of thermoelectric devices[137]. As outlined in the literature review current intrinsically conductive polymers are typically costly and are not stable at high temperatures. As such conductive additions have been investigated with the SILRES polymer, a resin with high temperature stability.

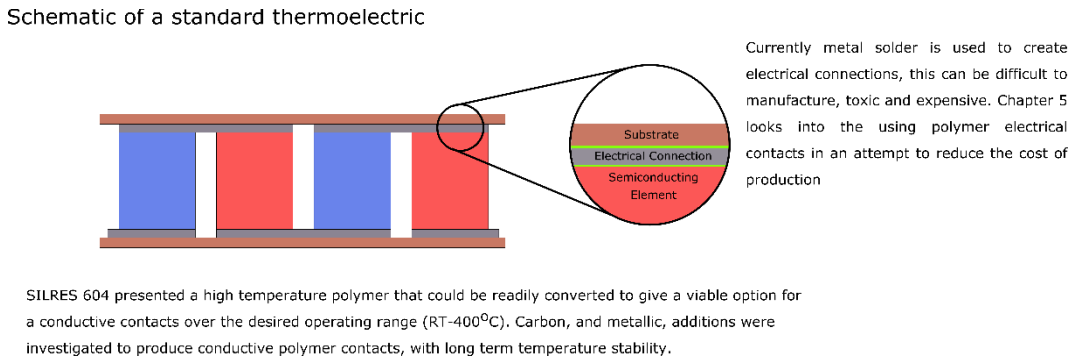

Figure 5.1 Infographic image of a traditional thermoelectric device, with focus on the polymer electrical contacts

5.2 Production of Conducting SILRES Coatings

5.2.1 Powder Coat to Liquid Ink

The polysiloxane resins under the brand name SILRES are advertised as powder coatings with high-temperature performance. Whilst powder coatings have their advantages, for the application of thermoelectric connectors a printable liquid coating was needed. For the higher temperature applications, the SILRES 604 variant was chosen. SILRES 604 has a 99% silicone content and 4.5-6% OH group content. When mixed with additions of ferrous oxide the powder coat can be used to resist temperatures over 400°C.

SILRES 604 dissolves readily in acetone, IPA and ethanol. As such, most of this work was undertaken with a liquid mix of SILRES 604 in IPA to provide an ideal base ink.

Further additions of terpineol, carbon and metallic powders were used to develop the desired performance as a polymer ink for use as an electrical contact. The following section outlines the development process of this ink including a variety of additions and testing.

5.2.2 Carbon Addition Percolation Threshold

A wide range of additives were considered for providing the conductive pathway within a SILRES mixture. Pure silver and gold particles were determined to be too costly to reach the required percolation threshold. Initial studies into metal powders of copper and zinc mixed with the SILRES in IPA showed little or no mixing. These particles split off from the SILRES collecting at the base of every casting, likely due to the density of the particles and lack of complete mixing. The only addition initially tested which effectively provided a conductive pathway for the SILRES was carbon in the form of graphite. For initial tests 20μm graphite was used, with overall the resistivity improved in a logarithmic fashion up to 100wt% carbon loading. Regardless of graphite type this pattern was consistent, however overall values did change.

As seen below in Figure 5.2 resistance drops off considerably with increasing additions of graphite. Once a 1:1 weight ratio was reached there is little improvement from additional graphite being added as the resistivity does not decrease much more.

It has been shown that a 1:1 SILRES to graphite ratio allows the resistivity reaches close to that of other basic carbon inks ($6.3x10^{-5}\Omega m$)[138]. It is possible to add additional graphite to SILRES, however additional solvent must be added to allow complete mixing which in turn results in shrinkage cracking. In addition, adding high amounts of carbon leads to an increasingly brittle coating which flakes off as the SILRES cannot effectively coat and bond the carbon together.

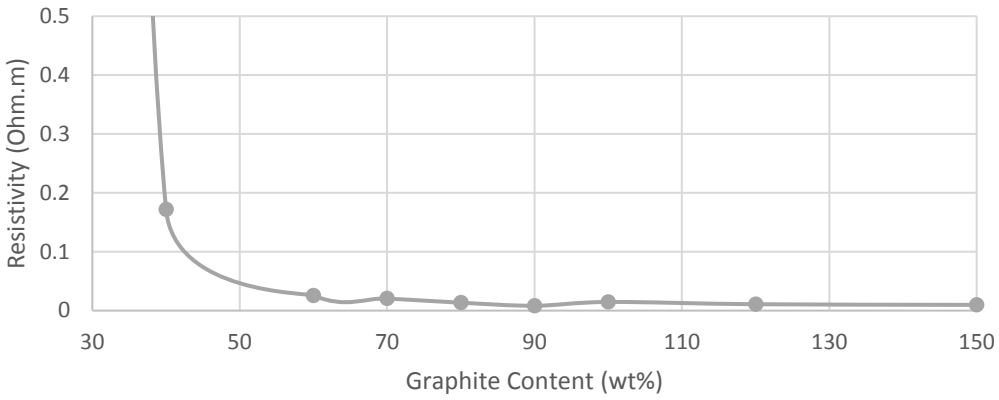

Figure 5.2 Effect on the resistivity of SILRES 604 inks with graphite additions. The data continues to higher resistivities with lower graphite contents (not shown)

5.2.3 Cracking Within Cast Layers

SILRES inks were tested with a range of carbon loadings in order to assess the optimum loading needed to achieve full percolation. Cracking has been seen to occur with all the higher graphite additions and further investigation was undertaken to determine if this cracking was due to shrinkage caused by solvent evaporation.

The following images shown in Figure 5.3 cover a range of carbon containing samples from 30 to 120wt% graphite. White patches in the 30-50wt% samples are due to charging in the SEM as the graphite fails to provide an adequate conductive pathway. It was determined that at least 50wt% carbon is needed to provide a clear conduction. Upon reaching 100wt% addition the carbon forms an almost complete layer with few non-conducting areas, which was determined to be the maximum ideal level needed. Additions above this resulted in little conductive improvement but an increase in visible cracking. A prime example of this can be seen in the 100% image.

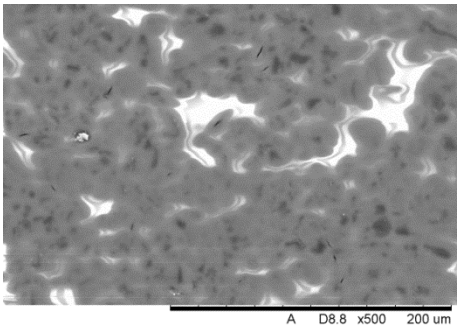

(a) 30wt% graphite addition

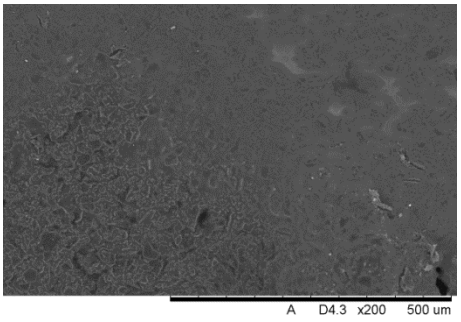

(b) 40wt% graphite addition

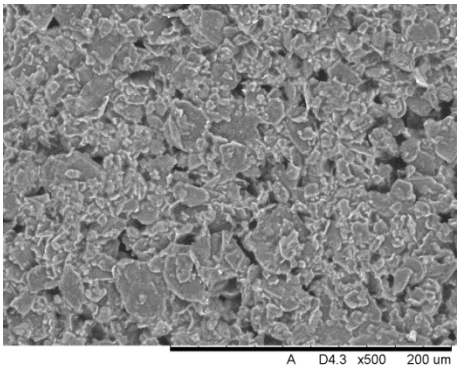

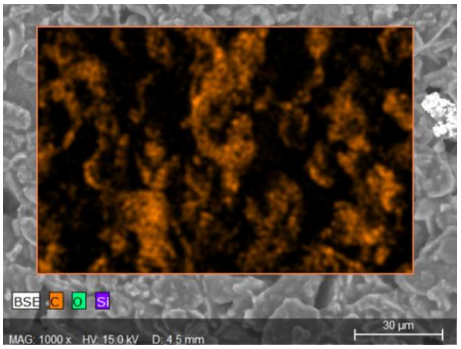

(c) 60wt% graphite addition

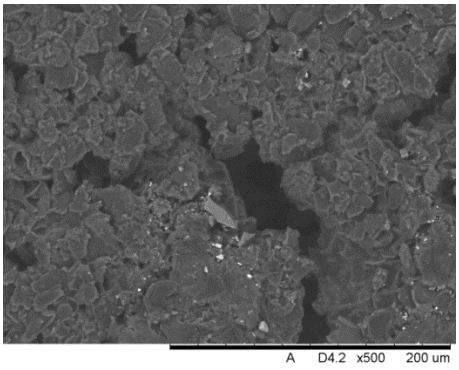

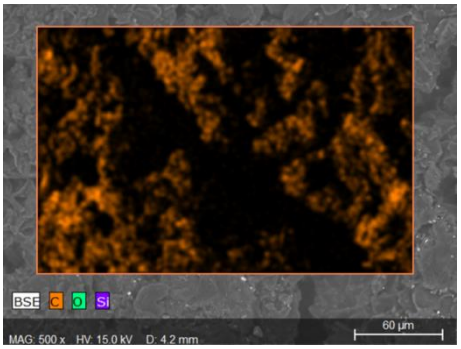

(d) 70wt% graphite addition

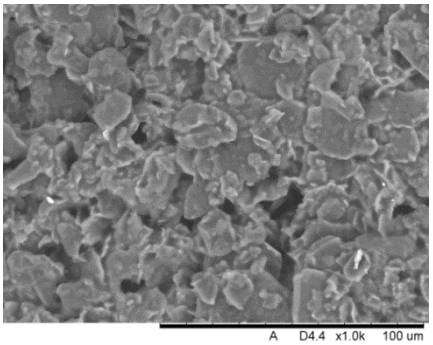

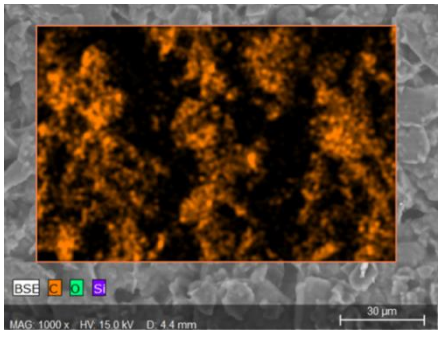

(e) 80wt% graphite addition

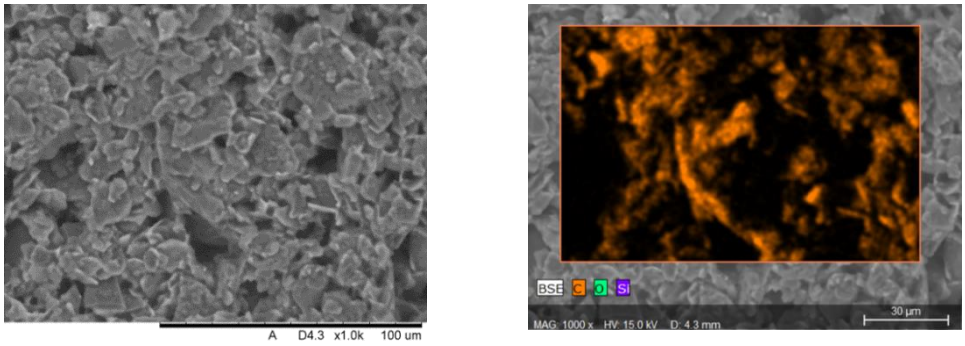

(f) 90wt% graphite addition

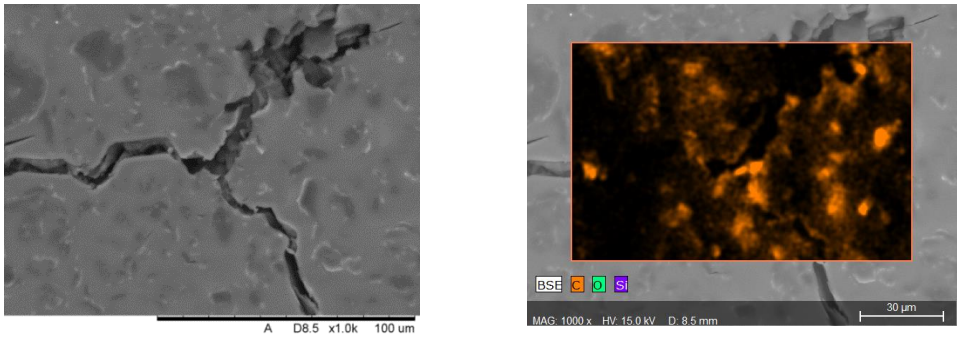

(g) 100wt% graphite addition

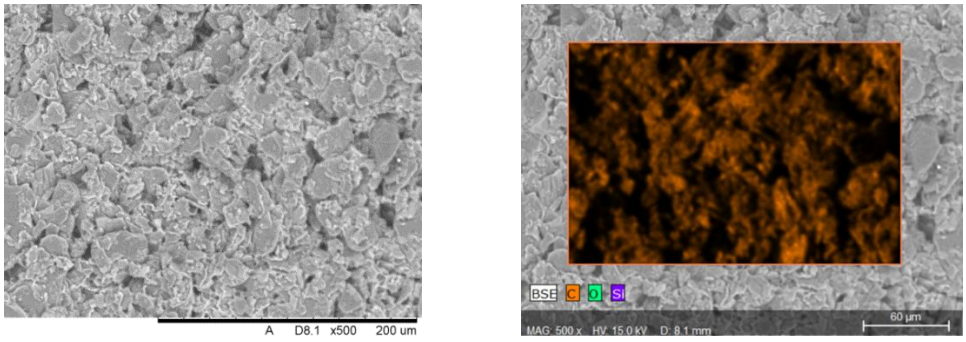

(h) 120wt% graphite addition

Figure 5.3 SEM micrographs of SILRES-graphite mixtures with varying additions of carbon

To analyse the mixing and ensure the dispersal of the carbon long dwell EDS scans were undertaken on the polished surface of the SFG15-SILRES mixture this is shown in Figure 5.4. The carbon (red), oxygen (green) and silicon (yellow) are not evenly distributed within the image. Some of this change was due to surface roughness as shown on the initial image, however carbon is seen at a higher intensity within areas of low silicon and oxygen, most notably the lower right of the images. Even with this lack of complete uniformity there is a continuous network of carbon, allowing the higher conductivity and

minimising charging. The liquid SILRES is likely to provide a complete coating around the carbon flakes, with the flakes able to make direct contact or be close enough to allow tunnelling.

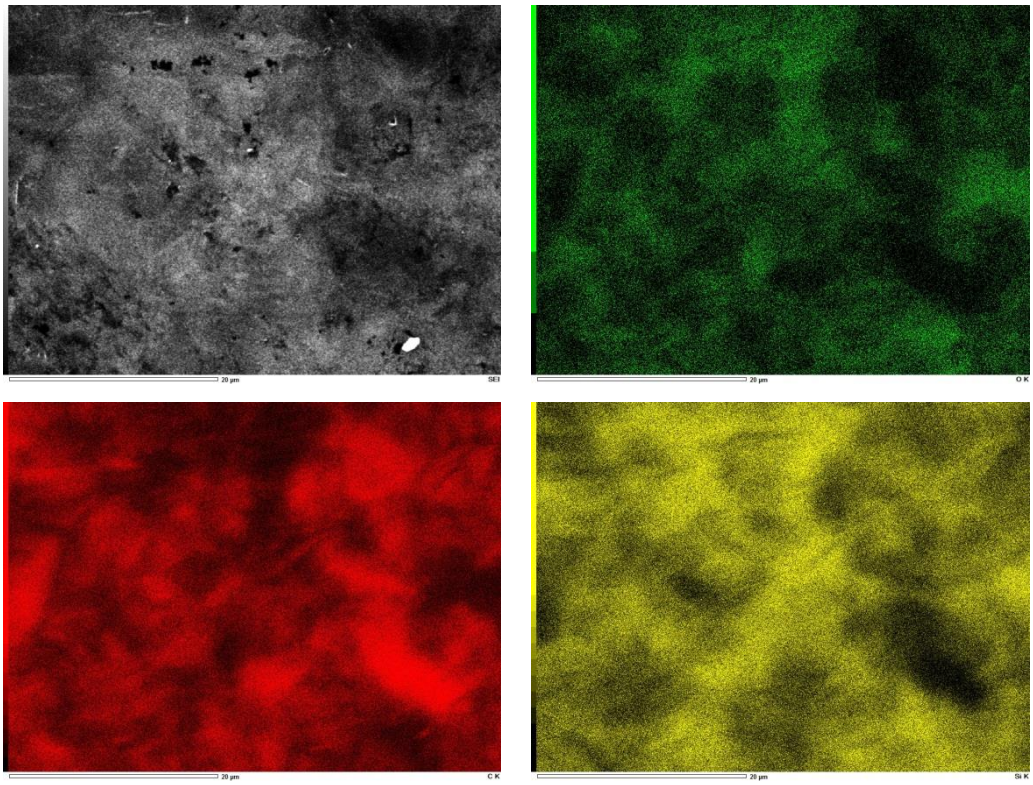

Figure 5.4 SEM-EDS image of SILRES 604-carbon coating, carbon is given in red, oxygen in green and silicon in yellow.

5.2.4 Carbon Types, Mixing and Treatment

After initial works to determine the optimum graphite loading, several types of graphite were tested, including carbon black (KS6), 20µm graphite, 2µm graphite and SFG15. Untreated samples were tested after a quick mixing, and Figure 5.5 shows how these perform when bar cast. The samples were polished to remove any loosely bound layers from the top of the cast. This was done with every sample, as unpolished samples occasionally contain a loosely bound layer of graphite after heating in the furnace, which significantly reduces the conductivity. This does not present any issue when they are directly contacting another material.

There were initially 3 mixing treatments tested: ultrasonic water bath treatment (US), vigorous shaking (shake) and gentle rotation mixing (Rot). The US treatment involved the liquid samples being placed in an ultrasonic bath for a period before casting. Shaking

involved putting the samples into a high-speed shaker, and the rotation treatments used a vial or tube roller, providing a gentler mixing.

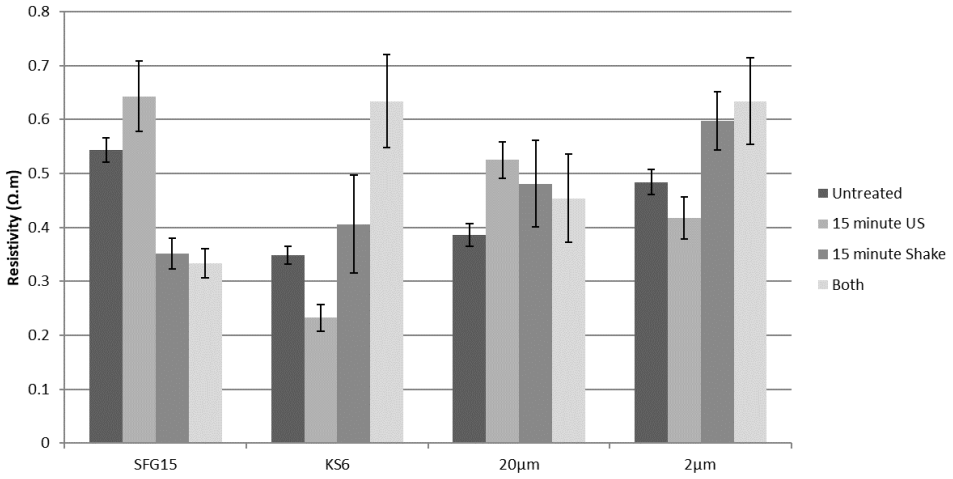

Figure 5.5 Chart showing the effect of treatments on the SILRES coating, with errors of ±1SD shown

It can be seen in Figure 5.6 that, whilst the US and shake mixing resulted in some improvement, continuing these for longer time scales results in a resistivity decrease. This is possibly due to the rapid breakup of the graphite sheets increasing the materials disorder. A combination of the two techniques at optimum times did not give any improvement, supporting the decomposition theory. Multiple graphite types were treated, with SFG15 presenting the best overall effect, as such this was chosen to be the primary graphite addition.

The most promising longer-term treatment was using a gentle rotation mixer on its own. A 30-minute rotation treatment showed a resistivity value of 0.0016Ωm, with a 60-minutes treatment giving a value of 0.0008Ωm. The US and shake treatments exhibited an increase in resistivity over long time periods which is undesirable for a large-scale process. Rotation treatments were tested up to 20 hours, the results can be seen in Figure 5.7. With this it was shown that 3 hours rotation gives the most promising improvement, with any longer treatment giving little or no change in the electrical properties. This is beneficial as it allows a large vat to be kept continuously mixing for as long as needed without any property degradation, making it a very stable treatment process. The maximum performance achieved so far with the SILRES graphite mix was a resistivity

of 0.00066Ωm which equates to around $1.52x10^3$S/m conductivity. This is within the appropriate region for amorphous carbon or graphite randomly dispersed[139]. Graphite has a conductivity of $2x10^5$ S/m in the basal plane but $3x10^2$ S/m perpendicular to the plane, so the value achieved was comfortably within this region.

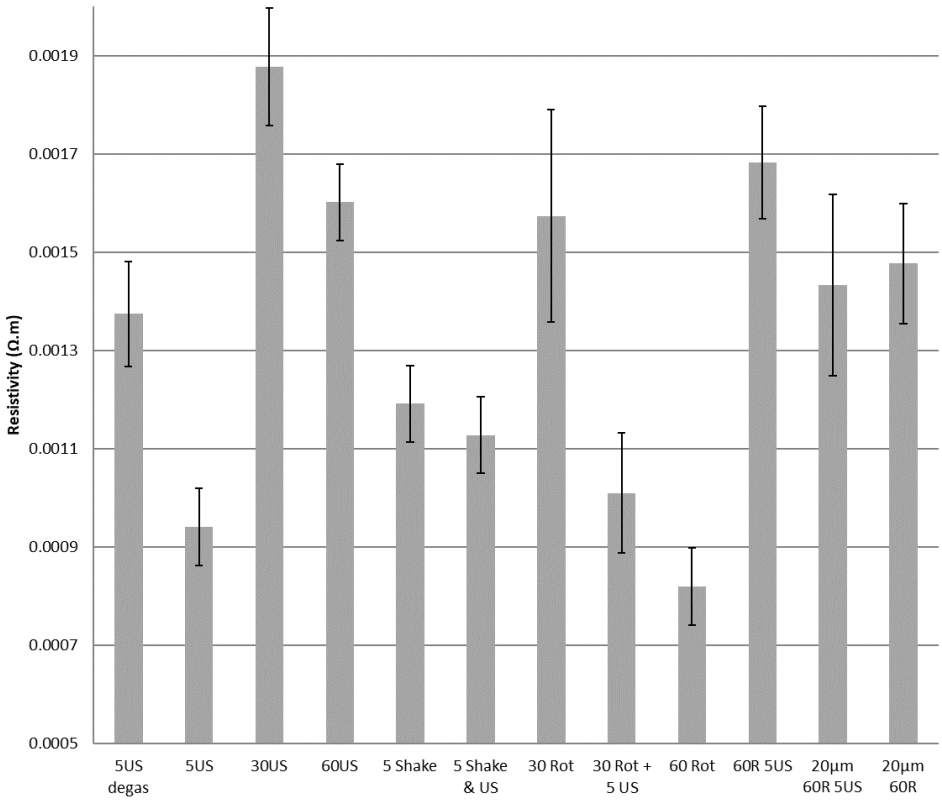

Figure 5.6 Chart showing the effect of treatment types on the resistivity of the coating, with errors of ±1SD shown

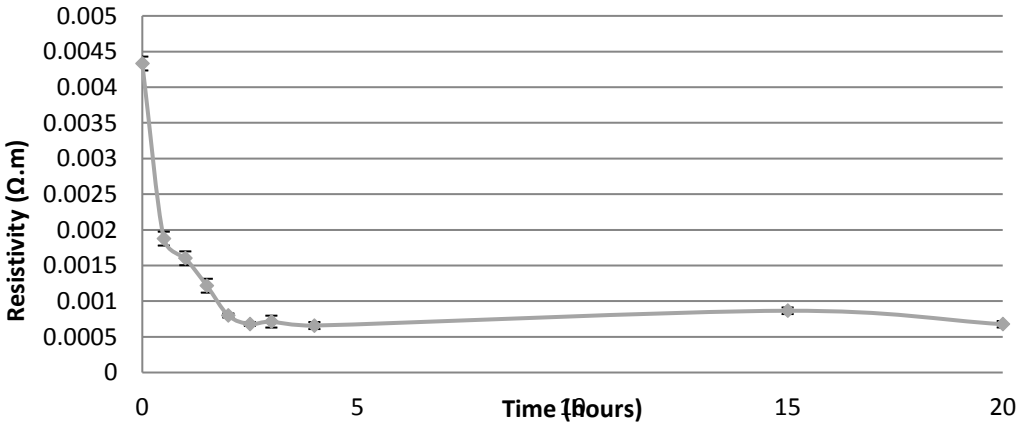

Figure 5.7 Graph showing the effect of slow rotation duration on the resistivity of the SILRES-graphite coating, with errors of ±1SD shown

5.3 Metallic Additions

5.3.1 Effect of Metallic Powders upon Conduction

Having reached a limit of conductivity with pure carbon additions, the focus of the work then moved onto several different metal powders. Metallic additions were added to improve the conductive and thermal properties of the polymer. Zinc, magnesium, and copper powders were tested with weight additions up to 100wt%. It can be seen in Figure 5.8 that all additions resulted in a resistivity increase of the polymer. The addition of magnesium powder rapidly increased the resistivity making the coating effectively useless. Copper powder also resulted in an increase is resistivity, however this was much lower than that of magnesium. Zinc additions were the only metal tested to show any real improvement, for small concentrations at least. The main reason for the increase in resistivity is the suspected reaction with the oxides in the SILRES to produce metal oxides, which will increase stability but in turn significantly increase resistivity. The effect of the additions on high temperature stability will be discussed next, followed by the arrangement of these metallic additions within the polymer casts.

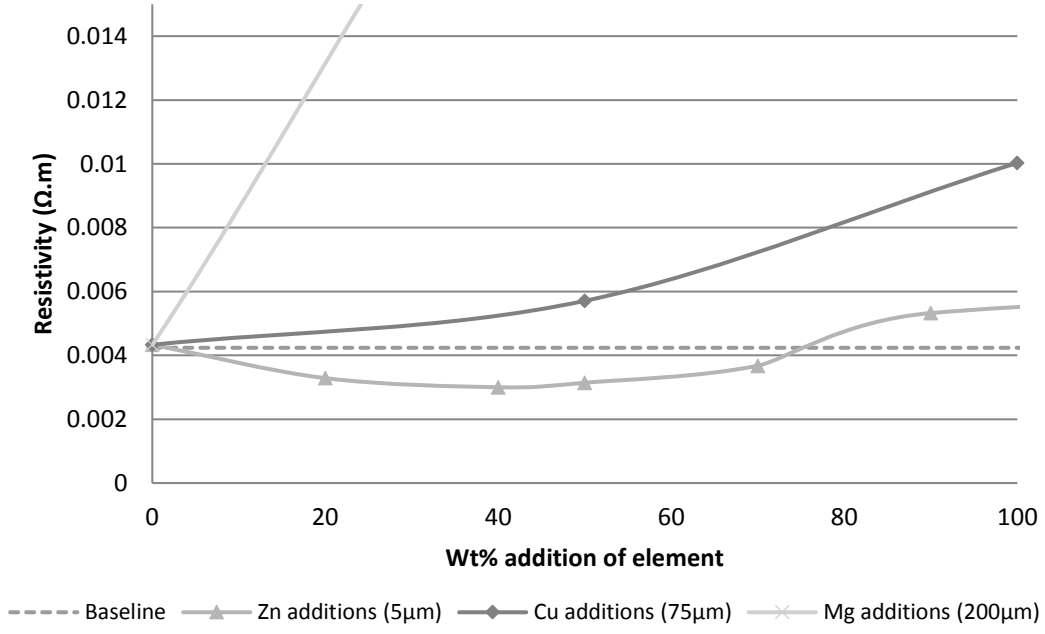

Figure 5.8 Effect of metal additions on the resistivity of SILRES-100wt% graphite ink, magnesium rapidly rises off scale.

5.3.2 Stabilisation Effect of Carbon and Metallic Additions

The SILRES 604 resin on its own possesses limited high temperature stability, decomposing at around 250^{o}C. This is not suitable for the mid-range TEGs whose ideal operating temperatures are up to 400^{o}C. As such investigations were required into a range of additions to increase the thermal stability. This began by looking at how carbon additions would affect the stability, and then moving onto a range of metallic additions. Thermal stability was tested using the TGA technique. Varying heating rates where trialled to see their effect on the time scale of the decomposition event, with higher heating rates resulting in the decomposition onset temperature being offset. This gives the link between time and temperature.

As discussed previously carbon additions were added to SILRES to increase their conductivity. Figure 5.9 shows the weight loss with increasing temperature, for varying amounts of carbon additions. The 0% line shows the pure SILRES which undergoes weight loss at around 250^{o}C. The additions of carbon result in this temperature dropping to 230^{o}C in all cases and causes an initial dog-leg that is not observed in the 0% curve. This reduction is likely due to the carbon reacting with the base hydroxyl groups reducing the initial stability and allowing some burn-off. This reaction, and possibly the transformation of carbon to CO/CO_2 may aid the polymer decomposition[140]. Additional carbon within the structure is likely to allow the production of formaldehyde and Benzene rings during decomposition, as indicated within literature[141,81]. It is worth noting that the SILRES coating has its final stability initially reduced with carbon additions however the critical drop-off point is increased. This is most likely to be due to the additional weight of carbon meaning there is less polymer to degrade for the relative weight.

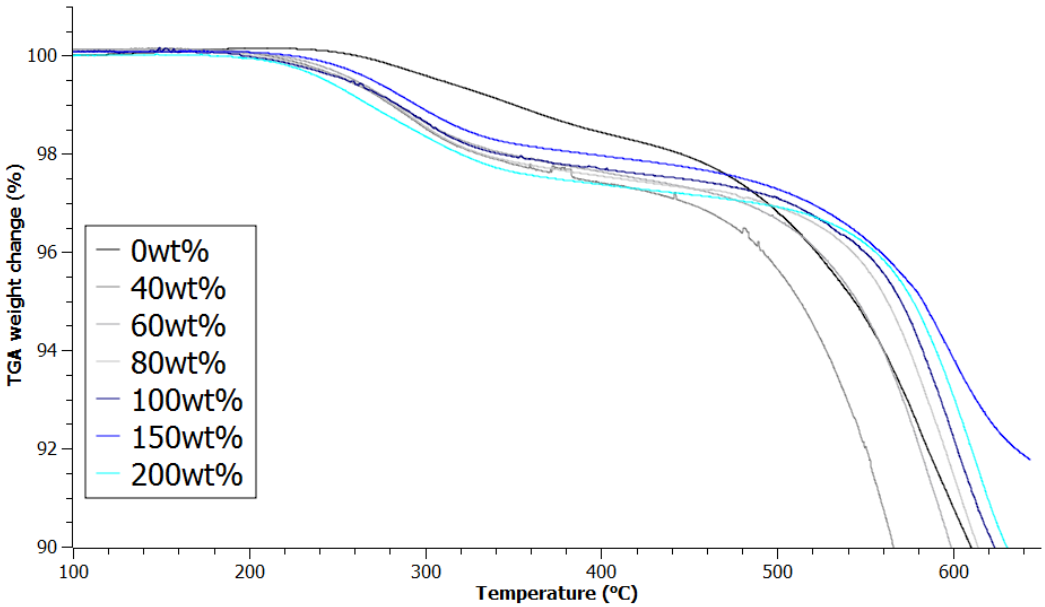

Figure 5.9 TGA traces showing the decomposition of SILRES coating with graphite additions

5.3.3 Stabilising Additions

Given this material is expected to operate up to 400°C stability improvements were required. This was attempted by considering additions previously mentioned in literature[108,109,142–144]. Of these, 3 additions were trialled for thermal stability and conductivity effects. These were black iron oxide, aluminium oxide and zinc dust. Samples were added initially at a 50wt% to the SILRES mixture and heated at 10°C/minute up to 700°C. The results are shown in Figure 5.10.

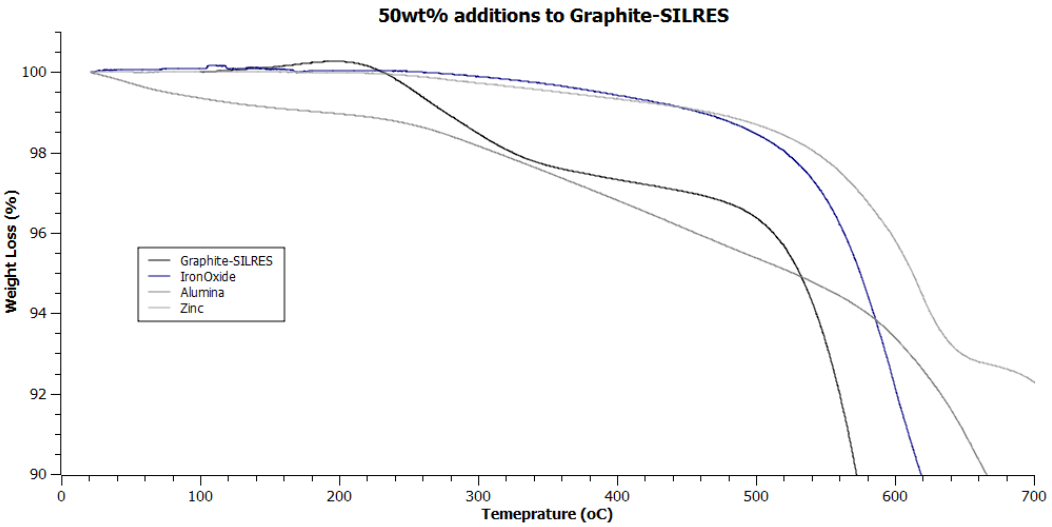

Figure 5.10 TGA trace of the stabilisation effect of metal-based additions

It is shown that Al_2O_3 has no positive effect on the stability, most likely due to lack of reaction with the substrate, as it is already a stable oxide. Additions of zinc and Fe_3O_4 both provide an increase in temperature stability; however earlier works showed the negative effects of metallic additions on conductivity. Both zinc and black Fe_3O_4 have an additional oxidation state, allowing them to combine with any loosely bound O. In the case of zinc this is a simple zinc + oxygen = ZnO reaction. Black iron oxide, Fe_3O_4, contains two ionic states (Fe^{2+} and Fe^{3+}, resulting in a $FeO.Fe_2O_3$ structure). This has three possible transformation states: rapid heating in air can produce α-Fe_2O_3, hematite ($2Fe_3O_4 + ½O_2 = 3[\alpha\text{-}Fe_2O_3]$), this process is called calcining. Slower, traditionally more controlled heating can produce λ-Fe_2O_3, maghemite ($2Fe_3O_4 + ½O_2 = 3[\lambda\text{-}Fe_2O_3]$). The final option is a reduction reaction, usually seen in blast furnaces (as such unlikely to be present here) where Fe_3O_4 would be split into iron and CO_2. The first two oxidation reactions are the most likely.

Additions of Fe_3O_4 massively increased the resistivity of the coating, as such further tests were undertaken with a range of zinc additions only, as seen in Figure 5.11. All samples contained a base 100wt% SFG15 graphite addition and initial tests showed a rapid increase in the stability of the material in comparison to the standard SFG15 trace. This indicates that a small amount of zinc can be dispersed within the material acting as a reactive stabiliser. Tests between the values of 0 and 50wt% zinc were undertaken to look at the relationship between stability and the conductivity of the material to produce an optimum solution.

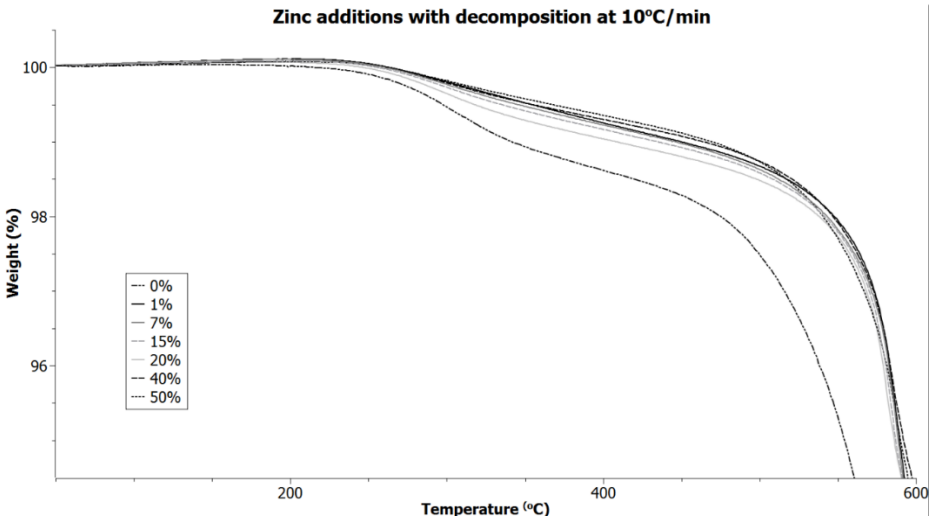

Figure 5.11 TGA trace of the zinc additions on the SILRES-graphite

When zinc is added to the mix it evidently takes priority over carbon when reaction with loose oxygen radicals and as such provides a stable addition, however with the negative effect on conductivity it was important to find an optimum mixture. 99wt% loss and resistivity were compared against temperature, as seen in Figure 5.12. An initial stability requirement of 1wt% loss through degradation was chosen for these tests allowing a direct comparison to be made and temperature effects to be determined. Pure SILRES with SFG15 underwent a 1% weight loss at around 280°C, whereas 1wt% addition of zinc brought this up to almost 400°C. This results in an 8%+ increase in resistivity. After this the stability increases at a lower rate while resistivity increases in a more linear fashion. As such depending on the stability needed conductivity can be tailored as required. 1% weight loss is used here as an indication of full decomposition commencing, any lower weight loss would be subject to large measurement errors. Two weight loss curves are shown in Figure 5.12, below, which relate to tests with different sample batches run on a TGA (99% weight) and a more modern STA (99% weight (2)) respectively. Whilst values are seen to vary the pattern is extremely similar, indicating the effects are reliable, even if the techniques vary.

Between the 1 and 3wt% zinc additions the stabilisation effect becomes less prevalent. A slightly slower increase in resistivity is observed for the same additions, however this continues to increase at the more linear rate with zinc additions. With 1wt% zinc addition a stability increase of 190°C was seen, which equates to a 70% increase in maximum temperature. However, this also results in a resistivity increase of around 13%, bringing

resistivity up to 0.0028Ωm. Whilst an increase in resistivity is not ideal, the improved stability allows the device to function at higher temperatures for much longer. To ensure no localised depletion of zinc occurs an addition of 3-5wt% zinc was chosen to ensure a stable polymer.

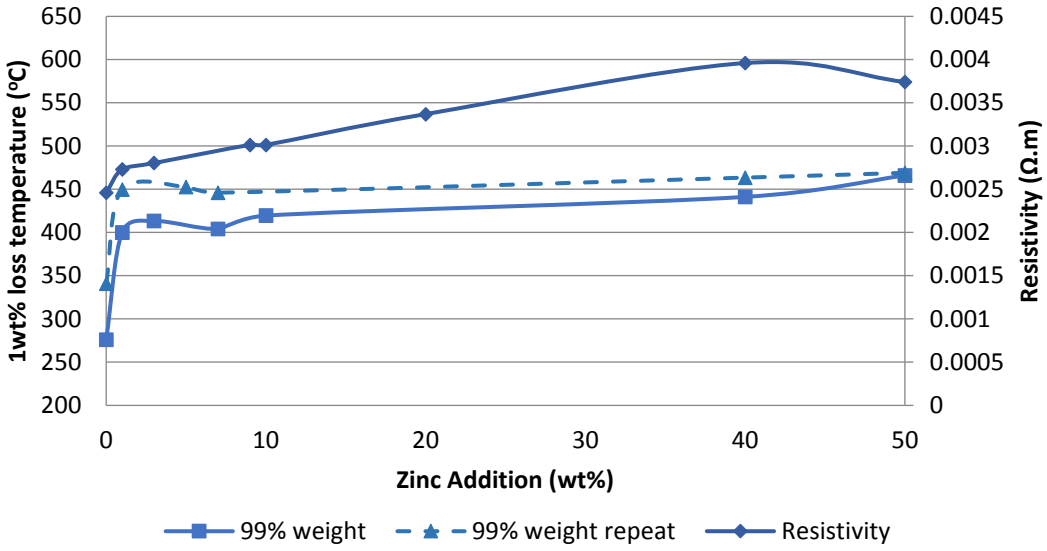

Figure 5.12 Comparison between the stability effect and resistivity of Zn containing samples

5.3.4 Long Term Stability of Zinc Additions

To test long term stability, samples containing the optimum compositions of 1g SILRES, 1g SFG15 and 0.03g zinc were tested by raising the temperature rapidly and holding at the isotherm. This can be seen in Figure 5.13. According to the information provided by Wacker, pure SILRES 604 is capable of long term stability up to 250ºC and short-term stability up to around 300ºC. Tests undertaken, not shown here, agreed with literature information[108,109,145].

For a small amount of zinc addition, it can be seen that the 200ºC and 300ºC curves show less than 1% loss on their long-term dwell, which follows a logarithmic growth, levelling out for 200ºC at 0.5% and for 300ºC at 0.55% loss. At 400ºC this does not level out after 30 hours, with a loss of 1.4wt% it appears to follow a similar logarithmic curve which is promising. At 400ºC the prediction is that the decomposition will level off at around 2-3% loss after a few days. It is possible there is some section of this material which may burn off similarly to how most polymers behave, however the stabilising agent and carbon results in a large amount of the coating remaining stable.

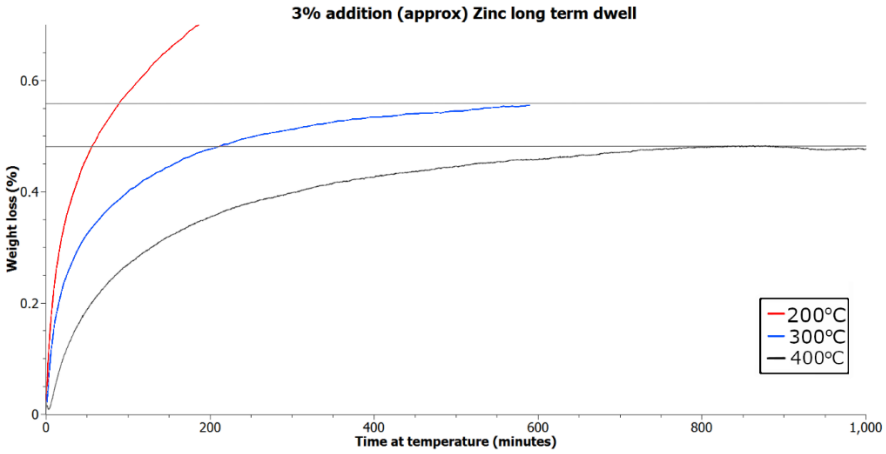

Figure 5.13 TGA trace showing the long-term stability scans for the SILRES-graphite-3wt% Zn mixture at a range of temperatures

In order to understand how this material decomposes a combined DSC/TGA test was undertaken. Figure 5.14 shows a combined weight loss and heat flow trace for the 15wt% addition of zinc. 15wt% zinc was used to emphasize the stabilisation effect, as lower amounts are difficult to see. The changes in decomposition rate relate to endothermic peaks at around 300°C and 570°C, absorbing extra energy. The initial peak indicates a slow absorption with the sharp peak showing a more rapid change. This initial peak is most likely a glass transition change, followed by melting or evaporation at the second peak. Given the nature of the material after the test and the weight loss, this secondary peak is likely to be rapid thermal decomposition of the coating.

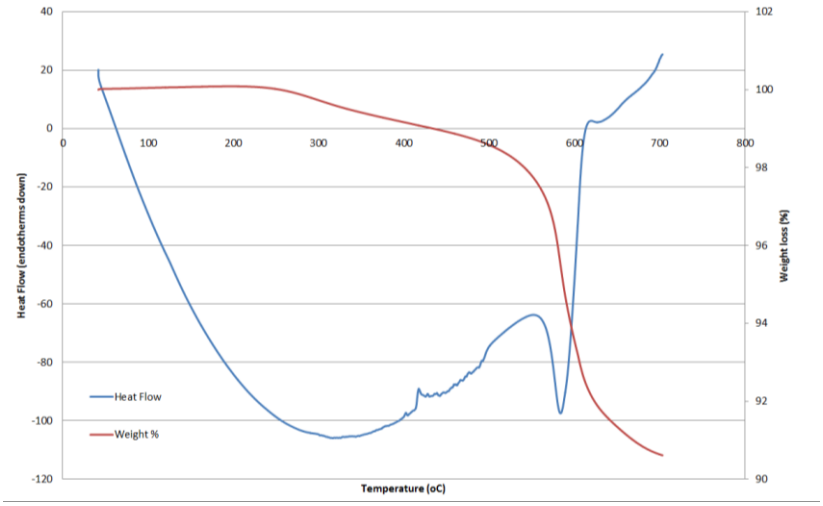

Figure 5.14 Combined DSC/TGA trace of the decomposition of SILRES-graphite-15wt% Zn

5.3.5 Cosmetic Flake Products for Conductivity

Given the reaction between most metal powders and the resin it was deemed that only noble metals would be suitable as a conductive addition for this coating. Costs must be kept as low as reasonably possible. Silver was chosen for further development, being readily available in flake form. Initial trials were undertaken using a pure silver flake material from Johnston Matthey, these additions showed a massive conductivity improvement and no negative stability effects. However, the cost of pure silver flakes easily reaches over £1000/kg, which would be much too expensive for the desired application.

Given only a small conductive pathway is needed cosmetic silver flake products were investigated. Average cost for these products is around £300/kg, making them significantly cheaper, primarily because they use less silver. A variety of these are available from 3 manufacturers (Metashine (NSG), glassflake and pottersbeads). Each sells a wide range of the products varying particle size, and coating thickness, with Glassflake selling for £273.20/kg. Given these products are used in cosmetics to provide sparkle for make-up, they will be biocompatible, non-toxic and readily available from several sources. All manufacturers contacted offered products in both fibre and flake form, with 9-40wt% silver content, surrounding the glass flake. Silver coated copper flakes were also available for a cheaper cost; however, these can suffer from diffusion at temperatures above 100^{o}C which would result in a property degradation over time due to the reduced conductivity of a Cu-Ag alloy.

NSG's Metashine product was utilised for initial testing due to availability of products. 3 flake variants were tested as additions, coded MC2080PS, MT1030PS and MC5480PS. These have particle sizes of 80µm, 30µm and 480µm respectively. As can be seen in Figure 5.15 there was a massive improvement in conductivity from the addition of these flakes. Additions to the ink increased the electrical properties rapidly, with the larger flakes producing the greatest increase in conductivity. The 5480-grade material has a length of 480µm and a thickness of 5µm giving a higher surface area for silver content, further conductivity improvements by the 5480-grade addition are shown in Figure 5.16. These large flakes may cause issues when printing fine lines, however for the large-scale electronics needed for thermoelectric applications the ink can be cast down to a 1mm track whilst still maintaining a high fill factor of flakes. The screen printing process

requires larger meshes, and any finer applications could easily use the 2080PS grade material, which presents a good balance between particle size and printability.

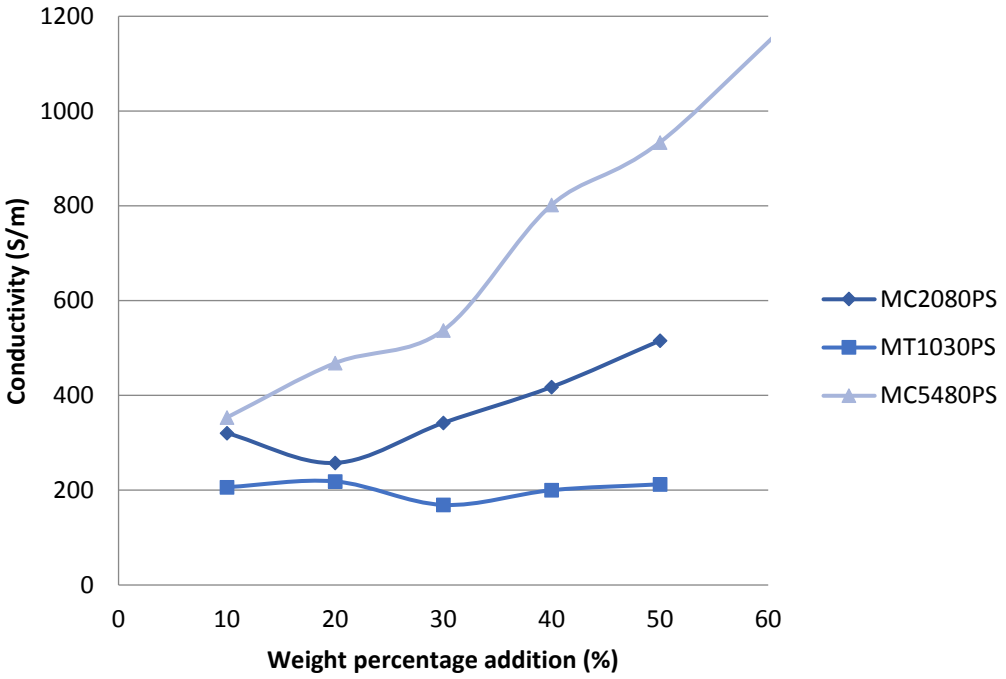

Figure 5.15 Graph showing the effect of Metashine conductive flake additions on the conductivity of the SILRES-graphite-3wt% zinc ink.

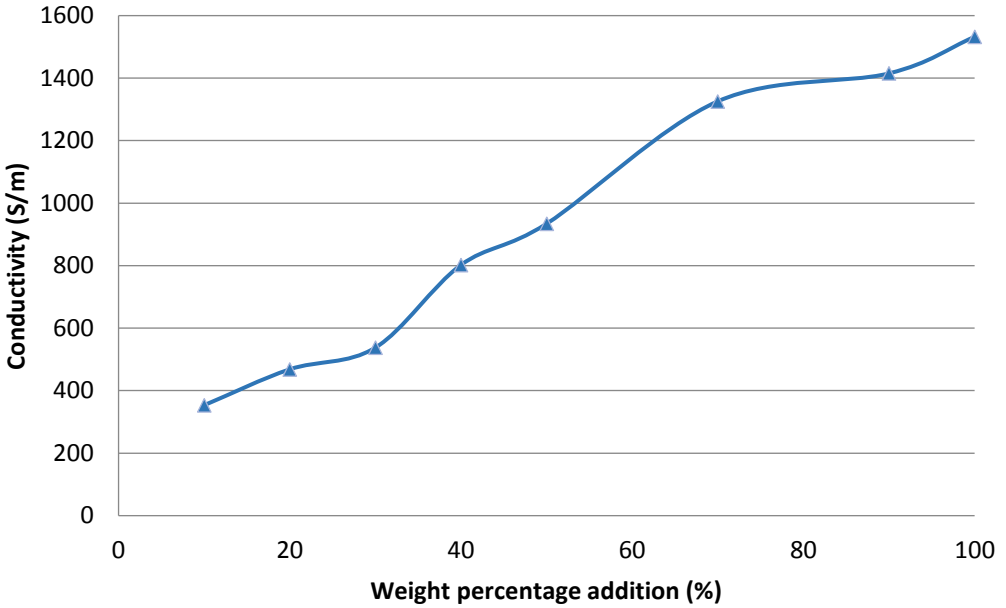

Figure 5.16 Graph showing the effect of additional MC5480PS additions up to an additional 100wt% of flake

5.3.6 Particle Locations within Bar Cast Samples

To better understand how metallic additions orientate within the polymer after casting, SEM imaging was used. Initial images of the varying carbon flakes show a uniform carbon distribution. Graphite flakes appear to lay flat over the glass substrate allowing for higher conduction in the print planes, as seen in Figure 5.17(a-c). There may however be some reduction in vertical conduction, making minimal difference for 2D prints with low thickness. KS6 graphite is likely to have the most homogeneous conductivity due to the particle's spherical nature, however its overall performance is poor in comparison to the larger graphite flakes of 20µm and SFG15, which have much larger plate-like structures. Metallic powders, seen as the lighter phase in Figure 5.17(d) and (e), appear to sit in gaps within the carbon structure, but fail to create any noticeable conductive pathways.

The addition of silver flakes, Figure 5.17(f) for the same weight percentage can be seen to provide a much wider coverage, giving a continuous conductive pathway, matching well with the data showing increased conduction from the previous section.

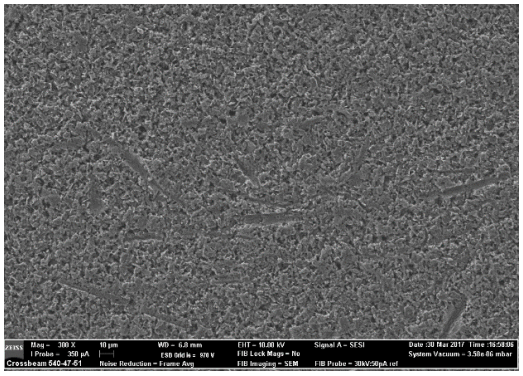

(a) KS6 Graphite

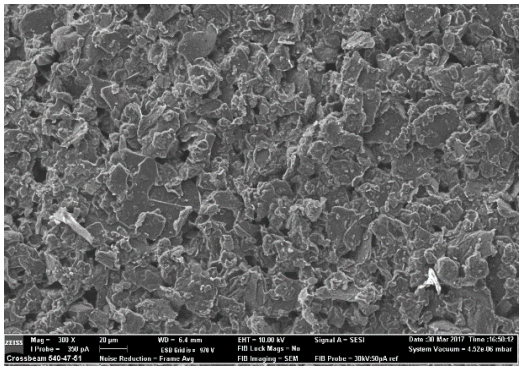

(b) 20um graphite

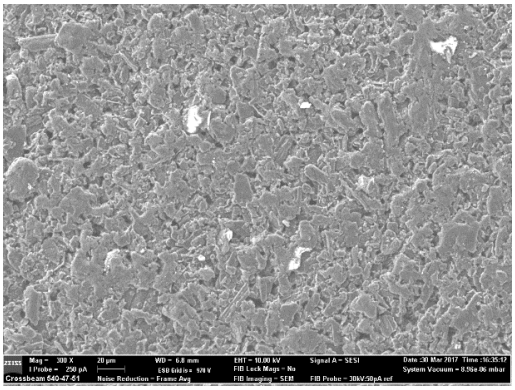

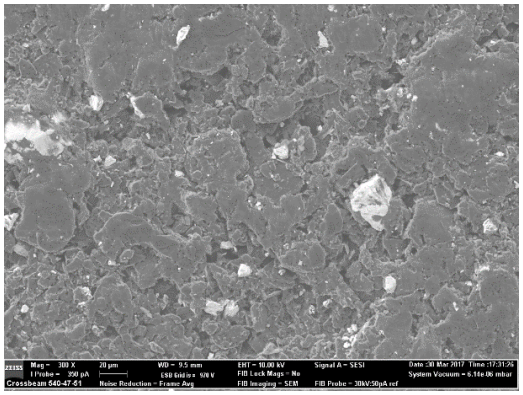

(c) 1-2um graphite *(d) 100wt% Sb Powder to SFG15*

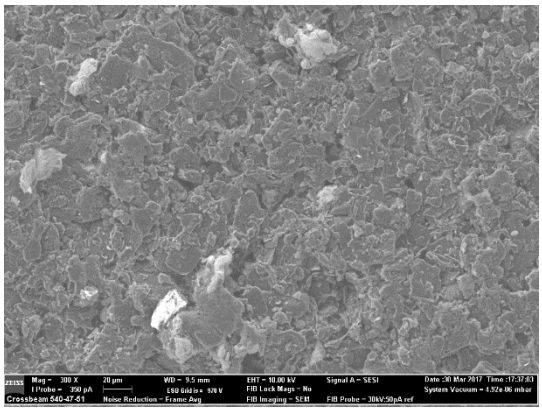

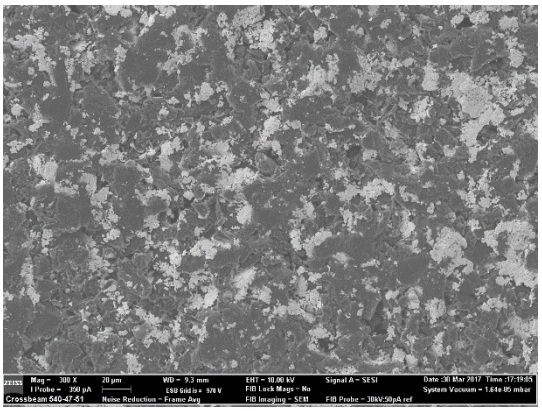

(e) 100wt% Fe Powder to SFG15 *(f) 100wt% Ag Flake to SFG15*

Figure 5.17 SEM micrographs showing the SILRES ink mixtures with (a-c) carbon and (d-f) metallic additions

5.4 Preparation for Scale-Up

5.4.1 Rheology and Effect of Solvent Additions

For screen printing applications rheology is an important factor. The first prints showed the impact of rapid drying on the prints, resulting in mesh marking and failing to allow bonding between layers. Figure 5.18 shows the results of trials with varying solvent amounts, measured in wt% addition to a SILRES-SFG15 mixture. Increasing solvent additions resulted in a logarithmic behaviour for any given shear rate. This indicates that the material thickens in a predictable way with varying solvent additions. All mixtures of these inks behaved in a thixotropic manner with the liquid exhibiting shear thickening behaviour. As such printing speed is limited and the ink is tailorable to the printing application.

Varying mixtures of IPA and terpineol were trialled and shown to have a similar behaviour. Terpineol allows for a much longer time at liquid without having drying issues which IPA presented during initial trials. Around 50% of the solvent should be IPA as SILRES does not dissolve rapidly within pure terpineol.

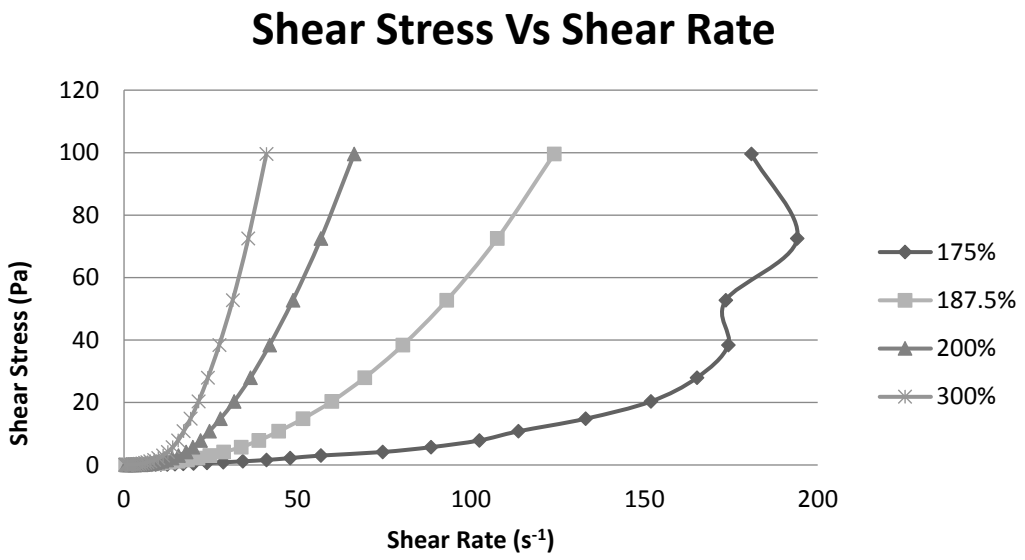

Figure 5.18 Rheological tests showing the shear stress applied (by rotation of the disk) and the corresponding shear rate, with wt% of solvent additions

5.4.2 Long Cast Test

As proof of concept, a pure SFG15 mixture with 5wt% zinc was cast onto a glass sheet, silver flake was not used with this trial. This provides a visible representation of the materials conductive properties and printability. The SILRES was cast as a track of around 213cm long with a width of 1cm. As the Figure 5.19 shows, there was sufficient conductivity over this distance to illuminate the LED.

The total resistance over the 213cm length was 16.92 k Ω. This equates to approximately 7.94 k Ω/. For a conductive ink containing only graphite this is lower than commercial grade inks for similar thickness prints[146], however further optimisation may improve this. The addition of silver flakes will likely result in significant improvements. A smaller 10cm strip containing the silver flakes showed a resistance of 54.5Ω, representing a value much closer to that of the commercial 75 Ω/square at 25µm thickness, a much more useful value.

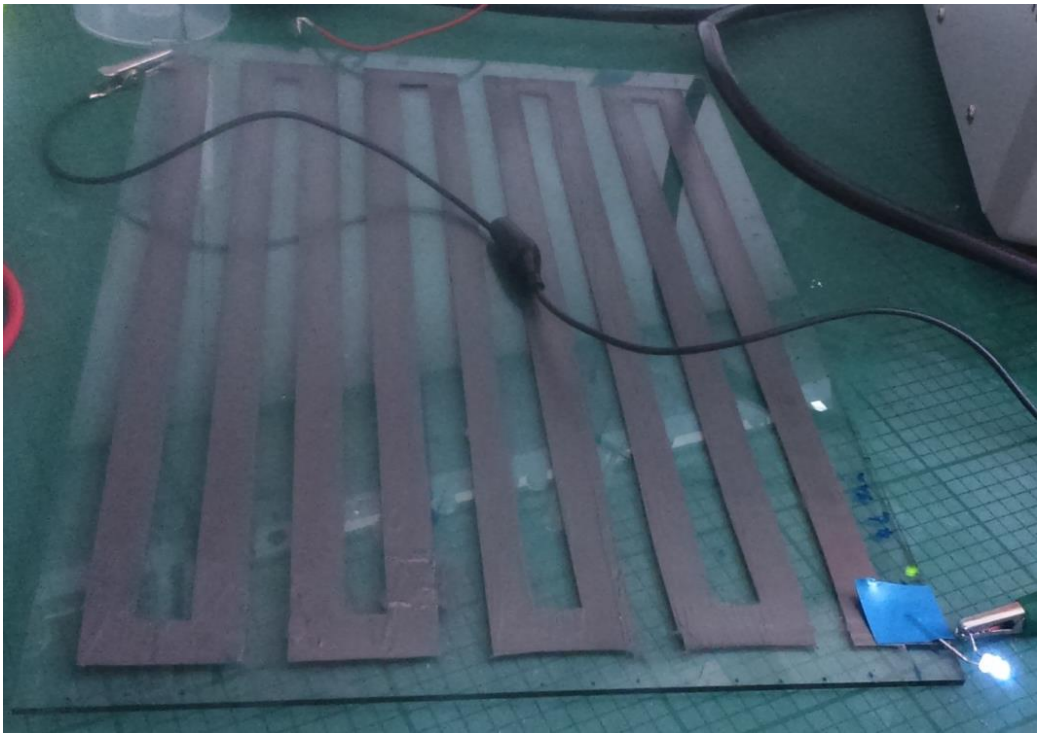

Figure 5.19 Long distance printed strip test over a glass substrate, total length was over 2.18m

5.5 Cost Analysis

Often when developing new conducting polymers cost is of little consequence. For the application of mass-scalable thermoelectrics it is important to consider how much this product would cost. The following section outlines costs of a graphite mix and then the effect of adding the silver flake.

5.5.1 SILRES-Graphite-Zinc Mixture

In order to determine costs, the ink coverage was calculated. This was done by performing a series of bar casts from a 5.5g total sample weight. 5.5g of material was capable of covering 42.6cm^2, at a thickness of 0.0016cm. In volume, this would result in a coverage of 0.682cm^3, therefore allowing coverage of 6.8cm^2 at 1mm thickness. 1mm thickness was used as the value for the thickest ideal print, typical prints may be much thinner.

Raw materials costs were then calculated. SILRES 604 is valued at £15/kg, with a minimum order of 300kg at this time. Standard Fuel Grade 15, by Timrex costs £9.45/kg, if brought as a pallet with £48 delivery. (£9.97/kg for 100kg – 1 pallet, £13.64/kg for <100kg with £60 delivery). Standard laboratory grade IPA and terpineol (from Sigma) used currently as the solvents in varying amounts allows a close control of rheology if

needed (IPA costs £7.70/kg and terpineol costs £12.90/kg). Current mixtures consist of 1g SILRES, 1g SFG15 and 3.5g solvent. Using these amounts, a cost of £10.67/kg have been calculated. Given that these materials are extremely low density they will cover a larger surface area than a similar weight of conventional solders.

A 3wt%+ zinc addition will result in an approximate cost increase of 5p per kg if sourced from Sigma Aldrich (at 98% purity), up to 98p cost increase if sourced from Goodfellow (at 99% purity). It is important this powder is as small as possible; however, purity is not too much of an issue. This will result in a cost increase to £10.87/kg and £12.37/kg respectively.

When equating this to the coverage discussed previously, a $10cm^2$ coating of 1mm thickness would cost 8.8p for its raw materials.

Treatments needed for this process are a gentle rotation for at least 3 hours to ensure compete dispersion and mixing of components. Screen printing, slot die, or inkjet could be used to layer the material onto the AlN or Al_2O_3 substrates. Curing would be needed for between 30 to 60 minutes between the temperatures of 130 and 200°C, which are all relatively cheap batch options, and are not accounted for in this analysis.

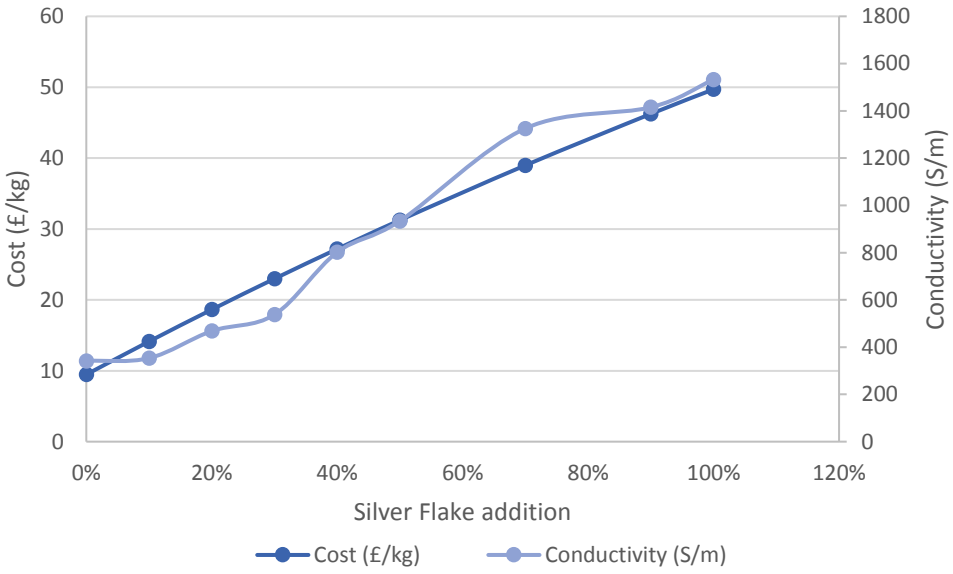

Figure 5.20 Conductivity vs cost comparison for MC5480PS flakes in the SILRES-Graphite-3wt%Zn ink

5.5.2 Silver Flake Additions

For the addition of silver flakes there is a clear trade-off between performance and cost as there is a significant increase per kg. This cost to benefit comparison is seen in Figure 5.20. Roughly doubling the material cost will double the conductivity of the material. Enhanced performance varying with cost allows the material to be tailored to the design need, allowing flexibility. Glassflake sells for £273.20/kg. The current utilized material will cost around £40.25/kg to provide the desired conductivity behaviour, equating to around 33p for a $10cm^2$ coverage at 1mm thick.

5.6 Conclusion

In conclusion the usage of this material in thermoelectric devices is possible. Devices would most probably be limited for long term use at around 300^{o}C, but able to withstand 400^{o}C temperatures for shorter periods. The SILRES material with 100wt% SFG15 and 3+wt% zinc seems to have a balance between the conductivity and stability values. The addition of glass coated silver flakes, to a weight value of 70-100%, allow a vastly improved polymer which can be printed for a low cost onto a wide variety of substrates with a high conductivity and stability.

Its ease of production, low toxicity, low cost and high thermal stability make it a rarity within the electrical polymer field, allowing it to fill a number of niches which are not otherwise possible with standard polymers.

With the thermal properties of this polymer it is viable for usage in a wide range of high temperature applications. For automotive applications devices could be placed upon several areas within the engine. Catalytic convertors and the exhaust pipe are the largest source of heat, operating at over 350^{o}C (up to 450^{o}C short term), which may be too much for this material. However, the outer skin of the convertor with passive cooling would allow this material to be used

More appropriate uses for this material would be in the lower end temperature areas, surrounding the main engine block, piston and coolant, all operating below 300^{o}C (coolant at 100^{o}C). Heat based power plants are also well within this polymers capacity.

Chapter 6 Thermoelectric Device Design and Prototyping

6.1 Introduction

The materials developed within this thesis open up the potential for the traditional design of thermoelectric devices to be changed. In this chapter a number of production methods and designs for complete devices were investigated and prototyped where appropriate. This can be seen in the area highlighted in Figure 6.1.

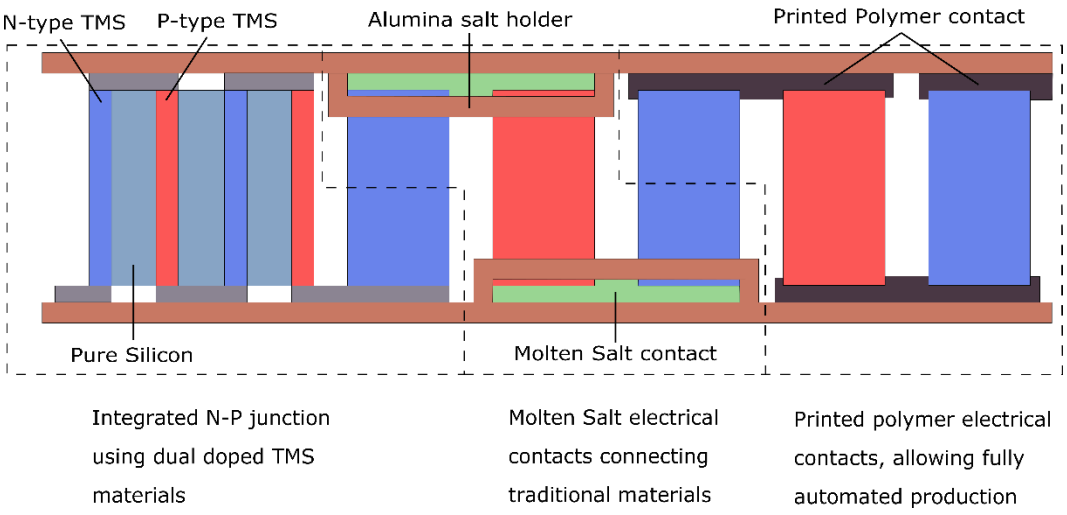

Figure 6.1 Infographic image of a traditional thermoelectric device, showing possible device designs discussed in this chapter

3 novel designs were considered within this work, stemming from the previous chapters. These designs were developed concurrently with the materials testing and initial designs were terminated when they were deemed to be not currently viable to the industry. Designs, possible production processes and developments are discussed in detail below. The work into pack cementation led to an integrated N-P junction design (see section 6.2). The work into salts led to the design of a liquid electrical contact construction (see section 6.3), whilst the conductive polymers led to a printed design (see section 6.4). Initial prototyping was undertaken with the printed polymer design, and the results summarised.

6.2 Integrated N-P Junction Design

The pack cementation process shows that a variety of materials can be deposited onto silicon substrates at controllable rates and known throwing powers. This allows the customisation of the substrates to integrate both N and P-type semiconductors sandwiching a neutral silicon barrier, which is intrinsic to the production process as a substrate. There are two primary design options for this of which the first is currently

achievable. In this a HMS-Si-Mg_2 silicon system which requires a two-step process shown in Figure 6.2. The role of P-type semiconductor is taken by HMS whilst the Mg_2Si serves as the N-type. Due to the variable treatment temperatures for the two materials this requires a two-step process.

The second option would be a Mg_2Si(Ag)-Si-Mg_2Si(Al) system. With slight modifications the pack cementation technique may allow the deposition of multiple elements at once onto substrates. This would allow the controlled self-doping, of for instance aluminium and magnesium, providing improved efficiency for the thermoelectric material. In this design Al-doped Mg_2Si would serve as the N-type semiconductor whilst a Ag-doped Mg_2Si would serve as the P-type.

Mass-producing this material would be possible using a batch process within an atmospherically controlled furnace. A pre-scored substrate of silicon would be placed inside a crucible surrounded by the desired pack material. The crucible would then be sealed, placed inside the inert atmosphere furnace and heated at the desired temperature and time. Once the heat treatment was completed the substrate would then be cleaned with compressed air and solvents to remove all powder residue. Laser cutting or mechanical fracturing along score lines would then allow the substrate to be broken into individual elements. Once separated, these elements are then sandwiched together with either inert Al_2O_3 or silicon wafers acting as a separator and soldered to connect the elements in series. This process is outlined in Figure 6.2 and it will result in a single block that will function as a TEG.

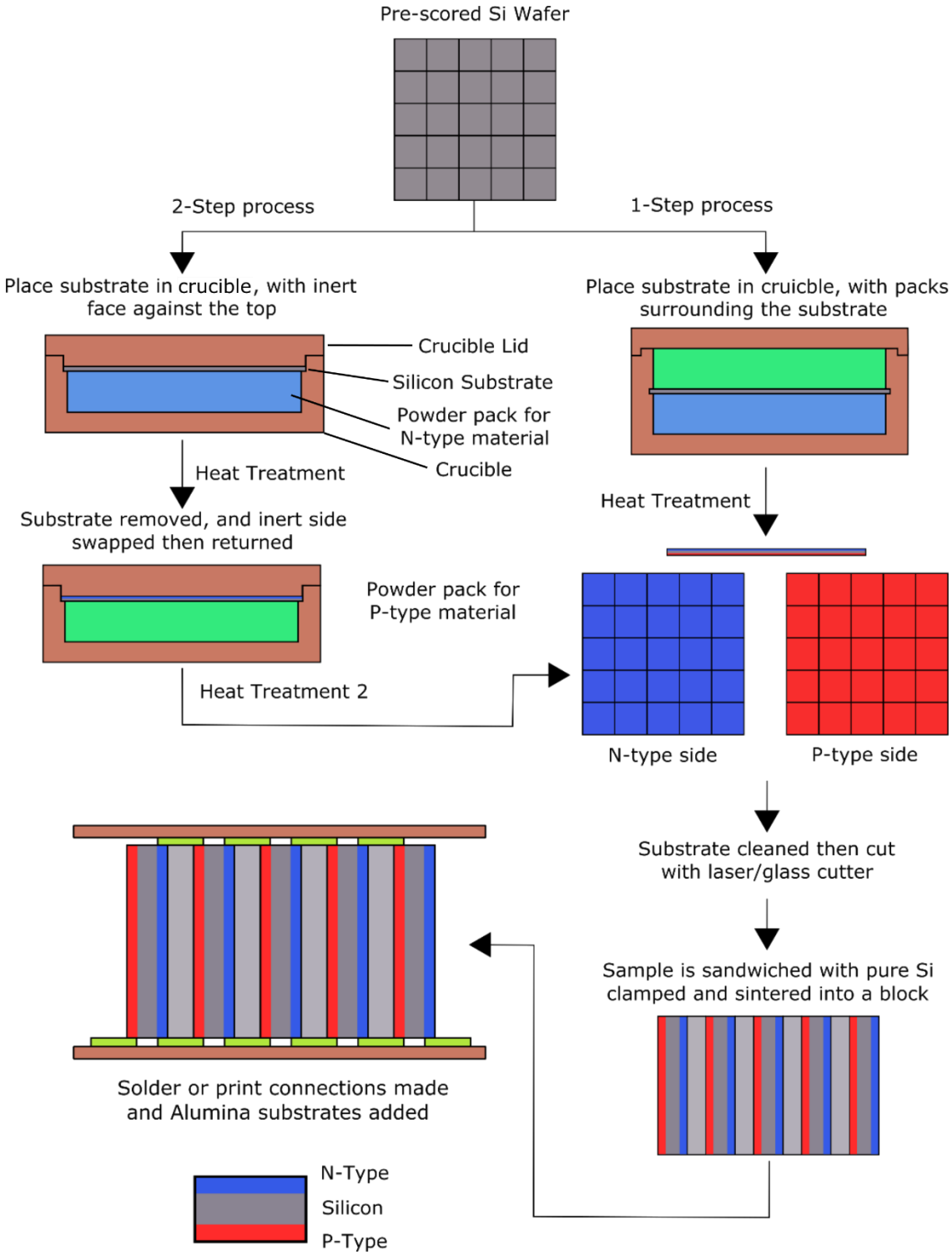

Figure 6.2 Schematic of the potential process for producing a thermoelectric device using pack cementation

6.3 Liquid Electrical Contact Design

The utilisation of molten salts as liquid electrical contacts was primarily due to the effects of fatigue observed within devices using lead-free solder. This ambitious design revolved around successful encapsulation of the salts up to temperatures of 400^{o}C. Utilisation of a custom Al_2O_3 substrate allowed the salt to be encapsulated around the elements shown in Figure 6.3. As seen previously this removed the danger of fatigue but given the corrosion issues and custom substrate requirements this design was not developed further.

6.4 Printed Polymers Design

The printed polymer design relies on the swapping of the soldered contacts with printed polymer, a proposal for this design and production method is shown in Figure 6.4. A polymer mask was applied onto the Al_2O_3 substrate, with the ink then applied to the surface using a bar cast. The mask was then removed, and the elements were added onto the substrate. This side was then heat treated at over 100^{o}C for up to an hour, allowing the polymer to cure. This secured the elements into the polymer and allowed the process to be repeated on the other side. The device was then clamped together, and heat treated to cure all polymer sections. This is an extremely rapid production method and can readily be scaled up for fully automated batch production. Using a printable polymer to replace the solder reduces the need for manual soldering and assembly, minimising the production cost of the device.

6.5 Device Prototyping

Of the 3 designs outlined above the printed polymer design set out in section 6.4 was chosen to be the most viable for prototyping. Commercial grade bismuth telluride N and P-type elements were provided by Scatec and used for the basic prototyping and testing, these elements were 5mm^3 cubes, allowing easy handling. 3 substrates were trialled during these prototyping stages. AlN and Al_2O_3 were tested as they best represent the materials used in industry, these are lightweight and have extremely good thermal conductivity. Due to the handmade nature of these prototypes it was difficult to ensure correct alignment of all parts. Mechanical alignment would be easy to do with basic machinery for large scale production, but for the purposes of these prototypes plain window glass was used to allow construction by hand. Glass substrates have a few

limitations including its lower thermal conductivity and much smoother surface. It is seen that the polymer mixtures bind well to the glass surface.

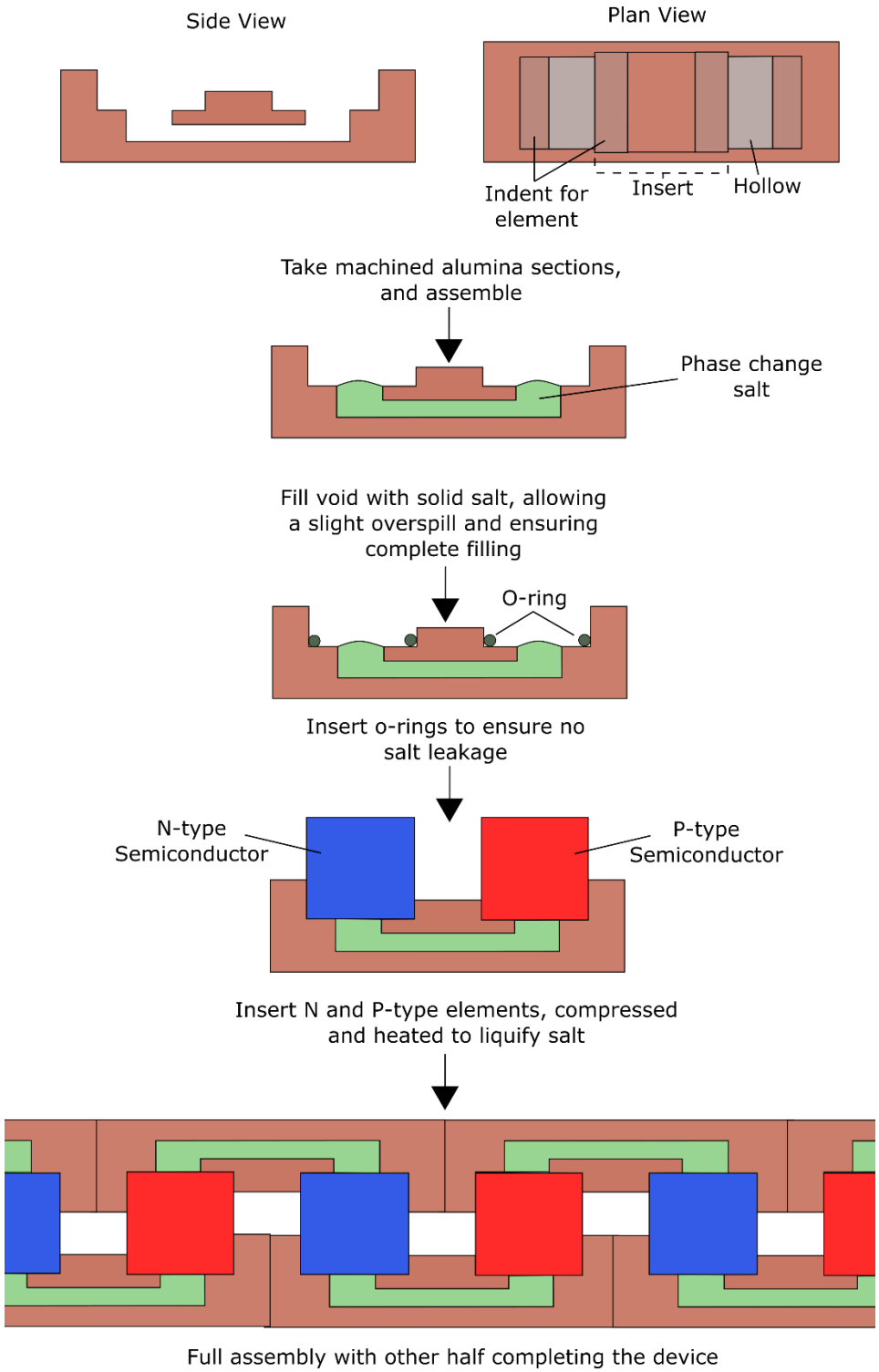

Figure 6.3 Schematic of the potential process for producing a thermoelectric device using conductive molten salts

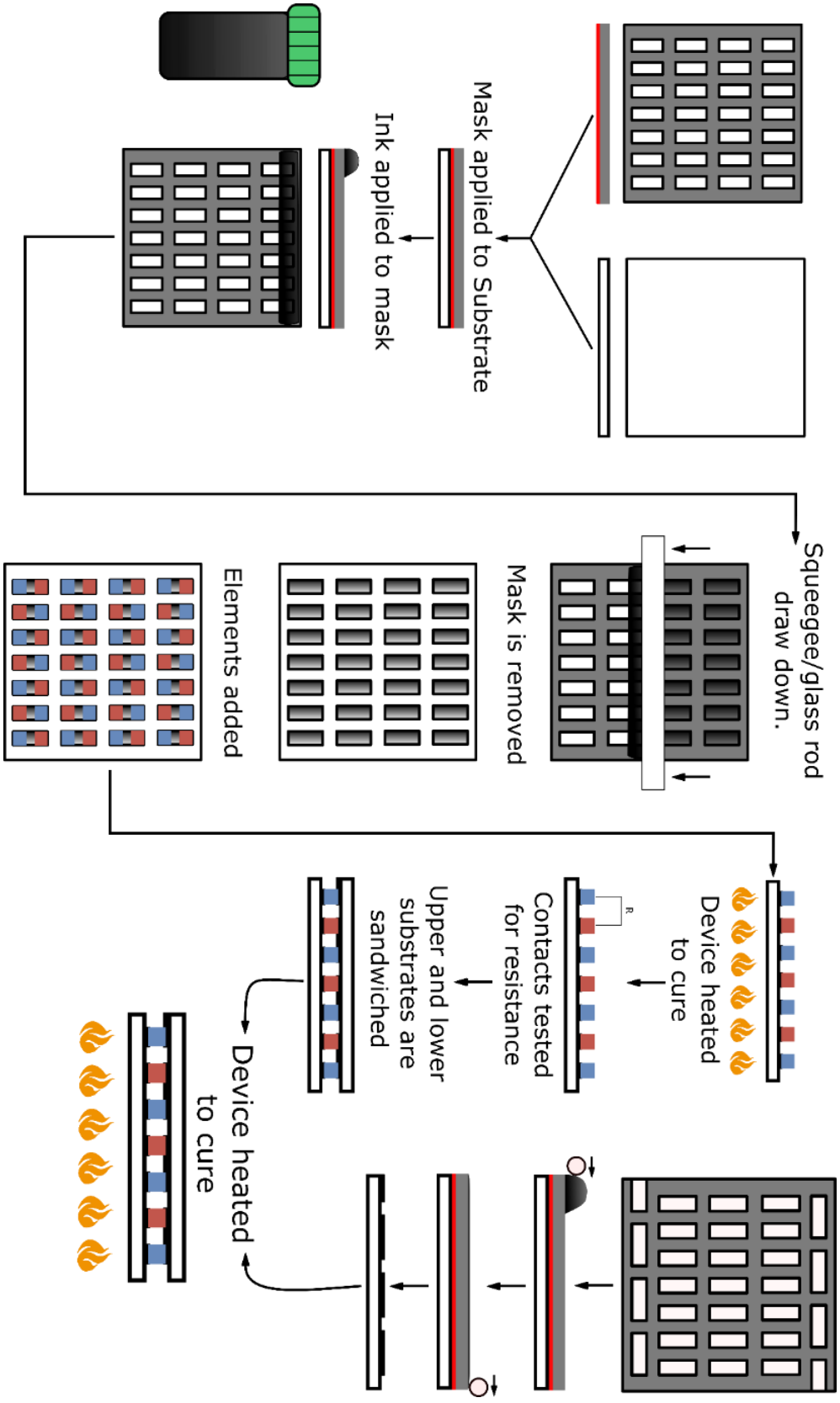

Figure 6.4 Schematic of the potential process for producing a thermoelectric device using conductive polymers

6.5.1 Initial Prototype

The first prototype was constructed using a 3x3 grid and relying on the pure graphite-SILRES mixture to provide the conductive pathways. This device is shown in Figure 6.5. Copper strips were used to allow easy connection to other devices. The device had a total resistance of 1.5k Ω, extremely high for this kind of device. Unloaded testing of this device was shown to have a maximum voltage of 0.5V at 100ºC, this equates to 0.16mW, which is far below the desired output. Whilst a section of the resistance came from the elements, the poor conductivity of the connections has a huge impact, which is variable couple to couple. This device underperforms compared to what was expected, leading to individual contact conductivity to be investigated.

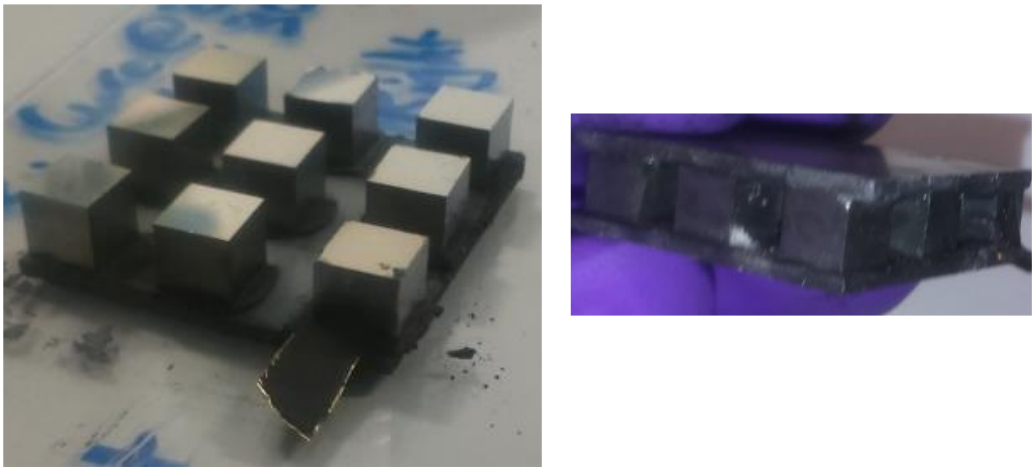

Figure 6.5 First prototype constructed on AlN substrate, with graphite-SILRES polymer contacts

6.5.2 Effect of Print Quality on Device Performance

As a quality control step prior to the sandwiching of the devices the resistivity presented between elements was tested using a multimeter connected to the topsides of the elements. The optimum resistance seen with manually painted contacts was 27Ω, with the maximum reaching as much as 2.27kΩ. The results from the testing of 100 couples is shown in Figure 6.6. This shows that an optimally printed device is likely to perform over 100 times better than a poorly made device. The few poor contacts result in severely reduced device performance. With the manual assembly technique, it is almost impossible to remove these high resistivity elements due to the nature of the device assembly process. Initial trials on couples produced using the masked printing process described earlier

showed an improvement in couple performance, with all couples lying between 10 and 70Ω. Printing optimisation would allow this to be further refined.

With all testing it can be safely assumed that the devices are performing below what they would be if mechanically printed.

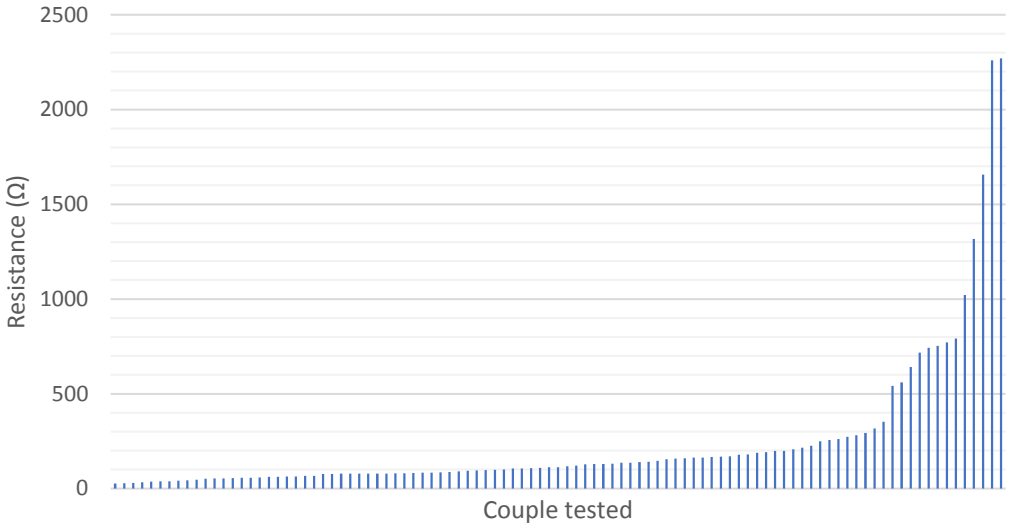

Figure 6.6 Resistance figures between each couple taken during prototyping

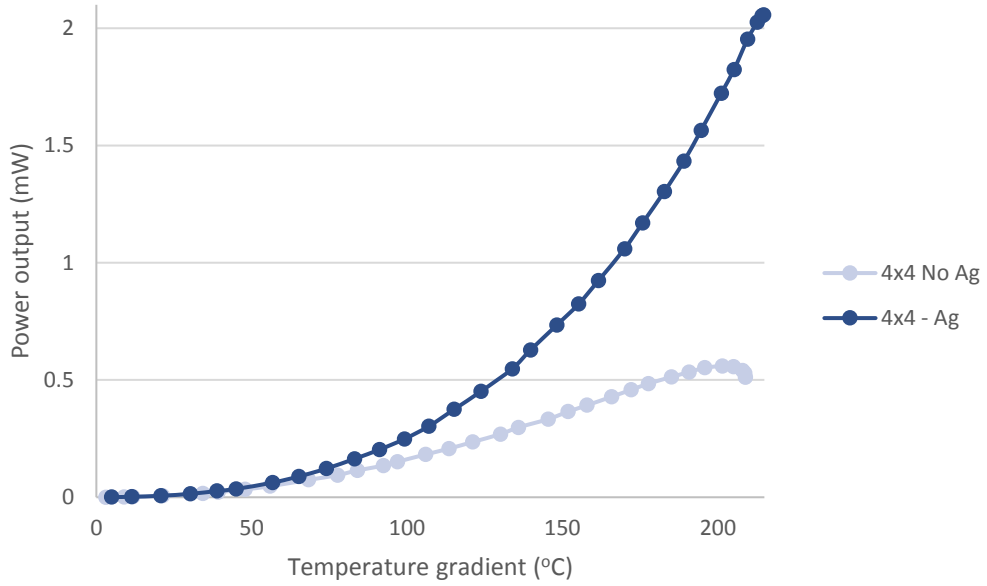

Figure 6.7 Comparative loaded performance between a 16-element device with graphite-SILRES contacts and one with additional silver flakes in the contacts

6.5.3 Device Performance with Silver Flake Additions

Figure 6.7 shows the mW generation from two like-for-like devices tested, each containing 16 elements in total. These devices were printed onto glass which lowered their overall performance somewhat. Devices tested can be seen in Figure 6.8. The device using just a Graphite-SILRES mixture was capable of a 0.56mW output before maxing out. The device with silver contacts outperformed its counterpart achieving a power output of 2.06mW. This shows that in like for like devices the increased conductivity of the silver containing SILRES allows up to a 3.5 times improvement.

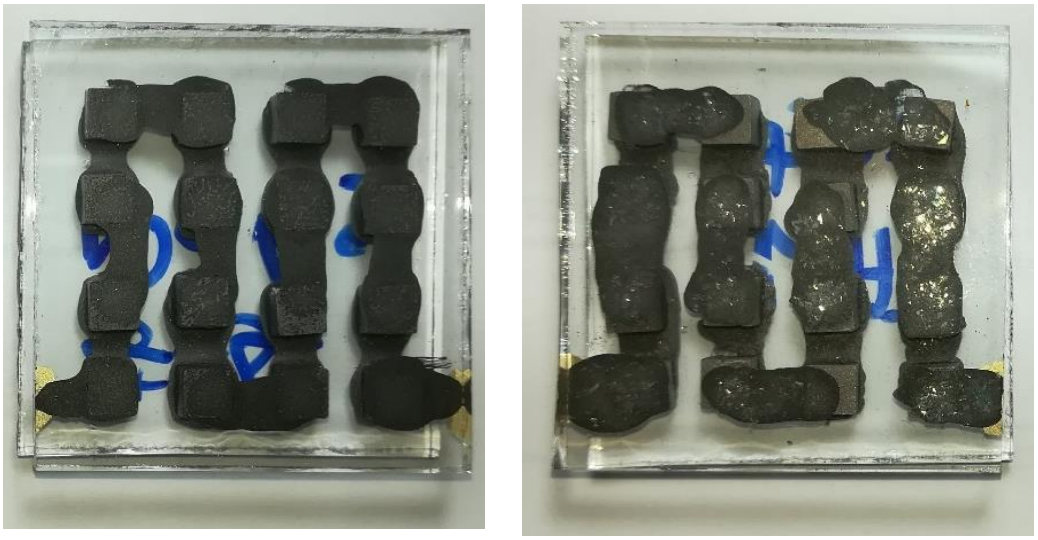

(a) *(b)*

Figure 6.8 4x4 element device using graphite-SILRES ink (a) with no silver flakes and (b) with silver flakes

6.5.4 Device Performance with respect to Substrates

To look at the effect of thermal conductivity with regards to the substrate, two devices with 5x5 elements were tested. Both glass and Al_2O_3 substrates were used. The results for this are shown in Figure 6.9 and Figure 6.10. The device using Al_2O_3 shows a three times improvement in maximum device performance in comparison to the glass. The Al_2O_3 device's power output reached a maximum at 240^{o}C, whereas the glass devices maximised at 290^{o}C, due to the low thermal conductivity of the glass. Figure 6.10 shows the effect with respect to the temperature gradient, here Al_2O_3 gradient decreases after reaching a maximum of 150^{o}C. The glass has an even greater gradient on its outer surfaces, however much less heat is transferred so the gradients on the elements are less, reducing the efficiency.

As can be seen these devices both perform poorly due to their large internal resistances. This is primarily due to the devices poor contacts and long connection lengths, which can be seen in Figure 6.11(a) and (b).

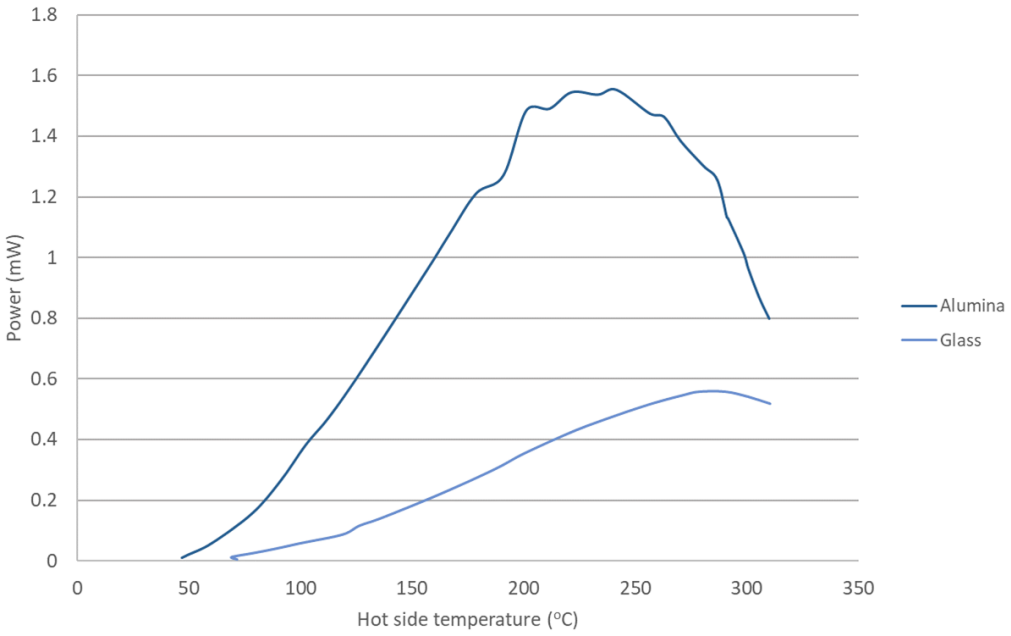

Figure 6.9 Comparative loaded performance between 25 element devices with glass or Al_2O_3 substrates

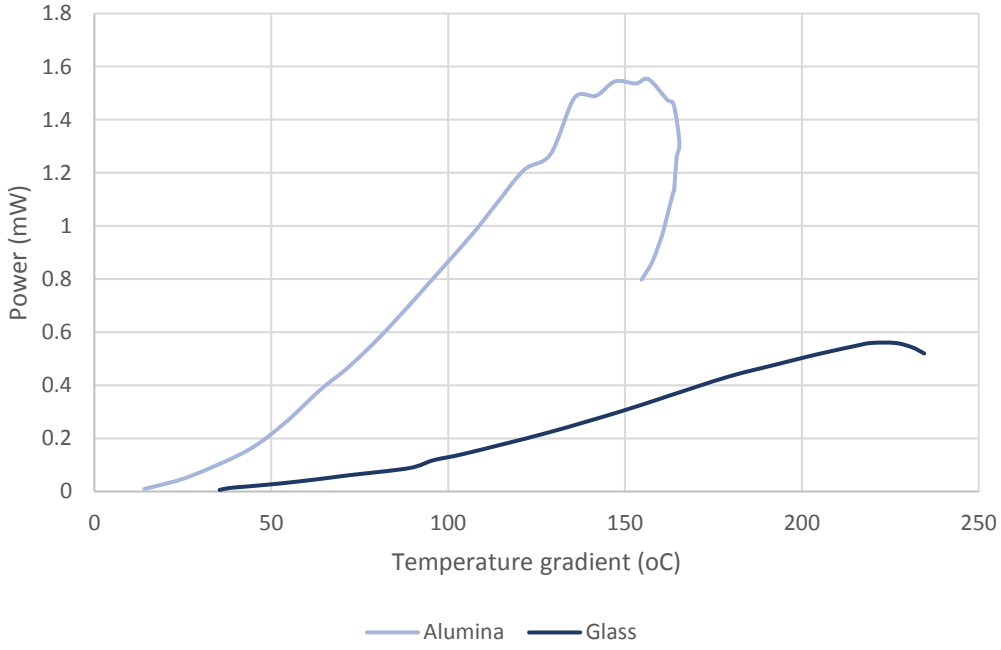

Figure 6.10 Comparative loaded performance between a 25-element device with glass and Al_2O_3 substrates with regards to their temperature gradient

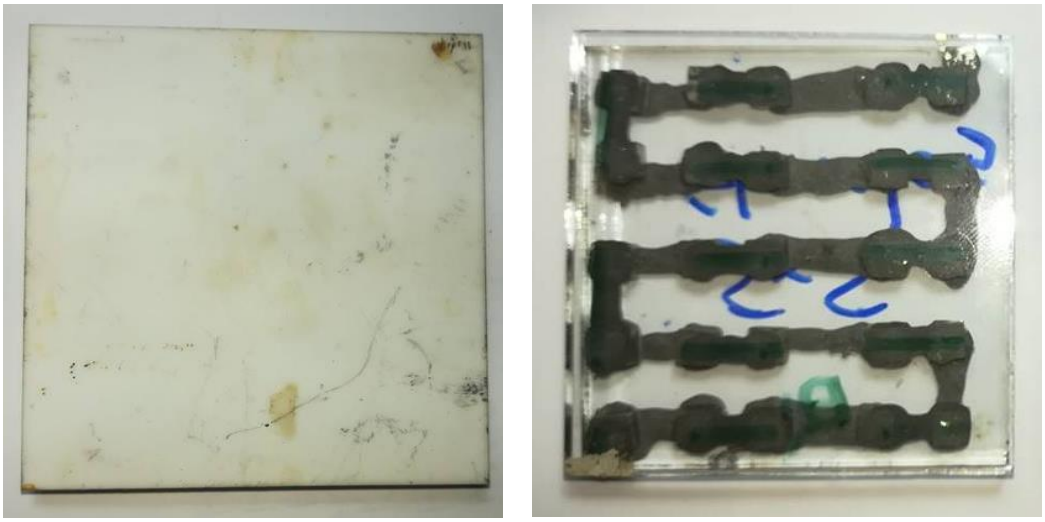

(a) *(b)*

Figure 6.11 5x5 element prototypes with (a) Al_2O_3 and (b) Glass substrates

6.5.5 Effect of Element Numbers on Performance

Typically, as shown in Figure 6.12, there is a mostly trend with the device output and number of elements, however more prototyping will be needed ton conclusively prove this. The power output increases with thermocouple number, which is to be expected. Fortunately, this means that there are no scale-up issues with the devices made using the polymer electrical contact.

6.5.1 Theoretical Device Scale-Up

Using the values taken from the previous sections, the 4x4 device performing at 2mW with glass could achieve up to 6mW with Al_2O_3 substrates. The number of elements seen above shows that there is a linear trend, therefore there could be a 16 times improvement if increased from 16 to 100 elements. This would lead to a 96mW device potential. This is in a reasonable level to allow effective commercial devices to be made. Process optimisation would allow further increases to be made.

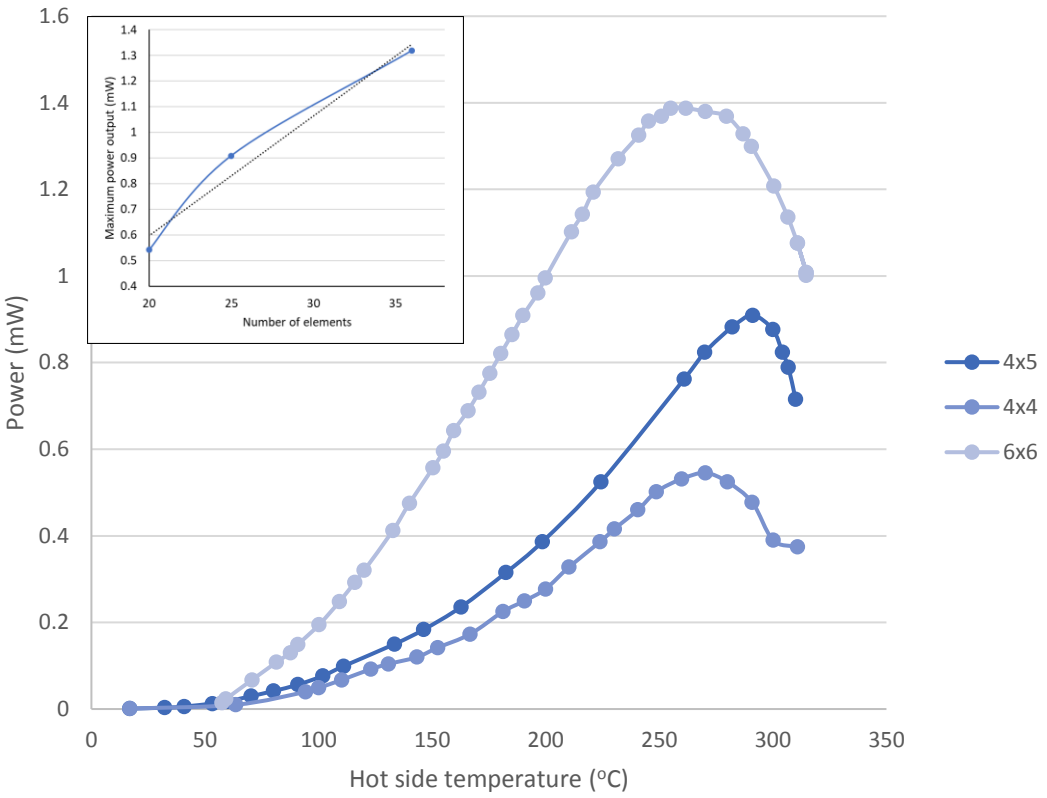

Figure 6.12 Comparison of devices with varying thermocouple quantities, with the inset showing the maximum power output vs number of elements

6.6 Summary

The 3 designs outlined above present alternatives to the traditional thermoelectric designs. Of the 3 discussed the use of conductive polymers for printing provides a unique solution which, whilst keeping the design largely the same, gives an alternative way of producing these devices with an almost entirely new design, allowing rapid scale up.

Initial prototyping proved that this design is a viable alternative to the original soldered design, and with some further work into automation and optimisation of a production line process could allow a technique that will result in a fully automated production line for thermoelectric devices[14,137]. This mass production method would reduce labour costs and allow the devices to be manufactured in western economies on a competitive scale.

Chapter 7 Conclusions and Future Work

7.1 Conclusion

Thermoelectric devices present an important opportunity to the terrestrial and space markets, providing power in a wide range of environments. Devices can be applied on a range of scales. From domestic heating systems for better air flow all the way up to powering the next generation of Mars Rovers. There are number of advantages of TEGs over conventional renewables including no moving parts, maintenance-free functionality in extreme environments, high-temperature resistance and long-term life span. However, this variety of markets makes it difficult to design for a single application.

Initially the aim of this project was to develop thermoelectric materials and devices for space applications. Due to the early experimental results and changing industrial focus the project moved to producing affordable and scalable thermoelectric devices. Allowing mass production by removing the manual production process of the current thermoelectric devices. These developments were focused on because of the large potential thermoelectric market and room for expansion in the EU due to high labour costs.

This project began with investigating current soldered junction thermoelectrics and areas of improvement were identified. Classically designed thermoelectric devices have 3 key areas of improvement that were focused on. These were: thermoelectric materials, device assembly and device design.

Current technologies use rare or costly materials, with Bi_2Te_3 and its variants costing around £600/kg. With these materials comprising of up to 50-80% of the device cost this became a large area of focus. TMSs were identified as a promising thermoelectric using only earth abundant materials with reliable and sustainable supply chains. These materials typically cost as little as £115/kg. Three silicides were investigated within these works (Mg_2Si, HMS and β-Fe_2Si). The pack cementation technique was chosen for the production method as it requires very little specialist equipment and is a variant of a large-scale technique for the coating of aerospace components, presenting scale-up opportunities.

Mg_2Si was first investigated using this technique, expanding on previous works. It was shown that films of over 150µm could be produced at 650^{o}C up to 60 hours. The purity of these layers was verified using SEM-EDS and XRD showing pure Mg_2Si. SEM-EBSD

showed the orientation of these films to be columnar in nature perpendicular to the silicon substrate.

HMS films were shown to be more difficult to produce, requiring a novel variation utilising the OOPC. This allowed growth of films of 40μm over 40 hours at 900ºC, a much slower rate than that of Mg_2Si. These films were again investigated fully and showed high purity and a columnar growth perpendicular to the substrates. This production method also produced high quality MnSi nanowires of high aspect ratios which may have alternative applications.

The final silicide investigated was β-Fe_2Si. This produced an extremely variable result which created extremely intriguing structures which have potential for high surface area. Whilst not used for thermoelectrics in its current form it is believed this material could have potential uses in hydrogen generation and as battery electrodes. Overall the transition metal silicides produced via pack cementation were high purity but the diffusion limitation prevented them from being used commercially in their current form, however powder variants may present a viable alternative.

The second area investigated was the device assembly considerations, this focused upon replacing the soldered connections in the devices with liquid or printed polymer contacts. The initial work into liquid connectors showed that a molten salt could be tailored to the 100-400ºC liquid operating temperature and provide a good conductive pathway. The reactivity of the molten salts, even in their ternary form, with skutterudites and other semimetals prevents their use currently. Further works showed that the developed LiCl containing salt could have alternative applications within the solar-thermal energy generation industry. The customised mixture was highly stable at high temperatures and melting at below 120ºC, making it ideal for thermal storage power plants such as the larger heliostats.

Due to the lack of application success with the molten salts, polymer electrical contacts were then developed. This revolved around a base SILRES 604 polysiloxane which has proven high temperature stability. SFG15 graphite flakes and zinc powder were added to increase conductivity and thermal stability of the polymer, resulting in a polymer that was stable for long-term use at 300ºC, with short-term spikes of 350ºC possible. To further increase the conductivity of this polymer Metashine silver coated glass was added. This

product sourced from the cosmetic industry provides a great cost-functionality balance as a conductive addition for engineering materials, being less than ¼ of the cost of traditional silver flakes, for the same size flakes. This conductive, high temperature polymer was then optimised for coating onto devices to replace traditional solder.

The final area investigated was focused around using the developed materials in devices. A few designs were trialled. Of these designs, the printed polymer set up was further developed to the prototype stage. The production process of these printed contacts for thermoelectrics has been developed and outline within this thesis and prototyping has been successfully undertaken to show how devices of this construct could be created. These prototypes are the first stage in developing a replacement for soldered devices, increasing manufacture speed and allow fully mechanised device construction.

7.2 Future Works

This thesis covers a wide range of techniques and materials development challenges due to its industrial focus. Therefore, there are several areas that need further investigation to ascertain their potential viability.

The TMS development process showed that high purity Mg_2Si and HMS layers can be grown on silicon substrates. Further development can be made with these materials to improve the pack cementation process. The primary area of development would be creating a powder variant of this process to create a high purity silicide source. This powder can then be shaped into blocks if needed, this should remove some of the diffusion rate limitations inherent with the pack cementation process.

The pack cementation of Fe-Si materials was seemingly uncontrollable; however, it does have a large amount of potential due to its high surface area. Future works could focus upon finding applications for the material including as a battery, or as an electrode for the electrolysis of water for hydrogen production. The variability between the Mg_2Si, HMS and β-Fe_2Si materials presents an interesting possibility for looking into other materials including titanium, copper and zirconia, as their behaviour would vary greatly.

Molten salts as heat transfer fluids is another promising area not chosen to be progressed within this thesis. Further work would be directed around the alternative additions possible for quaternary salts including the various metal nitrates overlooked in these

works. Chemical compatibility would also need to be studied with regards to the salts corrosion behaviour on a variety of storage mediums.

The conductive polymers is the most progressed part of this work, however there are still a number of areas open for development, including: further improvements to the stability, using additions like Fe_2O_3; conductivity improvements with the use of varied particle sizes; including carbon black and other metallic additions; and the rheological optimisation of the ink, generally improving the polymer for this application. The primary piece of future work necessary will be continued prototyping until an optimised design is reached, with further development on the automation of the device construction. This would include the production line design and the sourcing and programming of the machinery required for the prototypes developed to reach the mass production stage for a viable product.

Appendix 1

Research as Art Entries

Introduction

All of the following images have been entered into Swansea Universities Research as Art Competition in an attempt to increase the impact of the research and make STEM subjects more accessible to the general public. Two of these images have received highly commended awards and all have been displayed in the public exhibitions.

Success in Failure – Highly Commended - 2015

Lack of success in research can be demoralising, sometimes it can result in unforeseen success.

While looking into functional materials for the European Space Agency, a novel method was undertaken to produce a specific Ferrosilicon product from the gas phase.

The image shows an example of preferential crystalline growth in the gas phase, taken using a Scanning Electron Microscope. These highly organised crystals were formed with lengths of around 100 microns square.

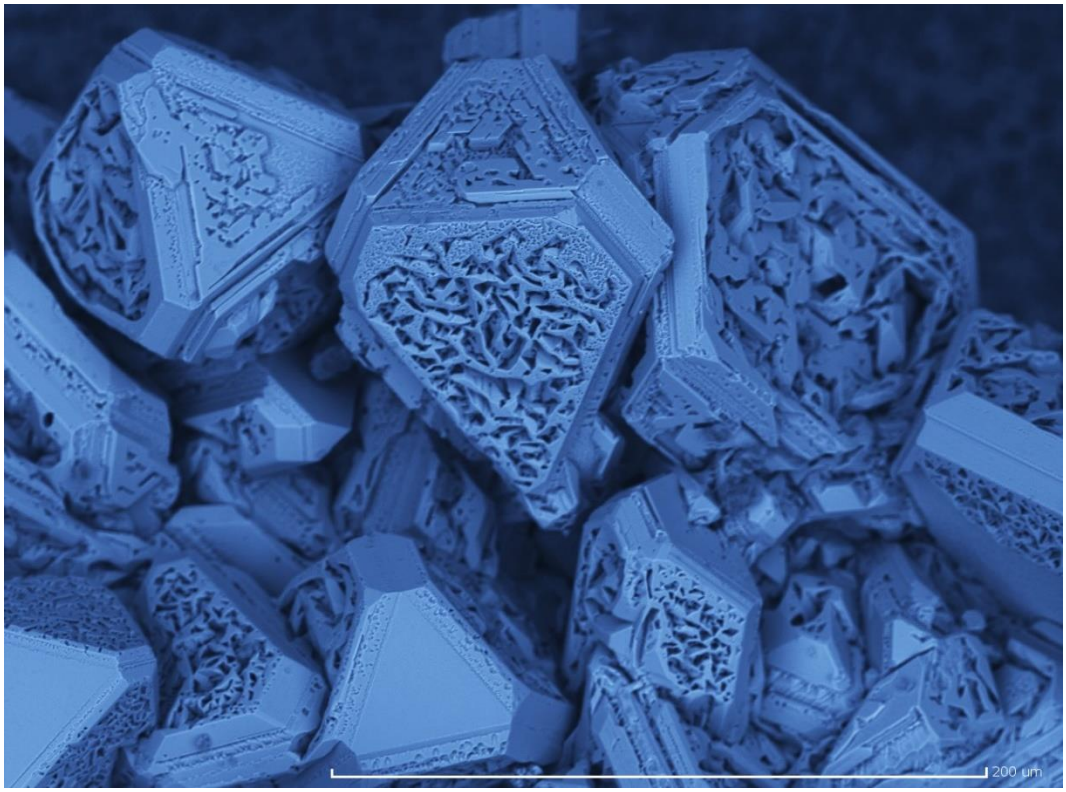

Science Fairies - 2015

Sometimes the results of research experiments are just magical. Whilst looking into functional materials for the European Space Agency, a novel method was undertaken to produce a specific Ferrosilicon product from the gas phase.

The image shows an interesting example of unexpected success. The structure was found in a void of the material and was imaged using a Scanning Electron Microscope. The box girder is an interesting example of preferential growth. Nanowires have been created around this tube with the structure in the top right appearing to be a winged fairy.

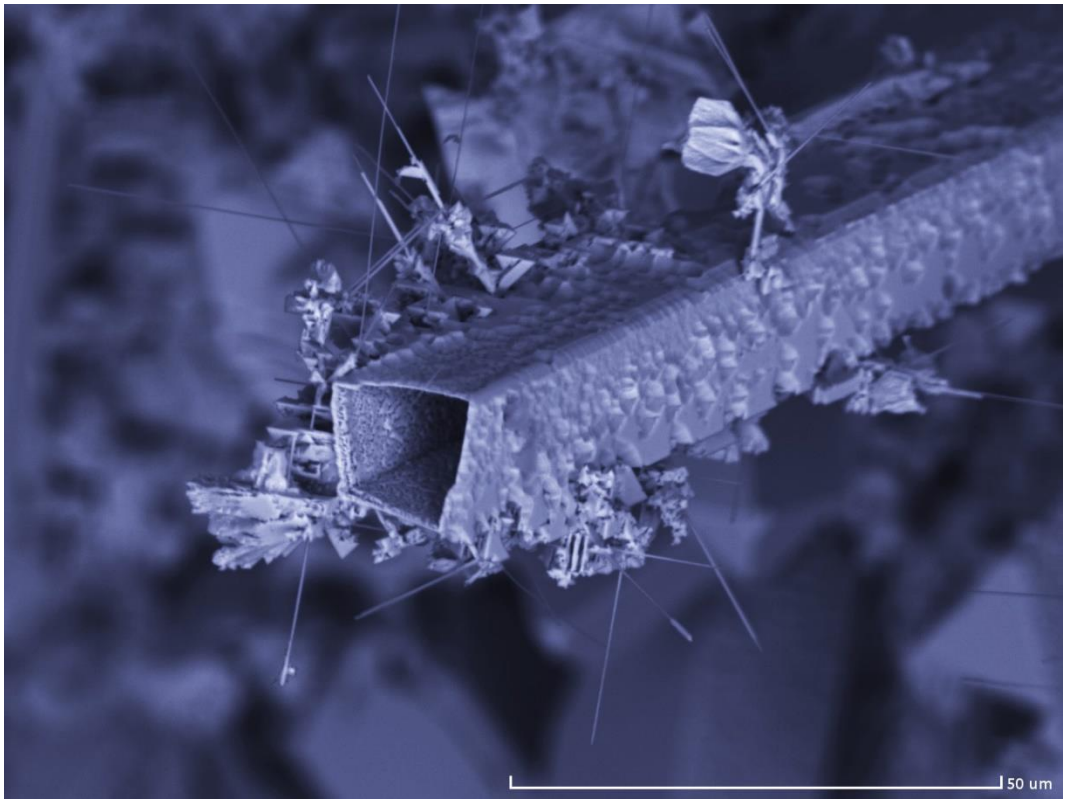

Snowflakes in Miniature (not submitted) - 2015

Often research does not quite go as planned and lack of success can result in techniques being classed as failures. But hidden within many failures can be a something completely unexpected and beautiful.

Making new materials for space applications often results in failures, particularly when novel methods are used. The image was taken using a Scanning Electron Microscope and shows how materials can grow in the gas phase. The flat plates seen have been described as snowflakes, each one individual and difficult to isolate

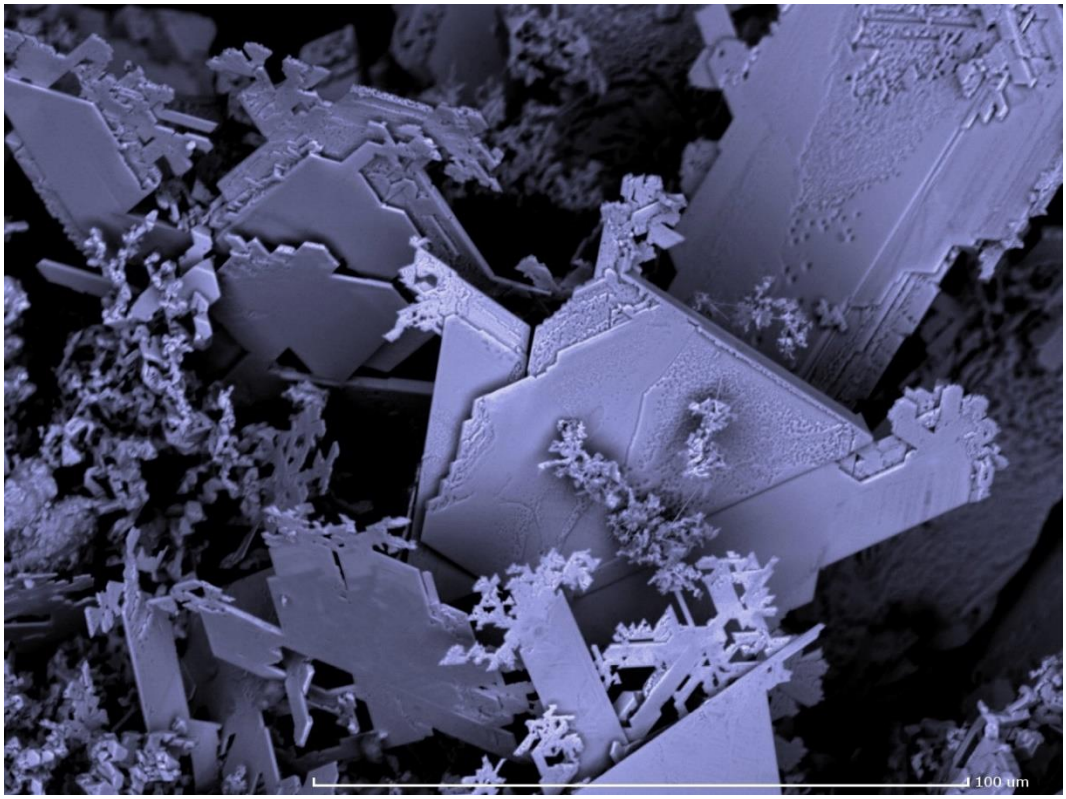

The Maze of Research – Highly Commended - 2016

Barriers surround you at every turn, sometimes the path is signposted, and others covered in mist and darkness. Your goal may be in sight but unreachable, or when turning a blind corner, you can discover something wonderful.

This image represents how research can be seen as a maze. You can choose to aim for the centre, or the exit. Some may choose to map every corner of the maze, others go straight to their destination. Both are valid and have their own benefits.

The pattern is based on the Hampton Court maze, one of the first used in experimental psychology by W.S.Small in 1900. The maze walls are the results of experiments developing a new coating over the past year. Coated glass slides representing experimental results, revealing paths clearly. Dead ends can represent unsuccessful tests or unexpected results. The green vials, outlining the rest of the maze represent the outlines of theory and assumptions, enough to give you some direction, but not always showing a path.

In sciences purest form it matters not whether you will reach the goal, or how many alternative routes you take along the way. It is the journey that counts.

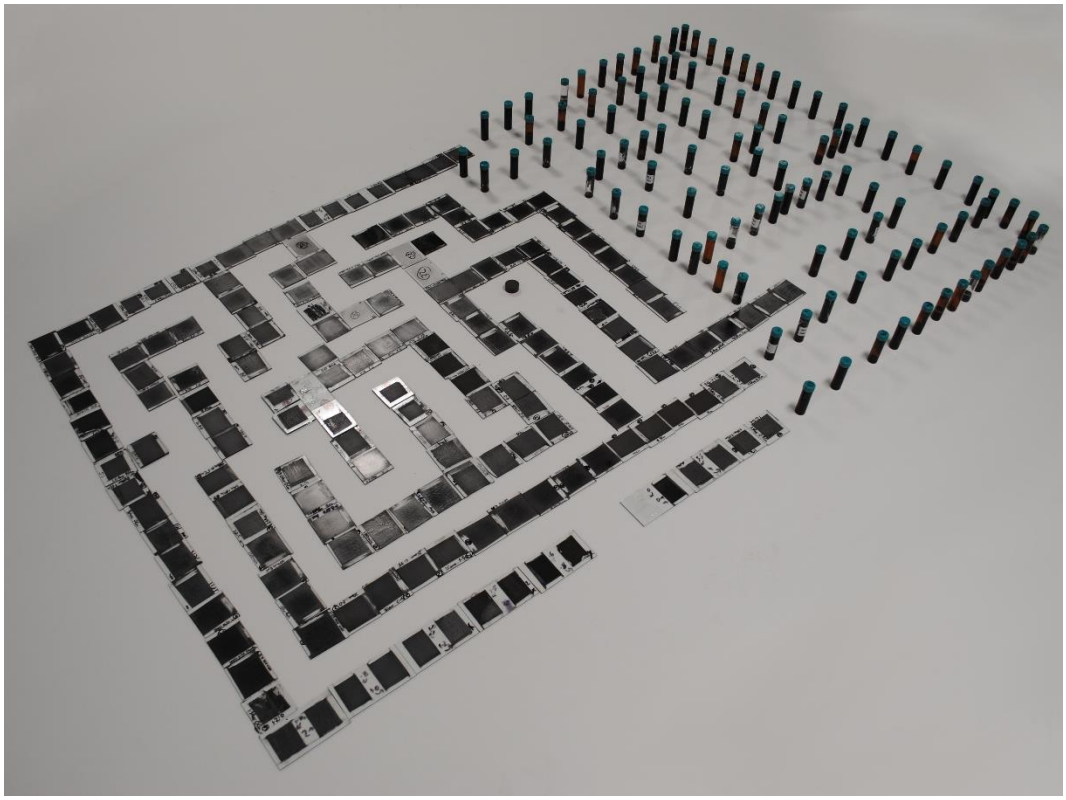

New Worlds Beneath the Ice – 2017

Collaborative with Dr Feras Korkees.

"All experience is an arch wherethrough gleams that untraveled world, whose margin fades for ever and for ever when I move" – Lord Tennyson

One of the beauties of teaching and demonstrating is that you are always learning and discovering new things. This image was taken during a second-year materials practical on fractured carbon fibre composites. If we join our students in descending into the icy depths of carbon fibre, we can see great rolling hills of epoxy. These sit atop a strata of glacial carbon fibres descending downwards to a hidden arctic ocean. All of this is under the beauty of a microscopic Aurora Borealis.

Demonstrating is more than teaching by rote, it is about allowing students to view and experience new worlds, giving them a glimpse into what can be discovered and the infinite possibilities of their future.

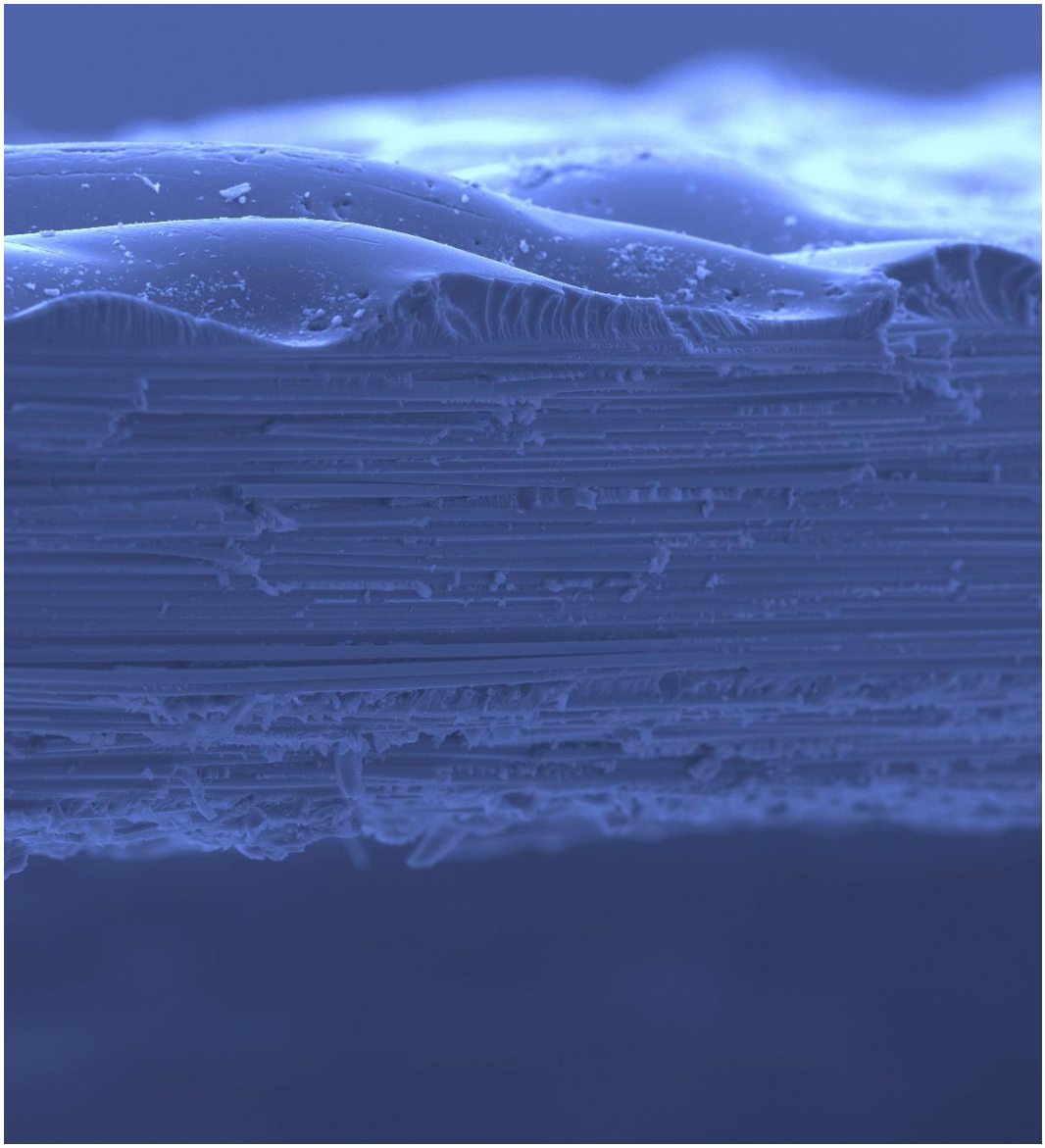

Appendix 2

Stabilization of molten salt materials using metal chlorides for solar thermal storage

SCIENTIFIC REPORTS

OPEN

Stabilization of molten salt materials using metal chlorides for solar thermal storage

Received: 21 February 2018
Accepted: 23 April 2018
Published online: 29 May 2018

T. O. Dunlop[1], D. J. Jarvis[2], W. E. Voice[2] & J. H. Sullivan[1]

The effect of a variety of metal-chlorides additions on the melting behavior and thermal stability of commercially available salts was investigated. Ternary salts comprised of KNO_3, $NaNO_2$, and $NaNO_3$ were produced with additions of a variety of chlorides (KCl, LiCl, $CaCl_2$, $ZnCl_2$, NaCl and $MgCl_2$). Thermogravimetric analysis and weight loss experiments showed that the quaternary salt containing a 5 wt% addition of LiCl and KCl led to an increase in short term thermal stability compared to the ternary control salts. These additions allowed the salts to remain stable up to a temperature of 630 °C. Long term weight loss experiments showed an upper stability increase of 50 °C. A 5 wt% LiCl addition resulted in a weight loss of only 25% after 30 hours in comparison to a 61% loss for control ternary salts. Calorimetry showed that LiCl additions allow partial melting at 80 °C, in comparison to the 142 °C of ternary salts. This drop in melting point, combined with increased stability, provided a molten working range increase of almost 100 °C in total, in comparison to the control ternary salts. XRD analysis showed the oxidation effect of decomposing salts and the additional phase created with LiCl additions to allow melting point changes to occur.

The potential of solar energy as a sustainable and affordable power source has resulted in a great deal of worldwide interest. Technological developments have progressed at great speed over the past decade, particularly within the field of solar thermal energy and photovoltaics[1]. Solar thermal plants can be used to concentrate the Sun's energy and convert it into electricity using molten salt mixtures and water steam generators. Utilization of relatively inexpensive molten salts also allows a period of heat storage, enabling the release of energy overnight.

Within Concentrated Solar Power (CSP) applications molten salts can be used as Heat Transfer Fluids (HTF) and/or as for Thermal Energy Storage (TES). TES technology is key for the efficiencies of solar thermal plants, HTF's allow electricity to be generated when there is no sunlight present. Molten salts can be used to improve plant efficiency and reduce cost by allowing more efficient device operation. For maximum efficiency, it is desired that the salts should have a low melting point and high temperature stability. The wider the working range the more effective the salt will be, working range is the operating temperature between the melting point and high temperature decomposition of the material. Two traditionally popular salt mixtures have been Solar Salt, a binary mixture of sodium nitrate ($NaNO_3$) and potassium nitrate (KNO_3), and HITEC (53 wt% KNO_3 – 40 wt% Sodium Nitrite ($NaNO_2$) – 7 wt% $NaNO_3$)[2,3]. The addition of sodium nitrite to the traditional binary mixture has reduced the melting temperature from 220 °C of the Solar Salt to 142 °C. HITECs upper operating temperatures have been reduced from the Solar Salts 600 °C to 454 °C for long term (and 538 °C for short term behaviour), giving a long term working range of 312 °C. Additions to this ternary mixture have been used to improve the stability somewhat, but little stability above 500 °C has been observed.

Low melting temperature eutectic materials are ideal for heliostat applications[4]. Materials such as Lithium Nitrate ($LiNO_3$), $NaNO_3$ and KNO_3 have eutectic temperature of 120 °C and below[5]. These eutectics and the result of other works[1] show that the melting temperatures of quaternary salts with cations of Ca, K, Li and Na may be reduced to below 100 °C, allowing improved salt performance. In particular Nitrate anions can result in melting points of less than 80 °C, providing large amounts of improvement if the upper decomposition temperatures can remain stable[1].

Metal Chloride salts have been introduced as a viable alternative for higher temperature applications chlorides, these have the advantages of a high latent heat and a high operating temperature (424–700 °C). Metal

[1]College of Engineering, Swansea University, Bay Campus, Fabian Way, Swansea, SA1 8EN, UK. [2]Gervaux Ltd, 79 Davies Road, West Bridgford, Nottingham, NG2 5JB, UK. Correspondence and requests for materials should be addressed to T.O.D. (email: t.o.dunlop@swansea.ac.uk)

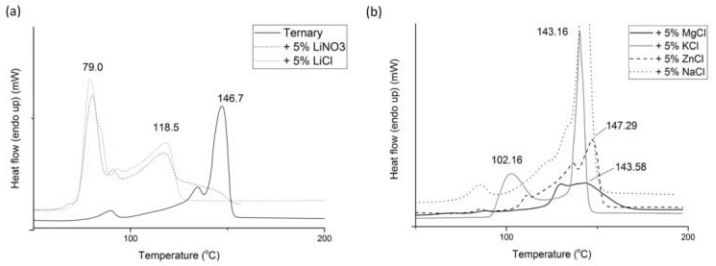

Figure 1. Melting behaviour of Ternary salts with varying chloride additions. Numbers indicate primary phase or state change temperatures.

Chlorides do however have disadvantages including being corrosive and its melting point being considerably higher, reducing its overall usefulness to the concentrated solar power industry. For CSP applications an ideal salt would have a melting point lower than 142 °C and long term stability closer to that of the metal chloride mixtures. The advantages of Li additions have been seen to give lower melting temperatures for ternary mixtures providing potential cost savings when utilised as a transfer fluid[4,6]. Lower melting temperatures may allow an increased temperature differential, allowing a greater operating range and increasing the energy stored per kg[7].

This work develops the combination of the commercial HITEC salt mixture with a variety of metal chlorides to create quaternary salts with the optimised properties for CSP.

Initial work into undisclosed chloride additions was undertaken by Peng *et al.*, however whilst this work showed an improvement in salt operating temperatures it failed to state which additions were tested[2,8]. A wide variety of metal chlorides were tested within this study, with their melting points initially compared to a standard HITEC salt to ensure no increases in melting behaviour occur with salt additions. Chosen salts were then tested for their thermal decomposition. Data was obtained through use of Thermo-Gravimetric Analysis – Differential Scanning Calorimetry (TGA-DSC) techniques. The top performing quaternary mixtures were investigated further using long term stability tests w to prove overall lifespan.

Results and Discussion

Melting behavior of salts. Initially, a ternary salt of 53 wt% KNO_3, 40 wt% $NaNO_2$ and 7 wt% $NaNO_3$ was tested using the DSC to serve as a control. This control showed a melting point of 146.7 °C, in agreement with other literature[9]. Following this a selection of salt additions of 5 wt% were prepared and tested in the DSC. Figure 1 shows the onset of melting for each mixture. It was seen that the additions of Magnesium Chloride ($MgCl_2$) and Zinc Chloride ($ZnCl_2$) both result in a reduction in the heat flow comparted to the ternary salt, as seen by the significant decrease in intensity. These $MgCl_2$ and $ZnCl_2$ also show no improvement in melting temperature, with the melting points being 143.58 and 147.29 °C respectively. Both have partial melting but the lower latent heat and lack of complete melting is undesirable. Sodium Chloride (NaCl) and Potassium Chloride (KCl) additions do not adjust the melting point considerably in comparison to the standard ternary salt, which allows these to be taken through for further study. LiCl was the most promising addition as the endotherm peak is significantly shifted down to 79 °C. This is an interesting addition of the Li salt. Whilst LiCl displays large amounts of deliquescence pre-treatments were undertaken in an attempt to minimise its impact on this study. These pre-treatments include keeping the salts in a low humidity environment, with heating remove any moisture prior to testing. For salt usage this may present a number of problems and salts would have to be kept moisture free prior to installation into the system, with care to prevent moisture ingress taken when in use. Pressure release valves may be needed to allow absorbed water to be removed at temperature without damaging the system. It can be seen that this is a direct result of the Li metal, as $LiNO_3$ also has a similar drop. The melting point of pure LiCl is over 600 °C whilst $LiNO_3$ is over 250 °C, so it can be assumed a new phase is being formed with the current eutectic. The molar ratios of these salts result in a significantly higher amount of Li cations being present in the LiCl mixtures. It is likely that as seen with the other salts Cl doesn't cause the melting point to drop and in some cases raises it, this has a stabilising effect on the melting behaviour reducing the impact of the increased Li+ cation additions on the eutectic melt.

Decomposition of salts. Short term behaviour of the chosen additions was tested using the TGA technique. Initial investigations showed metal-chlorides additions resulted in a stabilisation effect, as indicated by Peng *et al.*[2,9]. Onset of rapid decomposition was set at a weight of 99%, a 93% weight allowed the initial and rapid levels of degradation to be compared. Rapid decomposition was seen in the ternary control mixture at 610 °C as shown in Fig. 2(a). 5 wt% KCl additions resulted in a stability increase of 38 °C to 741 °C. Further additions of KCl result in further stability improvements. KCl has a large stabilisation effect allowing the operation at higher temperatures for periods of less than 30 minutes.

Lithium Chloride (LiCl) additions behave differently, with an increase in weight observed as shown in Fig. 2(b) suggesting oxidation. There is an initial stabilisation effect caused by the LiCl, allowing the sample to reach 685 °C before weight loss occurs. Additions of LiCl above 5 wt% result in a reduction in stability, this is

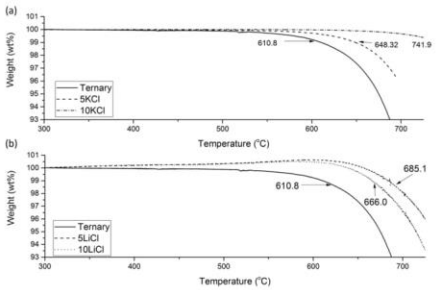

Figure 2. TGA analysis of the short term stability of (**a**) KCl; and (**b**) LiCl additions.

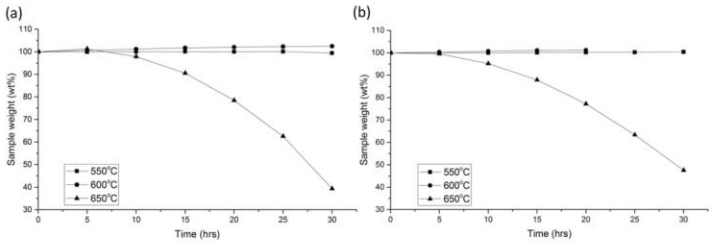

Figure 3. Long term decomposition of (**a**) ternary and (**b**) 5 wt%KCl addition salts.

shown by the lower temperature of decomposition seen in Fig. 2b. $LiNO_3$ shows a reduced the decomposition temperature compared to many other nitrates[1], it is believed that the Cl within the melt may aid in stabilisation, whilst the Li can cause some short-term instability decreases. Due to the melting behaviour similarities with $LiNO_3$ and LiCl additions it is believed that the Li cation is separated from the Cl anion and reacts with the current nitrates in a similar way to that of the $LiNO_3$ salt[10]. This implies a similar eutectic phase has been formed. Previous studies have shown that the $LiNO_3$ phase is unstable within salt mixtures, degrading into Li_2O_2 and Li_2O. These should exhibit peaks at 33° for Li_2O_2 and 34.8, 39 and 46.8° for Li_2O. The Li_2O_2 peak is clearly identifiable in the LiCl salt, with some evidence of the Li_2O peaks also being present, which possibly contribute to the structure changes, seen later in this work, with the larger eutectic phase. Similarly during the solidification, the Cl is located in the discrete lighter shaded phases. This Cl heavy phases solidifies first and will remain as a small amount of particulates in the melt, with the Li rich phase allowing earlier melting

Long term stability of salts. Long term stabilities were tested using standard muffle furnaces over the 30-hour time span. Long term tests showed a noticeable variation in long term stability with additions of both KCl and LiCl. Any weight gains shown in Figs 3 and 4 can be attributed to oxidation of the salts. It can be seen in Fig. 3(b) that 5 wt% KCl does provide a small improvements, with no weight gain below 600 °C. The ternary salt, seen in Fig. 3(a), can be seen toshow a 5 wt% gain at 600 °C indicating some oxidation reaction. Figure 4(b) allows the coparison of varying chloride additions after 30 hours at 650 °C. Figure 4(a) shows the weight loss of salts at 650 °C. This shows that the weight loss was 60.1% for the ternary salt, whilst a 5 wt% addition of KCl reduces this weight loss to 52.4 wt%. Weight loss of the all salts was low at 550 and 600 °C, possibly due to some cooling in the furnace. Small weight gains are seen in the ternary salt at all temperatures, most probably due to the conversion between NO_2 to NO_3. The most noticeable improvement is with the addition of LiCl, where a 5 wt% addition results in a weight loss of only 24.84 wt%. Figure 4(b) also shows that there is little or no improvement with additions of higher than 5 wt% LiCl additions. This ties up the data from the short-term experimentation.

XRD analysis. In order to determine the phases present, pure salts were initially scanned and used to identify the peaks of pure salt, other phases were sourced from an open database. Figure 5 shows the effect of the LiCl additions on the solid crystal structure of the ternary salts. There are 6 noticeable increases in peaks and two significantly reduced peaks with the addition of LiCl, marked by x and n respectively in Fig. 5. These peak increases are seen in both the LiCl containing samples and decomposed ternary samples (Fig. 5b and c). It is likely the LiCl allows for a room temperature transformation to produce a phase that shares a similar crystal structure to that of

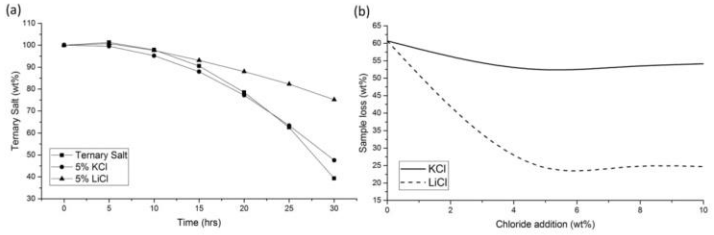

Figure 4. (**a**) Decomposition behaviour at 650 °C; (**b**) Salt weight loss after 30 hours at 650 °C.

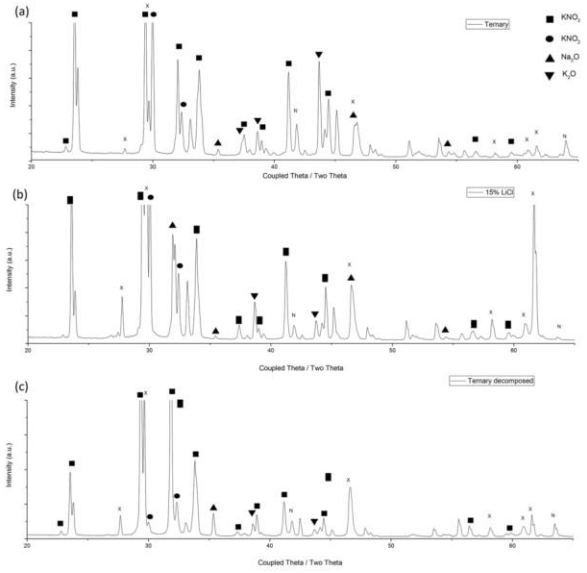

Figure 5. XRD trace of (**a**) ternary salt; (**b**) 5 wt% LiCl addition; and (**c**) ternary salt after 30 hours at 650 °C.

the decomposed ternary phase. The most likely decomposition phase, Sodium oxide (Na_2O), would increase the melting point. This is seen to form in the LiCl samples, however it doesn't raise the melting point of the eutectic, so it may be an additional phase. Given the change in melting point it can be assumed that the peaks, marked x in Fig. 5, (27.72, 29.7, 46.6, 58.2, 60.9 and 61.7) correspond to a beneficial phase that enables the more rapid melting.

Following the resultant decomposition of the ternary phase, there is a reduction in the primary KNO_2 peak and an increase in the peak relating to KNO_3. This is indicative of an oxidation reaction occurring. There is a noticeable increase in the Na_2O peaks, whilst a few peaks relating to KNO_2 and K_2O decrease, indicating that these are the primary phases decomposing. A similar peak (at 27.72°) can be seen in the XRD trace obtained in the case of HITEC with LiCl additions to that observed in the case of the decomposition phase. An increase in the peaks relating to Na_2O are also present in both curves. Na_2O is a high temperature phase that should remain solid until 1132 °C, however no signs of any solid are present at elevated temperatures, indicating that it is dissolving into the melt.

Resultant decomposition phases for ternary and LiCl containing phases are remarkably close to each other, indicating that the same bulk decomposition is occurring through the same process. There is less weight loss with

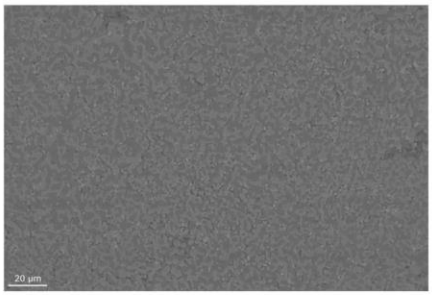

Figure 6. SEM image of Ternary Salt.

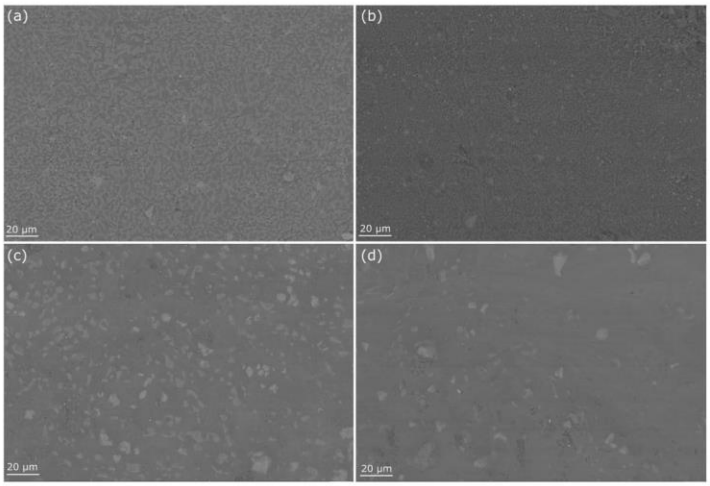

Figure 7. SEM images of Chloride additions (**a**) 10% KCl, (**b**) 20% KCl, (**c**) 10% LiCl and (**d**) 20% LiCl.

the LiCl stabilising addition, possibly due to binding of Na and O_2 preventing further oxidation and decomposition. There is a new decomposition phase forming with the LiCl indicated by the increase in peaks, particularly at 22°.

SEM imaging. In addition to attempting to determine phases with XRD, SEM imaging allowed the viewing of the solidified structure of the material. A standard ternary salt, shown in Fig. 6, has a fine structure with 3 separate phases possible to identify using Back Scatter Electrons. With the addition of KCl (see Fig. 7a and b), there is a slight increase in one phase, most likely a high potassium phase like K_2O. This changes the morphology of the salts makeup giving larger dendritic like structures. However due to the penetration depth of the electrons when using EDS analysis, it is difficult to scan phases without viewing deeper into the sample resulting in a mixed reading. Figure 7 show higher salt additions than that discussed in the prior data. Whilst the structural changes are still detectable at lower addition levels, by providing an overdose of salt within the salt we are able to exaggerate the microstructure to make it more visible.

Lithium additions (Fig. 7(c) and (d)) are seen to have a much greater effect on the solid structure of the salts. Although due to the limitations of the EDS it is impossible to detect Li within a phase, the structural changes are noticeable, with considerable increases in the darkest matrix phase. This can be related to the increase in Li

present, relating nicely to the generation of additional phases detected on the XRD. There are slight concentration variations within the darker matrix, seen in the Fig. 7d as shade variations. These are difficult to identify in the EDS software, as Li, which is a likely constitute of these phases, cannot be detected.

Conclusions

In comparison to the standard ternary HITEC salt, the additions of metal chlorides showed an overall improvement in the long-term stability of the salts. Additions of KCl and LiCl are shown to not raise the eutectic melting point of the salts, ensuring no detrimental effects on salt performance. The addition of 5 wt% LiCl allowed partial melting prior to the 140 °C eutectic point, further increasing the operating range of the material within solar-thermal generation and thermal storage applications.

Analysis indicates a new phase has been formed with the LiCl additions, which at room temperature allows more rapid melting. Small additions of LiCl reduce the weight loss over long time periods from 61% to 25% in comparison to standard ternary salts. Given $LiNO_3$ additions did not result in the stability increase seen with LiCl, it can be deduced that additional Nitrates do not improve stability and that Cl is the initial stabilising agent. With the Li in this case, allowing a phase with a lower melting temperature to be formed. Overall, small LiCl additions can potentially allow the standard HITEC salt to be molten from 100 °C, then reach over 630 °C in the short term, with the potential to operate longer term at temperatures above 550 °C, with no signs of oxidation. This provides a potential working range improvement of over 100 °C in comparison to the standard HITEC salt.

Materials and Methods

Materials and synthesis. Quaternary eutectic salts were prepared by mixing individual component salts, with analytical reagent grade materials being sourced from Sigma-Aldrich, and kept in a vacuum to dry prior to weighing and mixing. The preparation is explained in detail in other works[2,9]. The HITEC mixture (53 wt% KNO_3 – 40 wt% $NaNO_2$ – 7 wt% $NaNO_3$) was prepared initially, with additions of chlorides added later (KCl, LiCl, CaCl, ZnCl, NaCl and MgCl). After mixing, salts were heated to 200 °C for 2 hours to allow melting and homogeneity to be reached ready for testing.

Experimental procedure. Differential Scanning Calorimetry (Perkin Elmer – DSC 4000) was used to generate the actual eutectic melting point of the mixtures. With this method, 10–20 mg of sample were put in to an Aluminium pan, alongside an empty reference pan. Samples were heated at a standard rate of 20 °C/min, to 300 °C, in a nitrogen atmosphere with a 20 mL/min flow rate[11]. This cycle was completed twice, to ensure any moisture absorbed was is removed in the first run.

Following this, a Simultaneous Thermal Analysis (Perkin Elmer – STA 6000) was used to examine the short-term decomposition behaviour. 1–20 mg samples were placed into an Alumina crucible and heated at a slower rate of 10 °C/minute in air to 700 °C. For long term decomposition, 10 g of salt were placed in porcelain crucibles for periods of up to 30 hours, where they were heated to 550, 600 and 650 °C. Ramp rates of 3.5 °C/min were used to ensure the crucibles did not fracture and weight measurements were taken every 5 hours. Due to the ability of LiCl to absorb water all salts were mixed in a low humidity environment to reduce any moisture absorption.

Powder analysis X-Ray Diffraction (XRD) was undertaken on a D8 Discover (Bruker), with a Cu source (40 kV, 40 mA). Scans were taken at 20–60 2θ over a period of 20 min. The phase matching was completed using the Crystallographic Online Database[12].

Scanning Electron Microscopy (SEM) was undertaken using a Zeiss Evo SEM, using a tungsten source set to 10 kV with a probe current of 250pA. A oxford instruments backscatter electron (BSE) detector was used to generate an image with contrast for each of the phases at 500 × zoom. Prior to weight loss and SEM preparation all samples were preheated and held at 160 °C and held for an hour. This allowed any retained water to be removed ready for testing.

References

1. Bauer, T., Breidenbach, N. & Eck, M. Overview of molten salt storage systems and material development for solar thermal power plants. in *World Renewable Energy Forum* 1–8 (2012).
2. Peng, Q., Ding, J., Wei, X., Yang, J. & Yang, X. The preparation and properties of multi-component molten salts. *Appl. Energy* **87**, 2812–2817 (2010).
3. YongChang, C., YuTing, W., Nan, R. & ChongFang, M. Experimental study of viscosity characteristics of high-temperature heat transfer molten salts. *Sci. China Technol. Sci.* **54**, 3022–3026 (2011).
4. Cabeza, L. F. *et al*. Lithium in thermal energy storage: A state-of-the-art review. *Renew. Sustain. Energy Rev.* **42**, 1106–1112 (2015).
5. Villada, C., Bolívar, F., Jaramillo, F., Castaño, J. G. & Echeverría, F. Thermal evaluation of molten salts for solar thermal energy storage. *Renew. Energy Power Qual. J.* 622–625 (2014).
6. Zhou, D. & Eames, P. Thermal characterisation of binary sodium/lithium nitrate salts for latent heat storage at medium temperatures. *Sol. Energy Mater. Sol. Cells* **157**, 1019–1025 (2016).
7. Mancini, T. R., Gary, J. A., Kolb, G. J. & Ho, C. K. *Power Tower Technology Roadmap and cost reduction plan*. https://doi.org/10.2172/1011644 (2011).
8. Peng, Q., Wei, X., Ding, J., Yang, J. & Yang, X. High-temperature thermal stability of molten salt materials. *Int. J. Energy Res.* **32**, 1164–1174 (2008).
9. Peng, Q., Yang, X., Ding, J., Wei, X. & Yang, J. Design of new molten salt thermal energy storage material for solar thermal power plant. *Appl. Energy* **112**, 682–689 (2013).
10. Wang, T., Mantha, D. & Reddy, R. G. Thermal stability of the eutectic composition in $LiNO_3$–$NaNO_3$–KNO_3 ternary system used for thermal energy storage. *Sol. Energy Mater. Sol. Cells* **100**, 162–168 (2012).
11. Williams, A. E. *et al*. Perovskite processing for photovoltaics: a spectro-thermal evaluation. *J. Mater. Chem. A* **2**, 19338–19346 (2014).
12. Grazulis, S. *et al*. Crystallography Open Database (COD): An open-access collection of crystal structures and platform for world-wide collaboration. *Nucleic Acids Res.* **40**, 420–427 (2012).

Acknowledgements

The financial support from the Sêr Cymru National Research Network (NRN072) in Advanced Engineering and Materials (AEM) and the EPSRC, through COATED CDT (EP/K503228/1), is greatly appreciated, and without which this work would not be possible. Support from Materials and Manufacturing Academy and the Advanced Imaging of Materials (AIM) Swansea is also greatly appreciated. The authors would also like to thank Dr N. Wint and Miss S.-J. Potts for their proof reading and suggestions. Further Support was provided by the European Space Agency and Scatec No.

Author Contributions

T.D. wrote the main manuscript text and prepared all figures. D.J. and W.V. are the industrial supervisors for this project, and J.S. was the project coordinator. D.J., W.V. and J.S. provided direction, ideas and co-ordination, as well as improvements to the paper. All authors reviewed the manuscript.

Additional Information

Competing Interests: The authors declare no competing interests.

Publisher's note: Springer Nature remains neutral with regard to jurisdictional claims in published maps and institutional affiliations.

Bibliography

1. Araiz, M., Catalan, L., Herrero, O., Perez, G. & Rodriguez, A. The Importance of the Assembly in Thermoelectric Generators. in *Bringing Thermoelectricity into Reality* (2018).

2. U.S. Department of Energy. *Thermoelectric Materials , Devices and Systems : Technology Assessment*. (2014).

3. Thirugnanasambandam, M., Iniyan, S. & Goic, R. A review of solar thermal technologies. *Renew. Sustain. Energy Rev.* **14,** 312–322 (2010).

4. Hamid Elsheikh, M. *et al.* A review on thermoelectric renewable energy: Principle parameters that affect their performance. *Renew. Sustain. Energy Rev.* **30,** 337–355 (2014).

5. Alam, H. & Ramakrishna, S. A review on the enhancement of figure of merit from bulk to nano-thermoelectric materials. *Nano Energy* **2,** 190–212 (2013).

6. Fedorov, M. I. Thermoelectric Silicides : Past, Present and Future. *J. Thermoelectr.* **2,** 51–60 (2009).

7. Vullers, R. J. M., van Schaijk, R., Doms, I., Van Hoof, C. & Mertens, R. Micropower energy harvesting. *Solid. State. Electron.* **53,** 684–693 (2009).

8. Kraemer, D., McEnaney, K., Chiesa, M. & Chen, G. Modeling and optimization of solar thermoelectric generators for terrestrial applications. *Sol. Energy* **86,** 1338–1350 (2012).

9. ESA - New Materials and Energy Unit & Directorate of Human Spaceflight and Operations - Promotions Office. ThermoMag Project. Objectives (2011). Available at: http://www.thermomag-project.eu/objectives.html.

10. Prytuliak, A. *ThermoMag - 1st lecture on Thermoelectricity*. (European Space Agency, 2013).

11. Stark, J. P. W. Chapter 10: Electrical Power Systems. in *Spacecraft Systems Engineering* (eds. Fortescue, P., Swinerd, G. & Stark, J.) 327–355 (Wiley, 2011).

12. Vining, C. B. Desperately seeking silicon. *Nature* **451,** 132–133 (2008).

13. Vining, C. B. The Limited Role for Thermoelectrics in the Climate Crisis. in *Nanotechnology and New Materials* 1–10 (2008).

14. LeBlanc, S., Yee, S. K., Scullin, M. L., Dames, C. & Goodson, K. E. Material and manufacturing cost considerations for thermoelectrics. *Renew. Sustain. Energy Rev.* **32,** 313–327 (2014).

15. Finger, H. B. & Schulman, F. Power requirements of the NASA space program. in *Space Power Systems* (ed. Snyder, N. W.) 634–643 (American Institute of Aeronautics and Astronautics).

16. McClelland, D. H. Solar Concentrators for High Temperature Space Power Systems. in *Space Power Systems* 147–170 (1960).

17. Leicester, U. of. *Enabling Tech for space exploration Missions*.

18. Poinas, P., Vikhor, L., Lenior, B., Dausher, A. & Scherrer, H. Solar

Thermoelectric Generators based on Advanced Thermoelectric Materials. *21st Int. Conf. Thermoelectr.* 395–399 (2002).

19. Fleurial, J. *et al.* Thermoelectrics: From Space Power Systems to Terrestrial Waste Heat Recovery Applications. (2011).

20. Thiele, A. W. & Coombs, M. G. SNAP Thermoelectric Systems. in *Space Power Systems* 351–358

21. Bloom, J. L. & Weddel, J. B. Thirteen-Watt Isotope-powered Thermoelectric generators for space and lunar imace missions. in *Space Power Systems* (ed. Snyder, N. W.) 503–536 (American Institute of Aeronautics and Astronautics).

22. Jet Propulsion Laboratory. Mars Science Laboratory / Curiosity. *NASA* (2012).

23. JPL & NASA. Voyager Mission Operations Status Report. (2014). Available at: http://voyager.jpl.nasa.gov/mission/weekly-reports/index.htm. (Accessed: 24th April 2014)

24. Deng, Y., Zhu, W., Wang, Y. & Shi, Y. Enhanced performance of solar-driven photovoltaic–thermoelectric hybrid system in an integrated design. *Sol. Energy* **88,** 182–191 (2013).

25. Lewis, N. S., Crabtree, G., Nozik, A. J., Wasielewski, M. R. & Alivisatos, P. *Basic Research Needs for Solar Energy Utilization*. (2005).

26. Solar, C. CSP : bright future for linear fresnel technology ? 48–50 (2008).

27. Li, P. *et al.* Design of a Concentration Solar Thermoelectric Generator. *J. Electron. Mater.* **39,** 1522–1530 (2010).

28. Atticus Digital. Solar Energy 3D animation by Atticus Digital for Tessera Solar Suncatcher. (2009). Available at: www.atticusdigital.com/Tessera_Solar_Suncatcher. (Accessed: 26th May 2014)

29. Xie, M. & Gruen, D. M. Potential impact of ZT = 4 thermoelectric materials on solar thermal energy conversion technologies. *J. Phys. Chem. B* **114,** 14339–42 (2010).

30. Fuschillo, N., Gibson, R., Eggleston, F. & Epstein, J. Solar Thermoelectric Generator for Near-Earth Space Applications. *IEEE Trans. Electron Devices* **13,** 426–432 (1966).

31. MacDonald, D. *Thermoelectricity: An introduction to the principles*. (2006).

32. Zwolenski, P., Tobola, J. & Kaprzyk, S. A Theoretical Search for Efficient Dopants in Mg2X (X = Si, Ge, Sn) Thermoelectric Materials. *J. Electron. Mater.* **40,** 889–897 (2011).

33. Khan, A. U., Vlachos, N. & Kyratsi, T. High thermoelectric figure of merit of Mg2Si0.55Sn0.4Ge0.05 materials doped with Bi and Sb. *Scr. Mater.* **69,** 606–609 (2013).

34. Chen, X. *et al.* Effects of (Al,Ge) double doping on the thermoelectric properties of higher manganese silicides. *J. Appl. Phys.* **114,** 173705 (2013).

35. Saleemi, M. *et al.* Spark plasma sintering and thermoelectric evaluation of nanocrystalline magnesium silicide (Mg2Si). *J. Mater. Sci.* **48,** 1940–1946 (2012).

36. Tani, J., Takahashi, M. & Kido, H. First-principles calculation of impurity doping into Mg2Ge. *J. Alloys Compd.* **485,** 764–768 (2009).

37. Alleno, E., Gaborit, M., Ohorodniichuk, V., Lenoir, B. & Rouleau, O. Effect of Nanostructuring on the Thermoelectric Properties of Co0.97Pd0.03Sb3. *J. Electron. Mater.* **42,** 1835–1839 (2013).

38. Tani, J. & Kido, H. First-principles and experimental studies of impurity doping into Mg2Si. *Intermetallics* **16,** 418–423 (2008).

39. Il-Ho, K., Jae-Yong, J., Soon-Mok, C., Won-Seon, S. & Sun-Uk, K. Synthesis of Thermoelectric Mg_2Si by Mechanical Alloying. *J. Korean Phys. Soc.* **57,** 1005 (2010).

40. Zhou, A., Cui, H., Li, J., Zhu, T. & Zhao, X. Bulk higher manganese silicide thermoelectric materials and modules. *Procedia Eng.* **27,** 94–102 (2012).

41. Yoon, S. *et al.* The Effect of Grain Size and Density on the Thermoelectric Properties of Bi2Te3-PbTe Compounds. *J. Electron. Mater.* **42,** 3390–3396 (2013).

42. Martín-González, M., Caballero-Calero, O. & Díaz-Chao, P. Nanoengineering thermoelectrics for 21st century: Energy harvesting and other trends in the field. *Renew. Sustain. Energy Rev.* **24,** 288–305 (2013).

43. Vineis, C. J., Shakouri, A., Majumdar, A. & Kanatzidis, M. G. Nanostructured thermoelectrics: big efficiency gains from small features. *Adv. Mater.* **22,** 3970–80 (2010).

44. Varghese, T. *et al.* High-performance and flexible thermoelectric films by screen printing solution-processed nanoplate crystals. *Sci. Rep.* **6,** 6–11 (2016).

45. Fedorov, M. I. & Zaitsev, V. K. The features of silicide thermoelectrics development. 1–6 (1958).

46. Liu, W., Yin, K., Zhang, Q., Uher, C. & Tang, X. Eco-friendly high-performance silicide thermoelectric materials. *Natl. Sci. Rev.* **4,** 611–626 (2017).

47. Liu, W. Di, Chen, Z. G. & Zou, J. Eco-Friendly Higher Manganese Silicide Thermoelectric Materials: Progress and Future Challenges. *Adv. Energy Mater.* **1800056,** 1–18 (2018).

48. Yang, J., Fan, Q., Ding, Y. & Cheng, X. Predicting thermoelectric performance of eco-friendly intermetallic compound p-type CaMgSi from first-principles investigation. *J. Alloys Compd.* **752,** 85–92 (2018).

49. Luo, W., Li, H., Fu, F., Hao, W. & Tang, X. Improved Thermoelectric Properties of Al-Doped Higher Manganese Silicide Prepared by a Rapid Solidification Method. *J. Electron. Mater.* **40,** 1233–1237 (2011).

50. Wang, H., Jin, H., Chu, W. & Guo, Y. Thermodynamic properties of Mg2Si

and Mg2Ge investigated by first principles method. *J. Alloys Compd.* **499,** 68–74 (2010).

51. Zaitsev, V. *et al.* Highly effective Mg2Si1−xSnx thermoelectrics. *Phys. Rev. B* **74,** 045207 (2006).

52. You, S.-W. *et al.* Solid-State Synthesis and Thermoelectric Properties of Al-Doped Mg2Si. *J. Electron. Mater.* **41,** 1675–1679 (2011).

53. Choi, S.-M., Kim, K.-H., Kim, I.-H., Kim, S.-U. & Seo, W.-S. Thermoelectric properties of the Bi-doped Mg2Si system. *Curr. Appl. Phys.* **11,** S388–S391 (2011).

54. Jung, J.-Y., Park, K.-H. & Kim, I.-H. Thermoelectric Properties of Sb-doped Mg 2 Si Prepared by Solid-State Synthesis. *IOP Conf. Ser. Mater. Sci. Eng.* **18,** 142006 (2011).

55. Muthiah, S. *et al.* Double-Doping Approach to Enhancing the Thermoelectric Figure-of-Merit of n-Type Mg2Si Synthesized by Use of Spark Plasma Sintering. *J. Electron. Mater.* (2014). doi:10.1007/s11664-013-2944-x

56. Wang, S. & Mingo, N. Improved thermoelectric properties of Mg[sub 2]Si[sub x]Ge[sub y]Sn[sub 1−x−y] nanoparticle-in-alloy materials. *Appl. Phys. Lett.* **94,** 203109 (2009).

57. Akasaka, M. *et al.* Non-wetting crystal growth of Mg2Si by vertical Bridgman method and thermoelectric characteristics. *J. Cryst. Growth* **304,** 196–201 (2007).

58. Ioannou, M., Chrissafis, K., Pavlidou, E., Gascoin, F. & Kyratsi, T. Solid-state synthesis of Mg2Si via short-duration ball-milling and low-temperature annealing. *J. Solid State Chem.* **197,** 172–180 (2013).

59. Xiong, W., Qin, X., Kong, M. & Chen, L. Synthesis and properties of bulk nanocrystalline Mg& through ball-milling and reactive hot-pressing. *Trans. Nonferrous Met. Soc. China* **16,** 987–991 (2006).

60. Jin, H., Rae, Y. & Kim, I. Processing Research Synthesis of thermoelectric Mg 2 Si by a solid state reaction. **12,** 16–20 (2011).

61. Shanks, H. R. The growth of magnesium germanide crystal. *J. Cryst. Growth* **23,** 190–194 (1974).

62. Savary, E., Gascoin, F., Marinel, S. & Heuguet, R. Spark plasma sintering of fine Mg2Si particles. *Powder Technol.* **228,** 295–300 (2012).

63. Ersit, U. N. R., Bianco, R., Harper, M. A. & Rapp, R. A. Codeposition of Elements in Diffusion Coatings by Halide-Activated Pack Cementation Method. (1991).

64. Stathokostopoulos, D. *et al.* Formation of Mg2Si thick films on Si substrates using pack cementation process. **203,** 203–206 (2012).

65. Stathokostopoulos, D. *et al.* Structure, morphology and electrical properties of Mg2Si layers deposited by pack cementation. *Appl. Surf. Sci.* **285,** 417–424 (2013).

66. Stathokostopoulos, D. *et al.* Experimental and thermodynamic considerations of Mg2Si coatings deposited by pack cementation process. *Superlattices Microstruct.* **101,** 76–86 (2017).

67. Tong, L., Dengzun, Y. & Chungen, Z. Low-temperature Formation of Aluminide Coatings on Ni-base Superalloys by Pack Cementation Process. *Chinese J. Aeronaut.* **23,** 381–385 (2010).

68. Cockeram, B. V. Growth and oxidation resistance of boron-modified and germanium-doped silicide diffusion coatings formed by the halide-activated pack cementation method. *Surf. Coatings Technol.* **76–77,** 20–27 (1995).

69. Naji, A., Galetz, M. C. & Schütze, M. Design of Diffusion Coatings Developed via Pack Cementation. (2014).

70. Villada, C., Bolívar, F., Jaramillo, F., Castaño, J. G. & Echeverría, F. Thermal evaluation of molten salts for solar thermal energy storage. *Renew. Energy Power Qual. J.* 622–625 (2014).

71. YongChang, C., YuTing, W., Nan, R. & ChongFang, M. Experimental study of viscosity characteristics of high-temperature heat transfer molten salts. *Sci. China Technol. Sci.* **54,** 3022–3026 (2011).

72. Peng, Q., Wei, X., Ding, J., Yang, J. & Yang, X. High-temperature thermal stability of molten salt materials. *Int. J. Energy Res.* **32,** 1164–1174 (2008).

73. Peng, Q., Ding, J., Wei, X., Yang, J. & Yang, X. The preparation and properties of multi-component molten salts. *Appl. Energy* **87,** 2812–2817 (2010).

74. Cabeza, L. F. *et al.* Lithium in thermal energy storage: A state-of-the-art review. *Renew. Sustain. Energy Rev.* **42,** 1106–1112 (2015).

75. Bauer, T., Breidenbach, N. & Eck, M. Overview of molten salt storage systems and material development for solar thermal power plants. in *World Renewable Energy Forum* 1–8 (2012).

76. Zhou, D. & Eames, P. Solar Energy Materials & Solar Cells Thermal characterisation of binary sodium / lithium nitrate salts for latent heat storage at medium temperatures. *Sol. Energy Mater. Sol. Cells* **157,** 1019–1025 (2016).

77. Mojaki, S. C., Bhardwaj Mishra, S., Mishra, A. K. & Mofokeng, J. P. Influence of polysiloxane as nanofiller on the surface, optical and thermal properties of guar gum grafted polyaniline matrix. *Int. J. Biol. Macromol.* **114,** 441–452 (2018).

78. Ansari, R. & Keivani, M. B. Polyaniline Conducting Electroactive Polymers: Thermal and Environmental Stability Studies. *E-Journal Chem.* **3,** 202–217 (2006).

79. Conduction mechanisms in PANI.pdf.

80. Yu, Z., Xia, Y., Du, D. & Ouyang, J. PEDOT:PSS Films with Metallic Conductivity through a Treatment with Common Organic Solutions of Organic Salts and Their Application as a Transparent Electrode of Polymer Solar Cells. *ACS Appl. Mater. Interfaces* **8,** 11629–11638 (2016).

81. Kumar, D. & Sharma, R. C. Advances in Conductive Polymers. *Eur. Polym. J.* **34,** 1053–1060 (1998).

82. Heeger, A. J. Charge storage in conducting polymers: Solitons, polarons, and bipolarons. *Polymer Journal* **17,** 201–208 (1985).

83. Dai, L. Conducting Polymers. *Intell. Macromol. Smart Devices* **1980,** 41–80 (2004).

84. Dai, L. Conducting Polymers. *Intell. Macromol. Smart Devices* **1980,** 41–80 (2004).

85. Brédas, J. L., Chance, R. R. & Silbey, R. Comparative theoretical study of the doping of conjugated polymers: Polarons in polyacetylene and polyparaphenylene. *Phys. Rev. B* **26,** 5843–5854 (1982).

86. Lowell, M. Carbon Black Filled Conducting Polymers and Polymer Blends. **21,** 299–313 (2002).

87. Kaur, G., Adhikari, R., Cass, P., Bown, M. & Gunatillake, P. Electrically conductive polymers and composites for biomedical applications. *RSC Adv.* **5,** 37553–37567 (2015).

88. Yu, Z., Xia, Y., Du, D. & Ouyang, J. PEDOT : PSS Films with Metallic Conductivity through a Treatment with Common Organic Solutions of Organic Salts and Their Application as a Transparent Electrode of Polymer Solar Cells. *Appl. Mater. Interfaces* **8,** 11629–11638 (2016).

89. Gelves, B. G. A., Lin, B., Sundararaj, U. & Haber, J. A. Low Electrical Percolation Threshold of Silver and Copper Nanowires in Polystyrene Composites **. 2423–2430 (2006). doi:10.1002/adfm.200600336

90. Du, F., Fischer, J. & Winey, K. Effect of nanotube alignment on percolation conductivity in carbon nanotube/polymer composites. *Phys. Rev. B* **72,** (2005).

91. Bourrat, X. BLACK : STRUCTURE AND PROPERTIES. **31,** 287–302 (1993).

92. Miyasaka, K. *et al.* Electrical conductivity of carbon - polymer composites as a function of carbon content. *J. Mater. Sci.* **17,** 1610–1616 (1982).

93. Donaldson, K. *et al.* Carbon Nanotubes: A Review of Their Properties in Relation to Pulmonary Toxicology and Workplace Safety. *Toxicol. Sci.* **92,** 5–22 (2006).

94. Donaldson, K. Carbon Nanotube Health Hazard. (2016).

95. Phillips, C., Al-Ahmadi, A., Potts, S. J., Claypole, T. & Deganello, D. The effect of graphite and carbon black ratios on conductive ink performance. *J. Mater. Sci.* **52,** 9520–9530 (2017).

96. Boonstra, B. B. & Medalia, A. I. Effect of Carbon Black Dispersion on the Mechanical Properties of Rubber Vulcanizates. *Rubber Chem. Technol.* **36,** 115–142 (1963).

97. Sengupta, R., Bhattacharya, M., Bandyopadhyay, S. & Bhowmick, A. K. A review on the mechanical and electrical properties of graphite and modified graphite reinforced polymer composites. *Prog. Polym. Sci.* **36,** 638–670 (2011).

98. Pavel MACH, R. R. Electrically Conductive Adhesives With Micro-Nano Filler. (2011).

99. Kell, A. J. *et al.* Versatile Molecular Silver Ink Platform for Printed Flexible Electronics. *ACS Appl. Mater. Interfaces* **9,** 17226–17237 (2017).

100. Johnsen, G. K. *et al.* Conductivity enhancement of silver filled polymer composites through electric field alignment. *Compos. Sci. Technol.* **72,** 1841–1847 (2012).

101. Mach, P. & Radev, R. Electrically Conductive Adhesives With Micro-Nano Filler. in *NanoCon 2011* (2011).

102. PQ Corp - Conduct-O-Fil. Available at: https://www.pqcorp.com/products/conductive-particles. (Accessed: 6th July 2018)

103. Metashine - Silver Coat Series. Available at: http://www.metashine.com/en/Metashine-Microsite/Metashine/Products/Silver Coat Series. (Accessed: 7th June 2018)

104. GlassFlake - ECR Glass. Available at: http://www.glassflake.com/pages/products/by-product-type/glassflake/ecr-glassflake. (Accessed: 1st August 2018)

105. GlassFlake - AgFlake. Available at: http://www.glassflake.com/pages/products/by-product-type/glassflake/agflake. (Accessed: 1st August 2018)

106. Thermal-oxidative degradation of polymers. *Polymer Properties Database* (2018). Available at: http://polymerdatabase.com/polymer chemistry/Thermal Degradation.html. (Accessed: 29th July 2018)

107. Wacker Chemie AG. *SILRES ® 604 and SILRES ® 605:* (2012).

108. Wacker Chemie AG. *SILRES resins and intermediates - for coatings that dare*. (2015).

109. Dow Corning. *Silicone Resins and Intermediates Selection Guide Discover Innovative Technology*. (2014).

110. Boaretto, N., Horn, T., Popall, M. & Sextl, G. Electrochimica Acta Optimization of the transport and mechanical properties of polysiloxane / polyether hybrid polymer electrolytes. *Electrochim. Acta* **241,** 477–486 (2017).

111. Jewell, E. H., Hamblyn, S. M., Claypole, T. C. & Gethin, D. T. The impact of carbon content and mesh on the characteristics of screen printed conductive structures. *Circuit World* **39,** 13–21 (2013).

112. Saravanan, R. & Robert, M. C. Local structure of the thermoelectric material Mg2Si using XRD. *J. Alloys Compd.* **479,** 26–31 (2009).

113. Zhou, D. & Eames, P. Thermal characterisation of binary sodium/lithium nitrate salts for latent heat storage at medium temperatures. *Sol. Energy Mater. Sol. Cells* **157,** 1019–1025 (2016).

114. Floros, M. C., Kaller, K. L. C., Poopalam, K. D. & Narine, S. S. Lipid derived

diamide phase change materials for high temperature thermal energy storage. *Sol. Energy* **139,** 23–28 (2016).

115. Celina, M. C. Review of polymer oxidation and its relationship with materials performance and lifetime prediction. *Polym. Degrad. Stab.* **98,** 2419–2429 (2013).

116. Taylor, C., Elvins, J., Sullivan, J. & Worsley, D. Corrosion Performance Evaluation of Zn/Al Galvanized Steels Using the Scanning Vibrating Electrode Technique (SVET). *ECS Trans.* **13,** 95–103 (2008).

117. Monaghan, B. J. A Four-Probe dc Method for Measuring the Electrical Resistivities of Molten Metals. *Int. J. Thermophys.* **20,** 677–690 (1999).

118. Sigma-Aldrich. *Tellurium Safety Data Sheet*. (2016).

119. Stathokostopoulos, D. *et al.* Thermoelectric properties of Mg 2 Si coatings deposited by pack cementation assisted process on heavily doped Si substrates. *Phys. Status Solidi* **211,** 1308–1314 (2014).

120. Stathokostopoulos, D. *et al.* Formation of the Thermoelectric Candidate Chromium Silicide by Use of a Pack-Cementation Process. *J. Electron. Mater.* **43,** 3733–3739 (2014).

121. Stefanoski, S., Blosser, M. C. & Nolas, G. S. Pressure Effects on the Size of Type‑I and Type-II Si-Clathrates Synthesized by Spark Plasma Sintering. *Cryst. Growth Des.* **13,** 195–197 (2013).

122. Owen, E. . & Preston, G. . The atomic structure of two intermetallic compounds. *Struct. Intermet. Compd.* **36,** 341–348 (1924).

123. Franke, P. & Neushutz, D. Mg-Si. in *Binary Systems. Part 3: Binary Systems from Cs-K to Mg-Zr* (1983).

124. Barlock, J. G. & Mondolfo, L. F. Structure of som aluminium-iron-magnesium-manganese-silicon alloys. *Zeitschrift fuer Met.* **66,** 605–611 (1975).

125. Voort, G. F. Vander. Volume 9: Metallography and Microstructures. in *ASM Handbook Set* (2004).

126. Yamasaki, T., Okada, S., Kamamoto, K. & Kudou, K. Crystal Growth and Properties of Manganese-silicon System Compounds by High-temperature Tin Solution Method. *Psr.Kangnam.Ac.Kr* **14,** 275–279 (2012).

127. Zhou, a. J. *et al.* Composites of Higher Manganese Silicides and Nanostructured Secondary Phases and Their Thermoelectric Properties. *J. Electron. Mater.* **38,** 1072–1077 (2009).

128. Schmitt, A. L., Higgins, J. M., Szczech, J. R. & Jin, S. Synthesis and applications of metal silicide nanowires. *J. Mater. Chem.* **20,** 223 (2010).

129. Okamoto, H. Manganese Silicon Phase diagram. *J. Phase Equilibria* **12,** 505–507 (1991).

130. Predel, B. & Heidelberg, S. B. Fe-Si (Iron Silicon). *Gr. IV Phys. Chem.* **5e,** 1–6 (1995).

131. Mittermeier, T., Madkikar, P., Wang, X., Gasteiger, H. A. & Piana, M. Probing transition-metal silicides as PGM-free catalysts for hydrogen oxidation and evolution in acidic medium. *Materials (Basel).* **10,** (2017).

132. Goldfarb, I., Cesura, F. & Dascalu, M. Magnetic Binary Silicide Nanostructures. *Adv. Mater.* **1800004,** 1–11 (2018).

133. Peng, Q., Yang, X., Ding, J., Wei, X. & Yang, J. Design of new molten salt thermal energy storage material for solar thermal power plant. *Appl. Energy* **112,** 682–689 (2013).

134. Wang, T., Mantha, D. & Reddy, R. G. Thermal stability of the eutectic composition in LiNO3NaNO3KNO3ternary system used for thermal energy storage. *Sol. Energy Mater. Sol. Cells* **100,** 162–168 (2012).

135. Grazulis, S. *et al.* Crystallography Open Database (COD): An open-access collection of crystal structures and platform for world-wide collaboration. *Nucleic Acids Res.* **40,** 420–427 (2012).

136. Leszczynski, J., Wojciechowski, K. T. & Malecki, A. L. Studies on thermal decomposition and oxidation of CoSb3. *J. Therm. Anal. Calorim.* **105,** 211–222 (2011).

137. LeBlanc, S. Thermoelectric generators: Linking material properties and systems engineering for waste heat recovery applications. *Sustain. Mater. Technol.* **1,** 26–35 (2014).

138. Azim, S. S., Satheesh, A., Ramu, K. K., Ramu, S. & Venkatachari, G. Studies on graphite based conductive paint coatings. *Prog. Org. Coatings* **55,** 1–4 (2006).

139. Moskon, J., Dominko, R., Cerc-Korosec, R., Gaberscek, M. & Jamnik, J. Morphology and electrical properties of conductive carbon coatings for cathode materials. *J. Power Sources* **174,** 683–688 (2007).

140. Zhixiong, H., Wenfeng, X. & Dongcai, C. The Thermal Decomposition Kinetics of Polysiloxane / Polymethylacrylate IPNs Materials. *J. Wuhan Univ. Technol.* **21,** 2–4 (2006).

141. Wacker Silicones. *Safety Data Sheet (1907/2006/EC) - SILRES 604*. **2.2,** (2015).

142. Girois, S. Effect of Iron Compounds (Oxide, Salt, or Complexes) on Poly(vinyl chloride) Thermal and Photochemical Stability. *J. Vinyl Addit. Technol.* **5,** (1999).

143. Zhou, W., Yang, H., Guo, X. & Lu, J. Thermal degradation behaviors of some branched and linear polysiloxanes. *Polym. Degr* **91,** 1471–1476 (2006).

144. Decker, O. H. & Zhou, W. J. Heat Resistant Powder Coatings. (2007). doi:10.1037/t24245-000

145. Wacker Silicones. *Silres ® 604 product information sheet*. (2014).

146. Gwent Group. *C2030519P4 Carbon Paste Product Information Sheet*. (2018).

147. Donelson, R. parabolic_dishes. (2011). Available at:

http://arena.gov.au/project/thermoelectric-generator-for-concentrated-solar-thermal-systems/. (Accessed: 24th April 2014)

148. Minnich, A. J., Dresselhaus, M. S., Ren, Z. F. & Chen, G. Bulk nanostructured thermoelectric materials: current research and future prospects. *Energy Environ. Sci.* **2,** 466–479 (2009).